

ALMA MATER STUDIORUM - UNIVERSITÀ DI BOLOGNA

SCUOLA DI INGEGNERIA E ARCHITETTURA

DIPARTIMENTO DI INGEGNERIA INDUSTRIALE

CORSO DI LAUREA IN INGEGNERIA ENERGETICA

TESI DI LAUREA

In

IMPATTO AMBIENTALE DEI SISTEMI ENERGETICI

**DESIGN AND OPTIMIZATION OF TURBO-EXPANDERS
FOR ORGANIC RANKINE CYCLES**

CANDIDATO
Paolo Gabrielli

RELATORE:
Prof. Ing. Andrea DePascale

CORRELATORI:
Prof. Fredrik Haglind
Ph.D. Leonardo Pierobon
R.A. Jesper Graa Andreasen

Anno Accademico 2012/2013

Sessione III

Abstract

In un mondo sempre più concentrato sulla necessità di fornire energia ad una popolazione crescente, riducendo al contempo le emissioni di anidride carbonica, i cicli Rankine organici rappresentano una possibile soluzione per il raggiungimento di questo obiettivo. Questo studio riguarda, nella fattispecie, il progetto e l'ottimizzazione di turbine assiali per i suddetti cicli Rankine organici. Da un punto di vista progettuale, i fluidi organici esibiscono caratteristiche particolari, come un basso salto entalpico, una bassa velocità del suono o grandi rapporti di espansione.

Un modello computazionale per la determinazione delle performance di turbine assiali è stato sviluppato e validato utilizzando dati sperimentali. Il modello permette di prevedere le performance dell'espansore con un range di accuratezza di $\pm 3\%$. Il processo di design è accoppiato con una procedura di ottimizzazione che prevede l'utilizzo di un algoritmo genetico. L'efficienza total-to-static della turbina rappresenta la funzione obiettivo dell'ottimizzazione.

La routine di calcolo è integrata in una più ampia analisi del ciclo termodinamico, fornendo il punto di design ottimale della turbina. Per prima cosa, il modello computazionale è utilizzato nel contesto della piattaforma offshore di Draugen, dove tre sistemi di recupero calore sono confrontati. Le prestazioni della turbina sono state analizzate per tre possibili cicli di bottoming: ciclo Rankine organico (operante ciclopentano come fluido di lavoro), ciclo Rankine a vapore, ciclo air bottoming. I risultati dello studio indicano la turbina a gas come la soluzione più efficiente ($\eta_{ts} = 0.89$), mentre la turbina a ciclopentano si dimostra essere la tecnologia più flessibile e più compatta (2.45 ton/MW and 0.63 m³/MW). Inoltre, la tesi evidenzia come per i cicli Rankine organico e a vapore, la configurazione di design ottimale per la turbina non coincide con quella del ciclo termodinamico. Questa conclusione suggerisce la possibilità di ottenere un'analisi più accurata includendo il modello computazionale della turbina all'interno delle simulazioni del ciclo termodinamico.

Di seguito, le prestazioni dell'espansore sono analizzate confrontando tre diversi fluidi organici: ciclopentano, MDM e R245fa. I risultati dello stu-

dio propongono l'MDM come il fluido più efficace da un punto di vista dell'efficienza della turbina ($\eta_{tt} = 0.89$). D'altra parte, il cyclopentano garantisce una maggiore potenza del ciclo organico ($P = 5.35$ MW), mentre l'R245fa rappresenta la soluzione più compatta (1.63 ton/MW and 0.20 m³/MW).

Infine, la tesi valuta come la composizione di una miscela binaria di isopentano/isobutano influenza le prestazioni del ciclo termodinamico e l'efficienza della turbina assiale. I risultati mostrano come l'uso di fluidi binari possa portare ad un incremento delle performance in entrambi i casi.

Abstract

In a world focused on the need to produce energy for a growing population, while reducing atmospheric emissions of carbon dioxide, organic Rankine cycles represent a solution to fulfil this goal. This study focuses on the design and optimization of axial-flow turbines for organic Rankine cycles. From the turbine designer point of view, most of these fluids exhibit some peculiar characteristics, such as small enthalpy drop, low speed of sound, large expansion ratio.

A computational model for the prediction of axial-flow turbine performance is developed and validated against experimental data. The model allows to calculate turbine performance within a range of accuracy of $\pm 3\%$. The design procedure is coupled with an optimization process, performed using a genetic algorithm where the turbine total-to-static efficiency represents the objective function.

The computational model is integrated in a wider analysis of thermodynamic cycle units, by providing the turbine optimal design. First, the calculation routine is applied in the context of the Draugen offshore platform, where three heat recovery systems are compared. The turbine performance is investigated for three competing bottoming cycles: organic Rankine cycle (operating cyclopentane), steam Rankine cycle and air bottoming cycle. Findings indicate the air turbine as the most efficient solution ($\eta_{ts} = 0.89$), while the cyclopentane turbine results as the most flexible and compact technology (2.45 ton/MW and 0.63 m³/MW). Furthermore, the study shows that, for organic and steam Rankine cycles, the optimal design configurations for the expanders do not coincide with those of the thermodynamic cycles. This suggests the possibility to obtain a more accurate analysis by including the computational model in the simulations of the thermodynamic cycles.

Afterwards, the performance analysis is carried out by comparing three organic fluids: cyclopentane, MDM and R245fa. Results suggest MDM as the most effective fluid from the turbine performance viewpoint ($\eta_{tt} = 0.89$). On the other hand, cyclopentane guarantees a greater net power output of the organic Rankine cycle ($P = 5.35$ MW), while R245fa represents the most compact solution (1.63 ton/MW and 0.20 m³/MW).

Finally, the influence of the composition of an isopentane/isobutane mixture on both the thermodynamic cycle performance and the expander isentropic efficiency is investigated. Findings show how the mixture composition affects the turbine efficiency and so the cycle performance. Moreover, the analysis demonstrates that the use of binary mixtures leads to an enhancement of the thermodynamic cycle performance.

Preface

The present thesis represents the final project of my Master's degree in Energy and Nuclear Engineering at the University of Bologna. The whole study has been carried out at Denmark Technical University, department of Mechanical Engineering, Thermal Energy section. The Master's thesis consists in a 30 ECTS project and it was performed by the 1st of October 2013 to the 28th of February 2014. Supervisors were Associate Professor Fredrik Haglind, Ph.D. student Leonardo Pierobon and Research Assistant Jesper Graa Andreasen from DTU and Researcher Andrea DePascale from The University of Bologna.

I would like to thank supervisors Fredrik Haglind and Andrea DePascale for giving me the possibility to write my thesis in one of the best universities in Europe. I discovered an inspiring environment where Ph.D., Researchers and Professors collaborate as a team to produce the highest-level research.

A special thanks must go to Leonardo Pierobon and Jesper Graa Andreasen for their help and their patience from the very first to the very last day of this Master's thesis. This was not an easy project and their help was fundamental for its completion.

Design and Optimization of Turbo-Expanders for Organic Rankine Cycles

Contents

Abstract	i
Abstract	iii
Preface	v
Table of Contents	x
List of Figures	xv
List of Tables	xix
Nomenclature	xxi
1 Introduction	1
1.1 Aims	1
1.2 Methodology	2
1.3 Computational Tools	4
1.4 Structure of the Thesis	4
2 Background	5
2.1 Organic Rankine Cycles	5
2.1.1 Introduction	5
2.1.2 ORC Technology	6
2.1.3 Expansion Machines for Organic Rankine Cycles	7
2.2 The Axial-Flow Turbine Stage	8
2.3 Losses Classification	10
2.3.1 Profile Loss	11
2.3.2 Secondary Loss	11
2.3.3 Tip Clearance Loss	11
2.3.4 Trailing Edge Loss	12

3	The Case of Study: Draugen Offshore Platform	13
3.1	Electricity Generation	15
4	Design of Axial-Flow Turbines	17
4.1	Elements of Preliminary Design of Turbomachinery	17
4.2	Methodology	22
4.2.1	Preliminary Calculations	23
4.2.2	Iterative Cycle	30
4.2.3	Multi-Stage Considerations	39
5	Validation of the Computational Model	41
5.1	Introduction	41
5.2	Methodology	41
5.3	Results & Discussion	42
5.3.1	Ideal Gas Model	42
5.3.2	Real Fluid Validation	48
6	Optimization of Axial-Flow Turbines	57
6.1	Introduction	57
6.1.1	The Genetic Algorithm	57
6.2	Methodology	58
7	Weight of Axial-Flow Turbines	61
7.1	Introduction	61
7.1.1	Materials for Axial-Flow Turbines	61
7.1.2	Main Components of Axial-Flow Turbines	62
7.2	Methodology	65
7.2.1	Shaft	66
7.2.2	Bearings	68
7.2.3	Bearing Casing	69
7.2.4	Discs	69
7.2.5	Blades	70
7.2.6	Shrouding	71
7.2.7	Gear Box	72
7.2.8	Feeding and Exhaust Ducts	73
7.2.9	Labyrinth seal	74
7.2.10	Casing	74
7.2.11	Total Weight and Volume Requirements	75
8	Applications	77
8.1	Optimal Design Point	78
8.2	Efficiency Chart	78
8.3	Comparison between ORC, SRC and ABC Axial Expanders	79
8.4	Axial-Flow Turbine Performance for different Working Fluids	80

8.5	Performance Analysis for Axial-Flow Turbines Operating Binary Fluids	81
9	Results And Discussion	83
9.1	Heat Recovery System for Draugen Offshore Platform	83
9.1.1	Optimal Design Point for the ORC Axial-Flow Turbine	83
9.1.2	Efficiency Chart	88
9.1.3	Comparison between ORC, SRC and ABC Axial Expanders	93
9.2	Axial-Flow Turbine Performance for different Working Fluids	106
9.2.1	Optimal Design	106
9.2.2	Efficiency Chart	114
9.3	Performance Analysis for Axial-Flow Turbines Operating with Binary Fluids	116
10	Conclusions	123
10.1	Accuracy of the Simulation Model	123
10.2	Draugen Offshore Platform Applications	124
10.3	Comparison of Organic Working Fluids	125
10.4	Effects of Binary Mixtures as Working Fluid	125
11	Future Work	127
	Bibliography	132
A	Elements of Gas Dynamics for Axial-Flow Turbines	133
A.1	General Equations of Fluid Motion	133
A.2	Total and Static Quantities	134
A.3	Speed of Sound and Mach Number	135
A.4	Fluid Motion through a Duct	137
A.4.1	Fluid Flow and Critical pressure Ratio	137
B	Axial-Flow Turbine Stage	145
B.1	The Mass Flow Function	145
B.2	Nozzle Losses	146
B.3	Rotor Losses	147
B.4	Work Equations for Axial-Flow Turbines	148
B.5	Total to Total and Total to Static Efficiency	149
C	Losses Classification	153
C.1	Profile Loss	153
C.2	Secondary Loss	154
C.3	Tip Clearance Loss	155
C.4	Trailing Edge Losses	155
C.5	Shockwave Losses	155

D	Input Data of the Design Process	157
E	Insights of Design Methodology	163
E.1	Deich Formula	163
E.2	Blade Geometry Considerations	164
E.3	Fluid Outlet Angles	165
F	Craig & Cox Figures	171
G	Validation of the Computational Model	177
G.1	Ideal Gas Model	177
G.1.1	Single-Stage Gas Turbine	177
G.1.2	Multi-Stage Gas Turbine	180
G.2	Real Fluid Model	183
G.2.1	Multi-Stage Gas Turbine	183
H	Optimization Results for Draugen Offshore Platform Applications	191
H.1	ORC Results	191
H.2	SRC Results	193
H.3	ABC Results	193
I	Optimization Results for the Fluid Comparison Application	195
I.1	Cyclopentane Results	195
I.2	MDM Results	197
I.3	R245fa Results	198

List of Figures

1.1 Schematic of the computational procedure	3
2.1 Schematic view of an ORC with (right) and without (left) recuperator, (Quoilin et al. (2013)).	6
2.2 Optimum operating map for three expanders technology and three target applications, (Quoilin et al. (2013)).	7
2.3 Steam axial-flow turbine, (Siemens (2013c)).	8
2.4 Schematic representation of stator and rotor cascades, (Carleton University (2013)).	9
2.5 Aerodynamic features in a turbine cascade (Dahlquist (2008)).	11
2.6 Blade terminology (Dahlquist (2008)).	12
3.1 The Draugen platform (Offshore and Technology (2012)). . .	13
3.2 Draugen field location in the North Sea (Statoil (2012)). . .	14
3.3 SGT500 Siemens industrial gas turbine (Siemens (2013b)) . .	15
4.1 Velocity triangles for stator and rotor	17
4.2 Flared annulus (Siemens (2013a)).	18
4.3 Velocity diagram with constant axial velocity, obtained using the computational code Mamba.	19
4.4 Smith chart (Smith (1965)).	21
4.5 Preliminary determination of velocity triangles, thermodynamics states and blade geometry	23
4.6 h-s diagram representing the expansion occurring in a turbine stage (Wikipedia (2011)).	28
4.7 Iterative cycle within the computational routine	31
4.8 Conventional steam turbine profile (Xylon (2011)).	32
4.9 Relationship between gas outlet angles and $\cos^{-1}(o/s)$ for "straight-backed" operating at low Mach numbers (Ainley & Mathieson (1951)).	33

4.10	After expansion from supersonic nozzle having optimum degree of divergence (Deich et al. (1965)), computed with Vavra equation, Macchi (1977)	34
4.11	Schematic of the overall computational routine.	40
5.1	Velocity triangles for stage 4 of the multi-stage gas turbine. Ideal gas computational model.	43
5.2	Blade geometry for stage 1 of the multi-stage gas turbine. Computational result.	46
5.3	Blade geometry for stage 4 of the multi-stage gas turbine. Real fluid computational model.	47
5.4	T-s diagram for the four-stages low speed turbine gas turbine. Real fluid computational model.	47
5.5	Velocity triangles for the single-stage gas turbine. Real fluid computational model.	50
5.6	Blade geometry for the single-stage gas turbine. Real fluid computational model.	51
5.7	T-s diagram for the single-stage gas turbine. Real fluid computational model.	51
5.8	Velocity triangles for the single-stage R113 turbine. Real fluid computational model.	54
5.9	Blade geometry for the single-stage R113 turbine. Real fluid computational model.	55
5.10	T-s total and static diagrams for the single-stage R113 turbine. Real fluid computational model.	56
6.1	Objective function versus number of generations.	59
7.1	Turbine blades (Wikipedia (2012)).	62
7.2	Turbine disc (Walter (2013)).	63
7.3	Turbine bearings (Direct industry (2013)).	64
7.4	Schematic of shrouded blade (Major Engine Section (2012)).	64
7.5	Weight calculation process.	67
7.6	Turbine shaft with bearing (IMTS (2014)).	68
7.7	Inlet end of axial-flow turbines with first disc (Walter (2013)).	70
7.8	High-pressure blade profile (Xylon (2011)).	71
7.9	Power transmission gear box (ACE (2014)).	72
8.1	T-s diagram for cyclopentane, MDM and R245fa.	81
9.1	Velocity triangles of the optimal ORC single-stage turbine. Draugen offshore platform.	84
9.2	Blade geometry of the optimal ORC single-stage turbine. Draugen offshore platform.	86

9.3	T-s static diagram of the optimal ORC single-stage turbine. Draugen offshore platform.	86
9.4	Breakdown of the weight of the optimal ORC single-stage turbine. Draugen offshore platform.	88
9.5	Total-to-static efficiency as a function of the specific speed for p_{01} equal to 5, 10, 20, 30 bar. ORC single-stage axial turbine.	88
9.6	Group 1 loss fractions as a function of specific speed. ORC single-stage axial turbine.	90
9.7	Group 1 overall loss as a function of specific speed. ORC single-stage axial turbine.	91
9.8	Group 2 overall loss as a function of specific speed. ORC single-stage axial turbine.	92
9.9	Velocity triangles for ORC, SRC and ABC turbines single-stage axial turbines.	96
9.10	Blade geometry for ORC, SRC and ABC single-stage axial turbines.	98
9.11	T-s static diagram for ORC, SRC and ABC single-stage axial turbines.	99
9.12	Breakdown of the weight of ORC, SRC and ABC single-stage axial turbines.	101
9.13	Total-to-static efficiency as a function of the specific speed at design inlet pressure for ORC, SRC and ABC single-stage axial turbines.	102
9.14	Group 1 loss for SRC and ABC single-stage axial turbines.	104
9.15	Group 2 loss for SRC and ABC single-stage axial turbines.	105
9.16	Velocity triangles for the three ORC single-stage axial turbines.	107
9.17	Blade geometry for the three ORC single-stage axial turbines.	110
9.18	T-s static diagram for the three ORC single-stage axial turbines.	111
9.19	Breakdown of the weight for the three ORC single-stage axial expanders.	113
9.20	Total-to-static efficiency as a function of the specific speed; three inlet pressures for each fluid.	115
9.21	Total-to-static efficiency as a function of the specific speed; design pressure for each fluid.	116
9.22	Net power output as a function of the mixture composition for $\eta_{tt} = 0.8$	118
9.23	Expander efficiency as a function of the mixture composition.	118
9.24	Net power output as a function of fluid composition. Constant and variable expander efficiency.	119
9.25	Group 1 loss contributions as a function of the fluid composition.	120
9.26	Group 1 overall loss as a function of the fluid composition. Analysis of expander performance using binary mixtures . . .	121
9.27	Group 2 total loss as a function of the fluid composition. . . .	122

A.1	Stage expansion h-s diagram, (Wikipedia (2011)).	134
A.2	Horizontal-axis, constant section, free friction duct with pressure wave	135
A.3	Horizontal-axis, free friction duct with assigned upstream total conditions	137
A.4	Fluid velocity and speed of sound as functions of the ratio T_2/T_{01}	138
A.5	Mass velocity as a function of the pressure ratio	140
A.6	Mass flow rate as a function of the Mach number of the downstream section	142
B.1	Velocity reduction coefficient for the nozzle as a function of the pressure ratio for different fluid deviations	147
B.2	Velocity reduction coefficient for the rotor as a function of the fluid deviation	148
C.1	Aerodynamic features in a turbine cascade, (Carleton University (2013)).	153
C.2	Blade terminology, (Dahlquist (2008)).	154
F.1	Craig & Cox (1971) Fig. 1	171
F.2	Craig & Cox (1971) Fig. 3	171
F.3	Craig & Cox (1971) Fig. 4	172
F.4	Craig & Cox (1971) Fig. 5	172
F.5	Craig & Cox (1971) Fig. 6	173
F.6	Craig & Cox (1971) Fig. 7	173
F.7	Craig & Cox (1971) Fig. 8	173
F.8	Craig & Cox (1971) Fig. 9	174
F.9	Craig & Cox (1971) Fig. 17	174
F.10	Craig & Cox (1971) Fig. 18	175
F.11	Craig & Cox (1971) Fig. 19	175
F.12	Craig & Cox (1971) Fig. 21	176
G.1	Velocity triangles for the single-stage gas turbine. Ideal gas computational model.	179
G.2	Blade geometry for the single-stage gas turbine. Ideal gas computational model.	179
G.3	T-s static diagram for the single-stage gas turbine. Ideal gas computational model.	180
G.4	Velocity triangles for stage 1 of the multi-stage gas turbine. Computational results.	181
G.5	Velocity triangles for stage 2 of the multi-stage gas turbine. Computational results.	181
G.6	Velocity triangles for stage 3 of the multi-stage gas turbine. Computational results.	182

G.7	Blade geometry for stage 2 of the multi-stage gas turbine. Computational result.	182
G.8	Blade geometry for stage 3 of the multi-stage gas turbine. Computational result.	183
G.9	Velocity triangles of stage 1 of the multi-stage gas turbine. Real fluid computational model.	185
G.10	Velocity triangles of stage 2 of the multi-stage gas turbine. Real fluid computational model.	186
G.11	Velocity triangles of stage 3 of the multi-stage gas turbine. Real fluid computational model.	186
G.12	Velocity triangles of stage 4 of the multi-stage gas turbine. Real fluid computational model.	187
G.13	Blade geometry of stage 1 of the multi-stage gas turbine. Real fluid computational model.	187
G.14	Blade geometry of stage 2 of the multi-stage gas turbine. Real fluid computational model.	188
G.15	Blade geometry of stage 3 of the multi-stage gas turbine. Real fluid computational model.	188
G.16	Blade geometry of stage 4 of the multi-stage gas turbine. Real fluid computational model.	189
G.17	T-s diagram for the four-stage low speed gas turbine. Real fluid computational model.	190

Design and Optimization of Turbo-Expanders for Organic Rankine Cycles

List of Tables

3.1	Design point specification for the Siemens SGT500 (Siemens (2013b)).	16
4.1	Input data for the design routine.	24
4.2	Division of stage losses by Craig & Cox (1971).	35
5.1	Major input data for the validation process against Kotzing & Evers (1985).	43
5.2	Part A - Validation results for stage 1 and stage 2 of multi-stage gas turbine. Computational results.	44
5.3	Part B - Validation results for stage 3 and stage 4 of multi-stage gas turbine. Computational results.	45
5.4	Efficiency and power for the multi-stage gas turbine. Computational results.	45
5.5	Major input data for the validation process against Stabe et al. (1984).	48
5.6	Validation result the single-stage gas turbine. Real fluid computational model.	49
5.7	Major input data for the validation process against Verneau (1987).	52
5.8	Validation results for the single-stage R113 turbine. Real fluid computational model.	53
6.1	Optimization variables with lower and upper constrains.	60
7.1	Density of materials used for modelling the axial-flow turbine (Saravanamuttoo et al. (2009)).	65
7.2	Q factors defining the geometrical proportions of the turbine.	66
8.1	Cycle requirements imposed to the design and optimization process.	78
8.2	Modelling conditions for the ORC operating binary mixtures as working fluids.	82

9.1	Design Boundary conditions for the ORC single-stage axial-flow turbine. Draugen offshore platform.	83
9.2	Ideal set of optimizing parameters for the ORC single-stage turbine. Draugen offshore platform.	84
9.3	Optimal design features of the ORC single-stage turbine. Draugen offshore platform.	85
9.4	Weight and volume requirements for each component of the optimal ORC single-stage turbine. Draugen offshore platform	87
9.5	Maximum efficiency and optimal specific speed for variable inlet pressures. ORC single-stage axial turbine.	89
9.6	Boundary conditions for the design of ORC, SRC and ABC single-stage axial turbines.	94
9.7	Optimal design for ORC, SRC and ABC single-stage axial turbines.	95
9.8	Weight and volume requirements for ORC, SRC and ABC single-stage axial turbines.	97
9.9	Boundary conditions for the three ORC single-stage axial turbines.	106
9.10	Optimizing variables for the three ORC single-stage axial turbines.	108
9.11	Optimal design features for the three ORC single-stage axial turbines.	109
9.12	Weight and volume requirements for the three ORC single-stage axial turbines.	112
9.13	Maximum efficiency and optimal specific speed; three different pressures for each fluid are reported.	114
9.14	Optimal ORC design, in terms of maximum power output, as a function of fluid composition $\eta_{tt} = 0.8$	117
9.15	Optimal ORC design, in terms of maximum power output, as a function of fluid composition for variable η_{tt}	119
A.1	Critical pressure ratio for some fluids of interests	139
D.1	Input parameters for the design routine: optimizing parameters	157
D.2	Input parameters for the design routine: fixed variables . . .	158
D.3	Input parameters for the design routine: thermodynamic cycle parameters	158
G.1	Validation results for the single-stage gas turbine. Ideal gas computational model.	178
G.2	Part A - Validation results for Stage 1 and stage 2 of the multi-stage gas turbine. Real fluid computational model. . . .	184
G.3	Part B - Validation results for the Stage 3 and Stage 4 of the multi-stage gas turbine. Real fluid computational model. . . .	184

G.4	Efficiency and power of the four-stage low speed gas turbine. Real fluid computational model.	185
H.1	Optimization results for the ORC single-stage axial-flow turbine, $p_{01} = 30$ bar.	191
H.2	Optimization results for the ORC single-stage axial-flow turbine, $p_{01} = 20$ bar.	192
H.3	Optimization results for the ORC single-stage axial-flow turbine, $p_{01} = 10$ bar.	192
H.4	Optimization results for the ORC single-stage axial-flow turbine, $p_{01} = 5$ bar.	192
H.5	Optimization results for the SRC single-stage axial-flow turbine, $p_{01} = 12.57$ bar (design pressure).	193
H.6	Optimization results for the ABC single-stage axial-flow turbine, $p_{01} = 2.46$ bar (design pressure).	193
I.1	Optimization results for the cyclopentane single-stage axial-flow turbine, $p_{01} = 40$ bar.	195
I.2	Optimization results for the cyclopentane single-stage axial-flow turbine, $p_{01} = 30$ bar.	196
I.3	Optimization results for the cyclopentane single-stage axial-flow turbine, $p_{01} = 20$ bar.	196
I.4	Optimization results for the MDM single-stage axial-flow turbine, $p_{01} = 13$ bar.	197
I.5	Optimization results for the MDM single-stage axial-flow turbine, $p_{01} = 8.5$ bar.	197
I.6	Optimization results for the MDM single-stage axial-flow turbine, $p_{01} = 4$ bar.	197
I.7	Optimization results for the R245fa single-stage axial-flow turbine, $p_{01} = 33$ bar.	198
I.8	Optimization results for the R245fa single-stage axial-flow turbine, $p_{01} = 24$ bar.	198
I.9	Optimization results for the R245fa single-stage axial-flow turbine, $p_{01} = 17$ bar.	199

Design and Optimization of Turbo-Expanders for Organic Rankine Cycles

Nomenclature

Symbols

A	Area	[m ²]
b	Blade backbone length	[m]
C	Absolute fluid velocity	[m/s]
C _p	Constant pressure specific heat	[kJ/(kg K)]
CR	Contraction ratio	
C _v	Constant volume specific heat	[kJ/(kg K)]
c	Axial chord	[m]
D	Diameter	[m]
E	Enthalpy drop	[kJ/kg]
e	Back surface curvature radius	[m]
F	Thermodynamic function, Efficiency debit (wet loss)	
FL	Lift parameter	
g	Gravity acceleration	[m/s ²]
h	Specific enthalpy, Blade height	[kJ/kg], [m]
H/K	Boundary layer wake form-to-energy factor ratio	
i	Incidence	[°]
k	Specific heats ratio	
L	Blade overlap	[m]
l	Length	[m]
M	Mach number, Molar mass	[], [kg/kmol]
\dot{m}	Mass flow rate	[kg/s]
N	Rotational speed	[rpm]
N _a	Alternator rotational speed	[rpm]
N _s	Specific speed	
n	Number	
o	Opening	[m]
p	Pressure	[bar]
pr	Pressure ratio	
Q	Geometrical factor for weight calculation, vapour quality	

q	Specific heat exchanged by the system	[kJ/kg]
qM	Area ratio for isentropic flow	
R	Ideal gas constant	[J/(mol K)]
Re	Reynolds number	
r	radius	[m]
rec	Kinetic energy recovery coefficient	
s	Pitch, Specific entropy	[m], [kJ / (kg K)]
srcl	Stator-rotor clearance	[m]
T	Temperature	[K]
t	Thickness	[m]
U	peripheral velocity	[m/s]
V	Volume	[m ³]
v	Specific volume	[m ³ /kg]
W	Relative velocity	[m/s]
Ws	Specific work exchanged by the system	[kJ/kg]
w	Weight	[kg]
X	Dimensional loss coefficient	[MJ/kg]
x	Mass/molar fraction for binary fluids	
Y	Dimensionless loss coefficient	
z	Fluid height, Number of blades	[m], []

Greek Characters

α	Fluid absolute velocity angle	[°]
β	Fluid relative velocity angle	[°]
γ	Velocity reduction coefficient	
Γ	Thermodynamic losses of the system	[kJ/kg]
δ	Flare angle	[°]
Δ	Variation	
ϵ	Error	
ζ	Restriction factor	
η	Efficiency	
θ	Blade angle	[°]
Λ	Degree of reaction	
ρ	Density	[kg/m ³]
ϕ	Flow Coefficient	
χ	Loss correction factor	
ψ	Stage loading coefficient	
ω	Angular velocity	[rad/s]

Subscripts

a	Axial, opening condition (figure 4.10)
abs	Absolute
an	Annular
b	Bearing
bc	Bearing casing
bcb	Bearing casing base
bl	Blade
c	Casing
cd	Converging - diverging
crit	Critical conditions
d	Discs
des	Design point
e	Electric
ex	External radius
exh	Exhaust duct
feed	Feeding duct
g	Guess value
gb	Gear box
gbc	Gear box casing
i	Incidence
in	Inner radius, inlet section
is	Isentropic
K	Tip clearance
lab	Labyrinth seal
m	Mean radius
M	Mach
min	Minimum value
mass	Mass fraction
max	Maximum value
mol	Molar fraction
N	Nozzle
o	Opening section
P	Profile losses
R	Rotor
r	Root radius
rel	Relative
S	Stage, Secondary losses
s	Sound
sh	Shaft
spec	Specific
sr	Shrouding
st	stages

t	Tip radius
te	Trailing edge
tec	Trailing edge curvature
tot	Global
ts	Total-to-static
tt	Total-to-total
w	Whirl (tangential)
wh	Wheel
0	Total quantity, Basic loss coefficient
1	Section 1 of the stage: inlet nozzle
2	Section 2 of the stage: outlet nozzle
2'	Section 2' of the stage: inlet rotor
3	Section 3 of the stage: outlet rotor
I	Group 1 losses
II	Group 2 losses

Abbreviations

ABC	Air Bottoming Cycle
bcf	Billion cubic feet
CHP	Combined Heat and Power
CSP	Concentrated Solar Power
EA	Evolutionary Algorithm
GA	Genetic Algorithm
GBS	Gravity Based Structure
GHG	Green-House Gases
GIIP	Gas Initially In Place
HC	Hydrocarbon
HP	High Pressure
ICE	Internal Combustion Engine
GWP	Global Warming Potential
MFF	Mass Flow Function
mmbbls	Million of barrels
ODP	Ozone Depletion Potential
ORC	Organic Rankine Cycle
ORC-RO	Organic Rankine Cycle with Reverse Osmosis
rpm	race per minute
SRC	Steam Rankine Cycle
STOIP	Stop Tank Oil Initially In Place
srcl	stator-rotor clearance
1-D	One Dimensional
2-D	Two Dimensional
3-D	Three Dimensional

1

Introduction

The adoption of organic fluids instead of steam or gases as working fluid in power cycles exhibits significant advantages in a variety of applications. One of the most important is the possibility of designing low-stress, efficient and low-priced turbines in power and temperature ranges for which steam turbines would become unattractively costly and inefficient. The thermal and transport analysis are the same used for gas and steam turbines. Nevertheless, fluid properties play such an important role on the design process, that the optimization of an organic fluid turbine is likely to yield solutions that can appear quite unusual for a gas or steam turbine designer.

1.1 Aims

The core of the thesis consists in the development of a simulation model for the design and optimization of axial-flow turbines. In particular, turbine performance, blade geometry, thermodynamic states and weight requirements are predicted.

The first step in the design and optimization process of axial-flow turbines is to define the function to be optimized; next a set of variables able to completely describe the geometry and the aerodynamics of the machine should be selected. Additionally, a methodology for the evaluation of the losses must be defined. This study uses the methodology suggested by Craig & Cox (1971), which appears the most suitable in the case of organic fluids (see Macchi (1977)).

Thermodynamic cycles are often simulated by assuming a constant isentropic efficiency for the expander. Therefore, the scope of the thesis is to provide a computational tool that can be included in more comprehensive simulation models of thermodynamic cycles. This would allow to obtain more accurate calculations of the cycles performance.

First, the calculation routine is applied to the case of study of the Draugen offshore platform, described in Chapter 3. In this context the thesis enters in the analysis performed by Pierobon et al. (2013) aimed at defining the best heat recovery system for the platform. In particular, the topping cycle is constituted by the Siemens gas turbine SGT500, while three competing bottoming cycles are compared: organic Rankine cycle (ORC), steam Rankine cycle (SRC) and air bottoming cycle (ABC). In the above mentioned study the three thermodynamic cycles are modelled assuming a constant isentropic efficiency for the turbine. For this reason, the thesis investigates the performance of the ORC, SRC and ABC turbines at design conditions obtained for the three cycles. Additionally, the turbine efficiency is studied for different mass flow rates and inlet pressures. Finally, the three expanders are compared in terms of weight and volume requirements.

In a second moment, the study compares the turbine performance for three organic working fluids: cyclopentane, MDM and R245fa. The goal of this study is to understand how the working fluid affects turbine performance and geometry. Indeed, a new criterion for the selection of the working fluid for organic Rankine cycles might stem from the analysis of the expander performance.

Finally, the thesis investigates the possible benefits, in terms of turbine and cycle performance, arising when using binary mixtures as working fluids.

1.2 Methodology

The thesis started with a study of axial turbine theory, which can be found, for example, in Negri di Montenegro et al. (2009) and Saravanamuttoo et al. (2009). Then, it proceeded with the actual writing of the computational routine.

The overall procedure is summarized in figure 1.1. The computational routine can be seen as a box containing progressively smaller boxes. It began with the definition of a set boundary conditions, imposed by the optimal design configuration of the thermodynamic cycle. These boundary conditions represented the input data for the design and optimization process which then rendered the optimal axial-flow turbines. Ten optimizing variables were selected. They were mainly geometrical parameters, partially defining the turbine geometry, but also included some dimensionless parameter, such as the flow coefficient and the stage loading coefficient. When multi-stage configurations were examined, the computational model defined each stage separately, maintaining the maximum efficiency of the overall turbine as objective function of the optimization.

The computational model can be ideally divided in two branches:

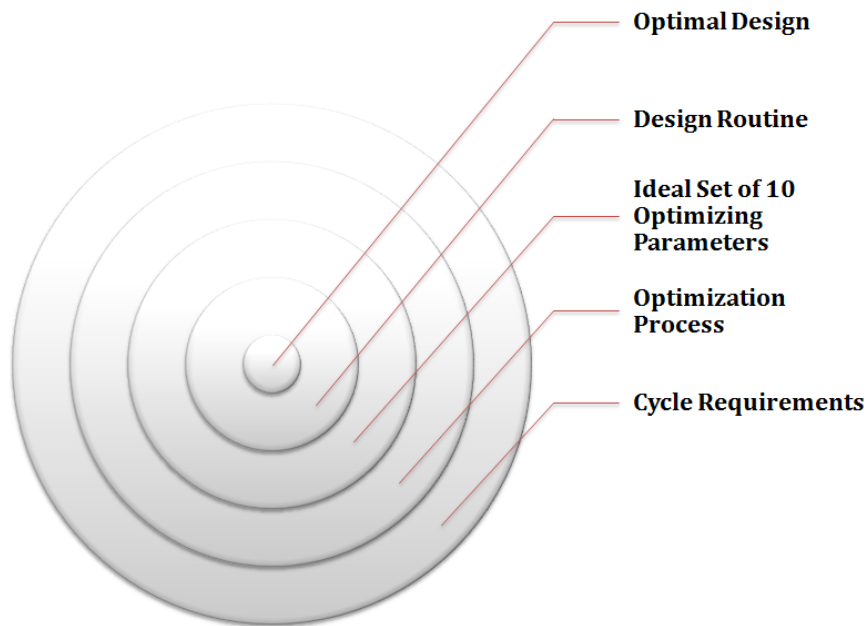


Figure 1.1: Schematic of the computational procedure

- Evaluation of the turbine performance, blade geometry, thermodynamic states and velocity diagrams;
- Estimation of turbine weight and volume requirements.

The former section involved an iterative process based on the stage efficiency, while the latter section proceeded with the weight calculation receiving the turbine geometry as an input.

Initially, the design procedure was carried out with a one-dimensional (1-D) approach, aimed at the definition of blade profile and the evaluation of losses at mean radius. Then, assuming *Free Vortex Theory*, some elements of two-dimensional (2-D) analysis were included. In this way, blade geometry, velocity triangles and losses were assessed at root, mean and tip radius, as recommended by Craig & Cox (1971).

The computational model was validated against experimental data provided by Stabe et al. (1984), Verneau (1987) and Kotzing & Evers (1985). The validation process included performance, geometry and thermodynamic properties of the expanders. It should be pointed out that the section concerning the weight calculation was not validated and provided for an approximated value of heaviness and compactness of axial-flow turbines.

1.3 Computational Tools

The computational code, named *Mamba*, was developed using the programming language MATLAB, provided by MathWorks (2013). MATLAB, acronym for Matrix Laboratory, is a numerical computing environment and fourth generation programming language developed by MathWorks. The thermodynamic properties were calculated using the database provided by the open-source *CoolProp* (Bell et al. (2014)), developed at the University of Liege, and by the commercial software *Refprop*, developed by Lemmon et al. (2007) at NIST. Also, plots were built using the commercial package *Excel 2010*.

The code involved an iterative method based on the stage efficiency. The convergence was considered to be reached when the discrepancy between two following iterations equalled a value lower than 0.0001. For all the investigated designs the convergence was reached within 50 iteration, with an average running time lower than 10 second per stage. On the contrary, the running time for the optimization strongly depended on the nature of the examined fluids and ranged from less than 15 minutes for air to more than 2 days for a mixture of isobutane and isopentane.

The computational code allow to determine the turbine performance with an accuracy of $\pm 3\%$.

1.4 Structure of the Thesis

The structure of the report can be summarized as follows:

- Chapter 2 provides the background for the present study.
- Chapter 3 concerns the description of the Draugen offshore platform, representing the case of study.
- Chapter 4, 5, 6 and 7 presents the methodology section of the thesis: chapter 4 describes the routine for the axial-flow turbine design; chapter 5 reports the validation of the computational model; chapter 6 presents the optimization methodology; chapter 7 describes the methodology followed for the weight estimation.
- Chapter 8 lists the investigated applications of the computational model.
- Chapter 9 presents and discusses the results of the thesis.
- Chapter 10 draws the main conclusions.
- Chapter 11 provides for some suggestions for further studies.

2

Background

2.1 Organic Rankine Cycles

2.1.1 Introduction

The world energy consumption has risen to a level never reached before, releasing in the same process large quantity of CO₂ into the atmosphere. Current concerns over climate change call for measures to reduce greenhouse gases emissions, which can be summarized in the following modifications (Quoilin et al. (2013)):

- A decrease in the energy intensity of buildings and industry;
- A shift from fossil fuels towards electricity in the fields of transportation and space heating;
- Clean power generation by a massive shift towards renewable energies;
- A reinforcement of the grid capacity and inter-regional transmission lines to absorb daily and seasonal fluctuations.

Among the proposed solutions, the organic Rankine cycles could play a non-negligible role. In particular:

- They can have a beneficial effect on the energy intensity of industrial processes, mainly by recovering waste heat. This approach is known as combined heat and power generation (CHP);
- They can be used to convert renewable heat sources into electricity. This mainly includes geothermal, biomass and solar sources (CSP) (Quoilin et al. (2013)).

Furthermore, in a rather new framework of decentralized conversion of low temperature heat into electricity, the ORC technology offers an interesting alternative, also due to its modular feature: a similar ORC system can be used with little modifications, in conjunction with various heat sources. These aspects make the ORC more suitable than steam power to the conversion of renewable energy sources, whose availability is generally more localized than that of fossil fuels, and whose temperature is lower than that of traditional fuels (see Quoilin et al. (2013)).

2.1.2 ORC Technology

Conceptually, the organic Rankine cycle is similar to a steam Rankine cycle and it involves the same components as a conventional steam power plant. The working principle is still based on the evaporation of a high pressure

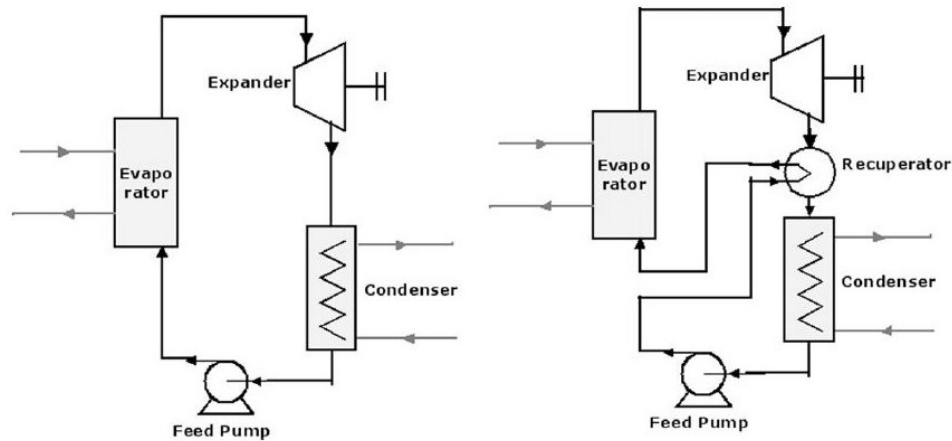


Figure 2.1: Schematic view of an ORC with (right) and without (left) recuperator, (Quoilin et al. (2013)).

liquid, which is in turn expanded to a lower pressure releasing mechanical work. After the expansion the working fluid is condensed and pumped to the high pressure, where the cycle restarts. Therefore, the basic components are the boiler, a work-producing expansion device, a condenser and a pump. However, the working fluid is an organic compound characterized by a lower ebullition temperature than water and allowing power generation from low heat source temperatures.

The layout of organic Rankine cycle is somewhat simpler than that of the steam Rankine cycle: there is no water-steam drum connected to the boiler, and one single heat exchanger can be used to perform the three evaporation phases: preheating, vaporization and super-heating. The variations of the cycle architecture are also more limited: reheating and turbine bleeding are generally not suitable for the ORC cycle, but a recuperator can be installed

as liquid preheater between the pump outlet and the expander outlet, as shown in figure 2.1. The simple architecture presented in the figure can be adapted and optimized depending on the target application.

The main applications of organic Rankine cycles range from solar power plants to biomass, geothermal energy and waste heat recovery. A very interesting overview on this topic is presented by (Quoilin et al. (2013)).

2.1.3 Expansion Machines for Organic Rankine Cycles

The performance of an ORC system strongly relates with that of the expander. The selection of the technology depends on the operating conditions and on the size of the system. Two main types of machines can be

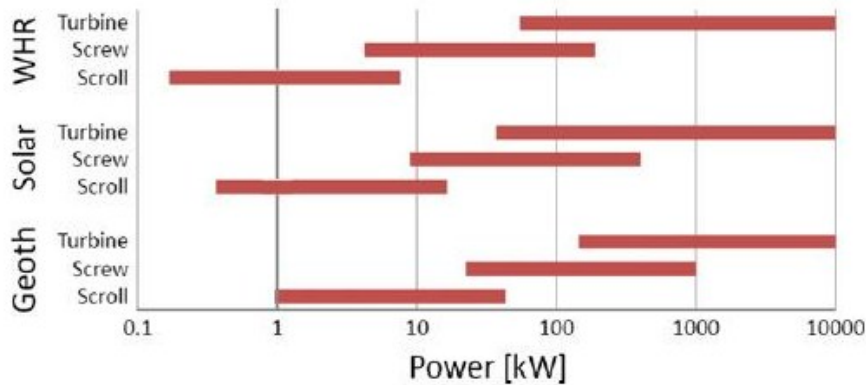


Figure 2.2: Optimum operating map for three expanders technology and three target applications, (Quoilin et al. (2013)).

distinguished: the turbo and positive displacement types. Displacement type machines are more appropriate in small-scale ORC units, as showed by figure 2.2, as they are characterized by lower flow rates, higher pressure ratios and much lower rotational speeds than turbo-machines. Since the present thesis is aimed at designing and optimizing a turbo-expander for organic Rankine cycles, it will focus only on turbo-machineries. In this category, a distinction is generally made between two main types of turbines: axial- and radial- flow turbines. This study will be concerned only with the former type.

Axial turbines show a distinct design when used in combination with high molecular weight working fluids. The main difference between organic fluids and steam is the enthalpy drop during the expansion, which is much higher for steam. As already mentioned, fewer stages are required in the case of an organic fluid. Even single-stage turbines can be employed for low or medium

temperature ORC cycles. Another characteristic of organic fluids is the low speed of sound. As a result, this speed is reached much sooner in an ORC than in a steam cycle and constitutes an important limitation as high Mach numbers are related to higher irreversibility and lower turbine efficiencies. Radial inflow turbines are designed for high pressure ratios and low working fluid flow rates. Their geometry allows higher peripheral speeds than for axial turbines, and therefore a higher enthalpy drop per stage. They also have the advantage of maintaining an acceptable efficiency over a large range of part-load conditions (see Quoilin et al. (2013)).

2.2 The Axial-Flow Turbine Stage



Figure 2.3: Steam axial-flow turbine, (Siemens (2013c)).

Turbo-machineries are apparatus made up by several stator, or nozzle, blade passages, each of them in series with a rotating vane (rotor) coupled with a shaft, in order to exchange mechanical power with the external environment. Turbines, for which the rotation of the shaft is provoked by the movement of the rotor blades, and thus power is produced, are called *driving machines*. On the other hand, compressors, for which the shaft causes the rotation of the rotor blades, absorb power and are called *operating machines*. Focusing on turbines, the main function of the stator passages is to accelerate the fluid in order to produce work, actually extracted in the rotor vanes, due to the rotation of the shaft. Figure 2.3 displays an example of steam axial-flow turbine, i.e. with the fluid moving mainly in the direction of the axis of the turbo-machine. The figure shows on the external circumference a series of blades, a *cascade*, alternately mounted on a steady drum (nozzle) and on a moving drum (rotor) which is rotating with angular velocity ω . The word

"vane" indicates the physical space between two blades; it represents the duct in which the fluid evolves. A schematic representation of stator and rotor cascades is showed in figure 2.4.

The study of the stage of axial-flow turbines must start from the analysis of

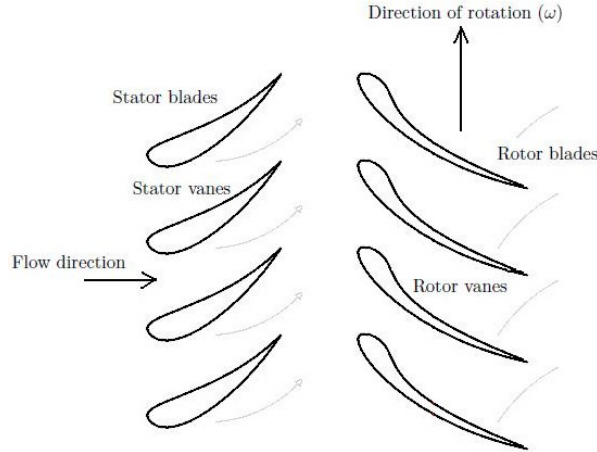


Figure 2.4: Schematic representation of stator and rotor cascades, (Carleton University (2013)).

those physical phenomena experienced by the fluid when crossing the vane between two blades. At this purpose, some elements of gas dynamics for axial-flow turbines are given in appendix A.

One of the key concepts in the investigation of axial flow turbines is represented by the efficiency of the stage (η). Two definitions can be used, depending on which type of enthalpy drop is accounted for. In particular, the *total-to-total* and *total-to-static* efficiency are given by the two equations below, respectively,

$$\eta_{tt} = \frac{h_{01} - h_{03}}{h_{01} - h_{03, is}} \quad (2.1)$$

$$\eta_{ts} = \frac{h_{01} - h_{03}}{h_{01} - h_{3, is}} \quad (2.2)$$

Where h indicates the enthalpy of the fluid; the subscript "0" refers to total conditions (Appendix A); the suffixes "1" and "3" indicate the different stations of the stage: inlet nozzle and outlet rotor, respectively. The total-to-total efficiency considers the total enthalpy drop, accounting for the kinetic energy of the fluid at the outlet of the rotor. On the contrary, the total-to-static efficiency involves the available enthalpy drop, without considering the exiting kinetic energy. For the central stages of multi-stage turbines, the total-to-total version appears more suitable, since the kinetic energy exiting from one stage is exploited, at least in part, in the downstream stage. On

the contrary, for single-stage turbines, as well as for the last stage of multi-stages turbines, the total-to-static version seems the best alternative since no kinetic energy is recovered in a following stage.

Other quantities involved in the analysis of a turbine stage are the specific work extracted at the shaft, also called *Euler work*, and the *degree of reaction*. It can be demonstrated (Appendix B) that the Euler work (Ws) is expressed as

$$Ws = U(C_2 \cos \alpha_2 + C_3 \cos \alpha_3) = U(C_{a2} \tan \alpha_2 + C_{a3} \tan \alpha_3) \quad (2.3)$$

Where U indicates the blade (peripheral) velocity, C is the absolute fluid velocity and α symbolizes the angle formed by the absolute fluid velocity and the axial direction; the subscript "a" refers to the axial direction, while "2" indicates the station at the outlet of the nozzle. Similarly, it can be proved (Appendix B) that the degree of reaction (Λ) is given by equations

$$\Lambda = \frac{W_3^2 - W_2^2}{C_2^2 - C_1^2 + W_3^2 - W_2^2} \quad (2.4)$$

Where W indicates the relative fluid velocity. The degree of reaction can also be expressed in terms of fluid enthalpy:

$$\Lambda = \frac{h_2 - h_3}{h_1 - h_3} \quad (2.5)$$

A turbine characterized by a degree of reaction equal to zero is called *impulse turbine*, while a *reaction turbine* has a degree of 0.5. Actually, the definition of the degree of reaction does not include any kind of loss. Therefore, the actual degree of reaction for an impulse turbine would be lower than zero. More insights on stage efficiency, Euler work and degree of reaction, together with a description of the losses occurring within stator and rotor, are provided by Appendix B.

2.3 Losses Classification

To handle the many different flow phenomena the overall loss in a row is divided into a number of different regions. These regions are then correlated separately and finally summed up to a total loss for the rotor, stator and total stage. In the following a brief description of the major types of loss included in this report is presented. It should be noted that many classifications have been proposed and that given here is only one of the possibles. Figure 2.5 reports the main aerodynamic features in a turbine cascade, helping in the comprehension of the losses classification. Additionally, figure 2.6 reports the main terminology of the blade. In this figure the angles are measured from the axial direction. A more detailed description of the different losses occurring within a turbo-machinery is provided by Appendix C.

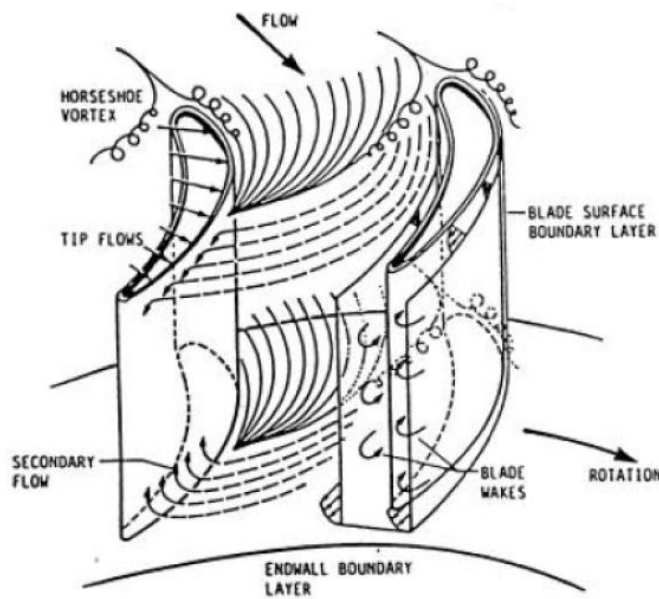


Figure 2.5: Aerodynamic features in a turbine cascade (Dahlquist (2008)).

2.3.1 Profile Loss

This is the loss that occurs on the blade surface due to increasing boundary layer, surface friction and flow blockage as the passage area is decreased because of an increase of the surface boundary layer thickness. It also includes the separation of boundary layer along the blade surface, and in some cases the trailing edge separation and downstream mixing.

2.3.2 Secondary Loss

This is the loss caused by the viscous and turbulent mixing and dissipation of energy when secondary flows and vortices are mixed together with the main flow and wall boundary layer. In the present work, the overall secondary loss is divided into two contributions: the fraction occurring inside the blade row, *secondary loss*, and that occurring in the space between the blade rows along the annular wall, *annulus loss*.

2.3.3 Tip Clearance Loss

The tip clearance loss is related with a leakage mass flow rate which is separate from the main flow. A distinction has to be made between shrouded and un-shrouded blades. In the first case, the leakage mass flow rate does not pass through the blades, therefore not performing any useful work. For

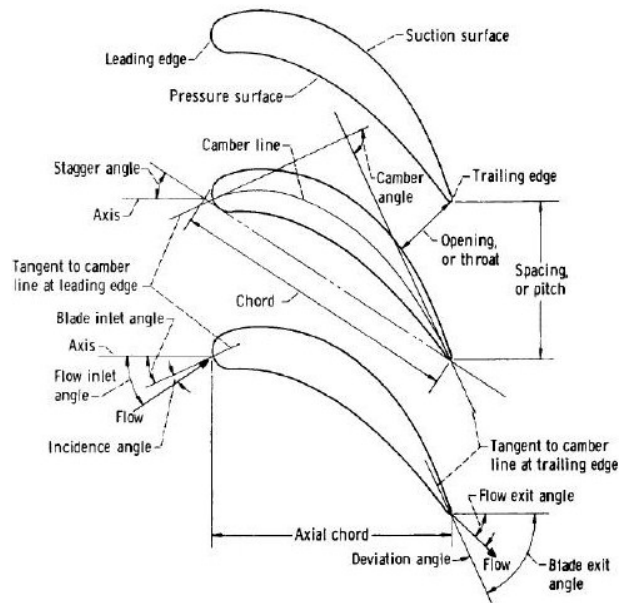


Figure 2.6: Blade terminology (Dahlquist (2008)).

un-shrouded blades the leakage occurs from the pressure to suction surface of the blade (see 2.6).

2.3.4 Trailing Edge Loss

According to Ainley & Mathieson (1955) the finite thickness of the trailing edge of the blade causes the flow to separate at both the pressure and suction surface close to the trailing edge and create a recirculation zone as can be seen in figure 2.5. In this wake the pressure is lower compared to the free stream pressure. Moreover, a high velocity gradient is seen between the free stream and the turbulent wake. The dissipation of energy is high as the wake is mixing out downstream.

3

The Case of Study: Draugen Offshore Platform



Figure 3.1: The Draugen platform (Offshore and Technology (2012)).

The Draugen oil field is located in the Haltenbanken of the North Sea and belongs to Norwegian continental shelf. The area (block 6407/9) is situated approximately 150 km north of Kristiansund in Norway and 200 Km south of the Arctic Circle, in water depths of 240 to 280 m (figure 3.2). The oil field was discovered in 1984 and named after Draugen, a fearsome sea figure

of Norse fairy tales. The production license PL093 was acquired by Royal Dutch Shell in the eighth licensing round in 1984. Government approval for field development was given in December of that year (see Statoil (2012)). The platform was installed in 1993, while the sub-sea structures designed



Figure 3.2: Draugen field location in the North Sea (Statoil (2012)).

for operation and maintenance were installed during the following months. Draugen was the first field to be developed in the Norwegian Sea, an area which later became one of the most important petroleum provinces in Norway. Norske Shell is the operator, holding a 26.20% interest. The remaining stake is held by Petoro (47.88%), BP Norge (18.36%) and Chevron (7.56%) (see Kable (2013)). The platform is a mono-pile gravity based structure (GBS) thrust five meters into the sea bed at a water depth of 251 m, being the first of its kind at that time (see Offshore and Technology (2012) and Dong Energy (2012)). The field went into production in 1993 having Norske Shell A/S as operator. The reservoir is made of sand stone which is situated 1650 m below the sea bed and is estimated to contain volumes of 1300 mmbbls (million barrels) stock tank oil initially in place (STOIP) and 420 bcf (billion cubic feet) gas initially in place (GIIP) (see Dong Energy (2012)). The structure has seven large concrete oil tanks (1.4 mmbbls capacity) situated on the seabed, which keep the platform in place. The oil tanks are connected to an off-loading buoy which exports the oil to a shuttle tanker once or twice per week (see Kandepu (2011)). The gas is exported through a small pipeline to the larger ATS-pipeline and then onwards to Karsto treatment plant. The concrete jacket of the GBS weights approximately 18500 tons and can accommodate 140 people at a time, 43 of which are regular crew (Andersen & Uhrbrand (2013)).

3.1 Electricity Generation

The platform requires electrical and mechanical energy to extract, process and transport oil and gas. The electricity is mainly used for gas compression, sea water lifts, pumping of oil/condensate and oil exportation. The platform operates in island (stand-alone grid) and has no onshore supply. Therefore, the required energy is provided by three 17 MW design load SGT500 turbines, manufactured by Siemens. The normal total electric load is estimated of 19 MW (gas compressors for the gas proceeding equipment and other pumps), while peak load of 24 MW occurs during the off-loading of oil to shuttle-tankers, during seawater lifting and during water injections. The turbines are fuelled by self-produced natural gas while diesel is kept for back-up. Only two out of three gas turbines are operating at a time, sharing 50% of the load each, while the third one is shut down for maintenance. This configuration guarantees that the required load can be supplied at any times and that the engine operates safety. Voltage and frequency are constantly controlled to be maintained at a value of 60 Hz and 11 kV respectively. A waste heat recovery unit is connected to each gas turbine generating heat for the condensate re-boiler and the crude oil heater (see Andersen & Uhrbrand (2013)).

The Siemens SGT500, showed in figure 3.3, is an aero-derivative twin-spool gas turbine and the engine model is the C-version launched in the beginning of 1980. The low firing temperature and the large capacious combustor en-



Figure 3.3: SGT500 Siemens industrial gas turbine (Siemens (2013b))

able the use of a wide range of fuels (gas fuels, liquid fuels and heavy fuels). In particular the low firing temperature contributes to excellent maintenance requirements: one overhaul every 9 years of operation on full load, one over-

haul every 18 years of operation at a 94% load. The compact layout and the easy on-site maintenance make this turbine adapt for offshore applications. Furthermore, in combined cycle the SGT500 has high efficiency independently from the kind of fuels. The compressor is a two multi-stages axial flow compressor with a pressure ratio of 13. It consists of 10 high pressure compression stages and 8 low pressure stages. There are seven annular combustion chambers with conventional combustion systems; the fuel-supply pressure required is 18 ± 0.5 bar. The turbine is a 3-stage turbine (1 high pressure stage and two low pressure stages), with a speed of 3600 rpm. The generator is designed as a 4-pole generator with a voltage of 11 kV and a frequency of 60 Hz. The design power generation is 16.5 MW_e and the electrical efficiency is 31.3%. At design the exhaust gas flow is 91.5 Kg/s and the exhaust temperature is $379.2 \text{ }^\circ\text{C}$. The temperature at the turbine inlet is $850 \text{ }^\circ\text{C}$. Table 3.1 summarizes the design specification for the SGT500. This

Table 3.1: Design point specification for the Siemens SGT500 (Siemens (2013b)).

Low pressure turbine stages	1
High pressure turbine stages	2
Low pressure compressor stages	10
High pressure compressor stages	8
TIT [$^\circ\text{C}$]	850
Exhaust Gas Temperature [$^\circ\text{C}$]	379.2
Exhaust gas mass flow [$^\circ\text{C}$]	91.5
Net power output [MW]	16.5
Heat rate [kJ/kWh]	11312

gas turbine represents the topping cycle for the applications investigated in the present work.

4

Design of Axial-Flow Turbines

4.1 Elements of Preliminary Design of Turbomachinery

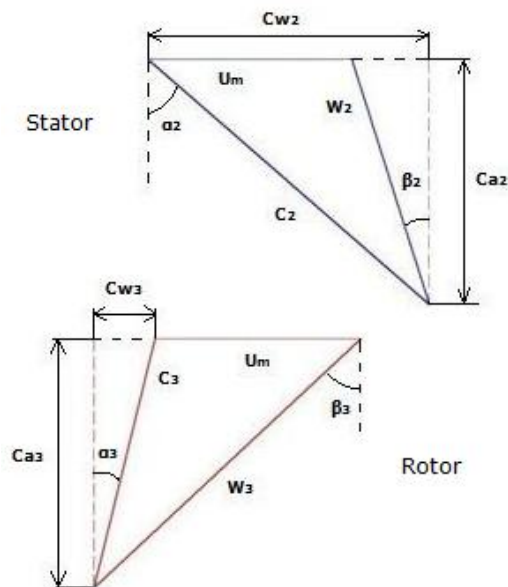


Figure 4.1: Velocity triangles for stator and rotor

A primary tool in the investigation of axial-flow turbines is given by the velocity triangles for stator and rotor, showed in figure 4.1. C and W sym-

bolize the absolute and relative fluid velocity, respectively; the subscripts "1", "2" and "3" indicates the stations of the stage: inlet nozzle, inlet rotor and outlet rotor, respectively; α and β are the angles formed by the absolute and relative velocity with the axial direction, respectively.

The gas enters the row of nozzle blades with a static pressure and temperature p_1, T_1 and a velocity C_1 ; it is expanded to p_2, T_2 and leaves with an increased velocity C_2 at an angle α_2 formed by the absolute velocity vector and the axial direction. The rotor blade inlet angle is chosen to suit the direction β_2 of the gas velocity W_2 relative to the blade at the inlet. β_2 and W_2 are found by vectorial subtraction of the blade speed U from the absolute velocity C_2 . After being deflected and usually further expanded in the rotor blade passages, the gas leaves at p_3, T_3 with relative velocity W_3 at angle β_3 . Vectorial addition of U yields magnitude and direction of the gas velocity at exit from the stage, C_3 and α_3 ; α_3 is known as *swirl angle*.

The present thesis assumed constant axial velocity through the stage. However, such hypotheses might imply a flared annulus as reported in figure 4.2 to accommodate the decrease in density as the gas expands through the stage. Usually, for a single-stage turbine C_1 is axial, i.e. $\alpha_1 = 0$ and

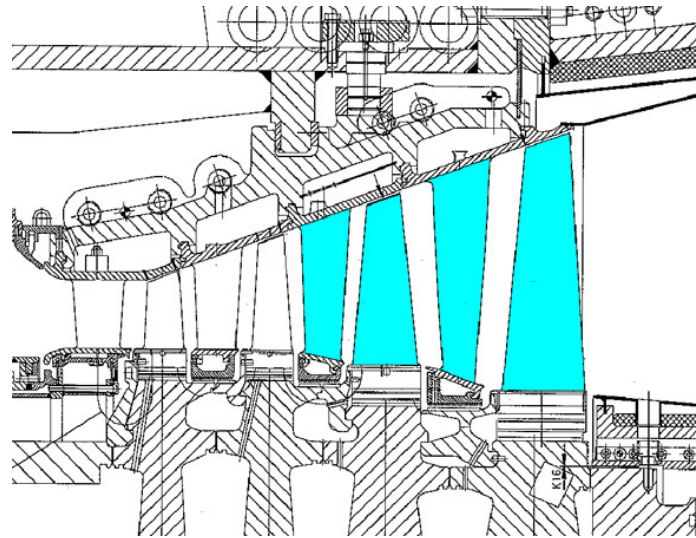


Figure 4.2: Flared annulus (Siemens (2013a)).

$C_1 = C_{a1}$. If on the other hand the stage is typical of many in a multi-stage turbine, C_1 and α_1 will probably be equal to C_3 and α_3 of the upstream stage, so that the same blade shapes can be used in successive stages: it is called a *repeating stage* configuration. In figure 4.1 the subscript "m" indicates that the blade speed U is considered at mean radius. However, because it increases with increasing radius, the shape of the velocity triangles varies from root to tip of the blade. In the present thesis a mean-line

one-dimensional (1-D) approach was initially followed, inserting some elements of two-dimensional (2-D) analysis in the calculation of the blade geometry and losses evaluation. Referring to figure 4.1, $(C_{w,2} + C_{w,3})$ represents the change in whirl (tangential) component of momentum per unit mass flow which produces the useful torque. The change in axial component, $(C_{a,2} - C_{a,3})$, produces an axial thrust on the rotor which may supplement or offset the pressure thrust arising from the pressure drop $(p_2 - p_3)$. With the restriction of constant axial velocity, when the velocity triangles are superimposed, the velocity diagram for the stage is given in figure 4.3. The

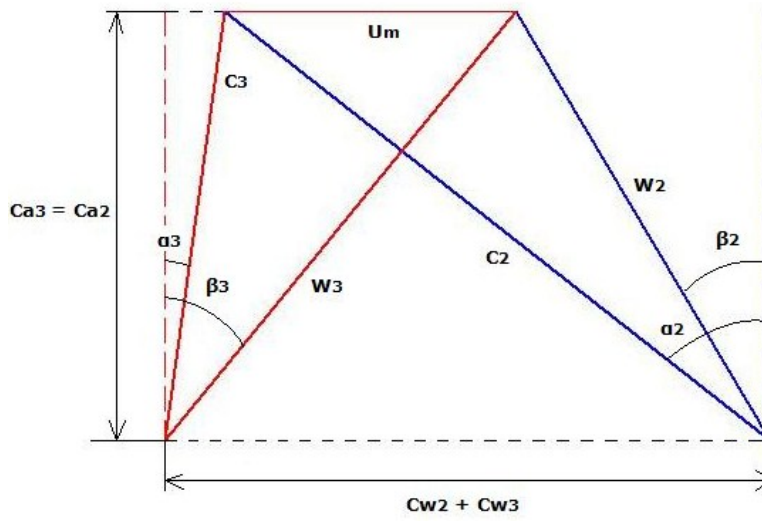


Figure 4.3: Velocity diagram with constant axial velocity, obtained using the computational code Mamba.

geometry of the diagram, along with $C_{a,2} = C_{a,3} = C_a$ gives immediately the relations

$$\frac{U_m}{C_a} = \tan\alpha_2 - \tan\beta_2 = \tan\beta_3 - \tan\alpha_3 \quad (4.1)$$

There are three dimensionless parameters found to be useful in turbine design. One, expressing the work capacity of the stage, is called the *blade loading coefficient* or *temperature drop coefficient*, ψ . This study adopted the NGTE practice (Saravanamuttoo et al. (2009)) and defined it as

$$\psi = \frac{2C_p \Delta T_0}{U_m^2} \quad (4.2)$$

Where the stagnation temperature drop in the stage (ΔT_0) is given for a perfect gas by

$$\Delta T_0 = \eta_S T_{01} \left[1 - \left(\frac{p_{03}}{p_{01}} \right)^{\frac{k-1}{k}} \right] \quad (4.3)$$

Where η_S is the isentropic stage efficiency. This study usually refers to the total-to-static efficiency since it is mainly focused on the analysis of single-stage turbines.

Another very useful parameter is the *degree of reaction* defined in chapter 2. With the assumption of constant axial velocity and $C_1 = C_3$, an approximated expression for Λ can be derived as suggested in Saravanamuttoo et al. (2009). In this case, the degree of reaction can be expressed as

$$\Lambda = \frac{C_a}{2U_m}(\tan\beta_3 - \tan\beta_2) \quad (4.4)$$

The third dimensionless parameter often referred to in axial-flow turbine design appears in both equations 4.2 and 4.4: it is the ratio C_a/U_m , called the *flow coefficient*, ϕ . With the constant velocity assumption this coefficient is equal for stator and rotor. Using this definition, equations 4.2 and 4.4 can be written, respectively,

$$\psi = 2\phi(\tan\beta_2 + \tan\beta_3) \quad (4.5)$$

$$\Lambda = \frac{\phi}{2}(\tan\beta_3 - \tan\beta_2) \quad (4.6)$$

At this point the gas angles can be expressed in terms of ψ , Λ and ϕ as follows. Adding and subtracting equations 4.5 and 4.6 in turn, gives

$$\tan\beta_3 = \frac{1}{2\phi}\left(\frac{1}{2}\psi + 2\Lambda\right) \quad (4.7)$$

$$\tan\beta_2 = \frac{1}{2\phi}\left(\frac{1}{2}\psi - 2\Lambda\right) \quad (4.8)$$

Then using equation 4.1

$$\tan\alpha_3 = \tan\beta_3 - \frac{1}{\phi} \quad (4.9)$$

$$\tan\alpha_2 = \tan\beta_2 + \frac{1}{\phi} \quad (4.10)$$

Even with the restrictions already introduced, there is still an infinite choice facing the designer. For example, although the overall turbine temperature drop is fixed by cycle requirements, it is open to the designer to choose one or two stages of large ψ or a large number of smaller ψ . It is possible to observe that in the context of organic Rankine cycles there is case for adopting turbine with a low degree of reaction and with a low number of stages.

A very useful preliminary design tool, commonly referred to as *Smith Chart* (Smith (1965)), resulted from a large amount of turbine testing carried out at Rolls-Royce. This chart, reported in figure 4.4, shows contours of constant isentropic efficiency as a function of stage loading coefficient and flow

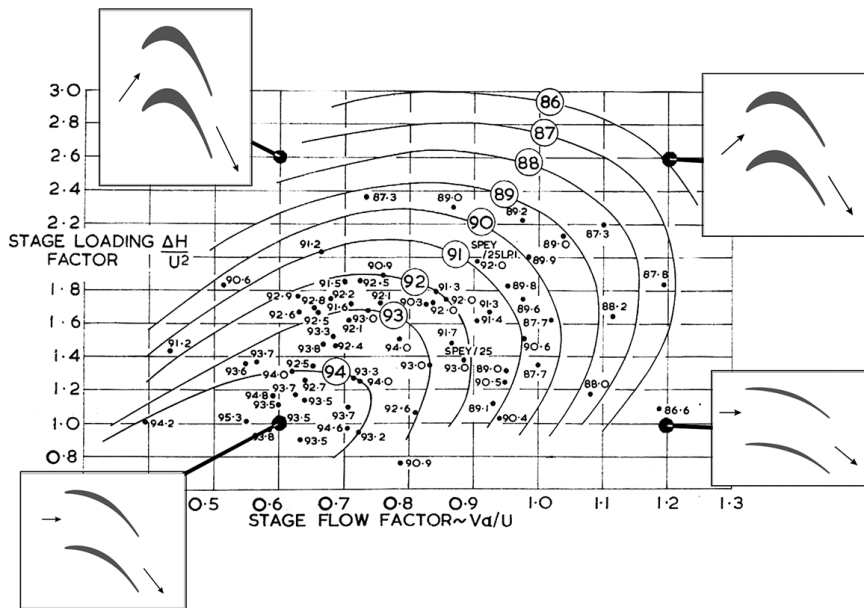


Figure 4.4: Smith chart (Smith (1965)).

coefficient. It should be noted that the efficiency quoted are for zero tip clearance and would be slightly lower in actual engines. Turbine stages for different engines have been designed over a wide range of locations on Smith chart.

Finally, it should be observed that the shape of the velocity triangles must vary from root to tip of the blade because the blade speed U increases with radius. Twisted blading designed to take account of the changing gas angles is called *Vortex blading*. Actually, it has been common turbine practice to design on conditions at the mean diameter. Indeed, the results of comparative tests between constant angle and vortex blading showed that any improvement in efficiency obtained with vortex blading was within the margin of experimental error (Johnston & Knight (1953)). Nevertheless Craig & Cox (1971) suggested to determine the losses at more than one radius, at least root, mean and tip, and to evaluate the overall loss through a weighted average. For this reason, some elements of 2-D analysis must be introduced. In particular, the thesis implemented the *Free Vortex Theory* analysis as described in Saravanamuttoo et al. (2009). It assumed:

1. The total enthalpy h_0 is constant over the annulus, i.e. $dh_0/dr = 0$;
2. The axial velocity is constant over the annulus;
3. The whirl velocity is inversely proportional to the radius;

A stage designed in accordance with the hypotheses above is called a *Free Vortex Stage*. Under these assumptions, it is possible to demonstrate (Saranamuttoo et al. (2009)) that α_2 at any radius is related to α_{2m} at the mean radius by

$$\tan\alpha_2 = \left(\frac{r_m}{r}\right)_2 \tan\alpha_{2m} \quad (4.11)$$

Similarly, the swirl angle at any radius can be calculated as

$$\tan\alpha_3 = \left(\frac{r_m}{r}\right)_3 \tan\alpha_{3m} \quad (4.12)$$

The gas angles at the inlet to the rotor blade, β_2 , can then be found using equation 4.10, namely

$$\tan\beta_2 = \tan\alpha_2 - \frac{U}{C_{a2}} \quad (4.13)$$

$$= \left(\frac{r_m}{r}\right)_2 \tan\alpha_{2m} - \left(\frac{r}{r_m}\right)_2 \frac{U_m}{C_{a2}} \quad (4.14)$$

Likewise, β_3 is given by

$$\tan\beta_3 = \left(\frac{r_m}{r}\right)_3 \tan\alpha_{3m} + \left(\frac{r}{r_m}\right)_3 \frac{U_m}{C_{a3}} \quad (4.15)$$

4.2 Methodology

The study started from a one-dimensional, mean-line design of axial-flow turbines. The inputs for the design process included a set of boundary conditions imposed by the thermodynamic cycles, ten optimizing variables, and other quantities which were considered as fixed values in this study. The optimal set of optimizing variables was provided by an optimization process including the design routine.

Initially, a preliminary calculation of velocity triangles, thermodynamic properties and blade geometry was based on a guessed stage efficiency. Afterwards, fixed the blade angles, velocity triangles and thermodynamic properties were updated. Finally, the evaluation of the losses was carried out and the stage efficiency calculated. At this point, an iterative cycle based on the stage efficiency started. Diagram 4.11, at the end of the chapter, summarizes the overall computational procedure.

The number of stages was chosen to be a fixed input rather than an optimizing parameter based on the total enthalpy drop. The analysis assumed a repeating stage configuration. For the first stage α_1 did not coincide with α_3 , even though C_{a3} was considered equal to C_{a1} .

The design routine was carried out in the computational environment provided by MathWorks (2013), first for an ideal gas and then for a real fluid. In

the former case the thermodynamic properties were calculated using equations valid for ideal gases and isentropic processes. On the contrary, for a real fluid the thermodynamic properties were computed exploiting the database furnished by Lemmon et al. (2007) and Bell et al. (2014).

Finally, it should be pointed out that in this study the suffix N is used to denote quantities associated with the nozzle row, but the term stator is often used in the text. However, the suffix S will be used to denote the stage. Also, as in the early days of gas turbines the blade angles were measured from the tangential direction following steam turbine practice, it is now usual to measure angles from the axial direction.

4.2.1 Preliminary Calculations

Figure 4.5 schematically shows the procedure followed for the preliminary determination of velocity triangles, thermodynamic properties and blade geometry. Basically, each block in the figure represents an internal function

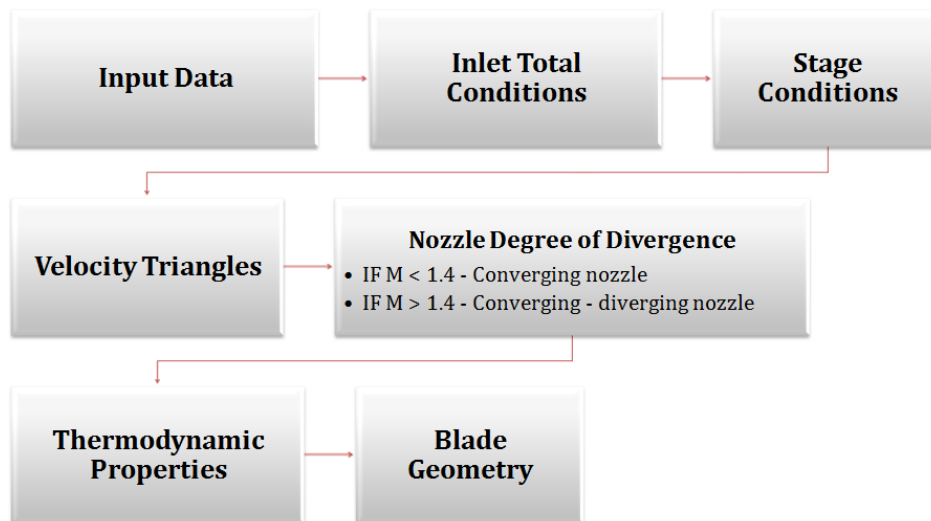


Figure 4.5: Preliminary determination of velocity triangles, thermodynamics states and blade geometry

of the design routine.

Input Data

As mentioned above, the input data included the boundary conditions imposed by the thermodynamic cycle, ten optimizing variables and other parameters which were considered to be fixed in this study. The ten optimizing variables were selected based on considerations found in literature (see Macchi (1977)), with the goal to obtain an easy computational routine. The

fixed parameters were basically indexes related to the possibility to investigate shrouded or un-shrouded blades, total or partial admission, or other similar design choices. Table 4.1 presents the list of the major input data for the design routine. The complete list of input data for the design procedure is reported in Appendix D. It should be pointed out that although the hy-

Table 4.1: Input data for the design routine.

Input Data	Symbol
Optimizing Variables	
Fluid inlet angle	α_1
Nozzle flow coefficient	ϕ_N
Stage loading coefficient	ψ
Nozzle throat [m]	o_{min}
Rotor opening [m]	o_R
Nozzle axial chord [m]	c_N
Rotor axial chord [m]	c_R
Nozzle opening-to-pitch ratio	o_N/s_N
Rotor opening-to-pitch ratio	o_R/s_R
Inlet rotor-to-outlet nozzle height ratio	$h_{2'}/h_2$
Cycle Requirements	
Mass flow rate [kg/s]	
Inlet total temperature [K]	T_{01}
Inlet total pressure [bar]	p_{01}
Pressure ratio	pr
Fluid	-
Rotational speed [rpm]	N
Fixed Inputs	
Mach number for conv. - div. nozzle	M_{cd}
Number of stages	n_{st}
Reynolds number	Re

pothesis of constant axial velocity was made in the design procedure, it was removed during the validation process. In the first case, the flow coefficient was constant across the stage, $\phi_N = \phi_R = \phi$; on the contrary $\phi_N \neq \phi_R$ in the validation process (the two values were given as inputs based on the available data).

Inlet Total Conditions and Stage Conditions

Once the input data were defined, the total conditions at the inlet of the nozzle and the stage conditions were calculated.

In particular, the total specific enthalpy, h_{01} , and the total specific entropy, s_{01} , were calculated from T_{01} and p_{01} . Next, known the number of stages,

n_{st} , the pressure drop for the single stage was determined by

$$pr_{0,S} = \sqrt[n_{st}]{pr_0} = \sqrt[n_{st}]{\frac{p_{03}}{p_{01}}} \quad (4.16)$$

Where the subscript "0" indicates the total condition, and "S" stands for stage. Equation 4.16 permitted to determine the total enthalpy drop for the stage, i.e. the stage specific work. Both for the ideal gas and real fluid cases, a first guess on the stage efficiency was necessary:

$$Ws = f(fluid, T_{01}, pr_0, \eta_S) \quad (4.17)$$

Afterwards, an approximated calculation of fluid angle and degree of reaction at mean radius was carried out. In this context, the swirl angle was assumed equal to zero, $\alpha_3 = 0$, while the blade velocity at mean radius was found by

$$U_m = \sqrt{\frac{2\Delta h_0}{\psi^2}} \quad (4.18)$$

Using equations 4.5 - 4.10 a simplified expression for the degree of reaction was obtained,

$$\Lambda = \phi \tan \beta_3 - \frac{1}{4} \psi \quad (4.19)$$

It should be observed that when 2-D effects are accounted for, the reaction increases from root to tip of the blades. Although negative values would be possible (see Appendix B), they must certainly be avoided because this would imply expansion in the nozzle followed by re-compression in the rotor and thus larger losses. A check on the degree of reaction at the root was included in order to have positive values along the whole blade. Large swirl angles would help in having a positive reaction at every radius. On the other hands, the higher the swirl angles, the larger the deviation of the fluid and so the losses. For this reason, a trade-off between opposite needs is necessary. Finally, a first calculation of the fluid angles at mean radius was performed using equations 4.8 and 4.7.

Velocity Triangles

Starting from the fluid angles, the velocity triangles were drawn through the methodology described in the following.

Using the specific work obtained by equation 4.17, the axial velocity at the exit of the nozzle can be determined using equation 2.3:

$$C_{a,2} = \frac{Ws}{U_m(\tan \alpha_2 - \tan \alpha_3)} \quad (4.20)$$

Then, due to the assumptions of constant axial velocity and repeating stage, the axial velocity at the outlet of the rotor and at the inlet of the nozzle are expressed, respectively, as

$$C_{a,3} = C_{a,2} = C_a \quad (4.21)$$

$$C_{a,1} = C_{a,3} = C_a \quad (4.22)$$

At this point, the absolute velocity was computed as

$$C = \frac{C_a}{\cos\alpha} \quad (4.23)$$

While the relative velocity was found by

$$W = \frac{C_a}{\cos\beta} \quad (4.24)$$

Finally, the flow coefficients were updated as

$$\phi = \frac{C_a}{U_m} \quad (4.25)$$

Where the subscript "m" recalls that the flow coefficients were evaluated at the mean radius.

From the velocity triangles the Mach numbers were derived. Recalling its definition (see Appendix A) the Mach number for each station was obtained. In particular, the absolute Mach number at the exit of the nozzle and the relative Mach number at the exit of the rotor are reported,

$$M_2 = \frac{C_2}{C_{s,2}} \quad (4.26)$$

$$M_{3,rel} = \frac{W_3}{C_{s,3}} \quad (4.27)$$

Where C_s is the fluid speed of sound. Finally, the degree of reaction was re-evaluated through equation 2.4.

Degree of Divergence

The nozzle of axial-flow turbines can assume a convergent-divergent shape when the Mach number exceeds a certain value. The nozzle degree of divergence was evaluated using the empirical relationship suggested by Deich et al. (1965). In particular, they proposed a value of $M = 1.4$ to switch from a simply converging nozzle, to a converging-diverging configuration. Thus,

$$IF \ M < 1.4 \quad \frac{o_N}{o_{min}} o_{min} = 1$$

$$IF \ M > 1.4 \quad \frac{o_N}{o_{min}} = 1 + (0.5 M_2 - 0.4) \left(\frac{1}{q_{M_2}} - 1 \right)$$

Where o_{min} indicates the throat (minimum) opening and o_N the nozzle opening. q_M is the area ratio between the considered Mach number and the sonic throat, for an isentropic flow, given in section 2 by

$$q_{M_2} = \frac{M_2}{\left[\left(\frac{2}{k+1} \right) \left(1 + \frac{k-1}{2} M_2^2 \right) \right]^{\frac{k+1}{2(k-1)}}} \quad (4.28)$$

Equation 4.28 is valid for perfect gases only. Nevertheless, the present work assumed it to hold also for real fluids, using an updated specific heat ratio k based on the thermodynamic conditions.

Rotor blades, even for supersonic relative velocities, were assumed to be converging with a rectilinear profile.

Further considerations on Deich Formula, along with the corresponding section of the computational routine are reported in Appendix E.1.

Thermodynamics Properties

The next step was to calculate the thermodynamic properties for each station of the axial-flow turbine. The calculation of the thermodynamic properties started from the knowledge of the total conditions at the inlet of the nozzle: h_{01} , s_{01} , T_{01} and p_{01} .

- **Station 1.** First, the static enthalpy and entropy were calculated recalling their definition (Appendix A):

$$h_1 = h_{01} - \frac{C_1^2}{2} \quad (4.29)$$

$$s_1 = s_{01} \quad (4.30)$$

This completely determined the static thermodynamic state at the inlet of the nozzle.

For the real fluid model, the static pressure was determined using the database provided by Lemmon et al. (2007) or Bell et al. (2014):

$$p_1 = F(h_1, s_1, fluid) \quad (4.31)$$

Where F indicated the generic thermodynamic function implemented by the two database.

The other static properties, as well as the speed of sound, were then computed by

$$[T_1, \rho_1, C_{s,1}] = F(p_1, s_1, fluid) \quad (4.32)$$

The use of the couple (p, s) to define the thermodynamic state, stems from computational considerations¹. On the other hand, for the ideal

¹The thermodynamic database were found to be more reliable for this combination of thermodynamic properties.

gas model the static pressure was obtained through the isentropic equation

$$p_1 = p_{01} \left(\frac{T_1}{T_{01}} \right)^{\frac{k}{k-1}} \quad (4.33)$$

While the density was obtained from the ideal gas law, and the speed of sound by its basic definition (see Appendix A).

- **Station 2.** Recalling that $h_{02} = h_{01}$, since no work is extracted in the nozzle, the calculation proceeded finding h_2 and $s_{2,is} = s_1$. The thermodynamic states refer to figure 4.6. Then, $h_{2,is}$ was obtained

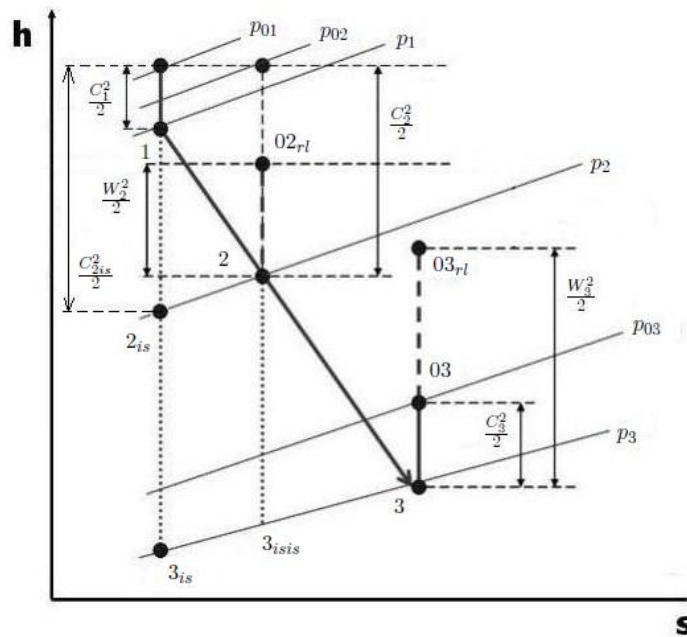


Figure 4.6: h-s diagram representing the expansion occurring in a turbine stage (Wikipedia (2011)).

using a guess value of the nozzle efficiency. It was expressed as

$$h_{2,is} = h_1 - \frac{h_1 + h_2}{\eta_{N,g}} \quad (4.34)$$

Where the suffix "g" indicates a guess value. Like the stage efficiency, also the nozzle efficiency was updated after the losses evaluation. At this point, the isentropic thermodynamic state at the exit of the nozzle was defined. The real fluid model proceeded with the calculation of the static pressure and entropy, respectively given by

$$p_2 = f(h_{2,is}, s_1, fluid) \quad (4.35)$$

$$s_2 = f(h_2, p_2, fluid) \quad (4.36)$$

The remaining static properties were calculated as described by equation 4.32. On the other hand, the ideal gas model repeated the procedure described for station 1.

- **Station 3.** The stage outlet pressure was known from

$$p_{03} = p_{01} pr \quad (4.37)$$

Where pr indicates the pressure ratio. Then, the real fluid model determined $h_{03, is}$ as

$$h_{03, is} = F(p_{03}, s_1, fluid) \quad (4.38)$$

$h_{3, is}$ was obtained from equation 4.29; in this way the isentropic thermodynamic state at the outlet of the rotor was defined. Thus, the pressure was computed as

$$p_3 = F(h_{3, is}, s_1, fluid) \quad (4.39)$$

Similarly, $h_{3, isis}$ was obtained from (p_3, s_2) . Then, h_3 was determined guessing the rotor efficiency,

$$h_3 = h_2 - \eta_{R,g}(h_2 - h_{3, isis}) \quad (4.40)$$

As that of the stator, the rotor efficiency was updated within the iterative process. At this point, the thermodynamic state at the outlet of the rotor was defined. Finally, the calculation of both the static and the total quantities were completed as described by equation 4.32.

On the other hand, the ideal gas model repeated the steps delineated for station 1, finding T_3 through a guess value of the rotor efficiency.

Blade Geometry

The last step of the preliminary calculation was an approximated determination of the blade geometry for each station of the turbine. The annulus area was found from the continuity equation as a function of mass flow rate (\dot{m}), density (ρ) and axial velocity (C_a),

$$A = \frac{\dot{m}}{\rho C_a} \quad (4.41)$$

The annulus area is also given by

$$A = 2\pi r_m h = \frac{U_m h}{N} \quad (4.42)$$

Where h indicates the blade height and N the rotational speed. Therefore, the height and radius ratio of the annulus can be found, respectively, from

$$h = \frac{AN}{U_m} \quad (4.43)$$

$$\frac{r_t}{r_r} = \frac{r_m + (h/2)}{r_m - (h/2)} \quad (4.44)$$

Where the subscripts "t" and "r" indicate the tip and root radii, respectively. Since the discussion of the effects of high and low annulus ratio are not of primary importance in the present study, further discussion on this topic is remanded to Appendix E.2.

Next, the flare angle² was calculated for stator and rotor. It was determined using the blade height and the blade axial chord (c), given as an input data,

$$\delta = \tan^{-1} \left(\frac{h_{out} - h_{in}}{2c} \right) \quad (4.45)$$

Where the subscripts "in" and "out" represent the inlet and outlet sections of the stage. Ainley & Mathieson (1955) suggested 25° as a safe limit for the flare angle.

Finally, the clearance between stator and rotor ($srcl$) was assumed to be linked with the nozzle axial chord:

$$srcl = 0.5 c_N \quad (4.46)$$

Where the coefficient 0.5 was suggested by Saravanamuttoo et al. (2009) (see Appendix E.2). It has to be noted that symmetrical flare angles were considered in this study.

4.2.2 Iterative Cycle

After the preliminary calculations, the computational routine included an iterative cycle based on the stage efficiency. Figure 4.7 schematically shows the iterative cycle. It started with the definition of blade and fluid angles. Afterwards, velocity triangles, thermodynamics properties and blades geometry were updated based on these angles. Finally, losses evaluation and efficiency calculation were carried out.

Blade and Fluid Angles

First, the pitch was found both for the stator and for the rotor from the opening-to-pitch ratio (o/s) and the blade opening (o). The correlation was given by

$$s = \left(\frac{o}{s} \right) o \quad (4.47)$$

²Angle of divergence of the annulus walls.

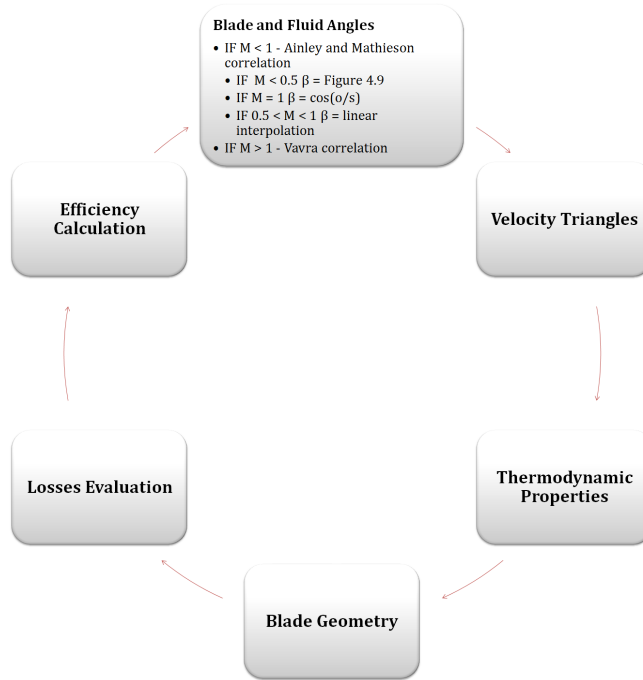


Figure 4.7: Iterative cycle within the computational routine

The opening-to-pitch ratio was an optimizing variable and it was established based on design requirements or optimization results. The nozzle opening was previously calculated from the throat opening using the correlation proposed by Deich et al. (1965).

Found the pitch, the number of blades was obtained from the geometrical relation

$$z = \frac{2\pi r_m}{s} \quad (4.48)$$

The next step was to choose stator and rotor blade shapes. The blade has to accept the gas incident upon the leading edge, and deflect it through the required angle with the minimum loss. Conventional steam turbine blades are shown in figure 4.8. The present thesis started from the determination of the *blade outlet angles* defined by

$$\theta_{out} = \cos^{-1} \left(\frac{o}{s} \right) \quad (4.49)$$

Obviously, the incidence of the fluid (i) upon the blade profile affected the profile loss. With reaction blading, the angle of incidence can vary approximately from -15° to $+15^\circ$ without increasing the profile loss coefficient. The picture is not very different even when three-dimensional losses are taken into account. In the present analysis, an incidence equal to 5° was assumed



Figure 4.8: Conventional steam turbine profile (Xylon (2011)).

for the rotor at each section, while 0° was considered for the nozzle. This was related to the consideration that the aerodynamic phenomena at the inlet of the nozzle are generally easier to control. In this way, the twisting of the blade simply followed the variation of the incident fluid angles, without considering any external requirements. On the other hand, ORC turbines are usually characterized by moderate blade height, which implies a small degree of twisting.

Therefore, the blade inlet angle was given for stator and rotor, respectively, by

$$\theta_1 = \alpha_1 + i_1 \quad (4.50)$$

$$\theta_{2'} = \beta_{2'} + i_{2'} \quad (4.51)$$

With $i_1 = 0^\circ$ and $i_{2'} = 5^\circ$. Where θ indicates the blade angle; α and β the fluid angles. The subscript "2'" indicates the station at the inlet of the rotor; it was assumed $\beta_{2'} = \beta_2$.

Afterwards, the calculation of the *fluid outlet angles* was carried out. They were obtained from the blade outlet angles using the following correlations:

IF $M < 1$ Correlation by Ainley & Mathieson (1951)

If $M > 1$ Correlation by Vavra (1969)

It is important to remember that the velocity triangles yield the gas angles, and they basically followed the choice of o/s.

The correlations proposed by Ainley & Mathieson (1951) and Vavra (1969)

provided the angular deviation between blade and fluid angle for subsonic and supersonic flows, respectively.

Ainley & Mathieson (1951) recommended different calculations for the fluid outlet angle depending on the Mach number. In particular,

IF $M < 0.5$ α_2, β_3 found from the linear relationship in figure 4.9

IF $M = 1$ $\alpha_2, \beta_3 = \cos^{-1}(o/s)$

IF $0.5 < M < 1$ α_2, β_3 found using a linear interpolation

A more detailed explanation of the correlations proposed by Ainley & Mathieson (1951), along with their implementation in the computational routine, is presented in Appendix E.3.

On the other hand, Vavra (1969) provided the correlation for $M > 1$. The-

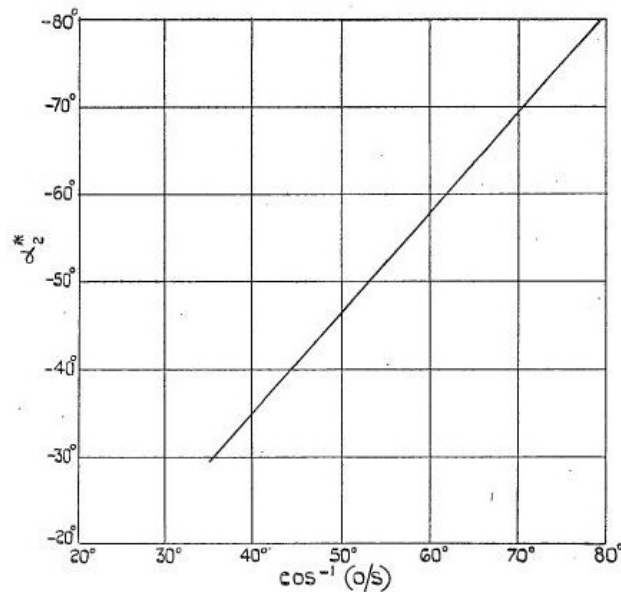


Figure 4.9: Relationship between gas outlet angles and $\cos^{-1}(o/s)$ for "straight-backed" operating at low Mach numbers (Ainley & Mathieson (1951)).

oretically derived by applying energy, momentum and continuity equations from the blade exit opening to the downstream conditions, assumed to be

uniform, Vavra equation for the nozzle takes the following form:

$$\Delta\alpha = \frac{\left(\frac{k}{k-1}\right)\left(\frac{p_2}{p_a}\right)\tan\alpha_A + \sqrt{\left(1 - \frac{p_2}{p_a}\right)\left[\frac{2k}{k-1}M_a^2 - 1 - \frac{k+1}{k-1}\frac{p_2}{p_a}\right] + \left[\frac{k}{k-1}\frac{p_2}{p_a}\tan\alpha_A\right]^2}}{1 + kM_a^2 - \frac{p_2}{p_a}} \quad (4.52)$$

Where the subscript "a" indicates the conditions at the blade opening section. The significance of the terms in the equation can be found in figure 4.10. Further considerations on the implementation of the Vavra equation

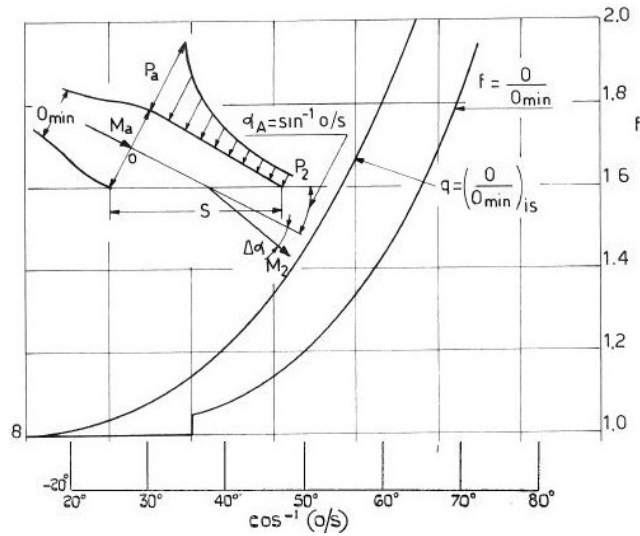


Figure 4.10: After expansion from supersonic nozzle having optimum degree of divergence (Deich et al. (1965)), computed with Vavra equation, Macchi (1977)

are given in Appendix E.3.

Until this point a 1-D mean radius analysis were carried out. As a result, the fluid outlet angles were obtained at the mean radius. Starting from these angles, velocity triangles, thermodynamic states and blade geometry at mean radius were updated through the functions described in Section 4.2.1. Afterwards, some elements of 2-D analysis were introduced by exploiting the Free Vortex Theory. In particular, equations 4.11 - 4.15 allowed to find angles and velocity triangles at root, mean and tip radii.

Evaluation of Losses with Craig-Cox Method

A brief classification of the losses was given in Chapter 2. Several models for the investigation of the losses were developed in the past. Nevertheless, the method proposed by Craig & Cox (1971) appears the most complete, coherent and realistic correlation available in literature for the study of organic

Rankine cycle turbines (see Macchi (1977)). The only important assumption which had to be added to the original loss correlation (which holds only for converging blade) was the information about losses in converging-diverging supersonic nozzles: it was assumed that at design point the loss coefficient of converging-diverging nozzles can be computed with the same procedure used for converging blades, adding a correction factor from Kacker & Okapu (1982).

Craig & Cox (1971) claimed that the method was valid both for gas and steam turbines. Moreover, they stated that for most of the tests the efficiency was predicted within a range of $\pm 1.25\%$. However, there were some prediction differences in the range of 10 to 25 MW, where the accuracy range was wider, around $\pm 3\%$. The test data used to obtain the correlation for profile and secondary losses were from linear cascade tests, while other losses, such as the tip clearance loss, were derived from specific turbine tests and data from annular air tests. The losses in a blade row were divided in two groups, provided by table 4.2. The methodology for the assessment of

Table 4.2: Division of stage losses by Craig & Cox (1971).

Group 1	Group 2
Nozzle profile loss	Nozzle leakage loss
Rotor profile loss	Balance hole loss
Nozzle secondary loss	Rotor leakage loss
Rotor secondary loss	Lacing wire loss
Nozzle annulus loss	Wetness loss (if two-phase occurring)
Rotor annulus losses	Windage loss
-	Partial admission loss

the first group and the two first losses in the second group is depicted in the following. The losses in the first group were described by a loss factor measured in J/kg, while the losses in the second group were given as a dimensionless decrease in the stage efficiency. The reason for this is that Craig & Cox (1971) found this to be the easiest way to derive the loss models from test data. Furthermore, although off-design considerations were treated and included in the Craig-Cox method, they were outside the purpose of the present thesis. Note that the angles were defined from the tangential plane in Craig-Cox equations and figures. For this reason, a careful angle conversion was necessary.

Group 1: Profile Loss. The overall profile loss was given by a base loss coefficient for incompressible flow ($Y_{P,0}$). Then it was corrected for variation of Reynolds number (Re), trailing edge thickness (te) and incidence (i) by some multipliers to the base loss. For the variation of Mach number (M) and curvature of the suction surface between the throat and trailing edge (tec)

a further coefficient was added to the overall profile losses. The structure of profile loss for Craig-Cox method is seen in the following equations,

$$Y_P = Y_{P,0} \chi_{Re} \chi_{te} \chi_i + \Delta Y_{P,M} + \Delta Y_{P,tec} + \Delta Y_{P,te} \quad (4.53)$$

Where Y indicates the loss dimensionless coefficient. The subscript "P" indicate the profile loss and "0" the base coefficient. χ indicates a multiplicative correction factor, while ΔY designates an additive correction factor. The base loss coefficient $Y_{P,0}$ was derived with low speed fluid flow and at an incidence corresponding to the minimum profile loss. $Y_{P,0}$ was given as a function of a lift parameter (FL), pitch-to-backbone length ratio (s/b), contraction ratio (CR) and outlet flow angle β_{out} . FL was in turn obtained from θ_{out} and $\alpha_{in} - i_{min}$. The contraction ratio was defined as the inlet to throat area ratio, where the inlet area was considered to be the maximum arc that can be drawn entirely within the blade passage and witch is normal to the blade surface. For more details and figures see Appendix F. To summarize so far:

$$Y_{P,0} = f(FL, CR, s/b) \quad (4.54)$$

$$FL = f(\alpha_{out}, \alpha_{in} - i_{min}) \quad (4.55)$$

$$CR = f(c/b, 1 - \frac{\sin\alpha_{out}}{\sin\alpha_{in}}) \quad (4.56)$$

Where b represented the backbone length of the blade, c the axial chord and s the blade pitch.

To correct for the loss related to separation for a real thickness at the trailing edge a theoretical derived correlation was presented in Fig.6 of Craig & Cox (1971) as a function of the fluid outlet angle (α_{out} or β_{out}) and the trailing edge thickness-to-pitch ratio t_{te}/s . This correlation gave both a multiplier χ_{te} and an extra added loss $\Delta Y_{P,te}$ to the base profile loss $Y_{P,0}$. For the correction of Re Craig & Cox (1971) presented a chart (Fig. 3) valid for different surface roughness and Reynolds number inside the range $10^4 < Re_o < 10^6$, where Re_o was based on blade throat opening (o). To correct for Mach number in excess of unit, the correction factor $\Delta Y_{P,M}$ was added. It was a function of o , t_{te}/s and M_{out} . Finally, a correction for the mean curvature between the throat and trailing edge suction surface was given in Fig. 9 for the input parameter M_{out} and s/e , where e represents the back surface curvature radius. The last correction on the profile loss was an off-design multiplier χ_i to the base profile loss due to the incidence i .

Group 1: Secondary Loss. Craig & Cox (1971) involved both true aerodynamic secondary loss and wall friction in their secondary loss correlation. They also suggested a discrepancy between the losses for shrouded and un-shrouded blades. However, they finally presented only a correlation for shrouded blades, which they claimed to be approximately valid also for

un-shrouded blades. For high aspect ratio (h/b), secondary losses inversely proportional to the aspect ratio were assumed. On the other hand, when h/b was decreased below a certain value the secondary flows present at the end-walls (see figure 2.5) interacted resulting in smaller losses. For this reason, Craig & Cox (1971) suggested a non-linear relationship against the aspect ratio.

Furthermore, they assumed that Reynolds number affected secondary loss similarly to profile loss. The overall secondary loss was given by

$$Y_S = Y_{S,0} \chi_{Re} \chi_{h/c} \quad (4.57)$$

Where,

$$Y_{S,0} = f(FL(s/b), (C_{in}/C_{out})^2) \quad (4.58)$$

$$\chi_{h/c} = f(C_{crit}/h) \quad (4.59)$$

Where C represented the relative velocity for the rotor and the absolute velocity for the stator. The subscript "crit" indicates the critical conditions.

Group 1: Annular Loss. The annular loss Y_{an} was separated from the secondary loss by Craig & Cox (1971) and was given as the sum of three separate sources of loss: annular, cavity and a cavity loss factor due to sudden expansion. The latter source was not considered in the present work.

Group2: Tip Clearance Loss. Tip leakage loss over the blade tip was given by equation 4.60, describing the reduction of the total-to-total stage efficiency ($\Delta\eta_{tt}$) compared to that for zero tip clearance (η_{tt}). The area ratio of tip clearance-to-throat (A_K/A_0) and an efficiency factor F_K were involved.

$$\Delta\eta_{tt} = F_K \left(\frac{A_K}{A_0} \right) \eta_{0,tt} \quad (4.60)$$

For an increase in the leakage area (A_K) the efficiency will decrease. The factor F_K was given as a function of geometrical parameters, stage loading coefficient (ψ) relative velocities (W),

$$F_K = f\left(\psi, \frac{W_2^2 - W_1^2}{W_2^2}, \Delta L\right) \quad (4.61)$$

Where ΔL represented the overlap of the blades. Actually, such a procedure was given for shrouded blades and implied different correction factors for each type un-shrouded blades.

Group 2: Miscellaneous Losses. Other losses evaluated in the computational routine included:

- Loss due to partial admission, assessed with the methodology proposed by Traupel (1962);
- Disc windage loss, evaluated with the methodology suggested by Balje' & Binsley (1968).
- Wet loss, evaluated using the methodology provided by Kotton (1998). In particular, if $Q < 0.984$,

$$F = 2(1 - Q) \quad (4.62)$$

Otherwise,

$$F = 0.032 + 0.76(1 - (Q + 0.016)) \quad (4.63)$$

Where Q is the vapour quality at the end of the expansion and F is the dimensionless efficiency debit. Wet losses were accounted for only for steam turbines, where two-phases occurs at the end of the expansion.

Final Considerations. Craig and Cox argued that the losses from group 1 should not be calculated at just one mean diameter. Instead they must be evaluated for at least three different diameters (root, mean and tip) and then an average value should be obtained with a parabolic loss distribution according to

$$Y_{avg} = \frac{1}{6} \sum_j Y_{j,root} + \frac{1}{6} \sum_j Y_{j,tip} + \frac{4}{6} \sum_j Y_{j,mean} \quad (4.64)$$

Where j indicates the different losses. Some of the figures presented by Craig & Cox (1971) are displayed in Appendix F.

Efficiency Calculation

The calculation of the stage efficiency was performed accordingly with the definition suggested by Craig & Cox (1971), consistently with the loss assessment. Stator and rotor efficiency were found with the following equations, respectively,

$$\eta_N = \frac{(h_1 - h_2)}{(h_1 - h_2) + X_{I,N}} \quad (4.65)$$

$$\eta_R = \frac{(h_2 - h_3)}{(h_2 - h_3) + X_{I,R}} \quad (4.66)$$

Where $X_{I,N}$ and $X_{I,R}$ represent the global group 1 loss coefficients for nozzle and rotor, respectively. They were consistently expressed in J/kg. Afterwards, the stage efficiency was computed as

$$\eta_S = \frac{Ws}{(Ws + rec \cdot \frac{C_3^2}{2}) + X_{I,N} + X_{I,R}} - Y_{II} \quad (4.67)$$

Where Ws is the Euler work, provided by equation 2.3, and Y_{II} indicates the total group 2 loss, calculated for the whole stage. Equation 4.67 was used to calculate both the total-to-static and total-to-total efficiency. The only difference regarded the kinetic energy recovery coefficient rec : in the first case $rec = 0$, while in the second case $rec = 0.5$, i.e. 50 % of kinetic energy of the exhaust gas was recovered.

Finally, the *restriction factors* were calculated. They are used in continuity equations, according to the method suggested by Vavra (1969):

$$\dot{m} = \zeta \dot{m}_{is} \quad (4.68)$$

Where \dot{m}_{is} is the mass flow rate given as an input (for an isentropic flow) and ζ indicates the restriction factor. According to Vavra (1969), ζ is calculated from equation

$$\zeta = \frac{1}{1 + Y_P(\frac{H}{K})} \quad (4.69)$$

Accounting only for profile losses. The *boundary layer wake form to energy factor ratio*, H/K , was assumed to be equal to 0.7 based on the validation results. Two different restriction factors, for stator and rotor, were computed.

Once the efficiency of the stage was found, an iterative process was triggered. Each function was updated until the difference between the efficiency of the stage of two next iterations was below a certain threshold, chosen equal to 10^{-4} .

4.2.3 Multi-Stage Considerations

The design procedure was repeated for each stage separately. The inlet conditions for the downstream stage were the outlet conditions of the upstream stage. This implied that T_{01} , P_{01} , C_1 , α_1 for the second stage were equal to T_{03} , P_{03} , C_3 , α_3 of the first stage, respectively. As mentioned above, the pressure drop was equally distributed among the stages using equations 4.16. Furthermore, the total-to-static efficiency was considered for the last stage, as well as for the turbine as a whole, while the total-to-total efficiency was used for the intermediate stages. Finally, it should be pointed out that for ORC turbines rarely the number of stages is higher than 3 (see Macchi (1977)).

Figure 4.11 schematically summarizes the overall computational procedure. The optimization process is investigated in more detail in Chapter 6.

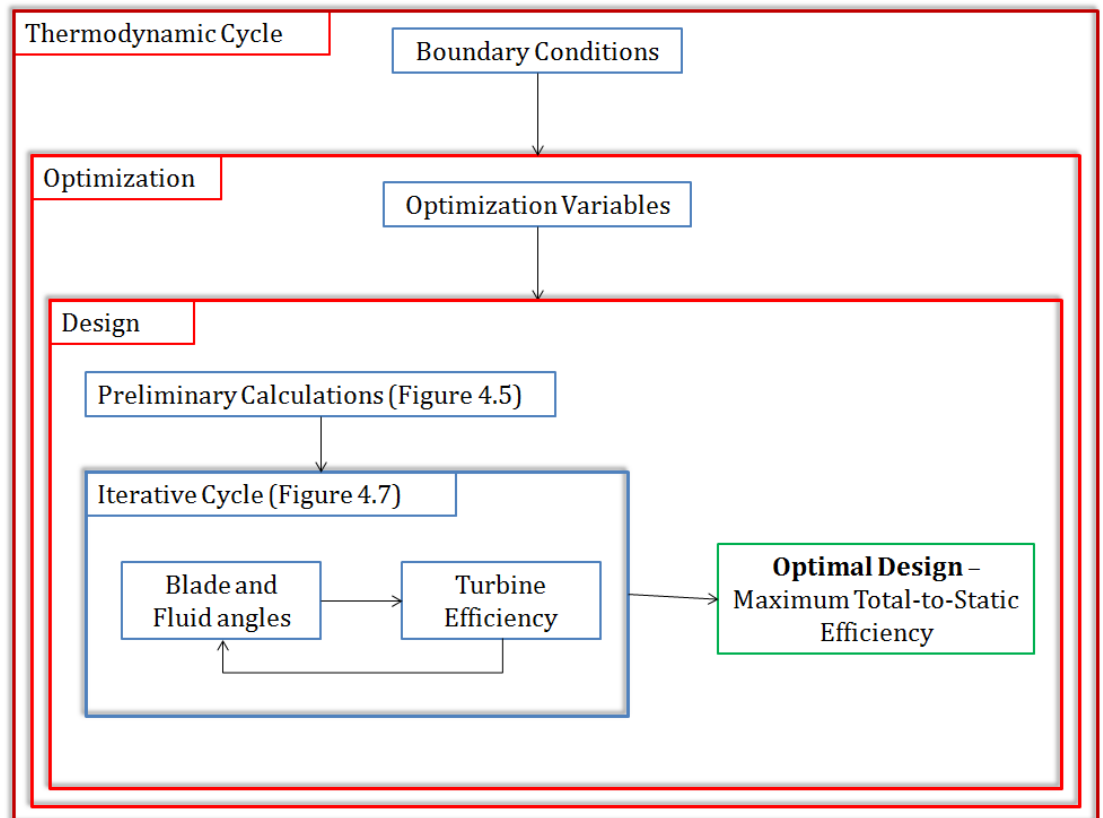


Figure 4.11: Schematic of the overall computational routine.

5

Validation of the Computational Model

5.1 Introduction

Both the ideal gas and the real fluid model were tested against experimental data. The ideal gas model was validated against Stabe et al. (1984) for a single-stage turbine and against Kotzing & Evers (1985) for a multi-stage configuration. Similarly, the real fluid model was validated against Stabe et al. (1984) and Verneau (1987) for a single-stage turbine, and against Kotzing & Evers (1985) for the multi-stage configuration. Since no major differences were detected between the validation results for the two models, in the following only some of these validations are presented. In particular, the multi-stage validation is examined for the ideal gas model, while the single-stage validation is described for the real fluid model. The remaining validations can be found in Appendix G. The results of the computational model were considered satisfying when affected by a relative error within a range of $\pm 3\%$; this was the accuracy range guaranteed by Craig and Cox method for the evaluation of the losses.

5.2 Methodology

The validation process started from the definition of the input data. The available experimental data were elaborated to determine the input parameters reported in table 4.1. When the inputs could not be retrieved by the experimental data, the study proceeded with a "try and fail" method in order to match the experimental results.

It should be pointed out that during the validation procedure the assumption of constant axial velocity was removed; indeed, none of the examined

turbines was characterized by this feature. As a result, a small change was performed in the computational routine: instead of considering $C_{a,2} = C_{a,3} = C_a$ the axial velocity was calculated using the flow coefficient ϕ ,

$$C_a = \phi U_m \quad (5.1)$$

Typically, the values of ϕ_N and ϕ_R could be determined working on the experimental data. Then, C_a was calculated for stator and rotor, separately. The validation was performed in terms of performance, geometry, velocity diagram and thermodynamic states of the turbines.

5.3 Results & Discussion

5.3.1 Ideal Gas Model

Multi-Stage Validation: Kotzing & Evers (1985)

This validation was performed against the report prepared by Kotzing & Evers (1985). The report regarded a test case on a four-stage low speed gas turbine. The aim of this validation was to verify the reliability of the computational routine for a multi-stage configuration. The analysis of the ideal gas model appeared reasonable since air was used as a working fluid. The turbine investigated by Kotzing & Evers (1985) was designed to have the same blade section in all the stages at a given radius. The blading was of the free-vortex type with a degree of reaction in the middle section equal to 0.5. The turbine had a constant hub diameter of 270 mm. The height of the rotor blades varied for the four-stage configuration between 64 mm and 89 mm for the first and last stage, respectively. The inputs deduced from the experimental data are reported in table 5.1. While the geometrical parameters were calculated from the report, the study proceeded with a "try and fail" method for the flow coefficients and the stage loading coefficient. Table 5.1 shows how the opening-to-pitch ratio was equal for all the stages, implying the same blade shapes in each stage. Similarly, the flow coefficients were very close for all the stages. As a result, the velocity diagram was analogous for each stage. Fig 5.1 shows the velocity triangles at mean radius for the fourth stage; however it can well be considered to represent all the four stages. The velocity triangles for each stage can be found in appendix G. Figure 5.1 explicates the fact that the turbine stages are characterized by a degree of reaction of 0.5, i.e. reaction stages. Indeed, the triangles for stator (blue) and rotor (red) look almost symmetrical, being the only discrepancy the small difference in axial velocity.

Table 5.2 presents the results of the validation procedure for the first two stages of the turbine, while 5.3 reports the results for the third and fourth stage. In the table the acronyms *CR* and *ER* indicates computational and experimental results, respectively. The comparison was carried out in terms

Table 5.1: Major input data for the validation process against Kotzing & Evers (1985).

	Stage 1	Stage 2	Stage 3	Stage 4
Optimizing Variables				
α_1 [°]	20	-	-	-
ϕ_N	0.6	0.61	0.59	0.605
ψ	4.3	3.5	3.6	3
o_{min} [m]	0.031	0.031	0.031	0.031
o_R [m]	0.027	0.027	0.027	0.027
c_N [m]	0.01	0.01	0.01	0.01
c_R [m]	0.01	0.01	0.01	0.01
o_N/s_N	0.36	0.36	0.36	0.36
o_R/s_R	0.39	0.39	0.39	0.39
h_2'/h_2	1.1	1.1	1.1	1.1
Cycle Requirements				
\dot{m} [kg/s]	7.8	7.8	7.8	7.8
T_{01} [K]	413	-	-	-
p_{01} [bar]	2.6	-	-	-
pr	0.393	-	-	-
N [rpm]	7500	7500	7500	7500
Other Inputs				
ϕ_R	0.62	0.64	0.61	0.63

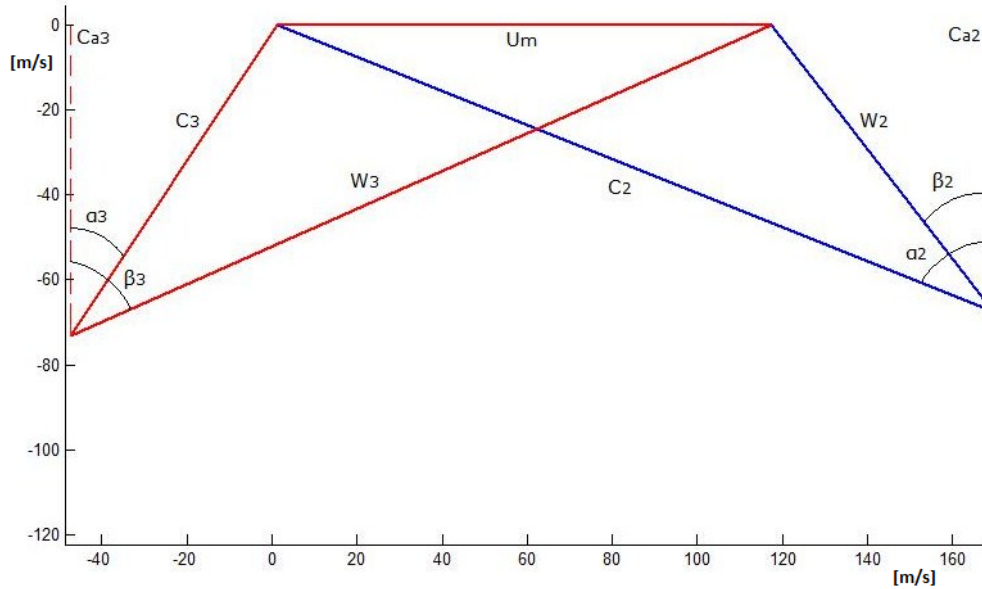


Figure 5.1: Velocity triangles for stage 4 of the multi-stage gas turbine. Ideal gas computational model.

of geometry, thermodynamic states and velocity triangles for the single stage; efficiency and power were investigated considering the turbine as a whole.

Table 5.4 reports the global total-to-total efficiency and the total power

Table 5.2: Part A - Validation results for stage 1 and stage 2 of multi-stage gas turbine. Computational results.

	Stage 1			Stage 2		
	<i>CR</i>	<i>ER</i>	$\Delta\epsilon_{rel}$	<i>CR</i>	<i>ER</i>	$\Delta\epsilon_{rl}$
Blade Geometry						
h_1 [m]	0.066	0.064	2.88%	0.070	-	-
h_2 [m]	0.071	-	-	0.075	-	-
h_3 [m]	0.076	-	-	0.076	-	-
r_m , [m]	0.135	0.135	0.05%	0.145	0.143	2.00%
Λ	0.501	0.5	0.24%	0.4973	0.5	0.54%
Thermodynamic States						
T_{03} [K]	388.6	384	1.18%	366.1	364	0.58%
p_{03} [bar]	2.098	2.13	1.54%	1.679	1.71	1.88%
p_3 [bar]	2.039	2.08	1.97%	1.648	1.67	1.63%
Velocity Diagram						
U_m [m/s]	106.0	-	-	123.0	-	-
C_3 [m/s]	77.96	78	0.051%	88.66	90	1.51%
α_2 [°]	67.81	68	0.28%	68.16	68	0.23%
β_2 [°]	38.63	39.6	2.51%	39.66	39.6	0.15%
β_3 [°]	66.03	66	0.05%	66.03	66	0.05%
α_3 [°]	22.47	20	11.0%	24.1	20	17.0%
M_2	0.421	-	-	0.477	-	-
$M_{3,rel}$	0.411	-	-	0.472	-	-

output of the four-stage turbine. Both the parameters were calculated with a satisfactory precision. As it can be noted from tables 5.2 and 5.3, many parameters were not accessible for the comparison. However, the validation against the available variables led to satisfying results for stage 1 and 2. Indeed, for these stages all the parameters were calculated with an accuracy range within $\pm 3\%$, except for α_3 . Nevertheless, although the angle was affected by a relative error above 10%, the absolute error was smaller than 3° , which appeared as an acceptable value. On the contrary, stage 3 and 4 presented some problems from the point of view of the blade geometry:

- The mean radius was affected by a high relative error: 13.9% for the third stage and 23.6% for the fourth stage. This stemmed from the fact that the code cannot predict an enhancement of the mean radius across the turbine. Indeed, r_m was calculated starting from U_m , which remains basically constant. Recalling that U_m was computed as

$$U_m = \sqrt{\frac{2\Delta h_0}{\psi^2}}$$

Table 5.3: Part B - Validation results for stage 3 and stage 4 of multi-stage gas turbine. Computational results.

	Stage 3			Stage 4		
	CR	ER	$\Delta\epsilon_{rl}$	CR	ER	$\Delta\epsilon_{rl}$
Blade Geometry						
h_1 [m]	0.079	-	-	0.097	-	-
h_2 [m]	0.101	-	-	0.105	-	-
h_3 [m]	0.102	-	-	0.103	0.102	1.16%
r_m [m]	0.141	0.161	13.9%	0.148	0.183	23.59%
Λ	0.508	0.5	1.57%	0.496	0.5	0.78%
Thermodynamic States						
T_{03} [K]	344.7	341	1.08%	325	319	1.86%
p_{03} [bar]	1.319	1.35	2.36%	1.051	1.05	0.14%
p_3 [bar]	1.279	1.31	2.55%	1.021	1.01	0.96%
Velocity Diagram						
U_m [m/s]	122.7	-	-	116.873	-	-
C_3 [m/s]	78.15	77	1.47%	88.57	86.5	2.34%
α_2 [°]	68.16	68	0.23%	68.16	68	0.23%
β_2 [°]	38.67	39.6	2.35%	38.75	39.6	2.19%
β_3 [°]	66.03	66	0.05%	66.03	66	0.05%
α_3 [°]	21.87	20	8.55%	22.87	20	11.0%
M_2	0.499	-	-	0.477	-	-
$M_{3,rel}$	0.503	-	-	0.472	-	-

Table 5.4: Efficiency and power for the multi-stage gas turbine. Computational results.

	Comp. Result	Experim. Result	$\Delta\epsilon_{rel}$
η_{tt}	0.914	0.913	0.17%
P [MW]	0.699	0.703	0.57%

a possible solution for this problem can be searched in a different distribution of the pressure drop respect to that implemented through equation 4.16. Indeed, this would affect the enthalpy drop occurring within the stage, which would turn in a variation of U_m .

- Although a detailed comparison regarding the blade heights was not possible, the calculation appeared consistent for the first three stages; on the contrary some inaccuracies seemed to arise for the fourth stage. Figures 5.2 and 5.3 show the blade geometry for the first and last stage, respectively. The blade geometry for stage 1 was consistent to

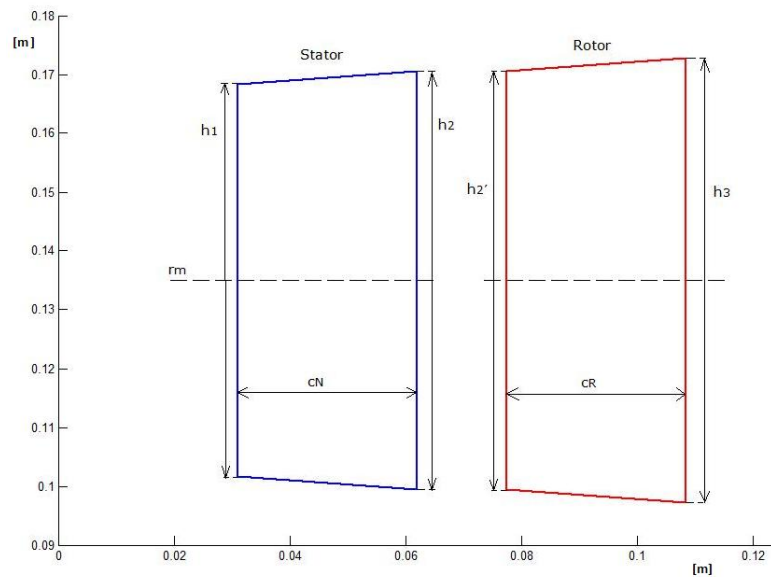


Figure 5.2: Blade geometry for stage 1 of the multi-stage gas turbine. Computational result.

that showed in Figure 2 of Kotzing & Evers (1985). Regarding stage 4, although the value of h_3 matched the experimental one, the overall shape did not correspond to that reported in Kotzing & Evers (1985). Recalling the continuity equation (Appendix A), the reason for this discrepancy might lay either on the calculation of the axial velocity (this would refer again to the calculation of U_m) or on the determination of the fluid density. Moreover, it should be pointed out that the computational model assumed symmetrical flare angles, while this was not the case of the gas turbine in Kotzing & Evers (1985).

As a result, further work must be done in order to obtain a more precise simulation of the blade geometry, especially in multi-stage configurations.

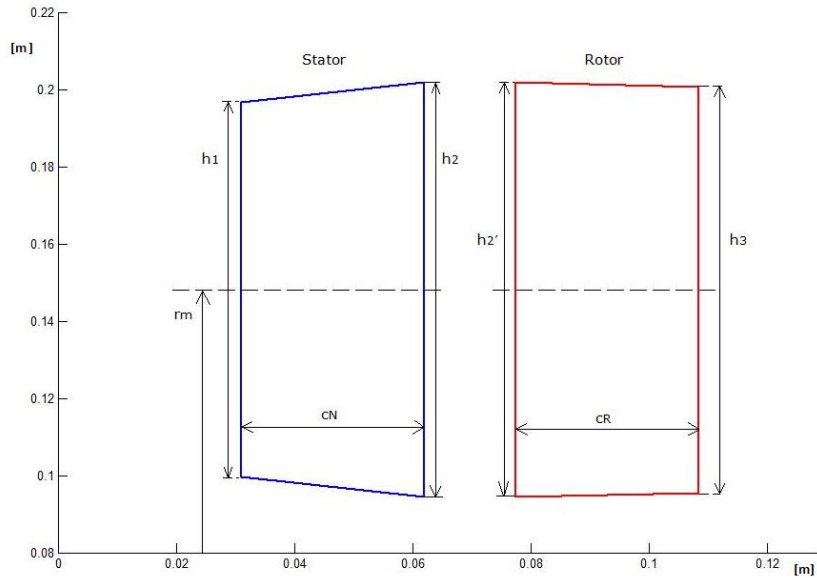


Figure 5.3: Blade geometry for stage 4 of the multi-stage gas turbine. Real fluid computational model.

The blade geometry for each stage is presented in appendix G. Finally, figure 5.4 shows the T-s diagram at mean radius for the four-stage expansion.

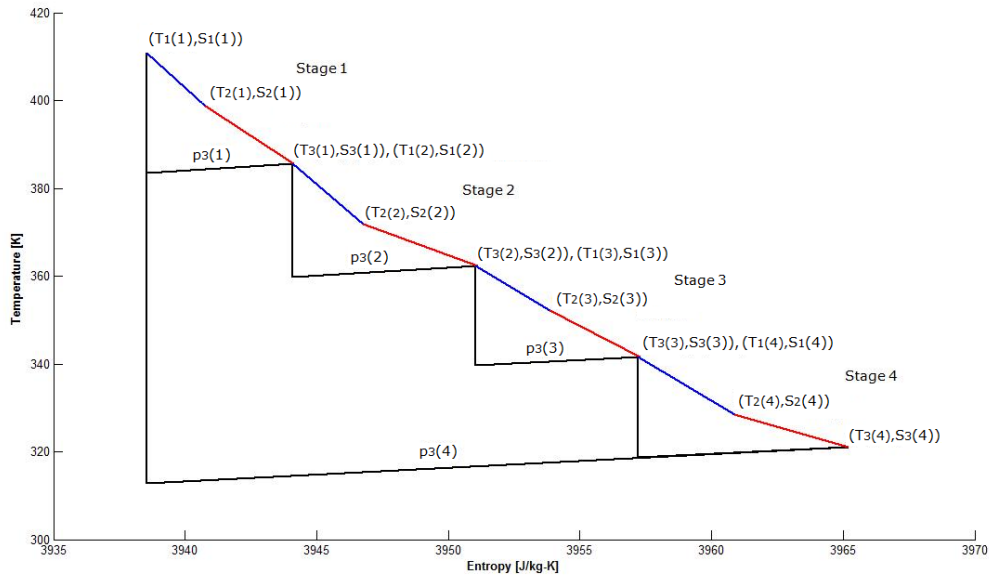


Figure 5.4: T-s diagram for the four-stages low speed turbine gas turbine. Real fluid computational model.

5.3.2 Real Fluid Validation

Single-Stage Validation: Stabe et al. (1984)

This validation was carried out considering the single-stage gas turbine described in Stabe et al. (1984). The experimental data allowed to determine all the inputs necessary for the design model. The values are reported in table 5.5. Although Stabe et al. (1984) reported only one flow coefficient,

Table 5.5: Major input data for the validation process against Stabe et al. (1984).

Optimizing Variables	
α_1 [°]	0
ϕ_N	0.366
ψ	3.35
o_{min} [m]	0.0147
o_R [m]	0.0115
c_N [m]	0.0355
c_R [m]	0.033
o_N/s_N	0.258
o_R/s_R	0.376
$h_2/h_{2'}$	1.1
Cycle Requirements	
\dot{m} [kg/s]	7.81
T_{01} [K]	422.2
p_{01} [bar]	3.103
pr	0.424
N [rpm]	9048
Other Inputs	
ϕ_R	0.532

$\phi = 0.449$, this simply represented the average flow coefficient between stator and rotor, given by

$$\phi = \frac{\phi_N + \phi_R}{2}$$

Indeed, Figure 1 by Stabe et al. (1984) displays the experimental velocity triangles, highlighting a variable axial velocity across the stage. Figure 5.5 shows the velocity triangles at mean radius obtained with the computational model Mamba. The blue triangle represents the outlet of the stator, while the red triangle indicates the outlet of the rotor, i.e. stations 2 and 3, respectively. The dashed lines indicate the axial velocity, different for stator and rotor. Table 5.6 reports the results of the validation in terms of performance, blade geometry, thermodynamic states and velocity diagram. The table compares computational and experimental results, reporting the

Table 5.6: Validation result the single-stage gas turbine. Real fluid computational model.

	Comp. Result	Experim. Result	$\Delta\epsilon_{rel}$
Performance			
η_{tt}	0.884	0.890	0.67%
P [MW]	0.824	-	-
Blade Geometry			
z_N	26	26	0%
z_R	47	48	2.1%
s_N [m]	0.057	0.057	0%
s_R [m]	0.031	0.031	0%
h_2 [m]	0.035	0.036	2.59%
h_3 [m]	0.035	0.036	1.71%
r_m [m]	0.232	0.233	0.56%
Λ	0.456	-	-
Thermodynamic States			
T_{02} [K]	422.1	-	-
p_{02} [bar]	2.961	-	-
T_{03} [K]	340.6	-	-
p_{03} [bar]	1.315	-	-
Velocity Triangles			
U_m [m/s]	219.5	218	0.7%
$C_{a,2}$ [m/s]	81.2	-	-
$C_{a,3}$ [m/s]	118	-	-
C_2 [m/s]	312	-	-
W_3 [m/s]	306	-	-
α_2 [°]	75.1	75	0.16%
β_2 [°]	45.9	45	1.91%
α_3 [°]	29.8	30.2	1.33%
β_3 [°]	67.6	67.5	0.37%
M_2	0.813	0.833	2.5%
$M_{3,rel}$	0.847	0.867	2.3%

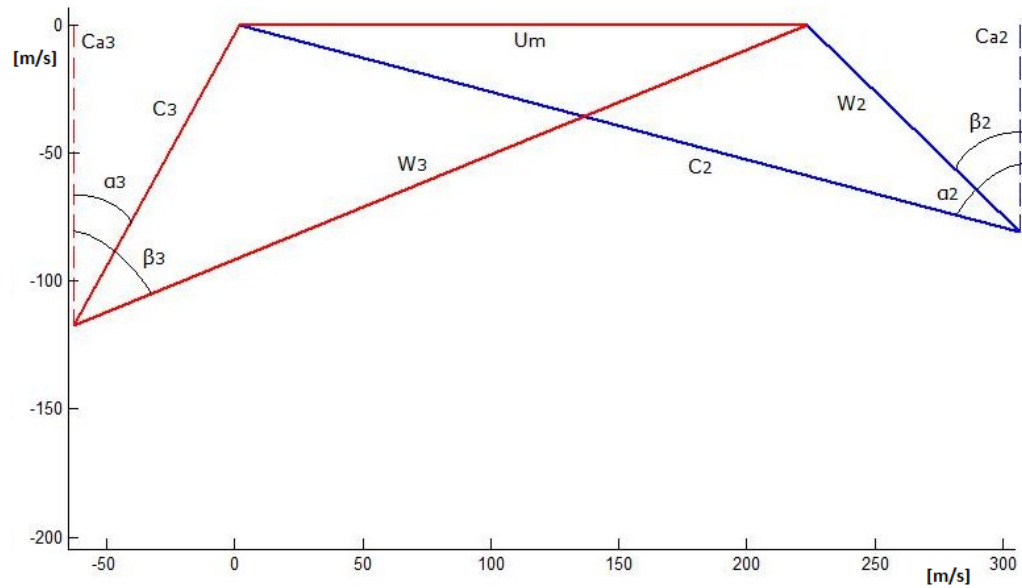


Figure 5.5: Velocity triangles for the single-stage gas turbine. Real fluid computational model.

relative error, $\Delta\epsilon_{rel}$, in percentage. The table actually exhibits a satisfactory outcome. Indeed, the relative error was within the acceptable range of $\pm 3\%$ for each parameter. This suggested a good behaviour of the code when dealing with a single stage.

Actually, some of the quantities reported in the table, such as the degree of reaction or the thermodynamic states, were not provided by Stabe et al. (1984). Nevertheless, the results given by the computational model appeared reasonable. For instance, a degree of reaction equal to $\Lambda = 0.46$ seemed to describe properly the velocity triangles drawn in Figure 1 of Stabe et al. (1984). In figure 5.6 the blade geometry is drawn. It well reproduces that reported in Figure 5 of Stabe et al. (1984). Finally, figure 5.7 shows the T-s static diagram at mean radius for the investigated turbine. The blue line represents the expansion in the stator, while the red line indicates the expansion occurring in the rotor.

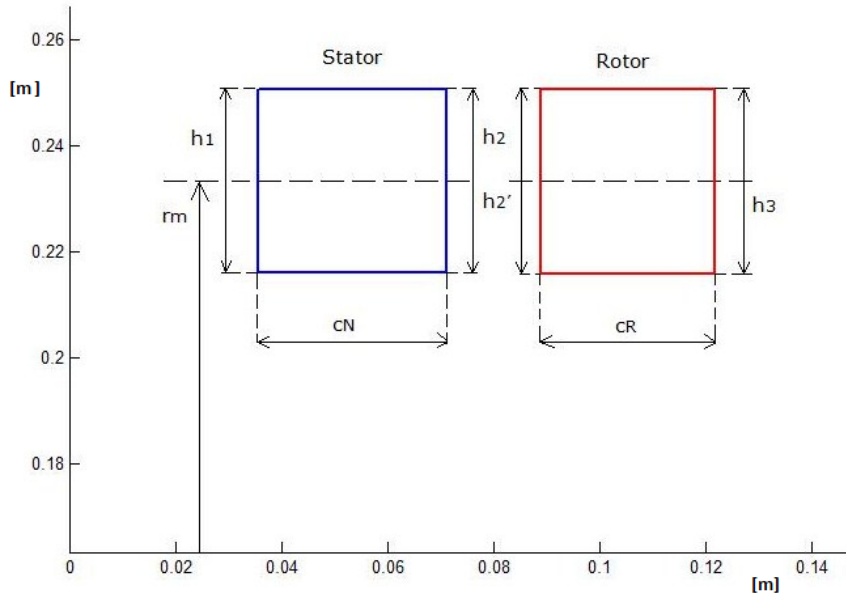


Figure 5.6: Blade geometry for the single-stage gas turbine. Real fluid computational model.

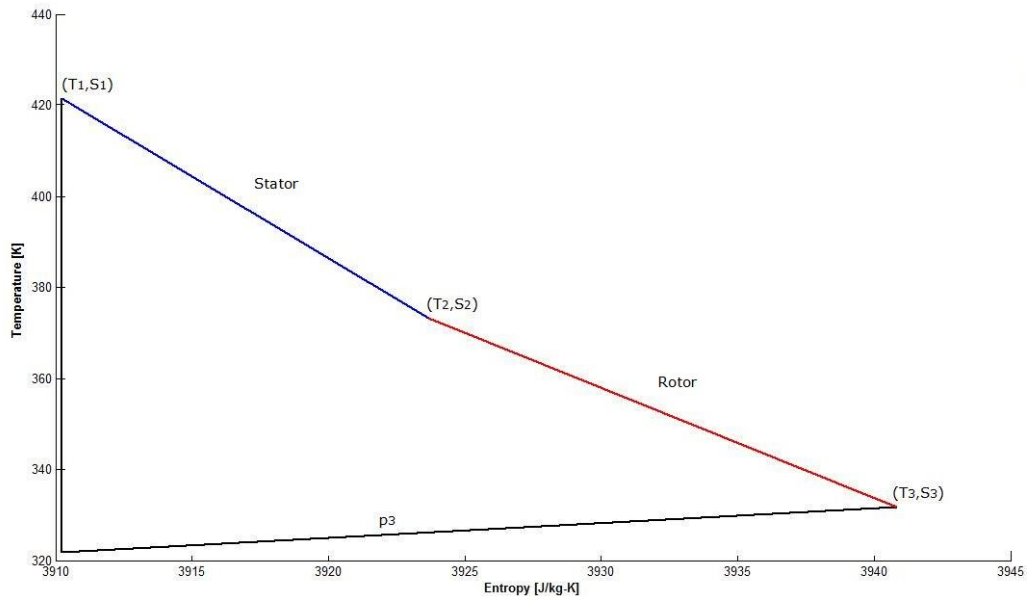


Figure 5.7: T-s diagram for the single-stage gas turbine. Real fluid computational model.

Single-Stage Validation: Verneau (1987)

The validation process was concluded by testing the model against the ORC turbine described in Verneau (1987). The investigated expander was a very low-power turbine built for researching on energy recovery from exhaust gas of car engines. R113 was chosen as working fluid. The theoretical degree of reaction was equal to zero, while the expected power output was close to 3 kW. For manufacturing reasons and aerodynamic efficiency a minimum external diameter of 100 mm was imposed. The target efficiency was pretty low, $\eta_{tt} = 0.65$, due to the very small size and partial admission. Indeed, a single admission arc of 142° was necessary. Small size brought to relevant Reynolds effect and significant tip clearance losses even with shrouded rotor blades. Finally, it should be pointed out that the turbine was supersonic. Table 5.7 presents the inputs obtained by elaborating the available experimental data. While the geometry was completely defined, the flow coefficients and the stage loading coefficient were calculated by working on the experimental data. Table 5.8 reports the comparison between computa-

Table 5.7: Major input data for the validation process against Verneau (1987).

Optimizing Variables	
α_1 [°]	0
ϕ_N	0.69
ψ	4.3
o_{min} [m]	0.0125
o_R [m],	0.0125
c_N [m]	0.0017
c_R [m]	0.001
o_N/s_N	0.258
o_R/s_R	0.4
$h_2/h_{2'}$	1.1
Input Data	
\dot{m} [kg/s]	0.18
T_{01} [K]	403
p_{01} [bar]	6.8
pr	0.167
N [rpm]	18000
Other Inputs	
ϕ_R	0.483

tional and experimental results. For some parameters the comparison was not possible, due to the lack of available information. Although the determination of the performance and the velocity diagram (figure 5.8) was accurate, the computational results were characterized by some imprecisions.

Table 5.8: Validation results for the single-stage R113 turbine. Real fluid computational model.

	Comp. Result	Experim. Result	$\Delta\epsilon_{rel}$
Performance			
η_{tt}	0.652	0.65	0.35%
P [kW]	3.089	3	2.89%
Blade Geometry			
z_N	24	22	8.33%
z_R	122	-	-
s_N [m]	0.013	0.0133	2.304%
s_R [m]	0.003	-	-
r_m [m]	0.484	0.48	0.85%
h_2 [m]	0.004	0.0035	12.5 %
h_3 [m]	0.032	0.005	62.5 %
Λ	-0.263	0	26.3 %
Thermodynamic States			
T_{02} [K]	397.2	-	-
p_{02} [bar]	4.049	-	-
p_2 [bar]	0.61	-	-
T_{03} [K]	366.5	-	-
p_{03} [bar]	1.136	-	-
p_3 [bar]	1.013	-	-
Velocity Diagram U_m [m/s]	91.23	90	1.41 %
$C_{a,2}$ [m/s]	62.9	-	-
$C_{a,3}$ [m/s]	44.08	-	-
C_2 [m/s]	240.1	240	0.05 %
W_3 [m/s]	108.8	-	-
α_2 [°]	74.7	74	1.05 %
β_2 [°]	65.8	65.5	0.5 %
α_3 [°]	10.4	-	-
β_3 [°]	66.09	65.4	1.04 %
M_2	1.87	1.76	5.77 %
$M_{3,rel}$	0.859	0.88	2.42 %

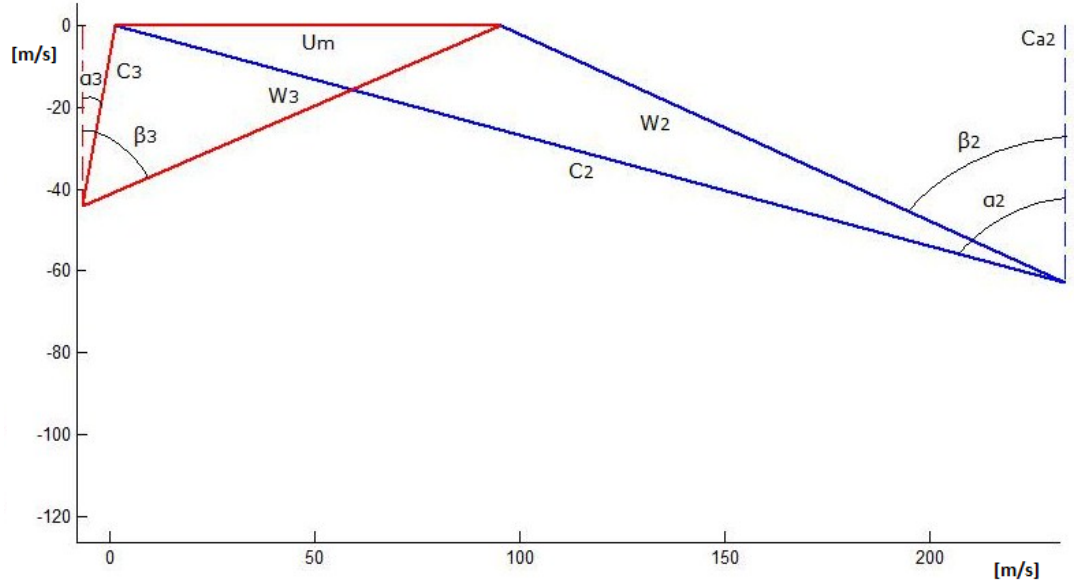


Figure 5.8: Velocity triangles for the single-stage R113 turbine. Real fluid computational model.

In particular:

- **Number of nozzle blades.** Although z_N was affected by a relative error $\Delta\epsilon_{rel} = 8.33\%$, the absolute discrepancy was of 2 blades. For this reason, this was not judged as a relevant error of the code.
- **Nozzle absolute Mach number.** A similar reasoning was applied. Even if M_2 was affected by a relative error of 5.77%, this did not appear as a significant problem, since no information related to the calculation of the speed of sound and the Mach number itself was provided.
- **Blade heights.** In this case a significant relative error was found: $\Delta\epsilon_{rel} = 12.5\%$ for h_2 and $\Delta\epsilon_{rel} = 62.5\%$ for h_3 . Moreover, a converging shape of the rotor, not consistent with that reported in Verneau (1987), was observed (figure 5.9). This was due to a static compression occurring within the rotor. Indeed, although the total conditions were characterized by a consistent pressure gradient, the static pressure at the inlet of the rotor was lower than that at the outlet (0.61 bar versus 1.013 bar). The total and static T-s diagram at mean radius are paralleled in figure 5.10. The unusual behaviour presented in figure 5.10b was connected to the supersonic feature of the turbine. Indeed, at the exit of the nozzle the absolute velocity was much higher than at

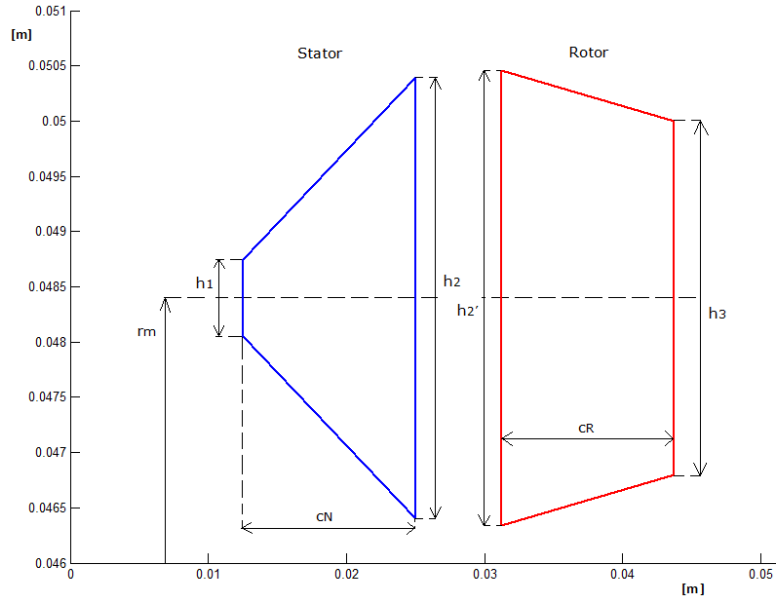


Figure 5.9: Blade geometry for the single-stage R113 turbine. Real fluid computational model.

the outlet of the rotor: $C_2 \gg C_3$ implied $p_2 < p_3$ and $\rho_2 < \rho_3$, even though $p_{02} > p_{03}$. The suffix "0" indicates the total conditions, while "1", "2" and "3" refers to the stations of the stage. This behaviour can actually be registered in supersonic turbo-machinery, as suggested by Sungho (2013): the fluid was strongly accelerated through the nozzle causing a severe pressure drop. Then, a recover in pressure followed inside the rotor, where the fluid had to win the adverse pressure gradient to return to the subsonic conditions. This caused an increasing in density and a reduction in annulus area, as observed in figure 5.9 showing the blade geometry.

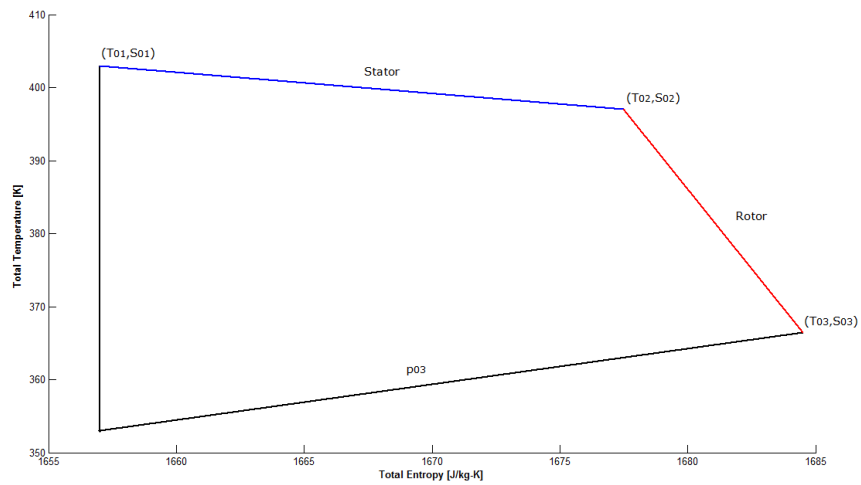
- **Degree of reaction.** The negative degree of reaction of an impulse turbine can be explained recalling its definition:

$$\Lambda = \frac{W_3^2 - W_2^2}{C_2^2 - C_1^2 + W_3^2 - W_2^2} \quad (5.2)$$

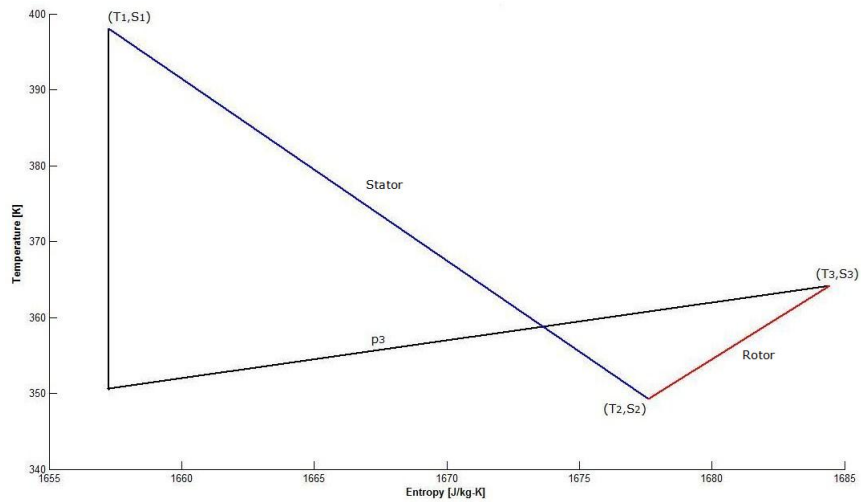
This definition does not include any kind of loss. On the contrary $W_3 < W_2$ due to the friction dissipation (Appendix B); this implies $\Lambda < 0$. Actually, Verneau (1987) stated that, even though the theoretical degree of reaction was equal to zero, the fluid experienced a deceleration through the rotor, $W_3 < W_2$. For this reason, a negative degree of reaction was expected.

Although a detailed comparison was not possible for the thermodynamic properties, the results appeared consistent with the data provided by Verneau (1987). In particular, the exit pressure of $p_{03} = 1.136$ bar agreed with the value of 1.08 bar after the recuperator, before the condenser. Similarly, the exit temperature of $T_{03} = 92.5$ °C was consistent with the value of 67 °C after the recuperator, before the condenser.

Figure 5.10: T-s total and static diagrams for the single-stage R113 turbine. Real fluid computational model.



(a) T-s total diagram



(b) T-s static diagram

6

Optimization of Axial-Flow Turbines

6.1 Introduction

6.1.1 The Genetic Algorithm

The optimization process was based on a genetic algorithm (GA) available through the `ga`-function in the programming language MATLAB (MathWorks (2013)).

For the purpose of the present study, a simple comprehension of the way in which the `ga`-function works is sufficient. For a detailed description of the principle of operation of genetic algorithms see Wikipedia (2013b).

Genetic Algorithms were formally introduced in the United States in the 1970s by John Holland at the University of Michigan. A genetic algorithm is a heuristic search that mimics the process of natural selection. This heuristic process is routinely used to generate useful solutions to optimization and search problems. The genetic algorithm can be applied to solve problems that are not well suited for standard optimization algorithms, including problems in which the objective function is discontinuous, non-differentiable, stochastic, or highly non-linear.

In a genetic algorithm, a population of candidate solutions to an optimization problem, called *individuals*, is evolved toward better solutions. Each candidate solution has a set of properties, its *chromosomes*, which can be mutated and altered. The evolution usually starts from a population of randomly generated individuals, and is an iterative process; the population at each iteration is called a *generation*. In each generation, the fitness of every

individual in the population is evaluated; the fitness is usually the value of the objective function in the optimization problem being solved. The fittest individuals are stochastically selected from the current population, and each individual's genome is modified to form a new generation. The new generation of candidate solutions is then used in the next iteration of the algorithm. Over successive generations, the population "evolves" toward an optimal solution. Each new "child" solution can be born in three different ways:

- Elite: individual in the previous generation with the best fitness values surviving to the new generation.
- Crossover: children created by combining the genotype vectors of a pair of parents.
- Mutation: children created by introducing random changes to a single parent.

Typically, a genetic algorithm requires:

1. A genetic representation of the solution domain;
2. A fitness function to evaluate the solution domain.

The generational process is repeated until a termination condition has been reached. Common terminating conditions are:

- A solution is found that satisfies minimum criteria;
- Fixed number of generations reached;
- The highest ranking solution's fitness is reaching or has reached a plateau such that successive iterations no longer produce better results;

6.2 Methodology

The numerical environment provided by MathWorks (2013) allows to solve single and multi-objective optimization problems. The present study only dealt with a single objective function. In particular, the total-to-static efficiency of the axial-flow turbine represented the objective of the optimization problem. Because the GA minimizes the objective function, the fitness function was defined as the reciprocal of the efficiency of the axial-flow turbine. The implementation of the genetic algorithm required the following steps:

- Definition of a set of boundary conditions. The input parameters given to the genetic algorithm were the cycle requirements reported in table 4.1.

- Definition of a set of optimizing variables (the maximum number of variable is 20). They were chosen based on computational requirements of the design routine.
- Definition of a lower and upper boundary for each optimizing variable. The study assumed the same variable ranges for each application (see table 6.1).
- Characterization of the GA using the command *gaoptimset*. This option allows, for example, to draw the fitness function versus the number of generations using the expression:

$$opts = gaoptimset('PlotFcns', @gaplotbestf)$$

An example of fitness function is displayed in figure 6.1. The figure shows how the algorithm was converging towards an optimum solution, characterized by the highest value of the efficiency.

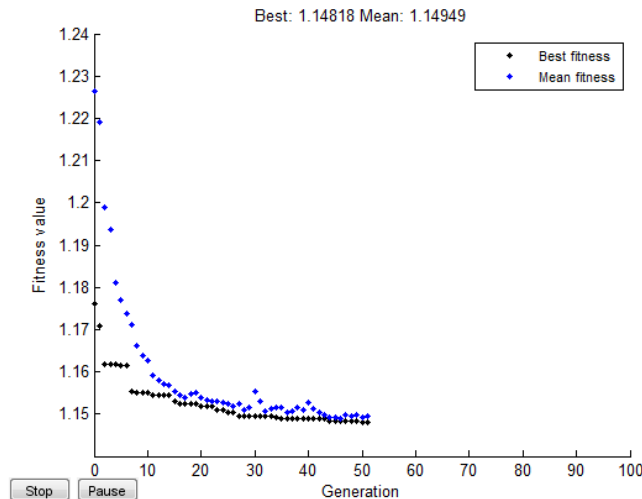


Figure 6.1: Objective function versus number of generations.

- Definition of the fitness function. It is basically the mathematical function to be optimized. This point required the definition of all the inputs for the fitness function, specifying the optimizing variables. They were described by the vector *kobe*, while the function representing the optimization problem was called *Mamba*. Therefore, the fitness function was defined by

$$fitnessfcn = @kobe Mamba(kobe, ...inputs...)$$

- Call of the genetic algorithm through the expression

$$[kobe, fval] = ga (fitnessfcn, nvars, [], [], [], [], lb, ub, [], opts);$$

Where the left-hand side of the expression represents the outputs of the optimization process: *kobe* is the vector characterized by the best set of optimizing variables; *fval* symbolizes the minimum value of the objective function. On the other hand, the right-hand side of the expression reports the inputs to the ga-function: *Fitnessfcn* indicates the call of the fitness function; *nvars* gives the number of optimized variables; *lb* and *ub* and represent the lower and upper boundaries for the vector *kobe*, respectively; *opts* indicates the options specified for the genetic algorithm.

The choice of the total-to-static efficiency as objective function relates to the consideration that mainly single-stage turbines were considered.

The optimization process can be seen as an external shell containing the design routine. Starting from the cycle requirements it rendered the best set of optimization parameters, in terms of turbine efficiency. The lower and upper bounds for each of the optimizing parameters are presented in table 6.1. For multi-stage configurations, each optimizing variable was chosen to

Table 6.1: Optimization variables with lower and upper constrains.

Variable	Lower Bound	Upper Bound
α_1 [°]	-15	+15
ϕ_N	0.2	0.9
ψ	2	7
o_{min} [m]	0.007	0.02
o_R [m]	0.007	0.02
c_N [m]	0.01	0.08
c_R [m]	0.01	0.08
o_N/s_N	0.2	0.5
o_R/s_R	0.2	0.5
$h_2/h_{2'}$	1	1.1

be equal for each stage; in this way, the same blade geometry was ensured for all the stages.

7

Weight of Axial-Flow Turbines

7.1 Introduction

In many ORC applications requirements on weight are not of secondary importance. For this reason, this chapter aims at developing a computational routine for an approximated calculation of the weight of axial-flow turbines. This routine was included in the computational model: starting from the results of the design and optimization process, the weight of the expander was estimated. Each component of the turbine was modelled in its easiest shape. The computational routine started from the definition of the volume of the turbine; then, the weight was determined based on the density of each component.

No validation was carried out in this case due to lack of available data. Therefore, the calculation provides an approximated value of the weight of axial-flow turbines and a relative comparison for different expanders. All the investigated turbines were characterized by similar geometrical proportions.

7.1.1 Materials for Axial-Flow Turbines

Materials have been played, and will continue to play, the key part in efforts to increase axial turbine performance.

The selection of materials for each component follows from the requirements imposed on the component. Therefore, in principle, each component, or a set of identical components may be made from different materials. On the other hand, thinking in term of minimum costs will naturally reduce the number of materials in an engine. Several types of materials are today in widespread use, namely titanium alloys, stainless steels and superalloys

(Saravanamuttoo et al. (2009)).

Titanium alloys are used in fan and compressor blades, discs and casings; *Stainless steels* have iron as the main element, while chromium, nickel and other elements provide resistance to rusting by generating a thin oxide layer on the surface;

In *superalloys* the main alloying element is nickel, cobalt or iron with the nickel-based alloys seeing the most extensive research and development.

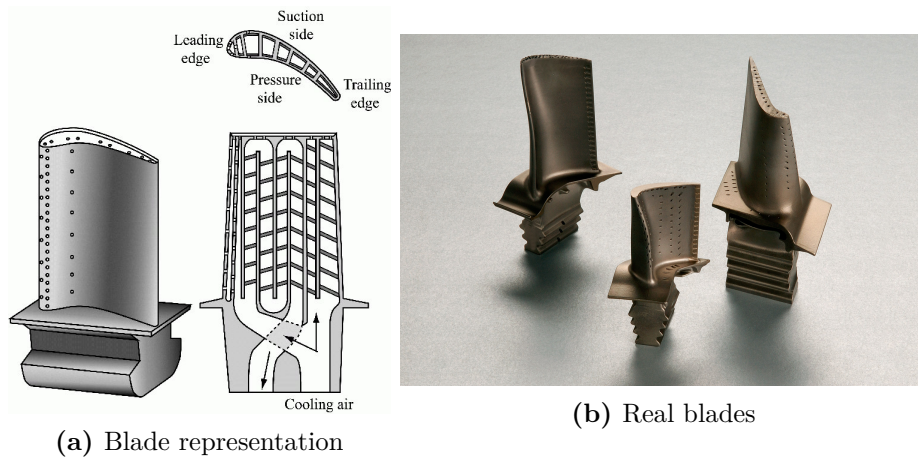
An interesting dissertation on the materials in use for axial-flow turbines is provided by Saravanamuttoo et al. (2009).

7.1.2 Main Components of Axial-Flow Turbines

Blades

Blades turn the flow; in compressors power is absorbed as a result, while in turbine power is generated. Being primarily aerodynamic devices, blades must have accurate aerofoil contours and high surface quality. In figure 2.6 the geometry of the blade and the terminology used to describe the blade profile were shown. Figure 7.1a shows a representation of a turbine blades, while figure 7.1b reports different shapes of actual turbine blades.

Figure 7.1: Turbine blades (Wikipedia (2012)).



Bladed Rotor Discs

A bladed rotor disc support the blades, transfers the torque generated or absorbed by the blades, and supports a pressure differential across the stage. Prime consideration in the design of discs is avoidance of burst, which is caused by elastoplastic failure of disc material. Nevertheless, since a detailed

disc design is outside of the purpose of this study, it assumed the simplest case of discs: uniform (constant thickness), with a bore, rotating at constant speed. Furthermore, the radius was linked to other turbine components based on proportions found in literature (Costa (2006), Babcock & Wilcox (1927)). Figure 7.2 shows a turbine disc with a simple shape.



Figure 7.2: Turbine disc (Walter (2013)).

Bearings

A bearing is a machine element that constrains relative motion and reduces friction between moving parts to only the desired motion. The design of the bearing may, for example, provide for free linear movement of the moving part or for free rotation around a fixed axis. Many bearings also facilitate the desired motion as much as possible by minimizing friction. The two principal types of bearings are rolling elements and hydrodynamic bearings, reported in figure 7.3a and 7.3b, respectively. The bearings are inserted within bearing casings, which provides a support and an attachment point.

Other Components

Other components of axial-flow turbines which were considered for the weight calculation include:

- **Shaft.** Depending on the applications it might be hollow. However, the present analysis assumed a solid cylindrical shaft;
- **Blade shrouding.** Many turbine rotor blades have a shrouding at the top, which interlocks with that of adjacent blades, to increase damping and thereby reduce blade flutter. Figure 7.4 shows a schematic of a shrouded blade;

Figure 7.3: Turbine bearings (Direct industry (2013)).

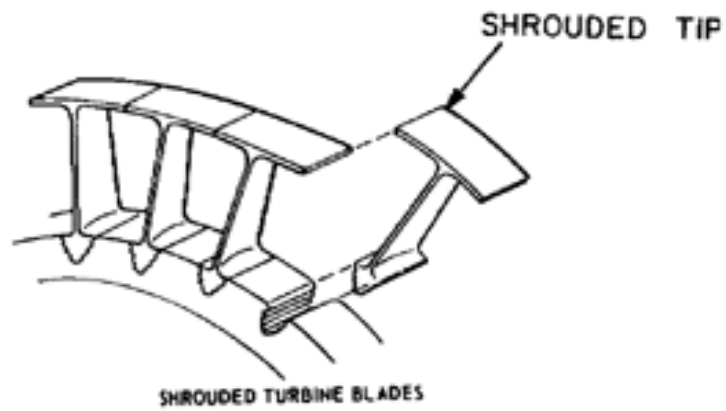


Figure 7.4: Schematic of shrouded blade (Major Engine Section (2012)).

- **Gear box.** It is necessary to couple expander and generator in case of different rotational speeds;
- **Labyrinth seal.** It is a type of mechanical seal that provides a tortuous path to help prevent leakage;
- **Turbine casing.** The external casing.

7.2 Methodology

First, the computational routine estimated the weight for each stage. Then, the heaviness of the turbine as a whole was computed by adding the components external to the stages (see figure 7.5). Initially, the volume of each component was defined starting from the geometry provided by the design and optimization routine. Afterwards, the weight was determined using the density of each component. Table 7.1 reports the density for some materials used for modelling the axial-flow turbine.

The present method did not proceed with the mechanical design of the

Table 7.1: Density of materials used for modelling the axial-flow turbine (Saravanamuttoo et al. (2009)).

Material	Component	ρ [kg/m ³]
Structural steels		
S355	shaft, casing	8000
St52	shaft, casing	7800
Stainless steels		
B23	bearings	7385
C93200	bearings	8910
13Cr5Ni	labyrinth seal	7750
16Cr5Ni	labyrinth seal	8050
Superalloys		
Rene41	discs, blades	8250
Waspalloy	discs	8200
CMSX-4	blades, vanes	8700
CMSX-10	blades, vanes	9050
Steels		
4340	bearings casing	7850
st	gear box	7800
Others		
DCI	bearings casing	7100
Cu	gear box	8933
Powder metals	gear box	6700
JM7	labyrinth	7600

components. On the contrary, it assumed certain geometrical proportions among components based on data found in literature; see Babcock & Wilcox (1927), Costa (2006) and Saravanamuttoo et al. (2009). Basically, the calculation was based on a set of parameters, called Q factors, necessary to define the geometrical dimensions of the expander. In the present analysis they were kept constant, thus assuming a similar geometry for each examined turbine. Table 7.2 reports value and meaning for each of the Q factors. A correction factor of 1.3 was applied to the overall calculation, rounding

Table 7.2: Q factors defining the geometrical proportions of the turbine.

Symbol	Value	Meaning
Q	0.4	shaft radius-to-blade root radius ratio
Q_b	1.25	outer-to-inner bearing radius ratio
Q_{bc}	1.3	outer bearing casing radius-to-inner bearing radius
Q_c	1.6	casing thickness-to-blade height ratio
$Q_{c'}$	1.2	casing length-to-shaft length ratio
Q_{duct}	0.3	duct thickness-to-blade height ratio
Q_{err}	1.3	expected error factor
Q_{lab}	0.05	relative weight of labyrinth seal
Q_{sh}	2	shaft axial length (stage section)-to-stage axial length
$Q_{sh'}$	2	shaft axial length (turbine section)-to-stage axial length
Q_{sr}	0.1	shrouding height-to-blade height ratio
Q_{wh}	0.25	wheel length-to-shaft length ratio
$Q_{wh'}$	1.05	wheel radius-to-shaft radius ratio
$Q_{wh''}$	0.4	gear box casing thickness-to-wheel radius ratio

up the results assuming an inaccuracy of 30%. This error was related to the presence of other, not considered, components and to the degree of approximation.

Figure 7.5 shows a schematic of the calculation process.

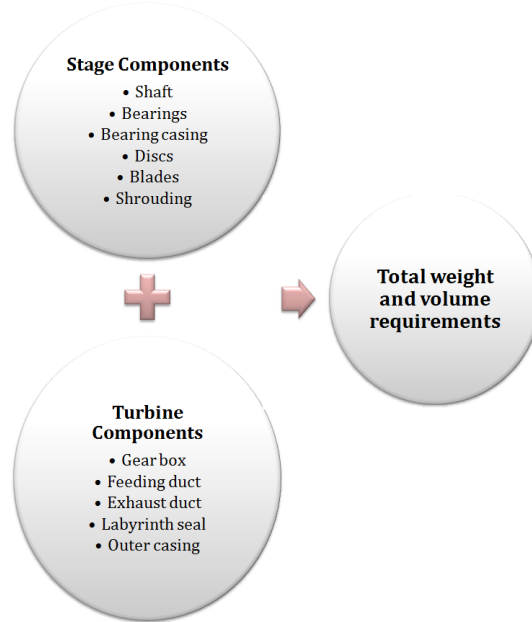
7.2.1 Shaft

The evaluation of the weight of the shaft started from the definition of its volume, based on the geometry defined by the design routine. The shaft was outlined as a solid cylinder, and its radius was considered to be 0.4 (Q) times the blade root radius, averaged upon the length of the stage. In formula, the radius of the shaft (r_{sh}) was given by

$$r_{sh} = \frac{Q(r_{r,1} + r_{r,3})}{2} \quad (7.1)$$

Where the suffix "sh" identifies the shaft, "r" indicates the blade root radius, "1" and "3" refers to the stations of the stage: inlet nozzle and outlet rotor,

Figure 7.5: Weight calculation process.



respectively. The base surface (A) of the shaft was found from the radius using the familiar equation

$$A_{sh} = \pi r_{sh}^2 \quad (7.2)$$

The overall length of the shaft was ideally divided in two sections: one related to the stage, and one linked to the feed and exhaust ducts of the turbine. The section related to the stage, denoted with suffix "S", was assumed to exceed the stage axial extension (the sum of the blade axial chords), by a factor $Q_{sh} = 2$. Thus,

$$l_{sh,S} = Q_{sh} (c_N + c_R + srcl) \quad (7.3)$$

Where l indicates the length, $srcl$ is the clearance between stator and rotor, c_N and c_R are the axial chords of stator and rotor, respectively.

Similarly, the section of the shaft related to the feed and exhaust ducts was assumed to exceed the stage extension by the factor $Q_{sh'} = Q_{sh}$. Therefore, the overall shaft length was

$$l_{sh} = 2 Q_{sh} (c_N + c_R + srcl) \quad (7.4)$$

The volume (V) was computed as

$$V_{sh} = A_{sh} l_{sh} \quad (7.5)$$

Finally, using structural steel S355 the weight (w) of the shaft was obtained by

$$w_{sh} = V_{sh} \rho_{S355} \quad (7.6)$$

7.2.2 Bearings

A similar procedure was followed for the bearings, which were modelled as hollow cylinders and denoted by the subscript "b". The internal and external radii were linked by the factor $Q_b = 1.25$. They were given by

$$r_{in,b} = r_{sh} \quad (7.7)$$

$$r_{ex,b} = Q_b r_{in,b} \quad (7.8)$$

Where "in" and "ex" indicates internal and external radius, respectively. Figure 7.6 shows a part of the turbine shaft with a rolling element and its casing. The base area of one bearing was given by



Figure 7.6: Turbine shaft with bearing (IMTS (2014)).

$$A_b = \pi(r_{ex,b}^2 - r_{in,b}^2) \quad (7.9)$$

The length of the bearings depends on the bore diameter. In practice, different configurations are possible. This study assumed a length-to-bore diameter ratio equal to 0.5, based on data provided by Bearing Work inc. (2013). Therefore,

$$l_b = r_{in,b} \quad (7.10)$$

The volume of the bearings were calculated through equation

$$V_b = n_b A_b l_b \quad (7.11)$$

Where n_b is the number of bearings; $n_b = 4$, since four bearings were accounted for. Finally, the weight of the bearings was determined using equation 7.6 considering stainless steel C93200.

7.2.3 Bearing Casing

The next step was to compute the weight of the bearing casings, denoted by "bc". The casing was modelled as the combination of a ring covering the bearing and a base providing support and an attachment point (IMTS (2014)). The external radius of the casing was defined by the factor $Q_{bc} = 1.3$. Thus, inner and outer radii of the ring were given, respectively, by

$$r_{in,bc} = r_{ex,b} \quad (7.12)$$

$$r_{ex,bc} = Q_{bc} r_{sh} \quad (7.13)$$

The base surface was calculated using equation 7.9. The axial extension of the ring was considered equal to that of the bearing, $l_{bc} = l_b$. Then, the volume the weight of the ring were determined using equation 7.11 and 7.6, respectively. To calculate the weight of the ring, the density of ductile cast iron was used.

Afterwards, the base of the bearing casing was computed. It took the shape of a parallelepiped characterized by:

$$l_{bcb} = 2 l_b \quad (7.14)$$

$$x_{bcb} = 2 r_{sh} \quad (7.15)$$

$$h_{bcb} = r_{ex,b} - r_{in,b} \quad (7.16)$$

Where "bcb" is the suffix identifying the bearing casing. Then, the volume was computed as

$$V_{bcb} = n_b l_{bcb} x_{bcb} h_{bcb} \quad (7.17)$$

And the weight obtained through equation 7.6 using the density of ductile cast iron. Finally, the global weight of the bearing casing was calculated as the sum of the weights of ring and base,

$$w_{bc,tot} = w_{bc} + w_{bcb} \quad (7.18)$$

7.2.4 Discs

Two discs were considered, one for the stator and one for the rotor. Uniform discs with constant thickness were modelled. Each disc was simulated as a hollow cylinder spanning from the shaft radius to the blade root radius, as shown in figure 7.7. Hence, inner and outer radii were given by

$$r_{in,d} = r_{sh} \quad (7.19)$$

$$r_{ex,d} = \frac{r_{r,1} + r_{r,3}}{2} \quad (7.20)$$

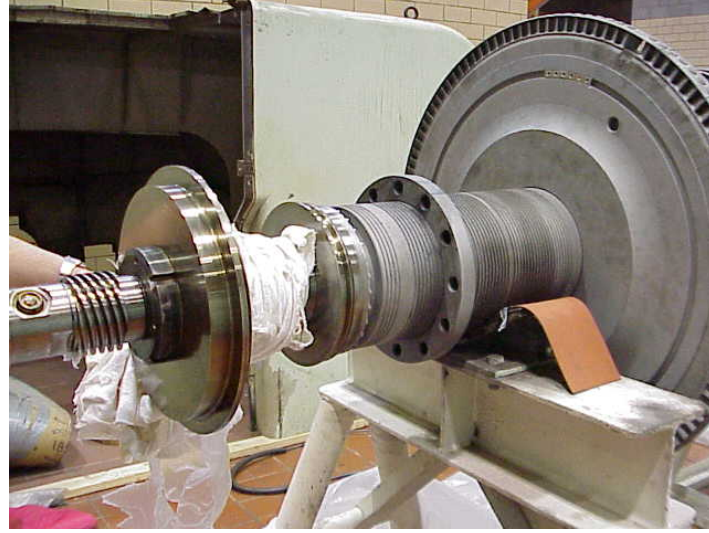


Figure 7.7: Inlet end of axial-flow turbines with first disc (Walter (2013)).

Where the subscript "d" characterizes the disc calculation. The axial extension of each disc was assumed to exceed that of the blade of 5% (Costa (2006)). Thus,

$$l_{dc} = 1.1(c_N + c_R) \quad (7.21)$$

The base surface and the volume of the discs were calculated using equation 7.9 and 7.5, respectively. Then, the weight was computed through equation 7.6 using the density of superalloy Rene41.

7.2.5 Blades

A basic blade profile, as shown in figure 7.8, was investigated. The trailing edge (subscript "te") accounted for the 10% of the overall blade length; its thickness, t_{te} , was defined during the design routine. Then, the thickness of the blade varied along the profile: 3 times that of the trailing edge for the central part; 4 times that of the trailing edge for the leading edge. The central part of the blade and the leading edge accounted for 70% and 20% of the overall blade length, respectively. Hence, the blade thickness (t_{bl}) was computed as

$$t_{bl} = 0.1t_{te} + 0.7(3t_{te}) + 0.2(4t_{te}) \quad (7.22)$$

Next, the blade volume was calculated as

$$V_{bl} = t_{bl} h_{bl} b z \quad (7.23)$$

Where "bl" indicates the blade; h is the blade height, b is the backbone length and z the number of blades. The blade height is actually an averaged



Figure 7.8: High-pressure blade profile (Xylon (2011)).

height given by

$$h_{bl} = \frac{h_{in} + h_{out}}{2} \quad (7.24)$$

Where h_{in} and h_{out} are the blade height at inlet and outlet station. Equations 7.22 and 7.23 were computed for stator and rotor separately. Finally, the weight of the cascade was calculated with equation 7.6 using the density of superalloy CMSX-4.

7.2.6 Shrouding

For shrouded tips, the weight of the shrouding ("sr") was accounted for. The thickness of the shrouding was related to the blade height trough the factor $Q_{sr} = 0.1$. The shrouding was modelled as a ring around the tip with internal and external radii given, respectively, by

$$r_{in,sr} = \frac{r_{t,1} + r_{t,3}}{2} \quad (7.25)$$

$$r_{ex,sr} = r_{in,sr} + Q_{sr} h_R \quad (7.26)$$

Where h_R is the rotor height given by equation 7.24. The shrouding included rotor and stator-rotor clearance. Thus, its axial extension was given by

$$l_{sr} = c_R + srcl \quad (7.27)$$

Next, base surface and volume of the shrouding were computed with equation 7.9 and 7.5, respectively. Finally, the weight was calculated with equation 7.6 where the density of superalloy Rene 41 was used.

With the shrouding, the calculation connected to the heaviness of the stage components was completed. Then, the computational routine concluded the estimation of the turbine weight by adding those components which are external to the stage: gear box, feeding duct, exhaust duct and outer casing.

7.2.7 Gear Box

The gear box was schematized as the ensemble of two shafts and two wheels, designed to bring the rotational speed at the conventional value of $N_a = 3000$ rpm. Therefore, it was implemented only when the axial-flow turbine was rotating at $N \neq N_a$. Both shafts and wheels were modelled as simple cylinders. Two identical shafts were considered. Figure 7.9 shows a power transmission gear box. The axial length of the shafts related to the gear box



Figure 7.9: Power transmission gear box (ACE (2014)).

was assumed to equal that of the "stage portion" of the shaft:

$$l_{sh,gb} = l_{sh,S} \quad (7.28)$$

Where the suffix "gb" indicates the gear box. Moreover, the radius of the gear box shafts was equal to that of the turbine shaft: $r_{sh,gb} = r_{sh}$. Then, base surface, volume and weight of the gear box shafts were computed through equations 7.2 - 7.6.

Afterwards, two wheels ("wh") were modelled, one rotating at turbine rotational speed, identified by subscript "1", and one rotating at alternator rotational speed, indicated with subscript "2". The axial length of the wheels

was linked to that of the shafts through the factor $Q_{wh} = 0.25$. In particular,

$$l_{wh} = Q_{wh} l_{sh,gb} \quad (7.29)$$

The radius of wheel 1 was related to that of its shaft through the factor $Q_{wh'} = 1.05$. Thus,

$$r_{wh1} = Q_{wh'} r_{sh,gb} \quad (7.30)$$

On the other hand, the radius of wheel "2" was computed as

$$r_{wh2} = r_{wh1} \frac{N}{Na} \quad (7.31)$$

Where N and Na are the turbine and alternator rotational speed, respectively. Then, the weight was calculated for the two wheels considering the density of copper.

The gear box was completed by an outer casing whose external radius was related to that of wheel 1 through the factor $Q_{wh''} = 0.4$. In particular, for $N > Na$, inner and outer radii are provided by

$$r_{in,gbc} = r_{wh2} + 0.005 \quad (7.32)$$

$$r_{ex,gbc} = r_{in,gbc} + Q_{wh''} r_{wh1} \quad (7.33)$$

Where the subscript "gbc" refers to the gear box casing. The weight of the casing was obtained using the density of copper. Finally, the total weight of the gear box was calculated as the sum of the components:

$$w_{gb} = 2 w_{sh,gb} + w_{wh1} + w_{wh2} + w_{gbc} \quad (7.34)$$

7.2.8 Feeding and Exhaust Ducts

Both the feeding duct and the exhaust duct were represented as hollow cylinders made up by Rene 41 and St52, respectively.

- **Feeding duct.** The thickness of the feeding duct was connected to the inlet blade height of the first stage through the factor $Q_{duct} = 0.3$. The inner and outer radii were given by

$$r_{in,feed} = r_{t,1,first\ stage} \quad (7.35)$$

$$r_{ex,feed} = r_{in,feed} + Q_{duct} h_{1,first\ stage} \quad (7.36)$$

The length of the duct was given by the factor $Q_{sh'}$ and axial extension of the first stage:

$$l_{feed} = \frac{Q_{sh'}}{2} (c_N + c_R + srcl)_{first\ stage} \quad (7.37)$$

The volume and weight of the duct were determined using equation 7.6.

- **Exhaust duct.** The thickness of the exhaust duct depended on the exit blade height of the last stage through the factor Q_{duct} . In particular,

$$r_{in,exh} = r_{t,3,last\ stage} \quad (7.38)$$

$$r_{ex,exh} = r_{in,exh} + Q_{duct} h_{3,last\ stage} \quad (7.39)$$

The length of the duct was given by factor $Q_{sh'}$ and axial extension of the last stage:

$$l_{feed} = \frac{Q_{sh'}}{2} (c_N + c_R + srcl)_{last\ stage} \quad (7.40)$$

The weight of the exhaust duct was computed in the usual way.

7.2.9 Labyrinth seal

The weight of the labyrinth seal was estimated by following a different approach. Indeed, it was purely assumed to account for a certain percentage of the total weight of all the other components, including the outer casing. Such a percentage was given by the factor $Q_{lab} = 0.05$. Therefore,

$$w_{lab} = Q_{lab} \sum_i w_i \quad (7.41)$$

Where the index i refers to each component of the turbine.

7.2.10 Casing

Finally, the expander outer casing was implemented. It was simulated as a hollow cylinder of structural steel St52. Its thickness was related to the blade height through the factor $Q_c = 1.6$. Internal and external radii were given by

$$r_{in,c} = r_{out,sr} + 0.01 \quad (7.42)$$

$$r_{ex,c} = r_{in,c} + Q_c \left(\frac{h_N + h_R}{2} \right) \quad (7.43)$$

The axial extension of the casing was connected to that of the turbine by the factor $Q_{c'} = 1.2$. Thus,

$$l_c = Q_{c'} l_{sh} \quad (7.44)$$

Then, volume and weight of the casing were computed through equations 7.5 and 7.6.

7.2.11 Total Weight and Volume Requirements

The calculations described from section 7.2.1 - 7.2.6 were computed for each stage. Then, the overall expander weight was calculated as

$$w_{tot} = \left(\sum_j \sum_i^{nst \text{ stage comp.}} w_{i,j} \right) + w_{gb} + w_{feed} + w_{exh} + w_{lab} + w_c \quad (7.45)$$

Where index j is related to the number of stages and index i to the stage components. Finally, the overall volume requirements for the turbine were computed as

$$V_{tot} = Q_{err} \pi r_{ex,tot}^2 l_{ex,tot} \quad (7.46)$$

Where $r_{ex,tot}$ was the maximum value between the outer radius of the external casing and that of the gear box casing; $l_{ex,tot}$ was the total extension of external casing and gear box:

$$l_{ex,tot} = l_c + l_{sh,gb} \quad (7.47)$$

8

Applications

In the present study, the computational model was used for the following applications:

1. Determination of the turbine optimal design for given cycle requirements;
2. Drawing of the turbine efficiency charts, studying the efficiency profile for different inlet pressures as a function of the specific speed N_s ;
3. Comparison of the turbine performance for three competing heat recovery systems, in the context of the Draugen offshore platform;
4. Comparison of the turbine performance for three organic working fluids;
5. Evaluation of the effects of binary mixture composition on turbine performance.

First, the computational model was applied to the case of study of the Draugen offshore platform (see Chapter 3). In this context, the thesis provided a tool for the prediction of the performance of the axial-flow turbine of the heat recovery system.

Afterwards, the simulation model was applied to the study of a different offshore platform, investigating three competing ORC heat recovery systems. In particular, the performance of the expander was investigated for three different ORC units handling cyclopentane, MDM and R245fa.

Finally, the effects of the composition of a binary mixture on both the turbine isentropic efficiency and the cycle performance were evaluated in the context of a liquid heat source at 120°.

8.1 Optimal Design Point

The computational simulations were performed modelling a single-stage turbine, with constant axial velocity through the stage. The input data for the design and optimization process derived from a previous optimization of the thermodynamic cycles; depending on the context different objective functions were selected. Table 8.1 presents the boundary conditions provided by the thermodynamic cycles. As already said, a complete list of the inputs for the design routine can be found in Appendix D. Starting from this in-

Table 8.1: Cycle requirements imposed to the design and optimization process.

Parameter	Symbol
Mass flow rate [kg/s]	\dot{m}
Total inlet temperature [K]	T_{01}
Total inlet pressure [bar]	p_{01}
Expansion ratio	pr
Fluid	
Designer choice	
Rotational speed [rpm]	N
Number of stages	n_{st}

put data, the optimization rendered the best set of optimizing variables in terms of optimal total-to-static efficiency of the axial-flow turbine. Then, the optimal design was obtained.

8.2 Efficiency Chart

Once the optimal solution was calculated for a given set of boundary conditions, the thesis investigated the turbine performance for different mass flow rates and inlet pressures. In particular, the total-to-static efficiency was drawn as a function of the specific speed (Ns).

The total-to-static efficiency was defined in chapter 2 using equation 2.2. The specific speed Ns is a dimensionless parameter related to the size and the rotational speed of the turbine. It is given by

$$Ns = \frac{N\sqrt{\dot{V}_{out}}}{\Delta h_{is}^{3/4}} \quad (8.1)$$

Where N is the rotational speed of the turbine expressed in [rev/s], $\sqrt{\dot{V}_{out}}$ is the volumetric rate at the exit of the stage and Δh_{is} is the isentropic enthalpy drop.

For a given value of the inlet pressure, the specific speed was changed by

varying the mass flow rate. Depending on the application, the mass flow rate ranged between 5 kg/s and 800 kg/s, resulting in a specific speed extending from 0.01 to 0.19. The same procedure was repeated for different values of the inlet pressure; depending on the situation and on the fluid, the inlet pressure covered a wide range, spanning from 2.36 bar for a gas turbine to 40 bar for a cyclopentane turbine. All the other boundary conditions remained unchanged during the drawing of the efficiency charts.

8.3 Comparison between ORC, SRC and ABC Axial Expanders

This comparison took place in the context of the Draugen offshore platform. A wider analysis of the platform, performed by Pierobon et al. (2013), took into consideration three competing heat recovery systems and compared them in order to find the most effective solution in terms of cycle performance, net present value, weight and carbon dioxide emissions. In particular, organic Rankine cycle (ORC), steam Rankine cycle (SRC) and air bottoming cycle (ABC) were paralleled. Nevertheless, this study did not account for variations of turbine efficiency. For this reason, the thesis participated in the investigation by providing a simulation model for the prediction of the performance of the expander for the three bottoming cycles. In the three cases, a single-stage turbine was designed using the data coming from a previous optimization of the thermodynamic cycle; the maximum net present value of the cycle was the objective function of the optimization problem. The three axial-flow turbines were analysed by comparing the three design points and the efficiency charts.

Something more should be said on the choice of the rotational speed for each turbine. This was equal to 3000 rpm for the ORC turbine, handling cyclopentane. Indeed, this rotational speed was found to be suitable for this kind of expander, allowing to couple turbine and generator without the need of a gear box. On the other hand, $N = 11700$ rpm was chosen for the steam turbine since this rotational speed appeared as the aptest choice for the design mass flow rate equal to $\dot{m} = 7.299$ kg/s, based on data proposed by Mitsubishi (2012). Finally, $N = 3600$ rpm for the ABC was selected to be equal to the rotational speed of the SGT500, i.e. the turbine of the topping cycle of the Draugen offshore platform; this would allow to use the same shaft for the two turbines.

Finally, it should be observed that at the end of the steam expansion two phases occur. Therefore, wet loss must be accounted for. This study calculated the efficiency penalization due to the wet loss using the methodology proposed by Kotton (1998), described in Chapter 4.

8.4 Axial-Flow Turbine Performance for different Working Fluids

A major topic in investigation of organic Rankine cycles is the working fluid selection, since it affects cycle performance and component design. Hazard levels, ozone depletion potential (ODP), global warming potential (GWP) and thermal stability must also be considered. When choosing a working fluid for an ORC, it is therefore necessary to consider many different parameters, in order to reach a feasible design. For this reason, another interesting application is related to the investigation of the turbine performance for different organic working fluids. In particular, the examination compared three heat recovery systems for an offshore application. The topping cycle was given by a gas turbine, while the bottoming cycle was an ORC unit operating with three representative working fluids:

- **Cyclopentane** as hydrocarbon (HC). It is a highly flammable alicyclic hydrocarbon with chemical formula C_5H_{10} . It occurs as a colourless liquid with a petrol like odor. Its melting and boiling point are at 94°C and 49°C , respectively;
- **MDM** as siloxane. Precisely it is an *octamethyltrisiloxane*, a heavy organic compound with molar mass equal to $M = 236.53$;
- **R245fa** as refrigerant. It is also called *pentafluoropropane* and it is a refrigerant used primarily for closed-cell spray foam insulation. Unlike CFC and HCFC, blowing agents formerly used for this purpose, it has no ozone depletion potential and is nearly non-toxic. It does have a high GWP, equal to 950.

The selected fluids are commercially available and suitable for ORC applications; also, they allow to operate under subcritical conditions. Moreover, the three fluids cover a wide range of thermodynamic properties: critical pressure varying from 14.1 bar to 45.1 bar, critical temperature ranging from 154.1°C to 291°C and molecular weight varying from 70.13 kg/kmol to 236.5 kg/kmol. Figure 8.1 shows the T-s diagram for the considered fluids. Furthermore, this fluid selection allowed to identify limitations and benefits of selected ORC fluids. In particular, R245fa and cyclopentane are characterized by high critical temperature in comparison with other refrigerants and linear hydrocarbons, respectively. Similarly, MDM steam temperature in subcritical conditions is close to best hydrocarbons value; it is a dry fluid with low critical pressure and for this reasons it is used in various commercial ORC units.

The comparison was performed analysing the optimal design for three single-stage turbines. The sets of boundary conditions was provided by a previous

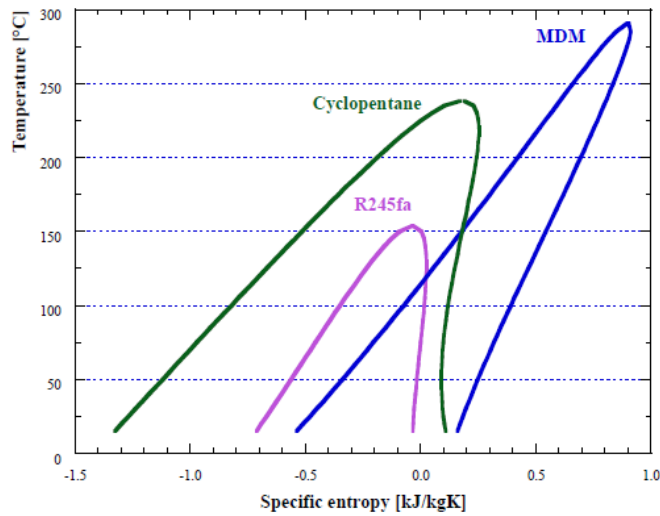


Figure 8.1: T-s diagram for cyclopentane, MDM and R245fa.

optimization of the thermodynamic cycle; for the three fluids, the temperature of the hot gases and the requirements of the cooling fluid remained unchanged. The maximum net power output of the cycle represented the objective function for the optimization process. It should be pointed out that the three cycles were modelled in order to work in subcritical conditions. Finally, the efficiency charts for the three turbines were also paralleled.

8.5 Performance Analysis for Axial-Flow Turbines Operating Binary Fluids

Although an abundant literature is available on fluid selection for pure fluids, binary working fluids have been studied far less, despite the available literature suggesting possible performance benefits when zeotropic mixtures are used in organic Rankine cycles. The non-isothermal change phase of zeotropic mixtures can be utilized to optimize the heat transfer processes in the evaporator and the condenser thus increasing the efficiency of the ORC. The thesis examined the effects of the composition of an isopentane/isobutane mixture on the performance of a single-stage axial-flow turbine. The case of study was given by the ORC unit simulated as described in table 8.2. The heat source was liquid water at 120 °C representing a geothermal heat source. The thermodynamic cycle was optimized considering the maximum net power output as the objective function of the optimization process. Initially, the organic Rankine cycle unit was optimized at different mixture compositions by assuming a constant isentropic efficiency. Subse-

Table 8.2: Modelling conditions for the ORC operating binary mixtures as working fluids.

Quantity	Value
Heat source (water)	
Heat source temperature	393.15 K
Heat source mass flow rate	50 kg/s
Heat source pressure	4 bar
Condenser	
Cooling water inlet temperature	298.15 K
Cooling water temperature rise	5 K
Min. temperature difference	5 K
Outlet vapour quality	0
Cooling water pressure	4 bar
Pump	
Isentropic efficiency	0.8
Boiler	
Min. temperature difference	10 K
Turbine	
Isentropic efficiency	0.8
Min. vapour quality at the outlet	1

quently, the turbine was designed for each optimal solution and the new cycle performance was evaluated including the actual expander efficiency. Finally, the analysis of the losses occurring within the single-stage turbine was carried out.

9

Results And Discussion

9.1 Heat Recovery System for Draugen Offshore Platform

9.1.1 Optimal Design Point for the ORC Axial-Flow Turbine

The design and optimization process was applied to the ORC heat recovery system of the Draugen offshore platform. The topping cycle was the gas turbine SGT500 described in chapter 3, while the bottoming cycle was an organic Rankine cycle operating with cyclopentane. The cycle requirements are reported in table 9.1. This set of data came from a previous optimiza-

Table 9.1: Design Boundary conditions for the ORC single-stage axial-flow turbine. Draugen offshore platform.

Parameter	Value
\dot{m} [kg/s]	45
T_{01} [K]	513
p_{01} [bar]	30
pr	0.0333
Fluid	Cyclopentane
Designer choice	
N [rpm]	3000
n_{st}	1

tion of the ORC unit, where the maximum net present value represented the objective function (Pierobon et al. (2013)). The optimal set of optimizing variables is described in table 9.2.

Table 9.3 presents the optimal design solution. For the meaning of the symbols in the table, see Chapter Nomenclature.

Table 9.2: Ideal set of optimizing parameters for the ORC single-stage turbine. Draugen offshore platform.

Variable	Optimal Value
α_1	0.8834°
ϕ_N	0.3356
ψ	3.4057
o_{min} [m]	0.02
o_R [m]	0.0077
c_N [m]	0.0773
c_R [m]	0.0422
o_N/s_N	0.2382
o_R/s_R	0.439
h_2/h_2'	1.0577

A representation of the velocity diagram is displayed in figure 9.1. The figure highlights how the analysis was carried out using the hypothesis of constant axial velocity. Moreover, it confirms that the optimal solution is given by an impulse turbine, with a degree of reaction of $\Lambda = 0.14$.

Figure 9.2 shows the blade geometry. It denotes a big increase in the ro-

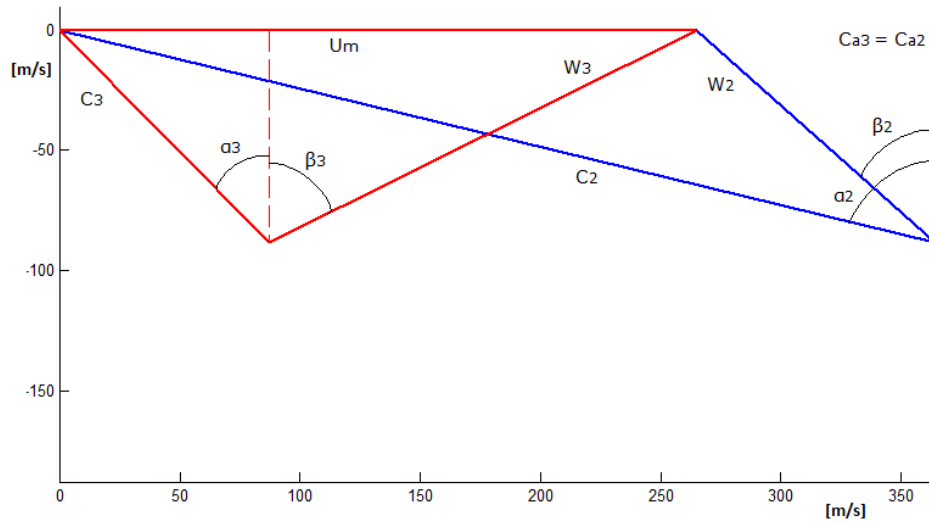


Figure 9.1: Velocity triangles of the optimal ORC single-stage turbine. Draugen offshore platform.

tor height (h_R) due to the density drop. Indeed the density decreases from 5.9 kg/m^3 to 1.7 kg/m^3 . Since mass flow rate and axial velocity remains basically constant, the density reduction turns in a proportional height enhancement, from 0.016 m to 0.054 m. Both the quantities are characterized

Table 9.3: Optimal design features of the ORC single-stage turbine. Draugen offshore platform.

Performance	
η_{tt}	0.746
η_{ts}	0.724
P [MW]	5.635
W_s [MJ/kg]	0.126
Blade Geometry	
z_N	44
z_R	303
s_N [m]	0.121
s_R [m]	0.018
h_1 [m]	0.001
h_2 [m]	0.016
h_3 [m]	0.054
r_m [m]	0.844
Λ	0.14
Thermodynamic States	
T_{02} [K]	494.5
p_{02} [bar]	11.62
ρ_2 [kg/m ³]	5.879
T_{03} [K]	422.8
p_{03} [bar]	1.001
ρ_3 [kg/m ³]	1.728
Velocity Diagram	
U_m [m/s]	265.0
C_a [m/s]	88.51
C_2 [m/s]	374.6
W_3 [m/s]	198.9
α_2 [°]	76.34
β_2 [°]	48.17
α_3 [°]	-44.55
β_3 [°]	63.58
M_2	1.619
$M_{3,rel}$	0.872
Craig-Cox Losses	
$X_{P,N}$ [MJ/kg]	1.006
$X_{S,N}$ [MJ/kg]	1.915
$X_{P,R}$ [MJ/kg]	0.166
$X_{S,R}$ [MJ/kg]	0.118
X_{an} [MJ/kg]	0.132
$X_{I,N}$ [MJ/kg]	2.454
$X_{I,R}$ [MJ/kg]	0.351
Y_{II}	0.040

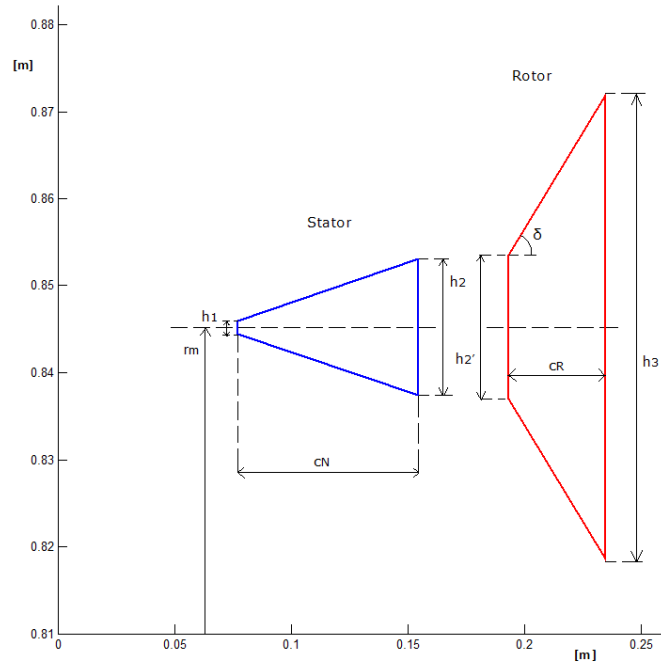


Figure 9.2: Blade geometry of the optimal ORC single-stage turbine. Draugen offshore platform.

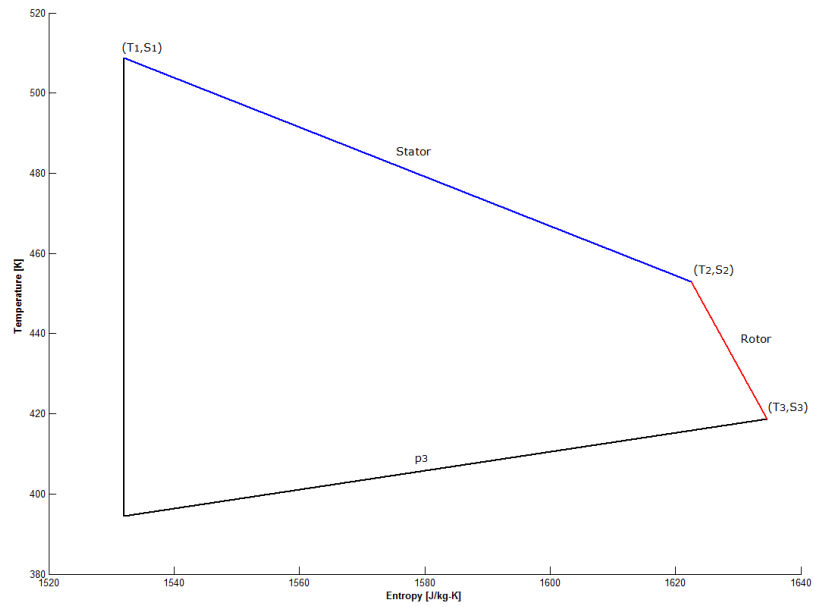


Figure 9.3: T-s static diagram of the optimal ORC single-stage turbine. Draugen offshore platform.

by a variation ratio of $h_3/h_2 = \rho_2/\rho_3 = 3.42$. The high increase in the rotor height translates in a value of the rotor flare angle equal to the upper constraint, $\delta_R = 25^\circ$. Because of this safety requirements on the flare angle, assuming fixed the blade height by an optimal annulus area, the rotor axial chord had to assume a precise value given by equation 4.45. In particular, $c_N = 0.044$ m.

The T-s static diagram of the expansion is reported in figure 9.3. From the diagram the efficiency of the rotor appears higher than that of the stator. Indeed, a smaller temperature drop occurs in the stator in spite of a higher entropy production. Moreover, the overall turbine efficiency, $\eta_{tt} = 0.746$, agrees with the observable temperature difference between real and isentropic conditions, around 25 K.

Finally, the results of the approximated calculation of weight and volume requirements are presented in table 9.4. The power output of $P = 5.63$ MW

Table 9.4: Weight and volume requirements for each component of the optimal ORC single-stage turbine. Draugen offshore platform

Component	Weight [ton]	Volume [m ³]
Shaft	2.852	-
Bearings	1.566	-
Bearings casing	0.422	-
Discs	2.768	-
Blades	0.020	-
Shrouding	0.017	-
Casing	1.964	-
Gear System	0	-
Seals	0.488	-
Feed Duct	0.100	-
Exhaust Duct	0.402	-
Other/Inaccuracy	3.225	-
Turbine	13.83	3.57

leads to a **specific weight of 2.45 ton/MW** and a **specific volume requirements of 0.63 m³/MW**.

Figure 9.4 shows the breakdown of the turbine weight. The plot shows that the heavier components are the shaft (21%), the discs (20%) and the casing (14%). In this case, the gear box is not accounted for due to the fact that the expander rotates at 3000 rpm.

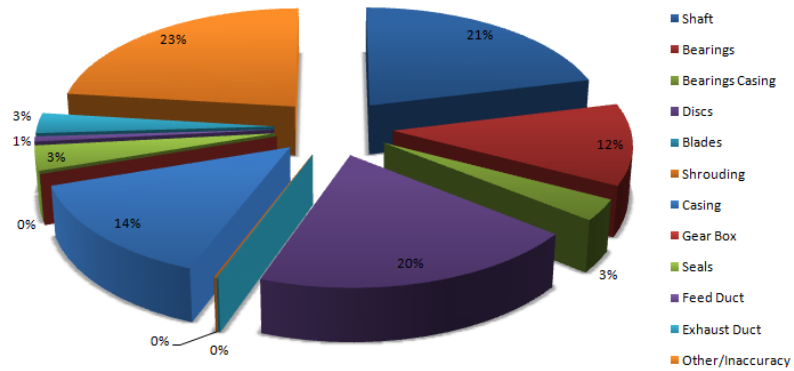


Figure 9.4: Breakdown of the weight of the optimal ORC single-stage turbine. Draugen offshore platform.

9.1.2 Efficiency Chart

After the determination of the optimal design, the study proceeded with the evaluation of turbine performance for different working conditions. In

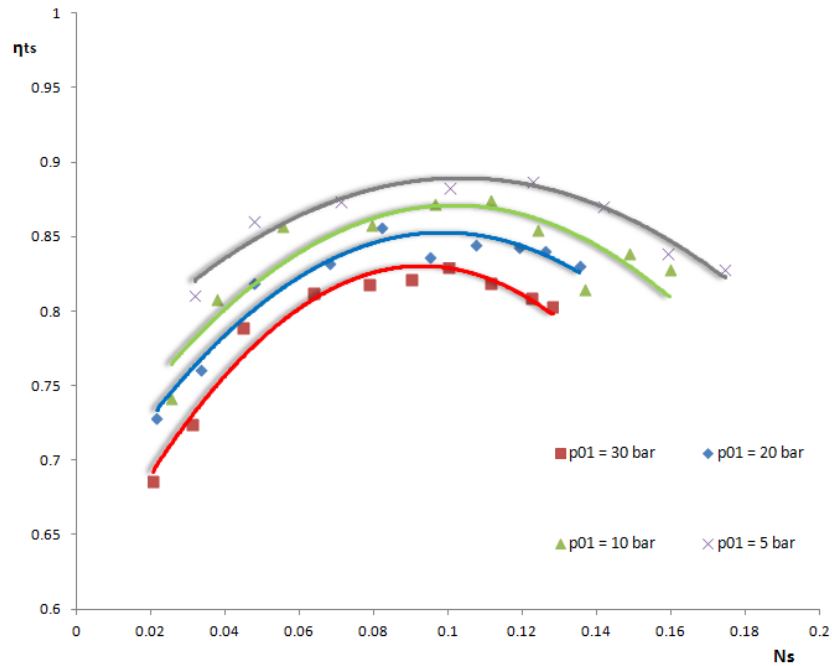


Figure 9.5: Total-to-static efficiency as a function of the specific speed for p_{01} equal to 5, 10, 20, 30 bar. ORC single-stage axial turbine.

particular, the optimal design was defined for different inlet pressures and

mass flow rates: for a given inlet pressure the total-to-static efficiency was drawn as a function of the specific speed. The mass flow rate ranged from 20 kg/s to 800 kg/s, causing a variation of the specific speed from 0.02 to 0.125 (equation 8.1). The procedure was repeated for four total inlet pressures (p_{01}) varying from 5 bar to 30 bar (design condition). The pressure ratio changed accordingly to the inlet pressure in order to maintain 1.01 bar at the exit of the turbine. Indeed, the final total pressure was assumed to be fixed by the condenser and it was considered slightly higher than one; this allowed to avoid depressions in the condenser, which would cause air leaking inside. Figure 9.5 shows the total-to-static efficiency as a function of the specific speed for inlet pressure of 5 bar, 10 bar, 20 bar and 30 bar. The plot was built exploiting the optimization results reported in Appendix H.3. Figure 9.5 highlights that the efficiency presents a maximum for a given specific speed. The optimal specific speed (Ns_{opt}) slightly increases when decreasing the inlet pressure, as summarized by table 9.5. The table suggests that

Table 9.5: Maximum efficiency and optimal specific speed for variable inlet pressures. ORC single-stage axial turbine.

p_{01} [bar]	$\eta_{ts,max}$	Ns_{opt}
30	0.849	0.1
20	0.860	0.107
10	0.884	0.111
5	0.897	0.122

the maximum efficiency for the expander is not reached in correspondence of the design configuration provided by Pierobon et al. (2013). Indeed, at design pressure, while the optimal net present value of the cycle is reached for $Ns_{opt} = 0.031$, the ideal condition for the turbine is given by $Ns_{opt} = 0.1$. In terms of mass flow rates, $\dot{m}_{opt} = 500$ kg/s for the expander, leading to a turbine efficiency of $\eta_{ts} = 0.849$; $\dot{m}_{opt} = 45$ kg/s for the ORC unit, implying a turbine efficiency of $\eta_{ts} = 0.724$. This might shift the optimal design condition of the cycle towards higher mass flow rates.

Furthermore, figure 9.5 also shows how the turbine efficiency increases when decreasing the inlet pressure and so the pressure drop. Indeed, lower pressure drops bring to smaller fluid accelerations and lower fluid deviations. Both these factors turn in reduced loss and higher turbine efficiency.

Finally, figure 9.5 highlights how the trend of the efficiency is not parabolic. Indeed, although the profile presents a maximum, the curve is steeper before the peak than after it. To understand the reasons underlying such phenomenon, an analysis of the losses as a function of the specific speed was carried out. The losses investigation was performed only at design pressure (30 bar), being conceptually analogous for each pressure. Several competing losses defines the turbine efficiency (Chapter 2). In the present thesis the

overall loss was divided into two groups, expressed in table 4.2, as suggested by Craig & Cox (1971). While the group 1 losses was expressed in [MJ/kg], the group 2 loss was provided as an efficiency debit to be subtracted to the efficiency calculated through the group 1 loss. While group 1 loss was examined for nozzle and rotor separately, group 2 loss was related to the stage as a whole.

Figure 9.6 displays all the fractions of group 1 dissipation as a function of specific speed. In the figure each contribution is added to the sum of the pre-

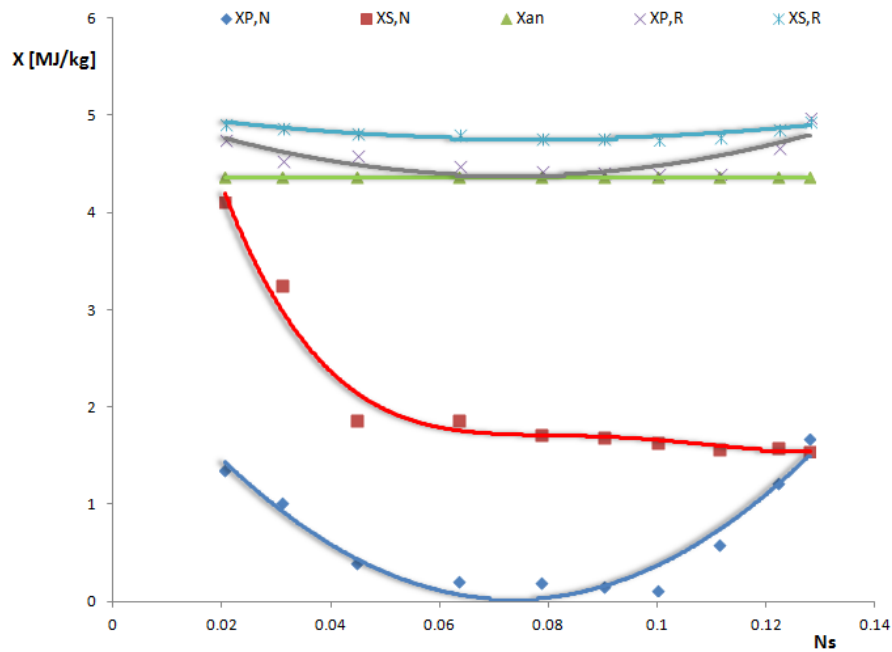


Figure 9.6: Group 1 loss fractions as a function of specific speed. ORC single-stage axial turbine.

vious ones, in order to highlight the different profiles. The annulus loss was given as a single coefficient for stator and rotor, since the nozzle share was found to be practically constant and overriding the rotor one. The meaning of the symbols in the figure is the following: X indicates the loss coefficient; the subscripts "N" and "R" stand for nozzle and rotor, respectively; "P" indicates the profile loss, "S" the secondary loss and "an" the annular loss. Figure 9.6 suggests that:

- Certain losses present a minimum, while other are characterized by a monotone trend. In particular, nozzle profile losses, rotor profile losses and rotor secondary losses present a minimum. Nozzle secondary losses and annulus losses decrease for increasing specific speed. The present

chapter will refer to the first type of loss as *A loss* and to second type as *B loss*;

- Within B loss, the annulus dissipation is practically constant, while nozzle secondary loss decreases remarkably;
- A and B losses compete after the minimum point. However, the enhancement of group A loss after the minimum point exceeds the reduction of B loss. As a result, the overall group 1 loss still presents a minimum, with the curve raising less steeply after it (figure 9.7);
- As a consequence of the decreasing trend of B loss, the absolute value of group 1 loss is higher for low specific speeds than for high specific speed;
- Rotor losses are less affected than the nozzle losses by the specific speed.

The last three points can be clarified drawing the profile of the group 1 overall loss, shown in figure 9.7. The figure displays the group 1 loss for the stator ($X_{I,N}$), the group 1 loss for the rotor ($X_{I,R}$) and the global group 1 loss given by the sum of the two ($X_{I,tot}$). The figure actually exhibits a min-

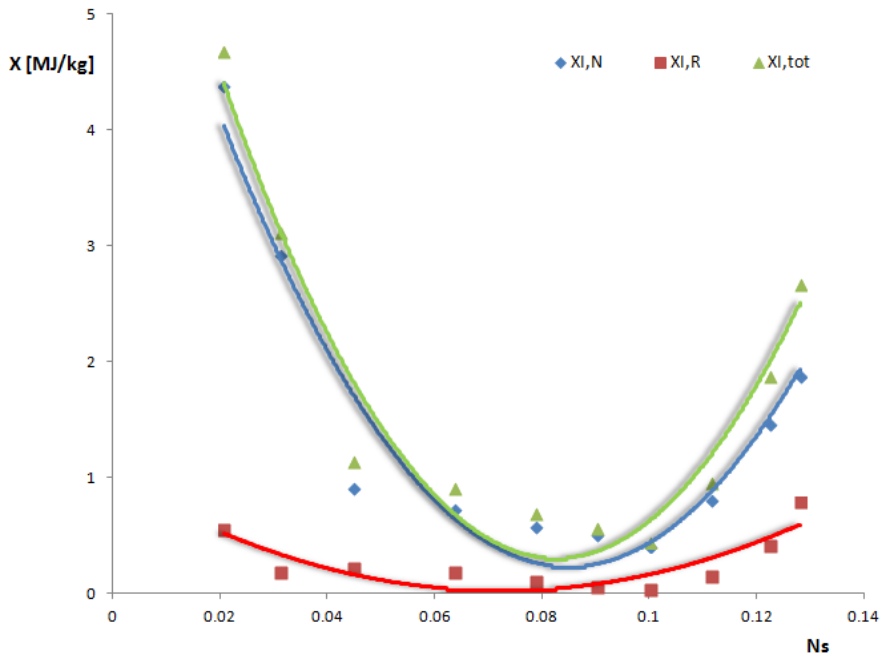


Figure 9.7: Group 1 overall loss as a function of specific speed. ORC single-stage axial turbine.

imum for the group 1 overall loss. Nevertheless, the curve is flatter after the minimum than before it. Moreover, the loss absolute value is smaller after the minimum than before it. Both of these facts are due to the competition of A and B losses. Furthermore, figure 9.7 confirms that the rotor loss is less significant than nozzle loss and it is less affected by the mass flow rate. Finally, the trend of group 2 loss (Y_{II}) is reported in figure 9.8; it reflects a monotone decreasing trend with the specific speed. Therefore, the same conflict experienced by A and B losses was repeated between group 1 and 2 losses. As a result, although the overall loss presents a minimum, the

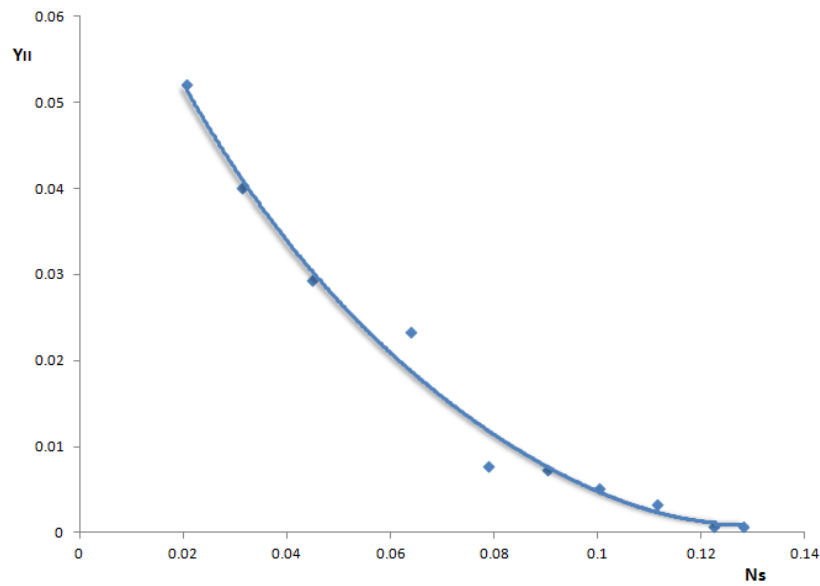


Figure 9.8: Group 2 overall loss as a function of specific speed. ORC single-stage axial turbine.

curve raises less steeply after the minimum than before it, causing a lower dissipation value. This behaviour of the losses explains why the efficiency profile presents a maximum and why after the maximum it decreases slower than before it.

On the other hand, the losses behaviour can be explained resorting to the methodology presented by Craig & Cox (1971). Actually, since the lift coefficient remained basically constant, due to an inlet blade angle ranging from -2° to 2° , the investigation should mainly focus on fluid velocity and fluid deviation. While the power output grows when increasing the mass flow rate, the specific work remains constant. Indeed it depends on the enthalpy drop, fixed by the pressure drop; also, it is given by a trade-off between blade velocity (U_m), axial velocity (C_a) and fluid deviation (see equation

2.3). In particular, group 1 loss profile can be examined before and after the minimum point:

- $Ns < Ns_{opt}$. Initially, the increase in size leads to an increase in blade velocity, which causes an enhancement of the contraction ratio (CR) and a decrease in fluid deviation; this produces smaller losses (Appendix B). Nevertheless, the reduction in fluid deviation cannot equalize the growth in U_m . For this reason the axial velocity slightly decreases, translating in smaller losses. In this context, the bigger mass flow rate is absorbed by taller blades. Further increasing the mass flow rate, the blade velocity grows slower, while the axial velocity remains basically constant; this produces a smaller loss reduction.
- $Ns > Ns_{opt}$. After the minimum, U_m starts to diminish, while C_a has to increase to absorb the mass flow rate; the higher axial velocity is the main responsible for the greater losses occurring in the axial-flow turbine. Moreover, in this zone the fluid deviation increases, also contributing to growing losses.

On the contrary, group 2 loss follows the so-called *size effect*. Indeed, tip leakage loss, disc windage loss and other group 2 losses are due to the fact that a certain fraction of fluid is lost without producing power. However, this portion of fluid becomes relatively less significant increasing the total power outcome, leading to lower group 2 losses.

9.1.3 Comparison between ORC, SRC and ABC Axial Expanders

In the context of a wider study of the Draugen offshore platform, three thermodynamic cycles were analysed in order to identify the most effective heat recovery system. The comparison was performed among organic Rankine cycle (ORC), steam Rankine cycle (SRC) and air bottoming cycle (ABC) by Pierobon et al. (2013). In this section the expanders for the three bottoming cycles are designed and compared.

Optimal Design

Cyclopentane was operated as working fluid for the ORC, while steam and air were used for SRC and ABC, respectively. Table 9.6 reports the boundary conditions provided by Pierobon et al. (2013), i.e. assuring the maximum net present value for each cycle. The table infers that the specific enthalpy drop for steam is much higher than that of cyclopentane and air, due to the high pressure drop. This leads to similar power outputs for ORC and SRC in spite of the difference in mass flow rate. Moreover, it should be observed that while the inlet pressure is close to the critical value (≈ 45 bar) for

Table 9.6: Boundary conditions for the design of ORC, SRC and ABC single-stage axial turbines.

	ORC	SRC	ABC
Fluid	Cyclopentane	Steam	Air
\dot{m} [kg/s]	45	7.299	87.5
T_{01} [K]	513.15	629.8	605.9
p_{01} [bar]	30	12.57	2.46
pr	0.033	0.010	0.407
Designer choice			
N	3000	11700	3600
n_{st}	1	1	1

cyclopentane, the steam and air expanders work far from critical conditions. Table 9.7 presents a comparison among the optimal designs for the three turbines. The table shows that the air turbine is characterized by the highest efficiency. This is probably connected to the fact that it is subsonic, while ORC and SRC expanders are supersonic machines.

The velocity triangles for the three turbines are shown in figure 9.9. The plot confirms the low degree of reaction for the three turbo-machineries. The steam turbine, especially, is characterized by $\Lambda = 0.107$. The low reaction, together with a high pressure drop, turns in high fluid acceleration within the nozzle which then implies high Mach number and high losses.

Figure 9.10 compares the blade geometry for the three single-stage turbines. The figure shows a relevant growth of the blade height across the stage for the expanders. This increase is provoked by the decrease in density, since mass flow rate and axial velocity do not change across the stage (recall the continuity equation). The main effect of the density drop is observable in the rotor, where the greater variation in blade height occurs:

$$h_3/h_2 = 3.425 \text{ for cyclopentane;}$$

$$h_3/h_2 = 21.5 \text{ for steam;}$$

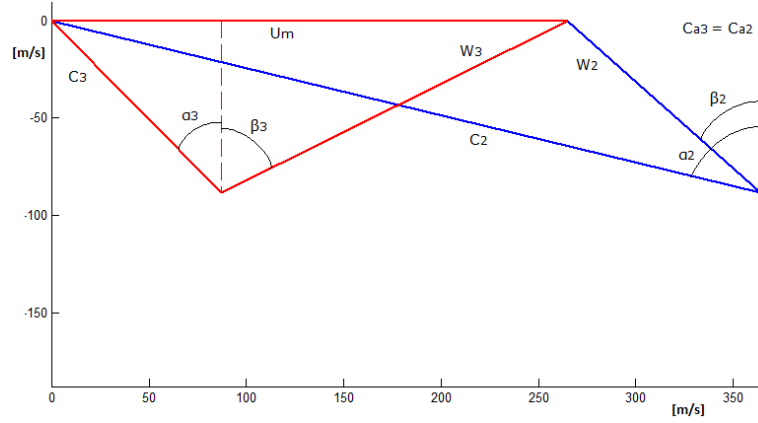
$$h_3/h_2 = 1.354 \text{ for air.}$$

This brings to different considerations:

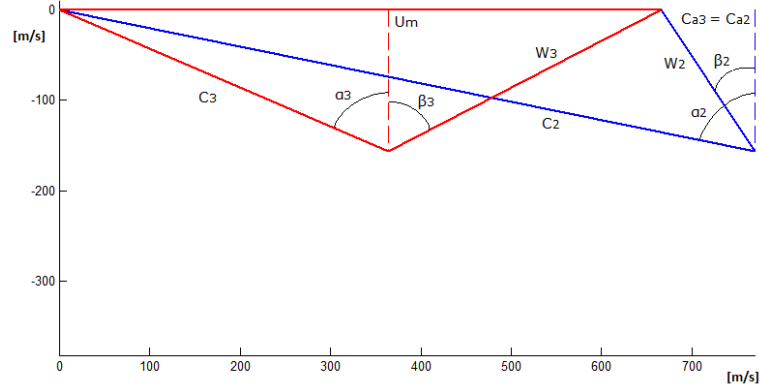
- **Cyclopentane.** See section 9.1.1
- **Steam (Fig. 9.10b).** The elevated pressure drop, higher than 100, is the main responsible of this decrease in density (21.5). In order to restrain the value of the flare angle, the rotor axial chord reaches the upper limit, equal to 0.08 m. Nevertheless the rotor flare angle assumes a value of $\delta = 54^\circ$, more than twice the safe limit proposed by Ainley & Mathieson (1955). This suggests that a multi-stage configuration is required. In this way, the pressure drop would be distributed among different blade rows, guaranteeing an acceptable load for each

Table 9.7: Optimal design for ORC, SRC and ABC single-stage axial turbines.

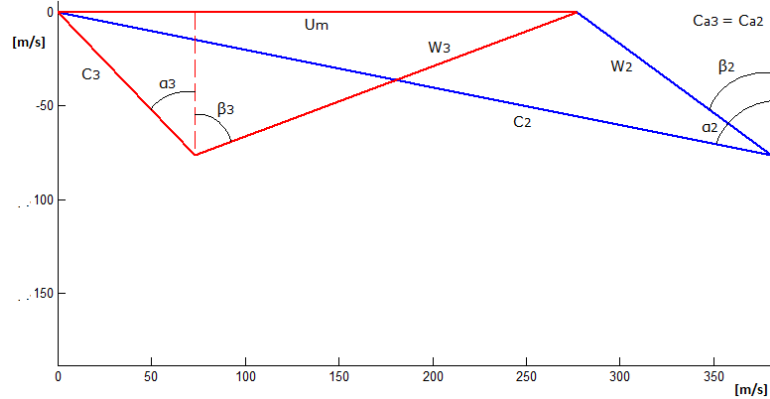
	ORC	SRC	ABC
Performance			
η_{tt}	0.746	0.89	0.922
η_{ts}	0.724	0.805	0.887
P [MW]	5.635	5.633	11.08
Ws [MJ/kg]	0.126	0.766	0.126
Blade Geometry			
z_N	44	78	28
z_R	303	82	29
s_N [m]	0.121	0.044	0.170
s_R [m]	0.0175	0.042	0.155
h_1 [m]	0.001	0.003	0.174
h_2 [m]	0.016	0.012	0.254
h_3 [m]	0.054	0.258	0.344
r_m [m]	0.844	0.547	0.735
Λ	0.14	0.107	0.175
Thermodynamic States			
T_{02} [K]	494.5	626.3	605.8
p_{02} [bar]	11.62	8.426	2.32
ρ_2 [kg/m ³]	5.879	1.109	0.954
T_{03} [K]	422.8	323.1	484.0
p_{03} [bar]	1.001	0.133	1.001
ρ_3 [kg/m ³]	1.728	0.055	0.698
Velocity Diagram			
U_m [m/s]	265.0	670.5	277.0
C_a [m/s]	88.51	156.5	76.35
C_2 [m/s]	374.6	784.3	388.5
W_3 [m/s]	198.9	329.8	217.6
α_2 [°]	76.34	78.49	78.67
β_2 [°]	48.17	33.68	53.72
α_3 [°]	-44.55	-67.3	-43.77
β_3 [°]	63.58	61.68	69.46
M_2	1.619	1.483	0.843
$M_{3,rel}$	0.872	0.216	0.498
Craig-Cox Losses			
$X_{I,N}$ [MJ/kg]	2.454	7.246	0.496
$X_{I,R}$ [MJ/kg]	0.351	0.529	0.157
Y_{II}	0.040	0.024	0.002



(a) ORC



(b) SRC



(c) ABC

Figure 9.9: Velocity triangles for ORC, SRC and ABC turbines single-stage axial turbines.

row. Real solutions also include more complex configurations, splitting the mass flow rate between two low-pressure stages.

This analysis considered a single-stage steam turbine in order to perform a consistent comparison among the three alternatives. Nevertheless, a more realistic simulation of steam turbines is recommended.

- **Air (Fig. 9.10c).** The situation of the air expander is between the previous cases: in spite of a low relative height growth (1.35) the absolute increase is remarkable (0.09 m). As a result, the upper limit for the flare angle (25°C) is reached together with the upper bound of the axial chord (0.08 m). Therefore, although the single-stage configuration is acceptable, multi-stage solutions should be taken into consideration for higher pressure drops or bigger mass flow rates.

Figure 9.11 reports the T-s static diagram for the three axial-flow turbines. The figure exhibits a higher efficiency of the rotor compared to that of the stator for ORC and SRC expanders. On the contrary, stator and rotor have similar efficiencies for the ABC turbine. Furthermore, the figure confirms a higher overall efficiency for SRC and ABC turbines compared to the ORC one. Indeed, the temperature difference between real and isentropic conditions is equal to 11 K for the steam turbine, 9 K for air turbine and 25 K for cyclopentane turbine.

Finally, the three axial turbines were compared in terms of weight and volume requirements. Same Q factors, thus same geometrical proportions, were assumed for the three expanders. Table 9.8 presents the weight and the volume of the expanders.

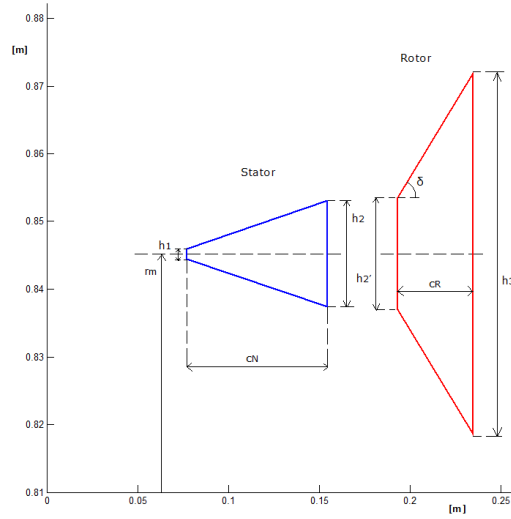
Analysing the table it is possible to state that:

Table 9.8: Weight and volume requirements for ORC, SRC and ABC single-stage axial turbines.

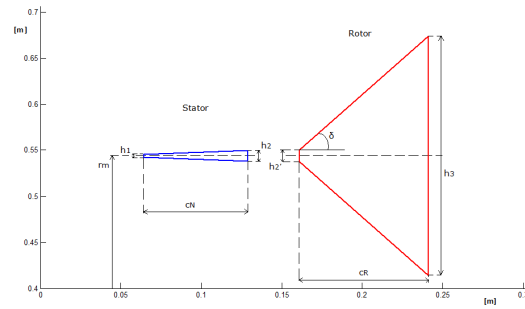
	ORC	SRC	ABC
Weight [ton]	13.83	17.97	50.87
Volume [m^3]	3.57	4.68	12.49
Specific Weight [ton/MW]	2.45	3.19	4.59
Specific Volume [m^3/MW]	0.63	0.83	1.13

- The ORC turbine is the smallest solution in terms of volume requirements and the lightest in terms of weight. Nevertheless, table 9.7 exhibits an external diameter of:
 $D_{ex} = 1.742$ m for ORC turbine;
 $D_{ex} = 1.352$ m for SRC turbine;
 $D_{ex} = 1.814$ m for ABC turbine.

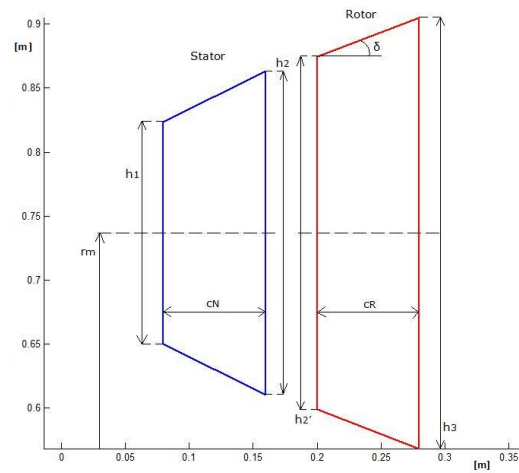
From which the steam turbine would appear as the most compact solution. On the other hand, it should be recalled that SRC and ABC



(a) ORC

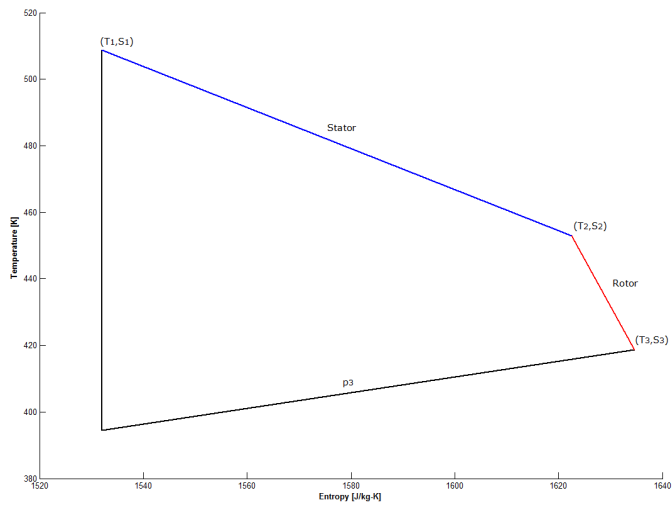


(b) SRC

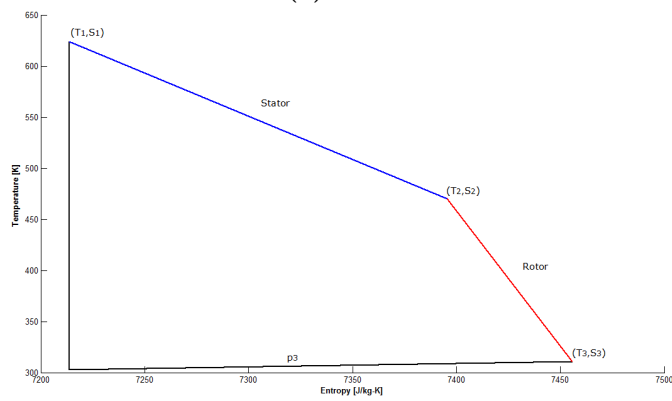


(c) ABC

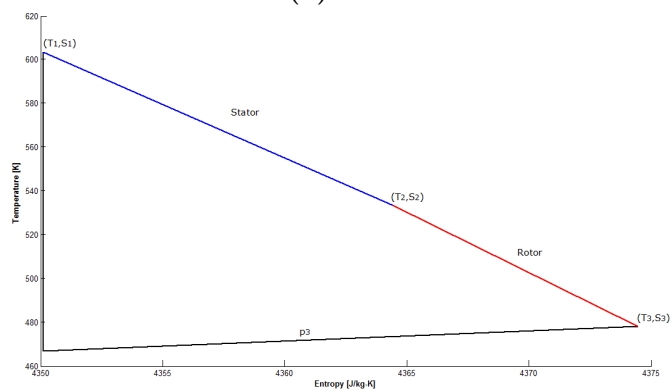
Figure 9.10: Blade geometry for ORC, SRC and ABC single-stage axial turbines.



(a) ORC



(b) SRC



(c) ABC

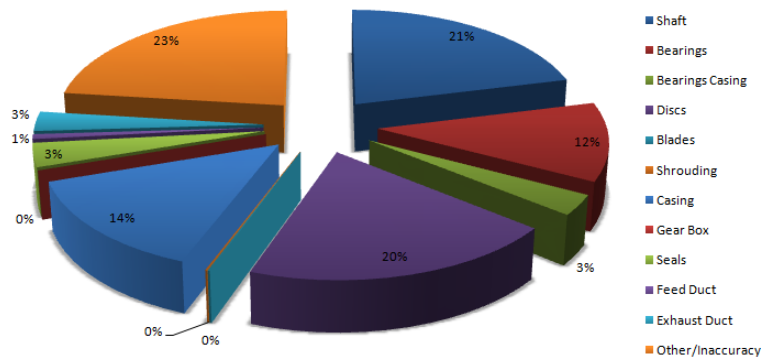
Figure 9.11: T-s static diagram for ORC, SRC and ABC single-stage axial turbines.

turbines use a gear box to reduce the rotational speed. In particular, the gear box of the steam turbine assumes a significant size due to the relevant rotational speed reduction from 11700 rpm to 3000 rpm. Therefore, this component is responsible for the higher weight and volume requirements of the SRC expander (figure 9.12).

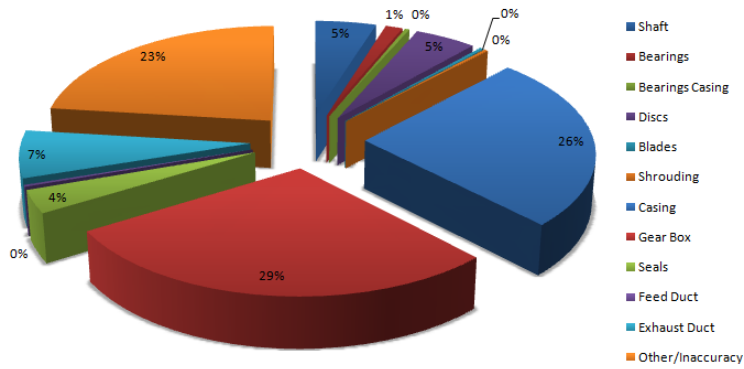
- The ABC turbine is the biggest and heaviest solution. The elevated absolute values of weight and volume (50.87 ton and 4.59 m³) are connected to the high power output (high mass flow rate), necessary to satisfy the compressor requirements. On the other hand, the high specific weight and volume can be explained considering the small specific work and the small density compared to SRC and ORC turbine, respectively. In the first case, a higher air mass flow rate is required to produce the same amount of power produced by steam. In the second case, although the specific work is the same, the same mass of air occupies a larger volume compared to cyclopentane.

Figure 9.12 shows the breakdown of the weight for the three expanders. Although the figures result from an approximate calculation, it is possible to observe that:

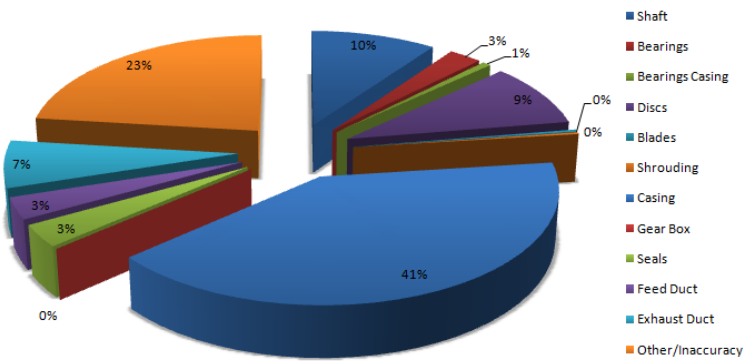
- The relative importance of the gear box is significant for the SRC turbine (29%), while is less relevant for the ABC turbine (6%). This relates to the rotational speed of the two turbines: $N = 11700$ rpm and $N = 3600$ rpm, respectively. The gear box is absent in the ORC turbine ($N = 3000$ rpm).
- The relative importance of the shaft decreases going from ORC (21%) to SRC (5%) to ABC (3%) turbine. A similar behaviour can be observed for the discs: their relative importance diminishes going from ORC (20%) to SRC (5%) to ABC (3%).
- The relative weight of the casing increases going from ORC (14%) to SRC (26%) to ABC (49%) turbine. This is connected to the increase in blade height registered for the three technologies. A similar trend is observed for feeding and exhaust ducts.



(a) ORC



(b) SRC



(c) ABC

Figure 9.12: Breakdown of the weight of ORC, SRC and ABC single-stage axial turbines.

Efficiency Chart

After the comparison between the optimal design conditions, the performance of the expanders at different mass flow rates was investigated. At design pressure, the mass flow rate varied between 5 kg/s and 35 kg/s for the SRC turbine and between 5 kg/s and 250 kg/s for the ABC turbine. This translated in a specific speed ranging from 0.06 - 0.16 and 0.007 - 0.15, respectively. Figure 9.13 compares the efficiency trends as functions of the

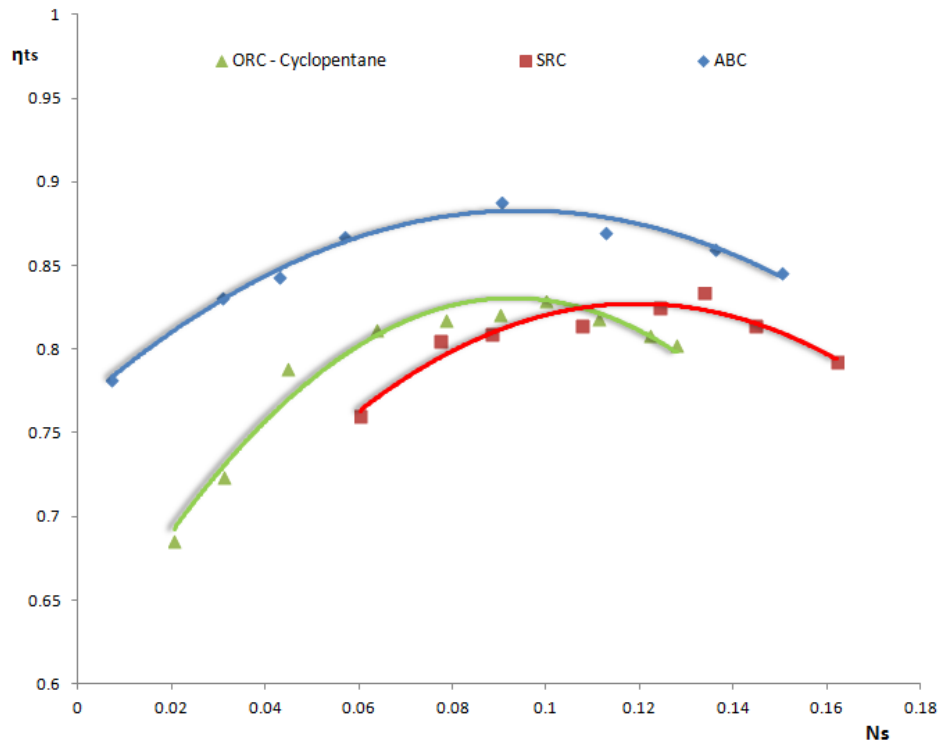
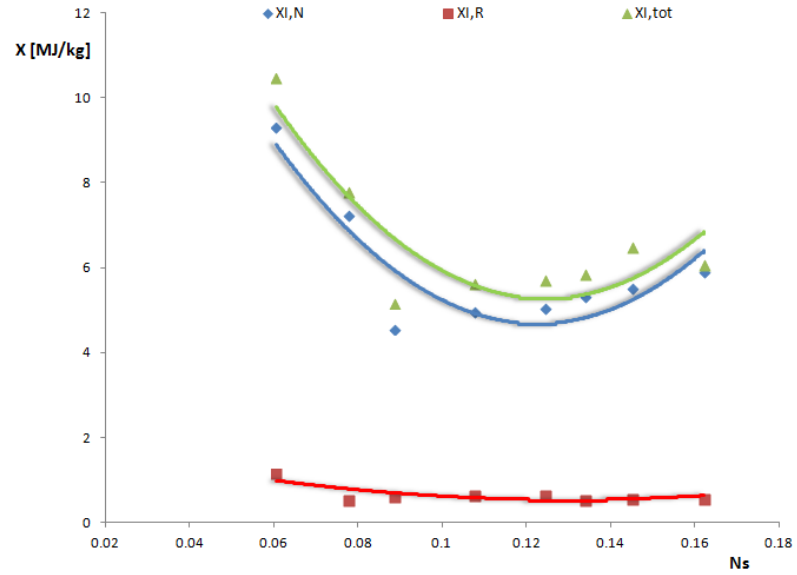


Figure 9.13: Total-to-static efficiency as a function of the specific speed at design inlet pressure for ORC, SRC and ABC single-stage axial turbines.

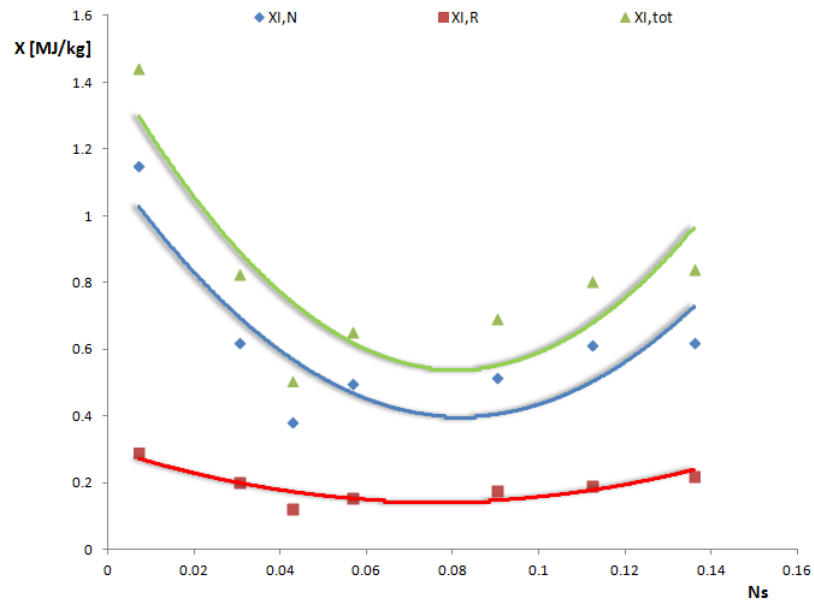
specific speed. The optimization results for SRC and ABC turbines are reported in Appendix H.3. The figure displays a similar maximum efficiency for SRC and ORC turbines, while this value is higher for the ABC expander. Additionally, the efficiency profile for air is wider than that computed for steam and cyclopentane. Indeed, the N_s range covered by the combination of the ORC and SRC turbines, is basically covered by the ABC expander alone. On the other hand, the N_s range is similar for ORC and SRC technologies, but the efficiency profile for SRC is shifted towards higher specific speed. This behaviour is probably linked with the greater rotational speed

of the SRC turbine. Finally, it should be noted that even though the air turbine curve is wider, the ORC turbine is the most flexible solution in terms of mass flow rate.

The trend of the efficiency can be explained through the losses analysis. The plots obtained for the ORC turbine are reported in figures 9.6 - 9.8. Similarly, group 1 and group 2 losses are paralleled for SRC and ABC turbines in figures 9.14 and 9.15, respectively. Similar considerations to those carried out for cyclopentane can be repeated. Indeed, while group 1 loss presents a minimum, group 2 loss is characterized by a monotone decreasing profile. The behaviour of group 1 loss relates to a trade-off between blade velocity, axial velocity and fluid deviation (Section 9.1.2). Moreover, figures 9.14 and 9.15 exhibit flatter loss profiles for the ABC turbine compared to the SRC one. In other words, the losses are less affected by the turbine size for the ABC expander. This might be connected to the fact that, in this case, the enhancement in mass flow rate is mainly absorbed by an increase in blade height, thus allowing for small variations of the axial velocity.

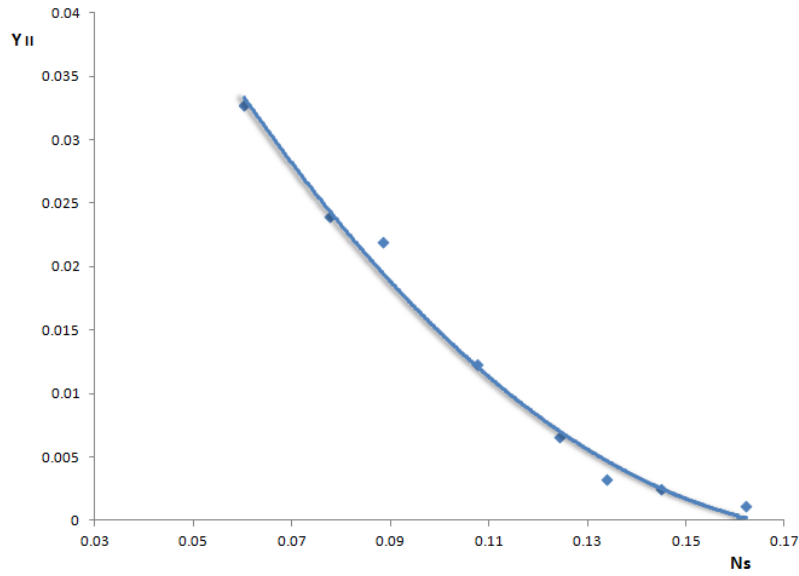


(a) SRC

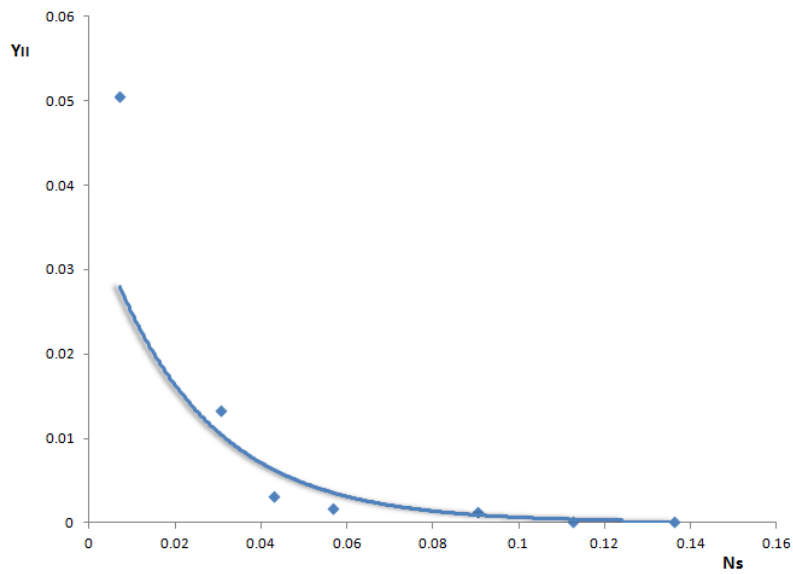


(b) ABC

Figure 9.14: Group 1 loss for SRC and ABC single-stage axial turbines.



(a) SRC



(b) ABC

Figure 9.15: Group 2 loss for SRC and ABC single-stage axial turbines.

9.2 Axial-Flow Turbine Performance for different Working Fluids

9.2.1 Optimal Design

In this context, the heat source consisted in a gas turbine of an offshore platform. Three bottoming cycles operating three organic fluids were compared. The set of boundary conditions for the turbine design was provided by a previous optimization of the thermodynamic cycle; the maximum net power output of the cycle represented the objective function of the optimization problem. Three subcritical organic Rankine cycles operating cyclopentane, MDM and R245fa were investigated. Three single-stage turbines were modelled.

Table 9.9 reports the cycle requirements. The optimal set of optimizing

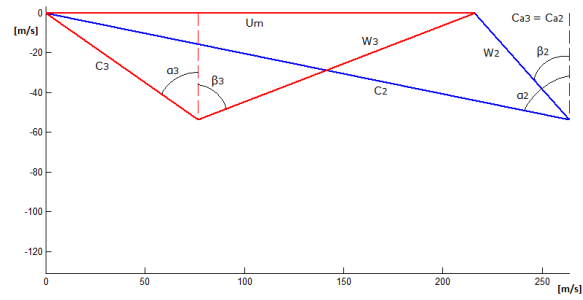
Table 9.9: Boundary conditions for the three ORC single-stage axial turbines.

	Cyclopentane	MDM	R245fa
\dot{m} [kg/s]	72.09	95.64	204.2
T_{01} [K]	502.4	558.5	421.6
p_{01} [bar]	40	13	33
pr	0.086	0.115	0.258
Designer choice			
N	3000	3000	3000
n_{st}	1	1	1

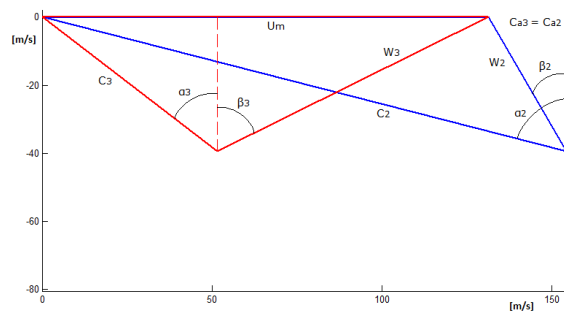
parameters for each fluid is presented in table 9.10, where the blue colour indicates that the maximum limit is reached, while the green colour refers to the lower constraints.

Table 9.11 presents the optimal design configuration for the three expanders. The table displays how MDM and R245fa cycles are characterized by a higher efficiency of the turbine. Nevertheless, more efficient expanders do not necessarily turn in more efficient cycles. Indeed, the table also shows a higher power output for cyclopentane in spite of a lower mass flow rate, suggesting a better efficiency for this cycle. An interesting application would consist in including the computational routine in more complex simulation models investigating the overall performance of the thermodynamic cycles. Figure 9.16 gives some more insights comparing the velocity triangles. The figure portrays three turbine with a low degree of reaction. In particular, the R245fa expander is characterized by a reaction of 0.085.

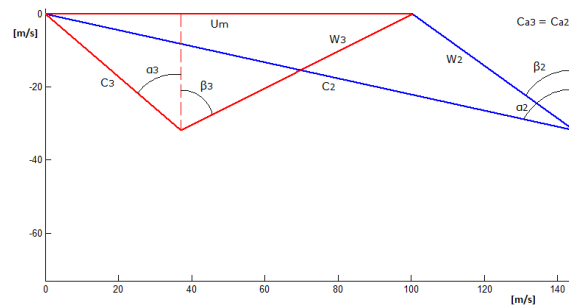
Furthermore, the velocity diagrams highlight a decrease in the axial velocity from cyclopentane to MDM and from MDM to R245fa. Although this trend seems to contradict the increase in mass flow rate, it is connected to the tur-



(a) Cyclopentane



(b) MDM



(c) R245fa

Figure 9.16: Velocity triangles for the three ORC single-stage axial turbines.

Table 9.10: Optimizing variables for the three ORC single-stage axial turbines.

	Cyclopentane	MDM	R245fa
α_1 [°]	1.8532	0.9999	0.8696
ϕ_N	0.3277	0.6780	0.7772
ψ	3.1515	3.2238	3.6213
o_{min} [m]	0.008	0.0095	0.0076
o_R [m]	0.0072	0.0116	0.0072
c_N [m]	0.0749	0.0427	0.0572
c_R [m]	0.0334	0.0768	0.0334
o_N/s_N	2.001	0.2471	0.2156
o_R/s_R	0.3540	0.4280	0.4304
$h_2/h_{2'}$	1.0996	1.0786	1.0397

bine specific work; indeed, this behaviour can be explained using equation 2.3: with a similar shape of the velocity triangles, i.e. similar fluid deviation, the axial velocity decreases with the specific work extracted from the turbine, being the two quantities directly proportional. Then, the increase in mass flow rate affects the blade geometry, presented in figure 9.17 for the three expanders.

The blade height basically depends on three factors: axial velocity, fluid density, mass flow rate (continuity equation). The tree stations are analysed:

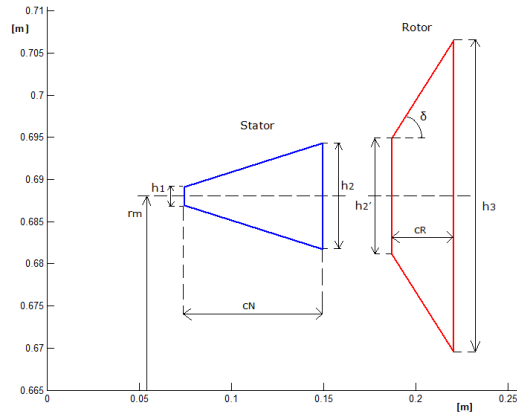
- **Station 1.** The blade height at the nozzle inlet increases from cyclopentane to MDM. Indeed, in this case all the three factors work in the same direction: decrease in axial velocity, increase in mass flow rate and decrease in density. Similarly, the blade height grows from MDM to R245fa. Indeed, the axial velocity reduction and the increase in mass flow rate overcome the density growth.
- **Station 2.** The same phenomenon occurs at the outlet of the nozzle.
- **Station 3.** At the outlet of the rotor the situation is slightly different: while the blade height increases from cyclopentane to MDM for the above mentioned reasons, it decreases from MDM to R245fa. This is due to the fact that the density enhancement overrides the reduction in axial velocity and the growth in mass flow rate. This also turns in a smaller flare angle (δ) for R245fa turbine.

Moreover, a reduction of mean radius is observed from cyclopentane to MDM and from MDM to R245fa. This is linked with the decreasing enthalpy drop, which turns in smaller blade velocities (equation 4.18).

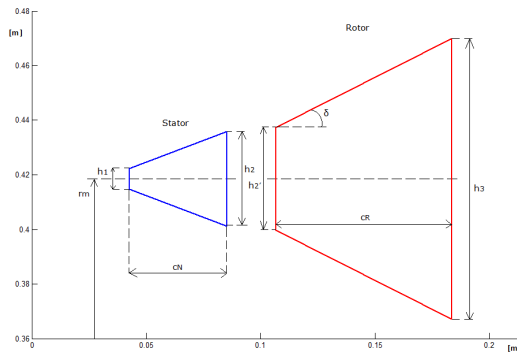
Figure 9.18 shows the T-s static diagram for the three expanders. From

Table 9.11: Optimal design features for the three ORC single-stage axial turbines.

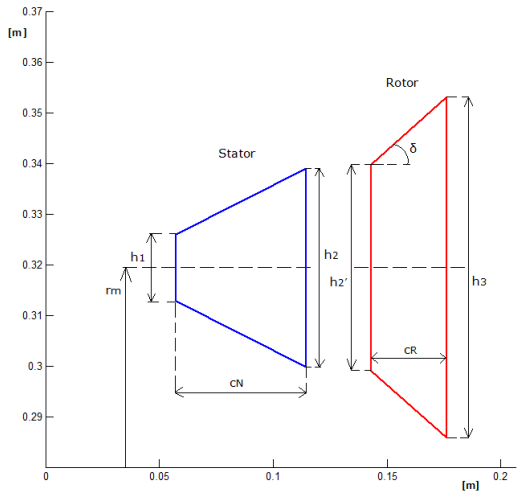
	Cyclopentane	MDM	R245fa
Performance			
η_{tt}	0.826	0.887	0.876
η_{ts}	0.786	0.832	0.828
P [MW]	5.351	2.577	3.699
W_s [MJ/kg]	0.074	0.027	0.018
Blade Geometry			
z_N	108	72	56
z_R	207	88	120
s_N [m]	0.040	0.036	0.035
s_R [m]	0.021	0.030	0.017
h_1 [m]	0.002	0.007	0.013
h_2 [m]	0.012	0.035	0.040
h_3 [m]	0.037	0.096	0.067
r_m [m]	0.688	0.416	0.318
Λ	0.197	0.199	0.085
Thermodynamic States			
T_{02} [K]	473.7	548.8	412.1
p_{02} [bar]	25.42	9.876	27.25
ρ_2 [kg/m ³]	24.33	24.04	77.84
T_{03} [K]	403.5	523.1	364.7
p_{03} [bar]	4	1.7	9
ρ_3 [kg/m ³]	8.117	8.708	45.31
Velocity Diagram			
U_m [m/s]	216.5	130.8	100.0
C_a [m/s]	53.46	42.85	32.16
C_2 [m/s]	267.3	164.9	149.2
W_3 [m/s]	147.5	94.63	71.40
α_2 [°]	78.46	74.94	77.55
β_2 [°]	40.71	33.56	54.84
α_3 [°]	-55.73	-47.32	-48.43
β_3 [°]	68.75	63.08	63.22
M_2	1.336	1.377	1.216
$M_{3,rel}$	0.692	0.729	0.541
Craig-Cox Losses			
$X_{I,N}$ [MJ/kg]	0.935	0.260	0.184
$X_{I,R}$ [MJ/kg]	0.154	0.047	0.038
Y_{II}	0.054	0.012	0.009



(a) Cyclopentane

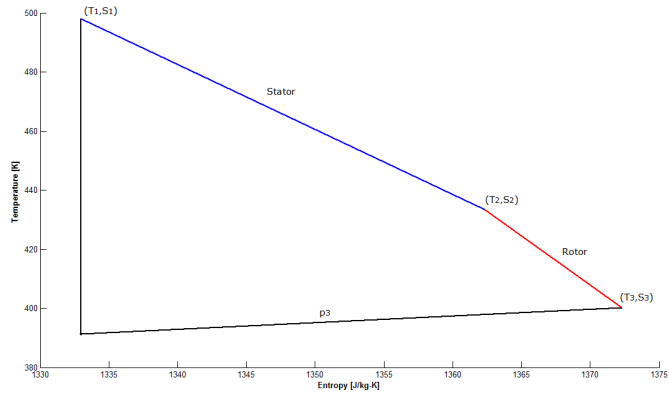


(b) MDM

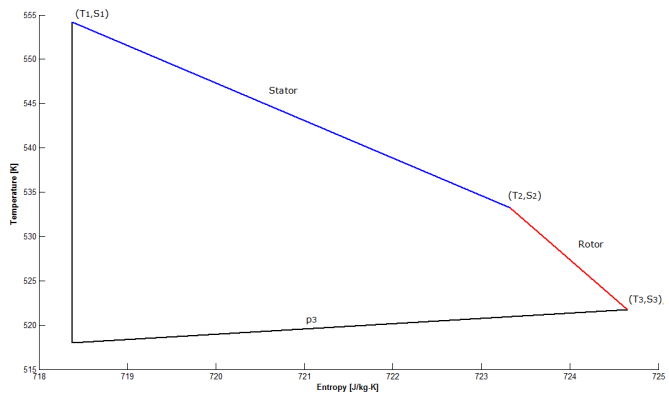


(c) R245fa

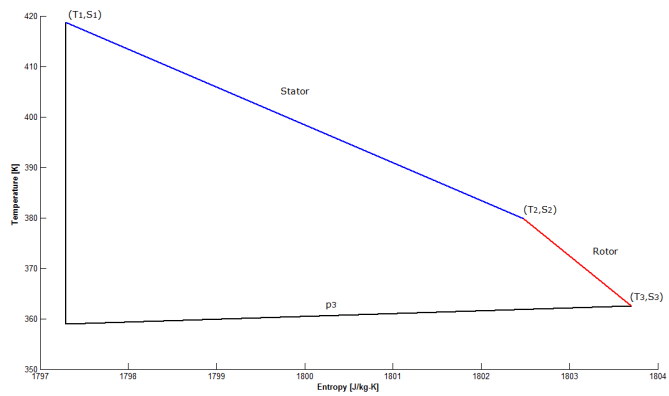
Figure 9.17: Blade geometry for the three ORC single-stage axial turbines.



(a) Cyclopentane



(b) MDM



(c) R245fa

Figure 9.18: T-s static diagram for the three ORC single-stage axial turbines.

the figure the rotor efficiency appears to be slightly higher than the stator efficiency for the three expanders. Moreover, a small entropy production, around 6 J/(kg K), is observed for MDM and R245.

Finally, the three axial turbines were compared in terms of weight and volume requirements. Similar geometries were assumed. Table 9.12 presents the results of the weight calculation. The table suggests that:

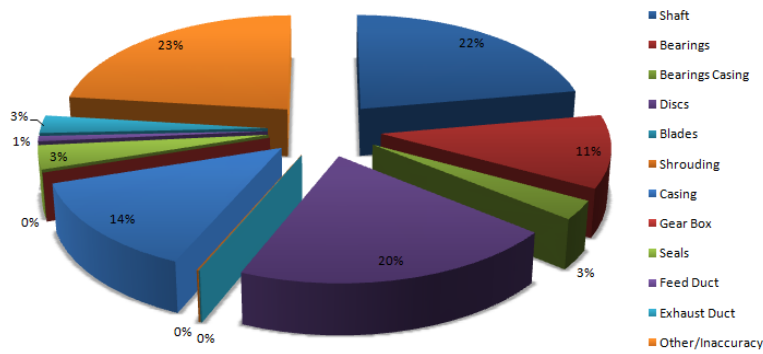
Table 9.12: Weight and volume requirements for the three ORC single-stage axial turbines.

	Cyclopentane	MDM	R245fa
Weight [ton]	9.77	7.82	6.054
Volume [m ³]	2.16	1.22	0.73
Specific Weight [ton/MW]	1.82	3.02	1.63
Specific Volume [m ³ /MW]	0.40	0.47	0.20

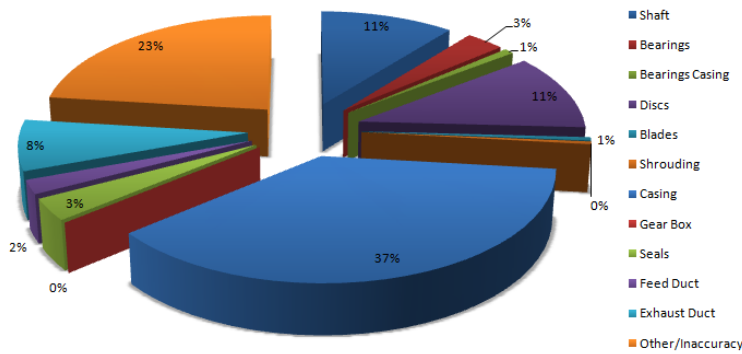
- The R245fa turbine is the lightest and most compact solution. This is connected to the small mean radius and to the high density of the fluid.
- The greater weight and volume for the cyclopentane turbine relate to the bigger external diameter:
 $D_{ex} = 1.413$ m for the cyclopentane turbine;
 $D_{ex} = 0.928$ m for the MDM turbine;
 $D_{ex} = 0.703$ m for the R245fa turbine.
 Nevertheless, the cyclopentane expander results lighter and more compact than the MDM one, in terms of specific weight and volume; this being due to the greater power output and smaller mass flow rate.

Figure 9.19 displays the breakdown of the weight for the three expanders. Even though the figure comes from an approximated calculation, it is possible to observe that:

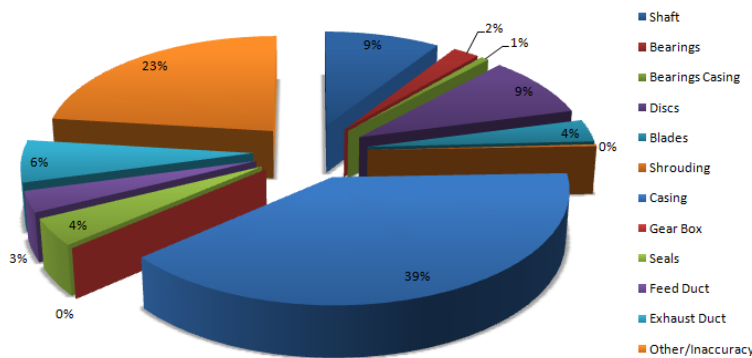
- For each of the three expanders, the heaviest components are the shaft, the discs and the external casing of the turbine.
- The relative importance of the bearings is significant for the cyclopentane turbine (11%).
- MDM and R245fa expanders register a similar weight breakdown; it is characterized by a greater importance of the casing (37% and 39%) and a smaller importance of the shaft (11% and 9%) compared to the cyclopentane turbine.
- A peculiarity of the R245fa turbine is the relevant weight of the blades (4%).



(a) Cyclopentane



(b) MDM



(c) R245fa

Figure 9.19: Breakdown of the weight for the three ORC single-stage axial expanders.

9.2.2 Efficiency Chart

After the investigation of the three optimal design points, the study proceeded by drawing the efficiency profiles as functions of the specific speed. Three inlet pressures were considered for each fluid. The pressure ratio varied accordingly to the inlet pressure in order to maintain the same outlet pressure, fixed by the conditions available at the condenser.

Table 9.13 summarizes the results of the optimization procedure. The effi-

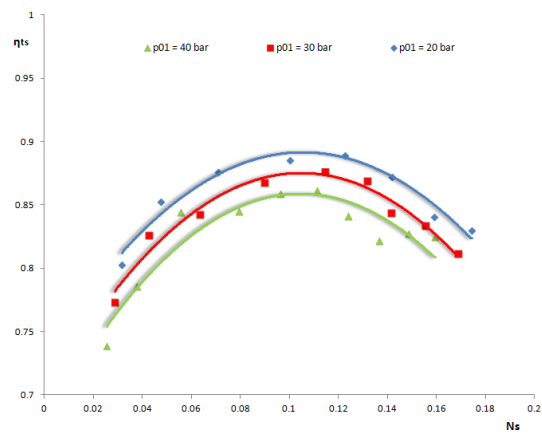
Table 9.13: Maximum efficiency and optimal specific speed; three different pressures for each fluid are reported.

	p_{01} [bar]	$\eta_{ts,max}$	\dot{m} range [kg/s]	Ns range	Ns_{opt}
Cyclopentane					
	40	0.861	20 - 700	0.026 - 0.149	0.111
	30	0.876	20 - 700	0.029 - 0.169	0.114
	20	0.889	20 - 700	0.032 - 0.189	0.123
MDM					
	13	0.851	20 - 700	0.031 - 0.187	0.121
	8.5	0.858	20 - 700	0.037 - 0.206	0.108
	4	0.877	20 - 300	0.050 - 0.204	0.115
R245fa					
	33	0.828	50 - 500	0.032 - 0.118	0.074
	24	0.889	20 - 900	0.020 - 0.145	0.103
	17	0.890	20 - 800	0.026 - 0.170	0.105

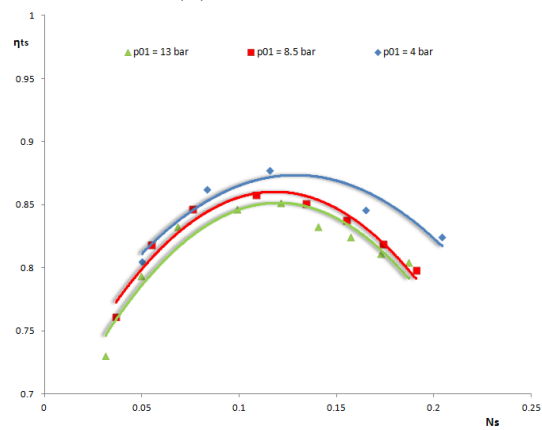
ciency charts of the three turbines are paralleled in figure 9.20, while figure 9.21 compares the efficiency profiles at design pressures. All the plots are built using the results of the design and optimization procedure reported in Appendix I.

The main results of the comparison can be described as follows:

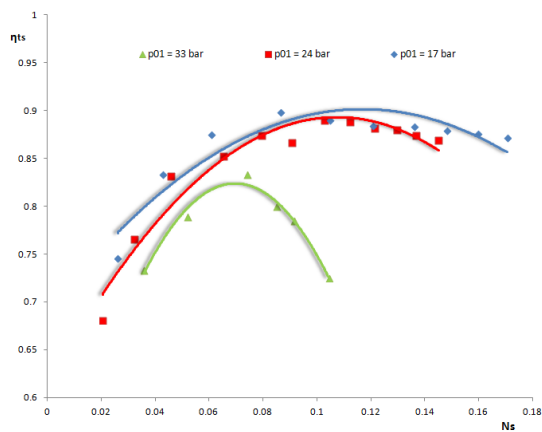
- For given fluid and mass flow rate, the turbine efficiency increases while decreasing the inlet pressure.
- Each efficiency curve presents a maximum. For cyclopentane and R245fa turbines, the optimal specific speed increases while decreasing the pressure. On the contrary, any definite behaviour is observed for the MDM expander.
- Contrarily to cyclopentane and MDM, the efficiency profiles at different pressures for the R245fa expander do not assume similar shapes. Indeed, for this fluid, the curve at design pressure is symmetrical and narrow; on the contrary, the trends become wider and less symmetrical when decreasing the inlet pressure. Referring to figure 9.20c, for $p_{01} = 24$ bar and 17 bar, the efficiency curves are flatter after the maximum



(a) Cyclopentane



(b) MDM



(c) R245fa

Figure 9.20: Total-to-static efficiency as a function of the specific speed; three inlet pressures for each fluid.

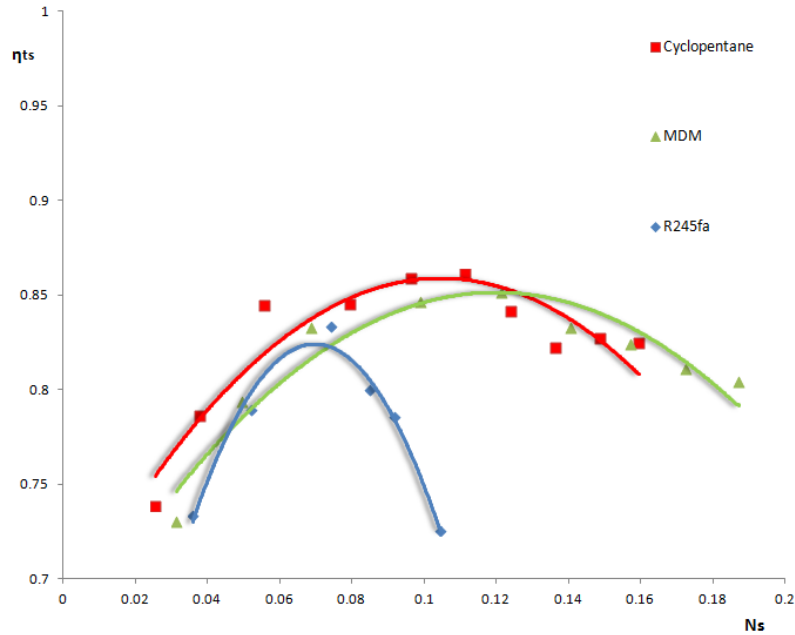


Figure 9.21: Total-to-static efficiency as a function of the specific speed; design pressure for each fluid.

point. This difference might relate to the fact that the design pressure is very close to the critical value (≈ 36 bar).

- Contrarily to cyclopentane and MDM, in the case of R245fa the optimal mass flow rate for the turbine coincides with that of the thermodynamic cycle (at design pressure).
- At design pressure ($p_{01,des}$), the average efficiency decreases from cyclopentane to MDM and from MDM to R245fa. Moreover, at $p_{01} = p_{01,des}$, R245fa is the less flexible fluid in terms of mass flow rate variation. Nevertheless, figure 9.20c shows that R245fa is the fluid with the highest efficiency and the widest mass flow rate range for $p_{01} < p_{01,des}$.

9.3 Performance Analysis for Axial-Flow Turbines Operating with Binary Fluids

This section is focused on the evaluation of the possible benefits arising when using binary mixtures in ORC applications. In particular, the effects of the composition of an isopentane/isobutane mixture on both the thermodynamic cycle performance and the expander isentropic efficiency are evaluated.

Initially, the ORC unit was optimized, in terms of maximum power output, at different mixture compositions, assuming a constant expander efficiency, $\eta_{tt} = 0.8$. Twenty-one mixtures compositions ranging from pure isopentane ($x_{mol} = 0$) to pure isobutane ($x_{mol} = 1$) were computed. The present work only considered eight compositions; the results of the cycle optimization are reported in table 9.14.

The maximum net power output of the cycle as a function of the com-

Table 9.14: Optimal ORC design, in terms of maximum power output, as a function of fluid composition $\eta_{tt} = 0.8$.

x_{mass}	x_{mol}	T_{01} [K]	p_{01} [bar]	m [kg/s]	P_{net} [kW]	pr
0	0	344.1	3.655	39.64	1541	0.247
0.168	0.2	349.3	4.860	40.27	1594	0.253
0.349	0.4	352.4	6.260	40.30	1572	0.268
0.446	0.5	352.8	6.977	40.59	1582	0.272
0.547	0.6	352.4	7.712	41.08	1602	0.275
0.763	0.8	349.6	9.281	42.65	1668	0.277
0.820	0.85	348.6	9.735	43.08	1679	0.278
1	1	345.9	11.54	43.91	1590	0.299

position is displayed in figure 9.22 ($\eta_{tt} = 0.8$). In this case, the net power output presents two maxima: one at isopentane/isobutane molar fractions of 0.9/0.1 and one at isopentane/isobutane molar fractions of 0.15/0.85. Moreover, pure isobutane seems to be more effective than pure isopentane.

Next, the turbine was designed for each of these eight optimal solutions and the effects of the mixture composition on the turbine performance were assessed. In particular, total-to-static and total-to-total efficiency for the expander are presented in figure 9.23 as a function of the mixture composition. The figure indicates that:

- Pure isopentane is characterized by the highest efficiency: $\eta_{ts} = 0.87$ and $\eta_{tt} = 0.93$;
- The efficiency profiles present a minimum: $\eta_{ts} = 0.78$ and $\eta_{tt} = 0.83$ for an isopentane/isobutane molar fractions of 0.8/0.2;
- The efficiency curves present a maximum for a isopentane/isobutane molar fractions of 0.4/0.6: $\eta_{ts} = 0.85$ and $\eta_{tt} = 0.89$.

Finally, the new cycle performance was evaluated including the actual expander efficiency. The total-to-total efficiency was computed. The new optimal configurations are reported in table 9.15. Figure 9.24 compares the net power output trends for constant and variable isentropic efficiency. The main discrepancies between the two profiles can be summarized as:

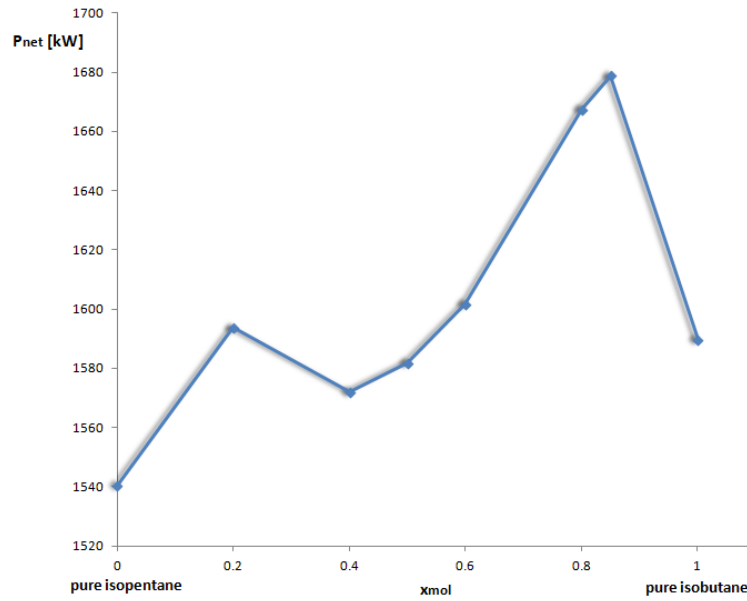


Figure 9.22: Net power output as a function of the mixture composition for $\eta_{tt} = 0.8$.

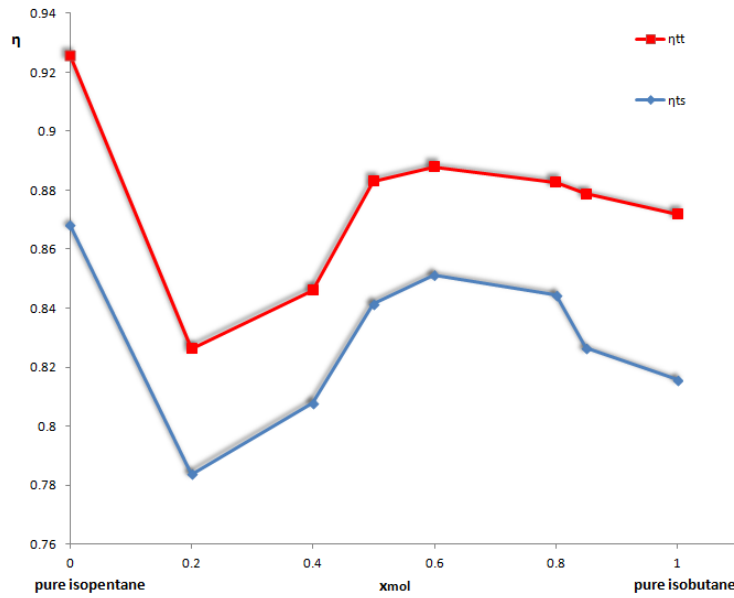


Figure 9.23: Expander efficiency as a function of the mixture composition.

Table 9.15: Optimal ORC design, in terms of maximum power output, as a function of fluid composition for variable η_{tt} .

x_{mass}	x_{mol}	T_{01} [K]	p_{01} [bar]	m [kg/s]	P_{net} [kW]	pr
0	0	344.2	3.667	39.61	1787	0.247
0.168	0.2	349.3	4.861	40.27	1648	0.253
0.349	0.4	352.5	6.264	40.28	1666	0.268
0.446	0.5	352.8	6.984	40.56	1751	0.272
0.547	0.6	352.5	7.721	41.04	1784	0.275
0.763	0.8	349.7	9.293	42.60	1847	0.276
0.820	0.85	348.7	9.747	43.04	1851	0.278
1	1	346.0	11.56	43.86	1740	0.299

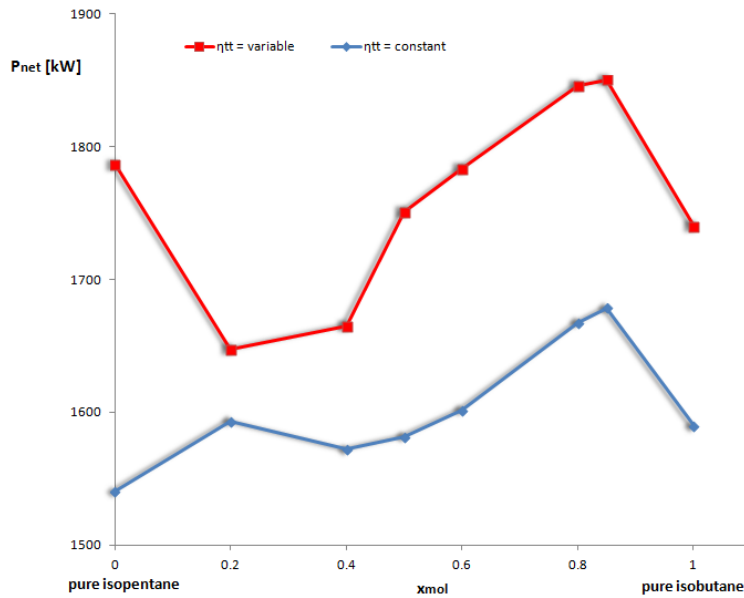


Figure 9.24: Net power output as a function of fluid composition. Constant and variable expander efficiency.

- The variable efficiency profile is characterized by a higher average net power. In particular, for pure isopentane the net power output registers a significant increase: 1787 kW versus 1541 kW (+13.7%).
- The variable efficiency curve presents only one peak: $P_{net} = 1851$ kW for an isopentane/isobutane molar fraction of 0.15/0.85. Such a peak is higher than for the constant efficiency curve: 1851 kW versus 1679 kW (+9.3%).
- While the constant efficiency curve presents a relative maximum for an isopentane/isobutane molar fraction of 0.8/0.2, the variable efficiency curve presents a minimum at this composition.

The explanation of the efficiency behaviour is not straightforward. However, some more insight can be provided by the analysis of the losses occurring within the single-stage turbine. Figure 9.25 displays the components of the total group 1 loss as a function of the mixture composition. The figure shows

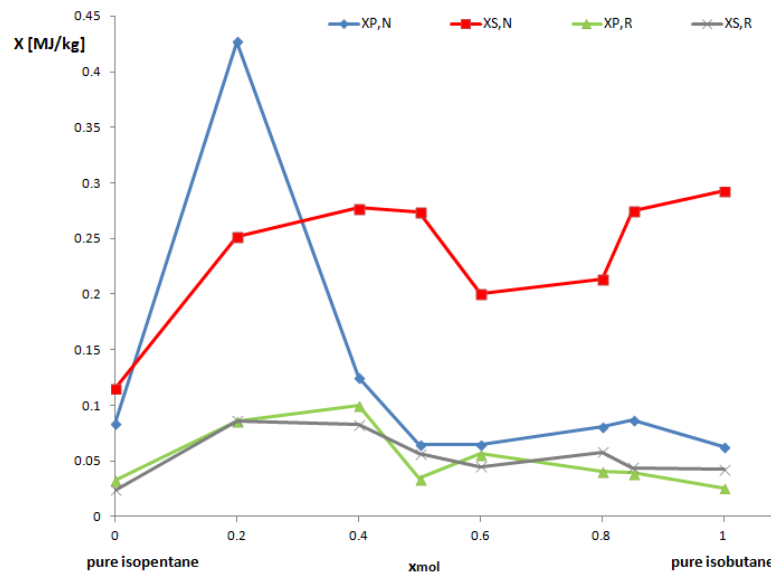


Figure 9.25: Group 1 loss contributions as a function of the fluid composition.

that the nozzle profile loss represents the main fraction of the overall group 1 loss up to an isopentane/isobutane molar fraction of 0.7/0.3. Moreover, it is the most affected by the fluid composition; in particular, the peak occurring at the isopentane/isobutane molar fraction of 0.8/0.2 explains the efficiency minimum at that composition.

The nozzle secondary loss is less affected by the fluid composition and represents the main contribution to the overall loss for isopentane/isobutane

molar fractions higher than 0.7/0.3.

On the contrary, the rotor losses are only slightly affected by the fluid composition and account for a minor share of the overall loss.

Figure 9.26 shows the behaviour of the overall group 1 loss. The trend of

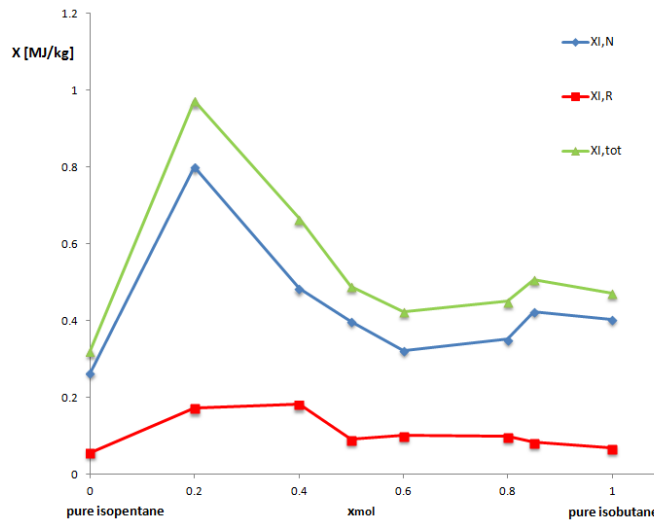


Figure 9.26: Group 1 overall loss as a function of the fluid composition. Analysis of expander performance using binary mixtures

total group 1 loss explains the efficiency profile for isopentane/isobutane concentrations lower than 0.15/0.85. On the other hand, for isobutane molar fraction higher than 0.85, the efficiency profile can be justified by looking at the group 2 loss, portrayed in figure 9.27.

The losses behaviour is probably connected with the nature of isopentane and isobutane. In particular, a peculiar drop in the mixture density is registered at the exit of the nozzle for an isopentane/isobutane molar fraction of 0.8/0.2. At this composition $\rho_2 = 2.85 \text{ kg/m}^3$, while $\rho_{2,\text{isopentane}} = 4.53 \text{ kg/m}^3$ and $\rho_{2,\text{isobutane}} = 15.2 \text{ kg/m}^3$. This decrease in density provokes an increase in fluid velocity, which is the main responsible for the higher losses.

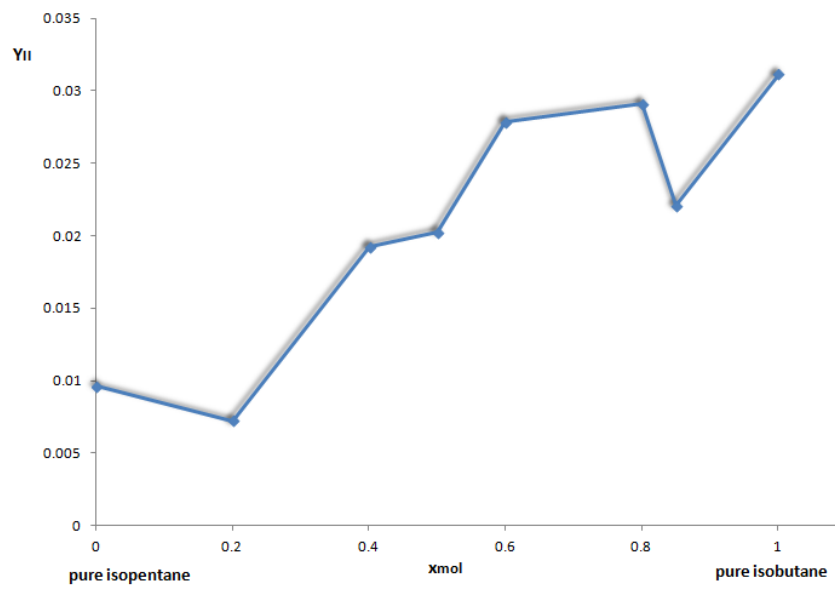


Figure 9.27: Group 2 total loss as a function of the fluid composition.

10

Conclusions

10.1 Accuracy of the Simulation Model

The computational model Mamba provided a tool for the prediction of performance, blade geometry, thermodynamic states and velocity diagram of axial-flow turbines. The validity of the simulation model was tested against experimental data provided by Stabe et al. (1984), Kotzing & Evers (1985) and Verneau (1987), both for the ideal gas and the real fluid cases. The ideal gas and real fluid models basically led to same results. The main conclusions can be summarized as follows:

- Performance, blade geometry, thermodynamic states and velocity diagram of **single-stage gas turbines** were predicted within an accuracy range of $\pm 3\%$.
- For **multi-stage gas turbines**, performance, blade geometry, thermodynamic states and velocity diagram of the **first two-stages** were predicted within an accuracy range of $\pm 3\%$. On the contrary, errors up to 25% arose in the calculation of the mean radius of the **last stages**.
- For **single-stage ORC turbines**, performance and velocity diagram are calculated within an accuracy range of $\pm 3\%$. On the contrary, errors up to 60% affected the calculation of the blade height. These errors were probably connected to an inaccurate evaluation of the thermodynamic properties at the exit of the nozzle (highly supersonic conditions). Moreover, although a detailed comparison was not possible due to the lack of available data, the pressure and temperature at the end of the expansion appeared consistent with the boundary conditions provided by Verneau (1987).

- An estimation of axial-flow turbine weight was carried out. However, no validation was performed because of the lack of available data. For this reason, the results provided approximated values for weight and volume requirements of axial-flow turbines, allowing for preliminary, relative considerations.

10.2 Draugen Offshore Platform Applications

The computational model entered in the wider analysis of the Draugen offshore platform by providing a tool for the prediction of the turbine performance. In particular, a single-stage axial-flow turbine was modelled for three competing bottoming cycles: organic Rankine cycle, steam Rankine cycle and air bottoming cycle.

Findings indicated that for the ORC and SRC turbines, the optimal working conditions do not coincide with those of the thermodynamic cycles (evaluated assuming constant efficiency for the expander). This suggested that the optimal working conditions of the cycles might shift towards higher mass flow rates and lower pressures. On the contrary, the optimal working point for the ABC turbine equalled that of the thermodynamic cycle. Moreover, the analysis of the expanders excluded the possibility of a single-stage steam turbine; this was caused by an excessive steam expansion ($h_3/h_2 = 21.5$).

Furthermore, the study indicated the ORC turbine as the most flexible solution in terms of mass flow rate range ($20 < \dot{m} < 800$ kg/s) followed by ABC ($5 < \dot{m} < 250$ kg/s) and SRC ($5 < \dot{m} < 35$ kg/s) expanders. On the other hand, the ABC turbine was found to be the most performing among the examined expanders ($\eta_{ts,des} = 0.89$) followed by SRC ($\eta_{ts,des} = 0.81$) and ORC ($\eta_{ts,des} = 0.72$) expanders; however, this is not necessarily related with the overall cycle performance.

The efficiency profile, characterized by a maximum, was explained by investigating the behaviour of the losses occurring within the stage. The analysis led to the conclusion that the efficiency mainly depends on a trade-off between blade velocity, axial velocity and fluid deviation.

The weight estimation proposed the ORC turbine as the lightest and most compact solution in terms of specific requirements: 2.45 ton/MW, 0.63 m³/MW; it was followed by the SRC (3.19 ton/MW, 0.83 m³/MW) and ABC (4.59 ton/MW, 1.13 m³/MW) turbines. Nevertheless, the SRC turbine was characterized by the smaller external radius: 1.35 m versus 1.74 m

for the ORC turbine and 1.81 m for the ABC turbine. This suggested that the greater weight and volume requirements for the SRC expander depends on the presence of the gear box (29% of the total weight).

10.3 Comparison of Organic Working Fluids

The computational model was implemented to compare the performance of three single-stage turbines operating cyclopentane, MDM and R245fa.

The analysis indicated MDM ($\eta_{ts,des} = 0.887$) and R245fa ($\eta_{ts,des} = 0.876$) as the most effective fluids from the turbine performance point of view. Nevertheless, although cyclopentane brought to a lower turbine efficiency ($\eta_{ts,des} = 0.83$), it allowed for a higher specific work; this implied a greater power output in spite of a lower mass flow rate, suggesting a higher efficiency of the thermodynamic cycle.

Moreover, the study showed how the optimal working conditions for the thermodynamic cycles do not coincide with those of the expanders, for each of the three fluids. On the contrary, better performance of the turbine was obtained by decreasing the inlet pressure and by increasing the mass flow rate. Furthermore, the R245fa turbine represented the less flexible solution at design condition ($50 < \dot{m} < 500$ kg/s); nevertheless, it became the most flexible technology when decreasing the turbine inlet pressure: $50 < \dot{m} < 900$ kg/s for $p_{01} = 24$ bar.

R245fa allowed for the lightest and most compact expander in terms of specific weight and volume: 1.63 ton/MW, 0.2 m³/MW; it was followed by cyclopentane (1.82 ton/MW, 0.40 m³/MW) and MDM (3.02 ton/MW, 0.47 m³/MW) turbines.

10.4 Effects of Binary Mixtures as Working Fluid

The study investigated the influence of the composition of an isopentane/isobutane mixture on both the thermodynamic cycle performance and the expander isentropic efficiency.

The analysis indicated that the expander performance was affected by the fluid composition, presenting two peaks in total-to-static efficiency: 87% for pure isopentane and 85% for a 0.40/0.60 (in terms of molar fractions) mixture of isopentane/isobutane. As a result, the net power output of the cycle remarkably varied depending on whether variable turbine efficiency was considered or not in the optimization procedure.

11

Future Work

Some suggestions for further studies are reported.

In spite of the previous considerations, the analysis of the turbine performance is not sufficient to establish the best heat recovery system or the optimal organic working fluid. At this purpose, the computational model for the expander should be coupled with the simulation model of the thermodynamic cycle.

Moreover, the computational model should be extended in order to describe the off-design behaviour of axial-flow turbines. This would be of a big interest in order to realistically predict the turbine performance in actual situations, providing for information regarding the flexibility of the expander.

Some improvements of the computational model should be performed. In particular, a more precise description of the blade geometry could be provided, especially in multi-stage configurations.

Furthermore, it should be possible to select the type of turbine depending on the investigated application. For this reason, the calculation routine should include the possibility to model radial-flow turbines.

Additionally, some elements of mechanical design might be included. In particular, stress considerations should be made regarding the blades and discs design.

A more precise weight estimation should be carried out. This might be done by implementing a library of materials and components for turbines. Also, different geometrical proportions could be considered depending on the application, based on more accurate experimental data.

Design and Optimization of Turbo-Expanders for Organic Rankine Cycles

A more detailed analysis on the fluid selection should be carried out. In particular, more insights should be provided about the actual importance of fluid and boundary conditions in affecting the turbine performance. Also, more fluids might be taken into consideration.

Bibliography

- ACE (2014). Power transmission gear, www.aceworldcompanies.com.
- Ainley, D., & Mathieson, G. C. R. (1951). A method for performance estimation of axial-flow turbine. *Her Majesty's Stationery Office, R&M*, 2974.
- Ainley, D., & Mathieson, G. C. R. (1955). An examination of the flow and pressure losses in blade rows of axial flow turbines. *Aeronautical research council, R&M*, 2891.
- Andersen, R. A., & Uhrbrand, J. (2013). *Design and Optimization of an Air Bottoming Cycle and an Organic Rankine Cycle utilising Gas Turbine Waste Heat for Enhanced Power Generation on Offshore Platforms*. Master's thesis Technical University of Denmark, DTU.
- Babcock, & Wilcox (1927). *Steam: Its Generation and Use*. The Babcock & Wilcox Company.
- Balje', O., & Binsley, R. L. (1968). Axial turbine performance evaluation, part a - loss geometry relationships and part b - optimization with and without constraints. *Journal of Engineering for Power, ASME, T*, 1–20.
- Bearing Work inc. (2013). Bearings sizes, www.bearingworks.com.
- Bell, I., Wronski, J., Quoilin, S., & Lemort, V. (2014). Pure- and pseudo-pure fluid thermophysical property evaluation and the open-source thermophysical property library coolprop. *Industrial & Engineering Chemistry Research*, 0, null.
- Carleton University (2013). Aerodynamic features in steam turbines, research.mae.carleton.ca.
- Costa, G. (2006). *L'esercizio della Turbina a Vapore*. Milano Editore.
- Craig, H. R. M., & Cox, H. (1971). Performance estimation of axial flow turbines. *Proceedings Institution of Mechanical Engineers*, 71, 185–232.

- Dahlquist, A. (2008). *Investigation of Losses Methods in 1-D for Axial Gas Turbines*. Master's thesis University of Lund.
- Deich, M. E., Filippov, G. A., & Lazarev, L. (1965). Atlas of axial turbine blade characteristic. *Mashinostroenic Publishing House*, 22, 379–98.
- Denton, J. D. (1993). Loss mechanism in turbomachines. *Cambridge*, 93-GT-435, 1–20.
- Direct industry (2013). Bearings, www.directindustry.com.
- Dong Energy (2012). Personal interview with people from dong energy e&p.
- IMTS (2014). Turbine shaft and bearings, www.imts.com.
- Johnston, I. H., & Knight, L. R. (1953). Tests on a single-stage turbine comparing the performance of twisted with untwisted rotor blades. *Aeronautical Research Council, R&M2927*, 1–30.
- Kable (2013). *Draugen Platform*. Technical Report <http://www.offshore-technology.com>.
- Kacker, S. C., & Okapuu, U. (1982). A mean line prediction method for axial flow turbine efficiency. *Journal of Engineering for Power*, 104, 111–119.
- Kandepu, R. (2011). *Introduction to Draugen Platform*. Technical Report Teknova.
- Kotton, K. (1998). *Evaluating and Improving Steam Turbine Performance*. Cotton Fact. Incl.
- Kotzing, P., & Evers, B. (1985). Test case e/tu, 4-stage low speed turbine. *University of Hannover, SFB61*, 364–379.
- Lemmon, E., McLinden, M., & Huber, M. (2007). Refprop: Reference fluid thermodynamic and transport properties. *NIST standard reference database*, 23.
- Macchi, E. (1977). Design criteria for turbines operating with fluids having low speed of sound. *Von Karman Institute for Fluid Dynamics*, 100, 1–57.
- Major Engine Section (2012). Shrouded blades, www.globalsecurity.org.
- MathWorks (2013). Matlab version 7.8.0.
- Mitsubishi (2012). *Steam Turbine Generator*. Technical Report Mitsubishi, heavy industries, LTD.
- Negri di Montenegro, G., Bianchi, M., & Peretto, A. (2009). *Sistemi Energetici e Macchine a Fluido*. Tecnoprint S.n.c.

- Offshore and Technology (2012). Draugen oil field, norway.
- Pierobon, L., Rambabu, K., Rossetti, N., Haglind, F., & Fermi, A. (2013). Technologies for waste he recovery in off-shore applications. *Proceedings of the ASME 2013 International Mechanical Engineering Congress, S*, 1–10.
- Quoilin, S., Broek, M. V. D., Declaye, S., Dewallef, P., & Lemort, V. (2013). Techno-economic survey of organic rankine cycle (orc) systems. *Renewable and Sustainable Energy Reviews*, 22, 168–186.
- Saravanamuttoo, H., Rogers, G., Cohen, H., & Straznicky, P. (2009). *Gas Turbine Theory*. Prentice Hall imprint.
- Siemens (2013a). Flared annulus area turbine, www.energy.siemens.com.
- Siemens (2013b). *Industrial Gas Turbines*. Technical Report www.energy.siemens.com.
- Siemens (2013c). *Steam Turbine*. Technical Report www.energy.siemens.com.
- Smith, S. (1965). A simple correlation of turbine efficiency. *Journal of the Royal Aeronautic Society*, 69, 467–70.
- Stabe, R., Whitney, W., & Moffitt, T. (1984). Performance of a high-work low aspect ratio turbine test with a realistic inlet radial temperature profile. In *20th Joint Propulsion Conference, AIAA, SAE, ASME, Cincinnati, Ohio*.
- Statoil (2012). *Draugen Platform*. Technical Report www.statoil.com.
- Sungho, Y. (2013). The effect of the degree of reaction on the leakage loss in steam turbines. *Journal of Engineering for Gas Turbines and Power*, 135, 022602 –1–9.
- Traupel, W. (1962). Termischen turbomachinen. *Springer Verlag*, 1, 1–20.
- Vavra, M. H. (1969). Axial flow turbines. *Von Karman Institute for Fluid Dynamics*, 15, 1–42.
- Verneau, A. (1987). Supersonic turbines for organic fluid rankine ccycle from 3 to 1300 kw. *Von Karman Institute for Fluid Dynamics, 07-1987*, 130–185.
- Walter (2013). Turbine disc, www.walter-tools.com.
- Wikipedia (2011). Stage expansion h-s diagram, openwam.webs.upv.es.
- Wikipedia (2012). Turbine blades, en.wikipedia.org.

Wikipedia (2013a). Carnot's theorem, en.wikipedia.org.

Wikipedia (2013b). Genetic algorithms, en.wikipedia.org.

Xylon (2011). Modern high-pressure turbine blade, www.logicbricks.com.

A

Elements of Gas Dynamics for Axial-Flow Turbines

Owing to the increasing tendency towards specialization even at first-degree and diploma level, it may be that some readers will not have been exposed to a course in gas dynamics, especially related to those phenomena occurring in axial-flow turbines. It is hoped that this appendix will provide them with an adequate summary of those aspects which are relevant to turbine theory.

A.1 General Equations of Fluid Motion

The study of turbo-machineries is performed considering the energetic transformation occurring within the blade profile. The most significant transformations are related to the conversion from kinetic energy to pressure, and vice versa. Such a conversion is accompanied by the variation of thermodynamic properties such as enthalpy, temperature, pressure and density. More precisely, the fluid is accelerated within the stationary vanes, which must be convergent for a subsonic fluid. Depending on the degree of reaction, the flow can be accelerated also in the moving blades, which then can be convergent or with a constant cross area. For a detailed description of the determination of the geometry of a duct crossed by a fluid in subsonic and supersonic conditions see Negri di Montenegro et al. (2009).

In order to study the behaviour of a fluid in a duct it is convenient to introduce the analytical model provided by the *General Equations of Fluid Motion*, in thermal and mechanical form. The equations are, respectively,

$$dh + CdC + gdz = dq - dWs \quad (\text{A.1})$$

$$CdC + gdz + vdp + d\Gamma = -dWs \quad (\text{A.2})$$

Where h stands for specific enthalpy, C is the absolute velocity, g the gravity acceleration, z the altitude of the fluid, q the exchanged heat, Ws the specific work, Γ the stage loss, v the specific volume and p the fluid pressure. It should be observed that for the stator, which obviously do not exchange work with the external environment, the term dWs is null.

A.2 Total and Static Quantities

The analysis of the phenomena occurring within the stage of a turbo-machinery should start from the observation that the variations of potential energy, as well as the geodetic variations, are negligible compared to those of enthalpy and kinetic energy for a compressible fluid. This stems from the small geodetic drop undergone by the fluid going through the turbo-machinery. On the other hand, the kinetic energy drop becomes of predominant importance, compared to the specific work exchanged by the fluid, as well as the enthalpy drop in steady and moving vanes. Studying the phenomena occurring within such vanes, it is convenient to refer to quantities called *total*, rather than to the static properties. The total thermodynamics properties, or *stagnation* thermodynamics properties, are defined as those quantities characterizing a fluid which is decelerated from an original velocity C_1 to a null velocity through an isentropic process. Referring to figure A.1, applying

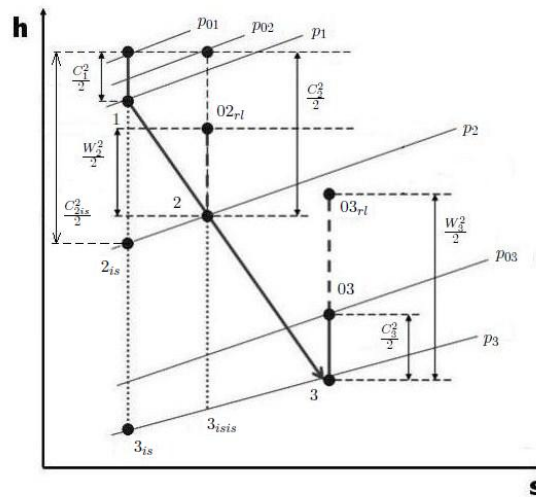


Figure A.1: Stage expansion h-s diagram, (Wikipedia (2011)).

the afore-mentioned definition of total thermodynamics property, the total enthalpy, h_{01} , can be expressed using the general equation of fluid motion

in its thermal form. Indeed,

$$h_{01} = h_1 + \frac{C_1^2}{2} \quad (\text{A.3})$$

where h_1 is the enthalpy of the fluid, called *static enthalpy* to distinguish it from the total enthalpy, in this study denoted by the subscript "0". Consequently, recalling that $h = CpT$, where Cp is the constant pressure specific heat, the total temperature can be expressed by

$$T_{01} = T_1 + \frac{C_1^2}{2Cp} \quad (\text{A.4})$$

With Cp constant and known for a given perfect gas. Moreover, due to the isentropic deceleration, i.e. for an isentropic compression,

$$\frac{p_1}{p_{01}} = \left(\frac{T_1}{T_{01}} \right)^{\frac{k}{k-1}} \quad (\text{A.5})$$

$$\frac{\rho_1}{\rho_{01}} = \left(\frac{T_1}{T_{01}} \right)^{\frac{1}{k-1}} \quad (\text{A.6})$$

Being p and ρ , respectively, pressure and density of the fluid, and k the specific heat ratio, defined by,

$$k = \frac{Cp}{Cv} \quad (\text{A.7})$$

A.3 Speed of Sound and Mach Number

Consider an adiabatic duct with constant section, without friction and with a resting fluid inside. Then, imagine a piston acting on the fluid providing an impulse, as represented in figure A.2. In this way, a perturbation will

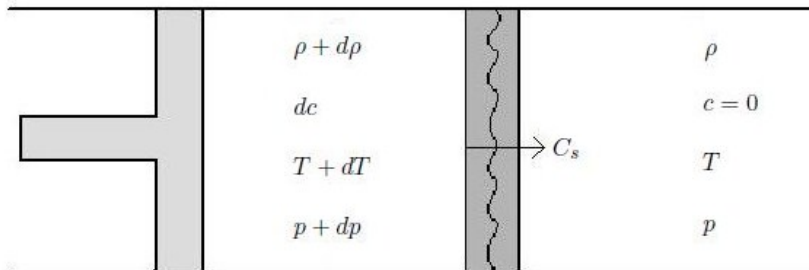


Figure A.2: Horizontal-axis, constant section, free friction duct with pressure wave

start to propagate along the duct, not instantaneously, but with a velocity equal to the speed of sound within the fluid, C_s . Indeed, any perturbation, i.e. a compression of the fluid, is travelling within a fluid with a wave front of velocity C_s . Such a wave front separates that part of the fluid affected by the perturbation from that part that is not affected yet. Furthermore, it looks appropriate to precise that the perturbation does not cause a longitudinal movement of the fluid, but simply an oscillation/compression. An observer united with the wave front would see the fluid moving with a velocity C_s , turning in a virtual mass flow rate given by

$$\dot{m} = \rho C_s A \quad (\text{A.8})$$

Differentiating equation A.8, being the mass flow rate and the section of the duct constant, it is possible to obtain,

$$\frac{d\rho}{\rho} + \frac{dC_s}{C_s} = 0 \quad (\text{A.9})$$

Applying the Equation of motion in its mechanical form and dividing by C_s^2 , it is possible to write,

$$\frac{dC_s}{C_s} + \frac{dp}{\rho C_s^2} = 0 \quad (\text{A.10})$$

From equations A.9 and A.10 the square of the speed of sound can be expressed as

$$C_s^2 = \frac{dp}{d\rho} \quad (\text{A.11})$$

Introducing the hypothesis of perfect gas, still considering an isentropic process, it is possible to write,

$$\frac{dp}{p} = k \frac{d\rho}{\rho} \quad (\text{A.12})$$

The ideal gas law states

$$pv = \frac{R'T}{M} \quad (\text{A.13})$$

where R' is the ideal gas constant, equal to 8.314 J/(K mol), and M the fluid molar mass. $R = R'/M$ is the ideal gas constant expressed in J/(K g). Therefore, for a perfect gas equation A.11 can be written as

$$C_s^2 = k \frac{p}{\rho} = kRT \quad (\text{A.14})$$

Thus, equation A.14 provides the expression of the speed of sound for an ideal gas,

$$C_s = \sqrt{kRT} \quad (\text{A.15})$$

Equation A.15 suggests the speed of sound to be strongly dependent on the absolute temperature of the fluid. The quantity usually adopted to

individuate the regime of motion is the ratio between the punctual velocity and the speed of sound in the same point; such a quantity is called *Mach Number* and it is given by

$$M = \frac{C}{C_s} \quad (\text{A.16})$$

From the definition it results that the Mach number will be higher than one for a velocity greater than the speed of sound, while the Mach number will result lower than one for a velocity smaller than the speed of sound. In the former case, the regime of motion is said *ipersonic* or *supersonic*, while it is said *iposonic* or *subsonic* in the latter case. On the other hand, if the velocity of fluid equals the speed of sound, the Mach number will be equal to one and the regime of motion is called *sonic*.

A.4 Fluid Motion through a Duct

A.4.1 Fluid Flow and Critical pressure Ratio

Consider a fluid exiting from a duct in which the upstream total conditions are assigned, i.e. $\rho_{01} = \text{const.}$, $T_{01} = \text{const.}$, $p_{01} = \text{const.}$, as showed in figure A.3. The duct be without friction, with horizontal-axis and adiabatic.

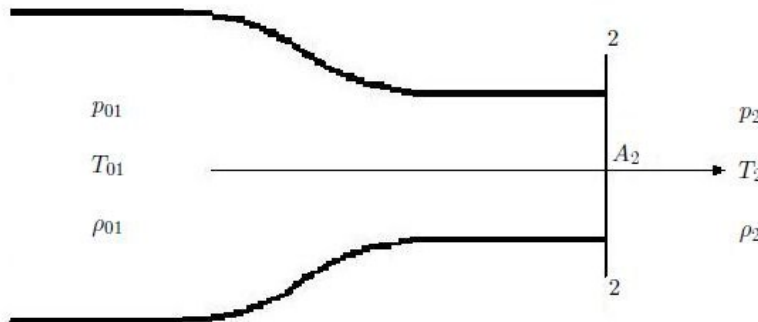


Figure A.3: Horizontal-axis, free friction duct with assigned upstream total conditions

Assume that the physical state of the upstream section be not affected by the mass flow rate exiting from the duct. In other words, the upstream conditions can be considered constant and independent from the downstream conditions. This can occur if the upstream section is much larger than the downstream section. Recalling equation A.1, neglecting the geodetic variations and assuming an isolated and adiabatic duct, it is possible to write,

$$CdC + dh = 0 \quad (\text{A.17})$$

Therefore, integrating between section 1 and 2 and considering an ideal gas, i.e. constant C_p with the temperature, it is obtained,

$$\frac{C_2^2}{2} - \frac{C_1^2}{2} = C_p(T_1 - T_2) \quad (\text{A.18})$$

Thus, referring to the total conditions in the upstream section,

$$C_2^2 = \frac{2kRT_{01}}{k-1} \left(1 - \frac{T_2}{T_{01}}\right) \quad (\text{A.19})$$

Where the subscript 01 refers to the total conditions in the upstream section, while the subscript 2 indicates the conditions of the downstream section. Equation A.14 in section 2 can be written as

$$C_s^2 = kRT_{01} \frac{T_2}{T_{01}} \quad (\text{A.20})$$

At this point, the velocity of the fluid in section 2 and the speed of sound can be compared referring to equations A.19 and A.20. Figure A.4 shows the trend of the two velocities as a function of the dimensionless quantity T_2/T_{01} . Both from the figure and from the equations, it can be noticed that for a

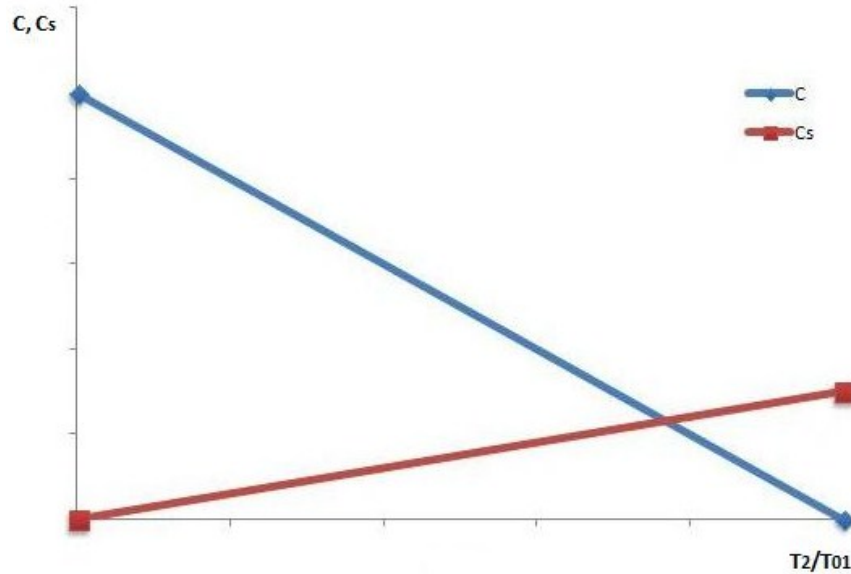


Figure A.4: Fluid velocity and speed of sound as functions of the ratio T_2/T_{01}

given value of the temperature ratio, called *critical value*, the two velocities result to be equal, $C_1 = C_s$. On the other hand, for values of T_2/T_{01} above the critical value the flow is subsonic, while for values lower than the critical

one the flow is supersonic. The critical temperature condition, characterized by sonic flow, can be determined by equalling equation A.19 and A.20. In this way,

$$\left(\frac{T_2}{T_{01}}\right)_{crit.} = \frac{2}{k+1} \left[1 - \left(\frac{T_2}{T_{01}}\right)_{crit.}\right] \quad (\text{A.21})$$

Thus,

$$\left(\frac{T_2}{T_{01}}\right)_{crit.} = \frac{2}{k+1} \quad (\text{A.22})$$

Similarly, the sonic condition can be expressed in terms of pressure ratio through the equation

$$\left(\frac{p_2}{p_{01}}\right)_{crit.} = \left(\frac{T_2}{T_{01}}\right)_{crit.}^{\frac{k}{k-1}} \quad (\text{A.23})$$

Giving the expression of the critical pressure ratio,

$$\left(\frac{p_2}{p_{01}}\right)_{crit.} = \left(\frac{2}{k+1}\right)^{\frac{k}{k-1}} \quad (\text{A.24})$$

In the following table, the critical pressure ratio for some fluids is reported. At this point, consider a perfect gas with given physical conditions, con-

Table A.1: Critical pressure ratio for some fluids of interests

Fluid	Specific heat ratio, k	Critical pressure value, $\left(\frac{p_2}{p_{01}}\right)_{crit.}$
Air	1.4	0.528
Superheated vapour	1.3	0.546
Saturated vapour	1.135	0.577
Cyclopentane	1.2374	0.5573

tained in a very big volume, i.e. physical state not modified by the flow rate exiting the volume, flowing through an adiabatic duct following an isentropic process, as reported in figure A.3. Decreasing the downstream pressure, the fluid will start to move following the pressure gradient. Therefore, there will be a mass flow rate flowing from the first to the second environment. Such a mass flow rate can be expressed with the continuity equation applied to section 2.

$$\dot{m}_2 = \rho_2 A_2 C_2 \quad (\text{A.25})$$

Density and the velocity in section 2 can be expressed in terms of upstream conditions through the following equations,

$$\rho_2 = \rho_{01} \left(\frac{p_2}{p_{01}}\right)^{\frac{1}{k}} \quad (\text{A.26})$$

$$C_2 = \sqrt{\frac{2k}{k-1} \frac{p_{01}}{\rho_{01}} \left[1 - \left(\frac{p_2}{p_{01}}\right)^{\frac{k-1}{k}}\right]} \quad (\text{A.27})$$

From equations A.25 - A.27, the ratio between mass flow rate and area in section 2 can be found by

$$\frac{\dot{m}}{A_2} = \sqrt{\frac{2k}{k-1} p_{01} \rho_{01} \left[\left(\frac{p_2}{p_{01}} \right)^{\frac{2}{k}} - \left(\frac{p_2}{p_{01}} \right)^{\frac{k+1}{k}} \right]} \quad (\text{A.28})$$

Such a ration take the name of *mass velocity*. The mass velocity as a function of the pressure ratio given is showed in figure A.5 (dashed parabolic trend). Note that when $p_2/p_{01} = 1$ the velocity is null and so the mass

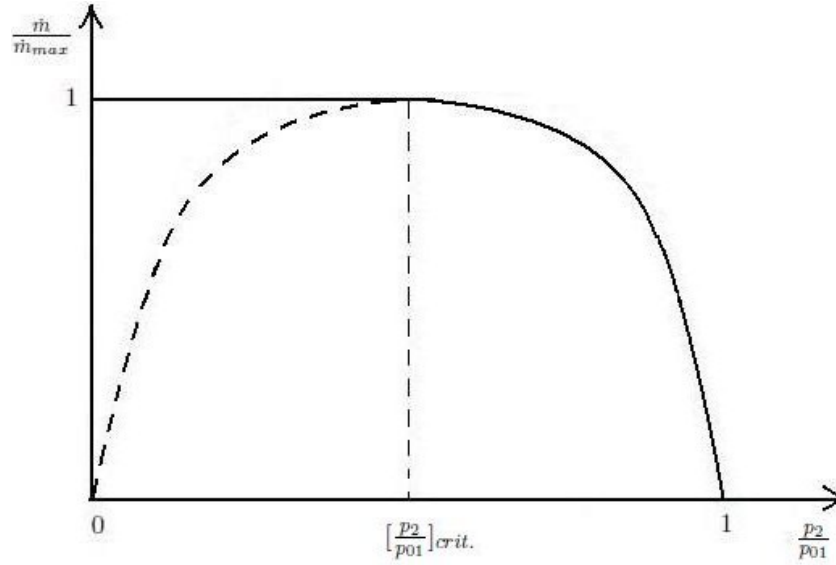


Figure A.5: Mass velocity as a function of the pressure ratio

velocity; likewise, for $p_2/p_{01} = 0$ the density is equal to zero (infinite specific volume) and so the mass velocity. The pressure ratio allowing the maximum disposable flow rate can be determined through the derivative of the term within square brackets in equation A.28. Posing such a derivative equal to zero,

$$\frac{d(\dot{m}/A_2)}{d(p_2/p_{01})} = \frac{2}{k} \left(\frac{p_2}{p_{01}} \right)^{\frac{2-k}{k}} - \frac{k+1}{k} \left(\frac{p_2}{p_{01}} \right)^{\frac{1}{k}} = 0 \quad (\text{A.29})$$

Which is null for a given value of the pressure ratio:

$$\frac{p_2}{p_{01}} = \left(\frac{p_2}{p_{01}} \right)_{crit.} = \left(\frac{2}{k+1} \right)^{\frac{k}{k-1}} \quad (\text{A.30})$$

Or, in terms of temperature,

$$\left(\frac{T_1}{T_{0T}} \right)_{crit.} = \frac{2}{k+1} \quad (\text{A.31})$$

It appears evident that this ratio coincides with the critical value. Equations A.30 and A.31 simply express a particular condition in terms of pressure ratio and temperature ratio, respectively, that allows the maximum disposable mass flow rate in the duct. Such correlations perfectly correspond to those provided by equations A.24 and A.22, expressing the critical pressure and temperature value, respectively. Therefore, it can be stated that the maximum disposable flow rate occurs for the critical value of the pressure ratio, when the fluid velocity of the fluid at the exit of the duct equals the speed of sound. Actually, this fact can be seen from equations A.27, too. Indeed, replacing the critical value to the pressure ratio,

$$\begin{aligned} C_{crit.} &= \sqrt{\frac{2k}{k-1} \frac{p_{01}}{\rho_{01}} \left[1 - \frac{2}{k+1} \right]} = \\ &= \sqrt{\frac{2k}{k+1} \frac{p_{01}}{\rho_{01}}} = \sqrt{\frac{2k}{k+1} RT_{01}} = \sqrt{kRT_{crit.}} = C_s \end{aligned}$$

Therefore, when the sonic conditions are reached in section 2, the fluid flows at the speed of sound, the Mach number is equal to 1 and the maximum mass flow rate is given by

$$\frac{\dot{m}_{max}}{A_2} = \frac{\dot{m}_{crit.}}{A_2} = \frac{p_{01}}{\sqrt{T_{01}}} \sqrt{\frac{k}{R} \left(\frac{2}{k+1} \right)^{\frac{k+1}{k-1}}} \quad (\text{A.32})$$

Equation A.32 suggests that, for given area and fluid, the maximum value of mass flow rate depends only on the total upstream conditions, and it is not affected by the downstream conditions.

At this point, it should be pointed out that the dashed parabolic profile (figure A.5) is only theoretical but it can not actually occur. Indeed, for a downstream pressure lower than the critical value the mass flow rate can not decrease, but has to remain constant (straight continuous line in figure A.5). Indeed, starting from a pressure ratio equal to 1, the fluid begins moving with increasing velocity while decreasing the pressure; once the critical pressure ratio is reached, the fluid velocity at the outlet section equals the speed of sound. In these conditions, any further downstream perturbation, such a reduction in pressure, cannot affect the upstream conditions since the above mentioned perturbation would propagate towards the upstream section with a velocity equal to the speed of sound, which is the same velocity of the fluid. In other words, any perturbation occurring at the downstream section cannot return upstream because the wave front is forced in a stationary position, since it is moving with the same speed of the flowing fluid, but in opposite direction. For this reason, the real profile of the mass velocity is given in figure A.5 where the straight continuous line replaces the dashed parabolic section.

To conclude, the Mach number at the outlet section can be expressed as a

function of the pressure ratio. Indeed, the equation of fluid motion in its thermal form states:

$$h_2 + \frac{C_2^2}{2} = h_1 + \frac{C_1^2}{2} \quad (\text{A.33})$$

Where the geodetic contribution has been neglected and the system assumed to be adiabatic and isolated. Therefore,

$$\frac{C_2^2}{2} = Cp(T_{01} - T_2) \quad (\text{A.34})$$

This equation provides the outlet velocity of a fluid knowing the upstream and downstream temperature. Recalling the definition of the constant pressure specific heat, given by equation A.35, it is possible to write the following equations,

$$Cp = R \frac{k}{k-1} \quad (\text{A.35})$$

$$\frac{T_{01}}{T_2} = 1 + \frac{k-1}{2} \frac{C_2^2}{kRT_2} = 1 + \frac{k-1}{2} \frac{C_2^2}{C_s^2} = 1 + \frac{k-1}{2} M_2^2 \quad (\text{A.36})$$

Thus,

$$\frac{p_{01}}{p_2} = \left(1 + \frac{k-1}{2} M_2^2\right)^{\frac{k}{k-1}} \quad (\text{A.37})$$

The last equation links the Mach number in the downstream section with the pressure ratio. Figure A.6 shows the trend of mass flow rate as a function of Mach number. Such a figure can be obtained combining equation A.28 and A.37. The figure shows how for Mach numbers ranging in a relatively

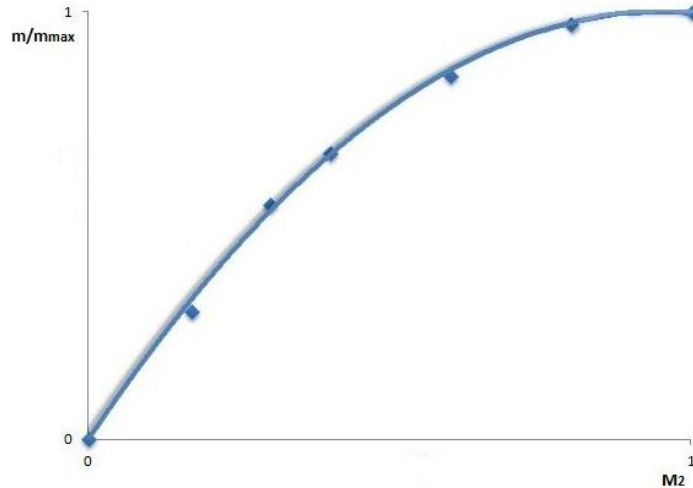


Figure A.6: Mass flow rate as a function of the Mach number of the downstream section

wide interval, from 0.8 to 1, the flow rate changes only of few percentage points respect to the maximum value.

B

Axial-Flow Turbine Stage

The space requirements for the Master thesis did not allow to give a detailed description of those key parameter involved in the study of axial-flow turbines. It is hoped that this appendix will provide readers with some deeper insight of the aforementioned parameters.

B.1 The Mass Flow Function

In order to describe the fluid behaviour in turbo-machinery, a useful parameter is the so called *Mass Flow Function*, expressed by

$$MFF = \frac{\dot{m}\sqrt{T_{01}}}{p_{01}} \quad (\text{B.1})$$

Its general definition can be obtained by Eq. A.28, using the Ideal gas law. Indeed,

$$MFF = \frac{\dot{m}\sqrt{T_{01}}}{p_{01}} = A_2 \sqrt{\frac{2k}{R(k-1)} \left[\left(\frac{p_2}{p_{01}} \right)^{\frac{2}{k}} - \left(\frac{p_2}{p_{01}} \right)^{\frac{k+1}{k}} \right]} \quad (\text{B.2})$$

Such parameter, for a given fluid and geometry, depends only on the pressure ratio and it reaches its maximum value at critical conditions,

$$MFF_{max} = MMF_{crit.} = \frac{\dot{m}_{max}\sqrt{T_{01}}}{p_{01}} = A_2 \sqrt{\frac{k}{R} \left(\frac{2}{k+1} \right)^{\frac{k+1}{k-1}}} \quad (\text{B.3})$$

It is interesting to notice that the maximum mass flow function does not depend on the fluid upstream condition (contrarily to the maximum mass flow rate), but it only depends on geometry of the duct and type of fluid.

Therefore, it is constant for values of the pressure ratio lower than the critical. Thus, for $0 < p_2 < p_{crit.}$,

$$MFF = MFF_{max} = MFF_{crit.} \quad (\text{B.4})$$

B.2 Nozzle Losses

The equations presented in Appendix A were obtained for an ideal fluid considering an isentropic expansion. On the other hand, an accurate analysis needs to consider real fluid behaviour and real transformations, with positive entropy production. The efficiency of the nozzle, η_N , can be defined as the ratio of the actual kinetic energy at the outlet of the nozzle, $C_2^2/2$ and the theoretic kinetic energy at the same section, $C_{2,is}^2/2$, without losses (see figure A.1). Therefore, the nozzle efficiency can be expressed as

$$\eta_N = \frac{C_2^2}{C_{2,is}^2} \quad (\text{B.5})$$

Introducing the *velocity reduction coefficient* for the nozzle, γ_N , defined as

$$\gamma_N = \frac{C_2}{C_{2,is}} \quad (\text{B.6})$$

The nozzle efficiency can be expressed as

$$\eta_N = \gamma_N^2 \quad (\text{B.7})$$

Furthermore, from the equation of fluid motion,

$$\frac{C_2^2}{2} = h_{01} - h_2 \quad (\text{B.8})$$

$$\frac{C_{2,is}^2}{2} = h_{01} - h_{2,is} \quad (\text{B.9})$$

Thus, the losses in the nozzle can be expressed as

$$\Gamma_N = h_2 - h_{2,is} = (1 - \gamma_N^2) \frac{C_{2,is}^2}{2} \quad (\text{B.10})$$

It has to be pointed out that the enthalpy is used instead of temperature. This is a necessary requirements to have an analysis holding for real fluids. Indeed, although an ideal gas analysis might be accurate for gas turbines, running air, it is certainly not suitable for ORC turbines, handling heavy organic fluids. Figure B.1 shows γ_N as a function of the pressure ratio, for a converging nozzle, for two different values of fluid deviation. Increasing the pressure ratio, and therefore the velocity, γ_N decreases, leading to higher losses. Additionally, the velocity reduction coefficient also decreases

increasing the deviation of the fluid. In fact, enhancing the fluid deviation the losses rise, especially because of the profile contribution. For a converging-diverging nozzles the penalization of γ_N is an increasing function of the ratio of downstream section to throat section. Thus, the higher the pressure ratio, the lower γ_N . Since for a converging-diverging nozzle the losses are higher, converging nozzles are used also for Mach numbers greater than 1. In the present thesis the nozzle was considered converging until a Mach number equal to 1.4, Deich et al. (1965).

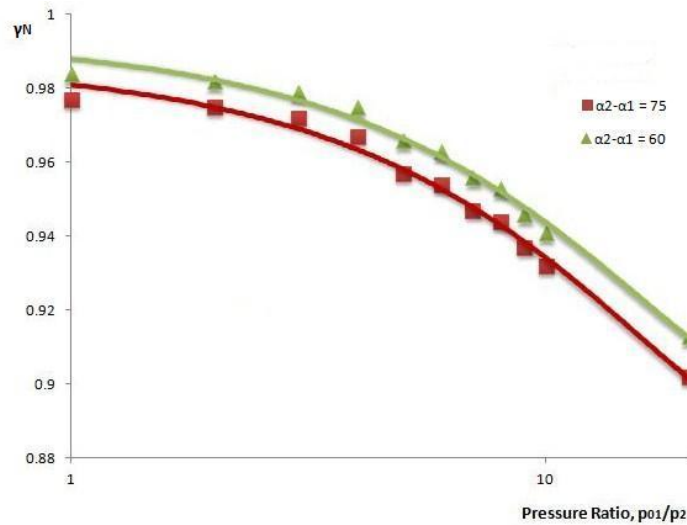


Figure B.1: Velocity reduction coefficient for the nozzle as a function of the pressure ratio for different fluid deviations

B.3 Rotor Losses

Also for the moving blades the losses can be evaluated through the relative velocity reduction coefficient, γ_R . Referring to figure A.1, in case of $p_2 > p_3$, and so $W_3 > W_2$, it is possible to write,

$$\gamma_R = \frac{W_3}{W_{3,is}} \quad (\text{B.11})$$

Therefore, for axial-flow turbines, with $U_1 = U_2$, applying the equation of fluid motion in its thermal form for an observer united with rotor blades, it is possible to write,

$$\Gamma_R = h_3 - h_{3,is} = (1 - \gamma_R^2) \frac{W_{3,is}^2}{2} \quad (\text{B.12})$$

Figure B.2 shows the velocity reduction coefficient for the rotor, γ_R , as a function of the fluid deviation within the rotor, which is the main dissipation source. As for the stator, the higher the fluid deviation the lower the velocity reduction coefficient, i.e. greater losses. Both Fig. B.1 and B.2 were obtained using the computational tool developed for the thesis.

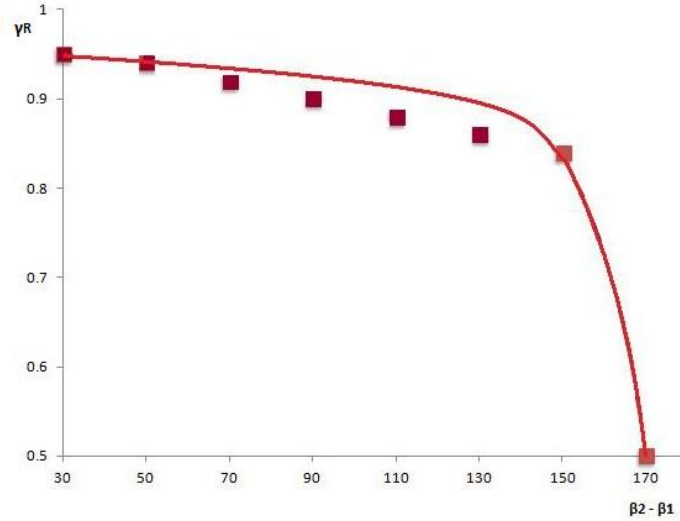


Figure B.2: Velocity reduction coefficient for the rotor as a function of the fluid deviation

B.4 Work Equations for Axial-Flow Turbines

Either equation A.1 or A.2, can be applied to a fluid operating in moving blades using a reference frame united with the impeller. Obviously, the term CdC will be replaced by WdW where C and W represent the absolute and relative velocity, respectively. Furthermore, the work dW_s will be null and a new term accounting for the centrifugal forces must appear. In particular, the work performed by centrifugal forces on a particle moving towards the periphery of dr is given by

$$(\omega^2 r)dr = U dU \quad (\text{B.13})$$

Where dr represent the infinitesimal radius. In the Energy Equation such a work has a negative sign, since it represents a work performed on the particle. Therefore, the equation of fluid motion in its thermal and mechanical form becomes, respectively,

$$dh + W dW + gdz = dq - (-U dU) \quad (\text{B.14})$$

$$WdW + g dz + v dp + d\Gamma = -(-UdU) \quad (\text{B.15})$$

Both these equations can be applied assuming a steady or a moving reference frame. Combining steady and moving options for one of the two equations it is possible to write,

$$CdC + dL = WdW - UdU \quad (\text{B.16})$$

Integrating between the section 2 and 3, the specific work performed by the rotating blades can be expressed as

$$W_s = \frac{C_2^2 - C_3^2}{2} + \frac{W_3^2 - W_2^2}{2} + \frac{U_2^2 - U_3^2}{2} \quad (\text{B.17})$$

On the other hand, recalling the *Carnot Theorem* (Wikipedia (2013a)) and naming α the angle formed by the velocity vector C and the axial direction, it is possible to write,

$$W_3^2 = U_3^2 + C_3^2 + 2U_3C_3\cos\alpha_3 \quad (\text{B.18})$$

Likewise,

$$W_2^2 = U_2^2 + C_2^2 + 2U_2C_2\cos\alpha_2 \quad (\text{B.19})$$

In this way, equation B.17 becomes

$$W_s = U_2C_2\cos\alpha_2 + U_3C_3\cos\alpha_3 \quad (\text{B.20})$$

Since the thesis is focused on the design and optimization of axial-flow turbo expanders, the radial component of velocity is neglected and so any variation in the peripheral velocity U . Therefore, writing $U_1 = U_2 = U$, Equations B.17 and B.20 become

$$W_s = \frac{C_2^2 - C_3^2}{2} + \frac{W_3^2 - W_2^2}{2} \quad (\text{B.21})$$

$$W_s = U(C_2\cos\alpha_2 + C_3\cos\alpha_3) = U(C_{a2}\tan\alpha_2 + C_{a3}\tan\alpha_3) \quad (\text{B.22})$$

Where the suffix "a" indicates the axial component of the velocity.

B.5 Total to Total and Total to Static Efficiency

To express the effectiveness of a stage, the concept of *stage efficiency* is introduced. This efficiency has two possible definitions, depending on which kind of enthalpy drop is accounted for. In particular, if the overall enthalpy drop is considered, the efficiency takes the name of *total-to-total efficiency*, while if the available enthalpy drop is taken into account the efficiency is referred to as *total-to-static efficiency*. The overall and available enthalpy drops are expressed by the two following equations, respectively.

$$E_{tt} = h_{01} - h_{03,ts} \quad (\text{B.23})$$

$$E_{ts} = h_{01} - h_{3,is} \quad (\text{B.24})$$

Where $h_{03,is}$ and $h_{3,is}$ are the total and static enthalpy, respectively, at the end of the isentropic expansion, at the stage outlet pressure. It should be pointed out that the total enthalpy is obtained from the static enthalpy adding the real velocity, as the theoretical is unknown. For the central stages of multi-stage turbines, the total-to-total version appears more suitable, since the kinetic energy exiting from one stage is exploited, at least in part, in the downstream stage. On the contrary, for single-stage turbines, as well as for the last stage of multi-stages turbines, the total-to-static version looks like the best alternative since no kinetic energy is recovered in a following stage. Summarizing, the total-to-total and total-to-static efficiency are provided by the two equations below, respectively.

$$\eta_{tt} = \frac{h_{01} - h_{03}}{h_{01} - h_{03,is}} \quad (\text{B.25})$$

$$\eta_{ts} = \frac{h_{01} - h_{03}}{h_{01} - h_{3,is}} \quad (\text{B.26})$$

It is possible to notice as the total-to-static efficiency is somewhat smaller than the total-to-total, in the measure in which it has a bigger denominator, due to $h_{3,is} < h_{03,is}$.

Degree of Reaction

The *degree of reaction* is defined as the ratio of the energy converted in kinetic energy along the moving vanes (assuming null losses inside the rotor) to the overall energy converted in kinetic energy (assuming null dissipations inside stator and rotor). Indicating with 1, 2 and 3 the sections at inlet of stator, outlet of stator/inlet of rotor and outlet of rotor, respectively, the degree of reaction is expressed as

$$\Lambda = \frac{\int_3^2 \frac{dp}{\rho} + \int_3^2 g dz - \Gamma_{2,3}}{\int_2^1 \frac{dp}{\rho} + \int_2^1 g dz + \Gamma_{1,2} + \int_3^2 \frac{dp}{\rho} + \int_3^2 g dz - \Gamma_{2,3}} \quad (\text{B.27})$$

Applying the equation of fluid motion in its mechanical form to the nozzle,

$$\int_2^1 \frac{dp}{\rho} + \int_2^1 g dz + \Gamma_{1,2} = \frac{C_2^2 - C_1^2}{2} \quad (\text{B.28})$$

Similarly, applying the energy balance between outlet and inlet of the rotor,

$$\int_3^2 \frac{dp}{\rho} + \int_3^2 g dz - \Gamma_{2,3} = \frac{W_3^2 - W_2^2}{2} + \frac{U_2^2 - U_3^2}{2} \quad (\text{B.29})$$

Therefore,

$$\Lambda = \frac{W_3^2 - W_2^2 + U_2^2 - U_3^2}{C_2^2 - C_1^2 + W_3^2 - W_2^2 + U_2^2 - U_3^2} \quad (\text{B.30})$$

Then, for axial-flow turbine, i.e. $U_2 = U_3 = U$,

$$\Lambda = \frac{W_3^2 - W_2^2}{C_2^2 - C_1^2 + W_3^2 - W_2^2} \quad (\text{B.31})$$

A turbo-machinery characterized by a degree of reaction equal to zero is called *impulse turbo-machinery*, while a *reaction turbo-machinery* has a degree of reaction higher than zero. Actually, the definition of the degree of reaction does not include any kind of loss. Therefore, in the reality an impulse turbine would have a degree of reaction lower than zero. Indeed, $\Lambda < 0$ results from $W_3 = \gamma_R W_2$, with $\gamma_R < 1$. Generally, for steam and gas turbine the value of the degree of reaction is comprised between 0 and 0.5. The present study found value within this range also for turbines operating with organic fluids.

Finally, it should be noted than the degree of reaction can be expressed in terms of the enthalpy drop experienced by the fluid inside nozzle and rotor. In particular, for the nozzle,

$$h_1 - h_2 + g(z_1 - z_2) = \frac{C_2^2 - C_1^2}{2} \quad (\text{B.32})$$

While for the rotor, assuming constant peripheral speed,

$$h_2 - h_3 + g(z_2 - z_3) = \frac{W_3^2 - W_2^2}{2} \quad (\text{B.33})$$

As a result, neglecting the geodetic term, much smaller compared to the enthalpy drop in the context of steam, gas or ORC turbines, the degree of reaction can be expressed as

$$\Lambda = \frac{h_2 - h_3}{h_1 - h_3} \quad (\text{B.34})$$

C

Losses Classification

The aim of this appendix is to provide some further detail about the different losses occurring within a turbo-machinery.

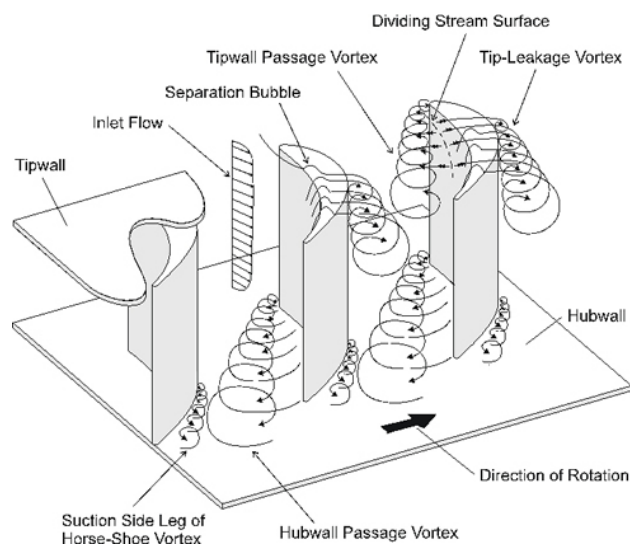


Figure C.1: Aerodynamic features in a turbine cascade, (Carleton University (2013)).

C.1 Profile Loss

Some general trends proposed by Ainley and Mathieson in Ainley & Mathieson (1955) is that the profile losses in a impulse stage will be higher compared to a reaction stage because of the higher fluid deviation. Furthermore,

Ainley & Mathieson (1955) suggested that a high outlet Mach number will reduce the profile losses of about ten percent compared to a lower value, even though the exact value of the lower Mach number is not given. Correction of the profile loss for Reynolds number is often made, and normally the outlet Mach number is taken in consideration, as well. According to Denton (1993) the enthalpy generation is proportional to the velocity to a power of three, and therefore the greatest part of the profile loss created at the suction surface where the velocity is higher.

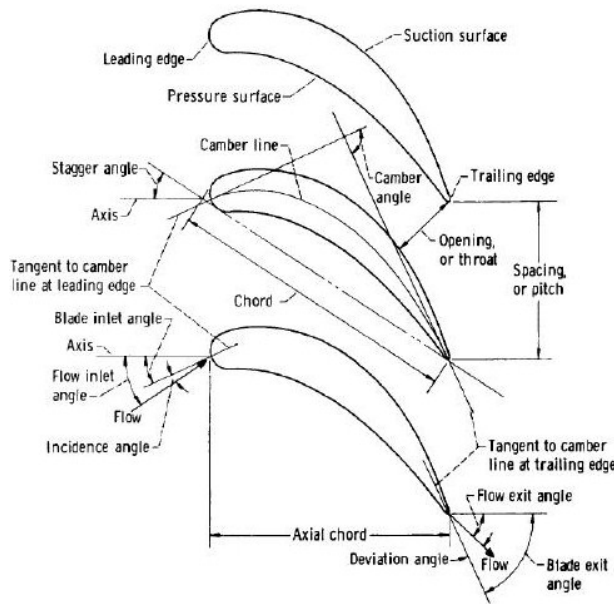


Figure C.2: Blade terminology, (Dahlquist (2008)).

C.2 Secondary Loss

The nature of this loss is complicated to understand and describe. However, it has been seen that important parameters for its analysis are the blade geometry, Mach number and inlet boundary layer. The believed most important blade shape are the turning angle, aspect ratio, pitch to chord ratio and diameter for the leading edge, (Dahlquist (2008)). For a high turning angle the secondary flow will increase, as the blade load and driving pressure gradient increases. The pitch to chord ratio also influences the blade loading. Mach number affects secondary losses in the measure in which a high acceleration reduces the boundary layer thickness and thus the area of secondary losses in the boundary layer.

C.3 Tip Clearance Loss

A distinction was made between shrouded and un-shrouded blades. In the first case, the leakage mass flow rate is not passing through the blades, therefore not performing any useful work. Additionally, the difference in speed and direction between leakage and main flow rate will lead to dissipation of energy and increased entropy creation as it remixes with the main flow. For un-shrouded blades the leakage occurs from the pressure to suction surface of the blade (see 2.6). Along with entropy generation and flow turning this leakage flow also creates an unloading of the tip of the blade and increases secondary flow. Therefore, less work can be extracted. The most important parameters are the relative tip clearance, incoming boundary layer thickness, blade load, and incidence angle (Dahlquist (2008)).

C.4 Trailing Edge Losses

The momentum thickness at trailing edge that reduces the effective flow area, and the fact that all mixing would not be completed before it reaches the next blade row also needs to be taken into consideration. Substantial parameters are back pressure, outlet flow angle, pitch, trailing edge thickness, Mach number and momentum thickness (Dahlquist (2008)).

C.5 Shockwave Losses

Across a shock wave there is a sudden increase in static pressure, boundary layer thickness and viscous dissipation of energy. To take into consideration this type of losses, generally a separate shock loss parameter is introduced and included in the profile losses. The most important parameters are Mach number and Reynolds number (Dahlquist (2008)). One positive effect of a shock is that if it does not create a massive and instant separation, the energy in the boundary layer increases and therefore withstand a higher rate of diffusion without separation.

D

Input Data of the Design Process

A complete list of the input parameters necessary for the design routine is provided by tables D.1 - D.3.

Table D.1: Input parameters for the design routine: optimizing parameters

Optimizing Parameters	
Fluid inlet angle	α_1
Rotor Flow Coefficient	ϕ_R
Stage Loading Coefficient	ψ
Nozzle Throat [m]	o_{min}
Rotor Opening [m]	o_R
Nozzle Axial Chord [m]	c_N
Rotor Axial Chord [m]	c_R
Nozzle Opening-to-Pitch ratio	o_N/s_N
Rotor Opening-to-Pitch ratio	o_R/s_R
Inlet Rotor-to-Outlet Nozzle Height ratio	h_2/h_2'

Table D.2: Input parameters for the design routine: fixed variables

Fixed Variables	
Number of stages	n_{st}
Kinetic energy recovery coefficient	rec
Incidence	
Nozzle minimum incidence[°]	$iminn$
Rotor minimum incidence [°]	$iminr$
Craig-Cox Input Parameters	
Equivalent sand grain size	$ksbr$
Reynolds number	Re
Nozzle stall incidence [°]	$istalln$
Maximum relative velocity ratio	$WWmax$
Nozzle trailing edge thickness-to-opening ratio	$teon$
Rotor trailing edge thickness-to-opening ratio	$teor$
Back surface curvature radius [m]	e
Blades overlap [m]	$overlap$
Indexes	
Mach number for conv.-div.nozzle	M_{cd}
Controlled/un-controlled expansion	$ctrlexp$
On/off-design	of_{des}
Shrouded/un-shrouded blades	$shroud$
Total/partial admission	$partadm$
Number of sector of partial admission	$nsecpa$

Table D.3: Input parameters for the design routine: thermodynamic cycle parameters

Thermodynamic Cycle Requirements	
Inlet total temperature [°C]	T_{01}
Inlet total pressure [bar]	p_{01}
Total pressure ratio	pr
Mass flow rate [kg/s]	\dot{m}
Rotational speed [rpm]	N
Type of fluid	
Gas constant [J/(mol K)]	R
Guessed stage efficiency	$etatsg$
Guessed nozzle efficiency	$etatsng$
Guessed rotor efficiency	$etatsrg$

Appendix D. Input Data of the Design Process

In addition to the input data list, an example of input script is here reported. In particular, this input data were related to the cyclopentane turbine design in the context of the organic Rankine cycle used to recover heat from the Draugen offshore platform.

```
%%
%%=====
%%                               CYCLOPENTANE Input Data
%%=====
%%
%% Definition of the input data for an off-shore application using
%% cyclopentane as working fluid.
%%
%%
%%=====
%%                               List of Parameters
%%=====
%%
%% - station 1 = inlet of the nozzle
%% - station 2 = outlet of the nozzle
%% - station 21 = inlet of the rotor
%% - station 3 = exit of the rotor
%% - m = mass flow rate [kg/s]
%% - T01 = total temperature at station 1 [K]
%% - pr0 = total outlet pressure at station 3 to inlet outlet pressure at
%%       station 1
%% - p01 = total pressure at station 1 [Pa]
%% - R = universal gas constant [J/kmol-K]
%% - M = molar mass of the working fluid [kg/kmol]
%% - gam = specific heat ratio of the working fluid
%% - Cp = constant pressure specific heat [J/kg-K]
%% - phi = stage flow coefficient
%% - alpha1 = fluid absolute angle at station 1 [degrees]
%% - N = rotational speed [rev/s]
%% - Um = periferal speed at the mean radius [m/s]
%% - e = blade back radius [m]
%% - sigmactmax = maximum limit of the centripetal tensile stress [N/m2]
%% - omin = minimum value of the nozzle opening (throat) [m]
%% - or = rotor opening (rotor is considered only converging) [m]
%% - Mcd = Mach number for which the nozzle shifts from converging to
%%       converging-diverging
%% - iminn = minimum incidence at nozzle inlet [degrees]
%% - teon = trailing edge thickness to opening ratio for the nozzle
%% - teor = trailing edge thickness to opening ratio for the rotor
%% - aspr = aspect ratio, height to chord ratio
%% - ksbr = equivalent sand grain size to blade backbone lenght ratio
%% - ksbrp = equivalent sand grain size to blade backbone lenght ratio to
%%       use in the plot
%% - Re = number of Reynolds
%% - istall = stalling incidence [degrees]
%% - WWmax = maximum square of the relative mean velocity ratio
%% - ctrlexp = index: if 0, controlled expansion, if 1, uncontrolled
%%       expansion
%% - overlap = overlap [m]
```

Design and Optimization of Turbo-Expanders for Organic Rankine Cycles

```
% - off_des = index: if 0, design conditions ,
%                   if 1, off-design conditions
% - shroud = index: if 0, shrouded turbine ,
%                   if 1, unshrouded turbine
% - partadm = index: if 0, total admission ,
%                   if 1, partial admission about Suter-Traupel
% - nsecpa = number of sector of admission (partial admission)

%%
%-----Optimizing Variables-----
%
% STAGE COEFFICIENTS
phin = [0.2489 0.2132 0.366];           % Nozzle flow coefficient
phir = [0.2656 0.3042 0.532];         % Rotor flow coefficient
psi = [3.4057 3 3.35];                 % Stage loading coefficient

% OPENING
omin = [0.02 0.0108 0.015];           % Nozzle throat opening
or = [0.0077 0.0106 0.0115];         % Rotor opening

% AXIAL CHORD
cn = [0.0773 0.0500 0.0355];          % Nozzle axial chord
cr = [0.0422 0.0272 0.0330];         % Rotor axial chord

% OPENING TO PITCH RATIO
osn = [0.2382 0.2 0.258];
osr = [0.439 0.295 0.376];

% HEIGHT RATIO
hhh = [1.0977 1.0092 1.08];           % Inlet rotor to outlet stator height ratio

%%
%-----Cycle Input Data-----
%
% EFFICIENCY GUESS
etatsg = 0.8;                           % Gussed stage efficiency
etatsng = 0.8;                           % Gussed nozzle efficiency
etatsrg = etatsg;                         % Gussed rotor efficiency
etats0 = 0.78;                           % Gussed efficiency to start the iterative cycle

fluid = 'Cyclopen.fld';                  % Working fluid

m = 45;                                   % Mass flow rate [kg/s]
mx = m;                                   % Fixed mass flow rate (restriction factors)
N = 3000 / 60;                            % Rotational speed [rev/s]

% THERMODYNAMICS
T01 = [513 0 0];                          % Total inlet temperature [K]
p01 = [3000000 0 0];                       % Total inlet pressure [Pa]
pr0 = 1/30;                                % Overall total pressure ratio
C1 = [75 0 0];                             % Inlet absolute velocity [m/s]
```

Appendix D. Input Data of the Design Process

```

% GAS PROPERTIES
M = refpropm('M', 'T', T01(1), 'P', p01(1)/1000, fluid); % Molar mass [kg/kmol]
Cp = refpropm('C', 'T', T01(1), 'P', p01(1)/1000, fluid);
Cp = Cp; % Constant pressure specific heat [J/kg-K]
Cv = refpropm('O', 'T', T01(1), 'P', p01(1)/1000, fluid);
Cv = Cv; % Constant volume specific heat [J/kg-K]
k = Cp/Cv; % Specific heat ratio
R = 8314; % Ideal gas constant

%-----Fixed Input Variables-----
%
nstr = 1; % Number of stages

rec = [0 0 0]; % Recuperated fraction of outlet kinetic energy

alpha1 = [0 0 0]; % Fluid absolute inlet angle

% INCIDENCE
imin = [0 0 0]; % Nozzle assumed optimal incidence
imr = [3 3 3]; % Rotor assumed optimal incidence

% CRAIG-COX INPUT PARAMETERS
ksbr = 0.0002; % Equivalent sand grain size
Re = 1d6; % Reynolds number
istalln = 15; % Stall incidence
Wwmax = 1; % Maximum relative velocity ratio
teon = 0.1; % Trailing edge to opening ratio for nozzle
teor = 0.1; % Trailing edge to opening ratio for rotor
e = 1d5; % Back surface curvature radius
overlap = 0.002;
% Overlap

% INDEXES
ctrlexp = 0; % Controlled expansion(0), un-controlled expansion(1)
off_des = 1; % Design(0), Off-design(1)
shroud = 0; % Shrouded blades(0), un-shrouded blades (1)
partadm = 1; % Total admission(1), partial admission(0)
nsecpa = 2; % Number of sector of partial admission
Mcd = 1.4; % Mach number at which switch to converging-diverging nozzle

```


E

Insights of Design Methodology

Due to the obvious space requirements on the Master thesis, some section of the design methodology was only hinted in thesis core. This appendix aims at providing some deeper explanation of the aforementioned sections.

E.1 Deich Formula

As mentioned in Section 4.2.2, Deich et al. (1965) proposed a value of $M = 1.4$ to switch from a simply converging nozzle, to a converging-diverging configuration. It proposed an empirical relationship between the Mach number and the blade degree of divergence. In particular, the nozzle opening was calculated through the formula

$$o_N = \frac{o_N}{o_{min}} o_{min} \quad (\text{E.1})$$

Where the ratio o_N/o_{min} depended on the value of the Mach number, as indicated in 4.2.2. As a result, the nozzle opening was obtained from the minimum opening, i.e. throat opening, which was one of the ten optimizing parameters. Actually, the value of o_N/o_{min} calculated in this way is somewhat less than the theoretical degree of divergence: this means that only a part of the supersonic expansion takes place in the diverging interblade channel, while its completion occurs after the blade outlet section by mean of the so-called "after-expansion" process.

The computational function for the calculation of the nozzle degree of divergence is here reported.

```
%%=====
%%                                     DEICH_R
%%=====

% The formula from Deich, is used to calculate the degree of divergence.

%%
%-----
%                                     List of Parameters
%-----
% - on = nozzle opening
% - omin = nozzle throat
% - M2 = absolute Mach number exiting the nozzle
% - k = heat capacity ratio
% - qM = area ratio between the considered Mach number
%       and the sonic throat, for isentropic flow

%%
function [on, qM2, onomin] = Deich_R (omin, M2, kn, Mcd)

qM2 = M2 / ((2 / (kn + 1)) * ((1 + ((kn - 1) / 2) * ...
    (M2^2))) ^ ((kn + 1) / (2 * (kn - 1))));
    % The area ratio is valid in case of isentropic process
    % and for a perfect gas

if M2 <= Mcd
    onomin = 1;
else
    onomin = 1 + (0.5 * M2 - 0.4) * ((1 / qM2) - 1);
end

on = onomin * omin;

end
```

E.2 Blade Geometry Considerations

Some considerations regarding the main geometry, not of major relevance for this study, can be done:

- Regarding the annulus radius ratio, it should be pointed out that values in the region of 1 - 4 would be regarded as satisfactory. If the rotational speed, assumed as an input, had led to an ill-proportioned annulus, it would have been necessary to rework the preliminary design. For example, r_t/r_r could be reduced by increasing the axial velocity, i.e. by using a higher value of the flow coefficient, ϕ . This would also increase the nozzle efflux velocity, and therefore a check on the Mach number at that section should always be included.
- Regarding the stator to rotor clearance, it should be observed that a

low value is desirable only to reduce the axial length and weight of the turbine. Vibrational stresses are induced in the rotor blades as they pass through the wakes of the nozzle blades, and these stresses increase sharply with decrease in axial space between the blade rows. A value of 0.2 is the lowest to be considered safe, but values nearer to 0.5 are often used and this would reduce both the vibrational stresses and the annulus flare.

E.3 Fluid Outlet Angles

Two correlations were implemented depending on the regime of flow. The correlation proposed by Ainley & Mathieson (1951) for subsonic flow, and that suggested by Vavra (1969) for supersonic flow. The correlation proposed by (Ainley & Mathieson (1951)) started from the consideration that under certain conditions the gas angles could be computed as $\cos^{-1}(o/s)$. Nevertheless, tests on gas turbine cascades had shown that the $\cos^{-1}(o/s)$ rule was an over correction for blades of small outlet angle operating with low gas velocities. Figure 4.9, from Ainley & Mathieson (1951), shows the relation between the rotor gas outlet angle, β_3 and the blade angle defined by $\cos^{-1}(o_R/s_R)$ under these conditions. However, the curve is applicable for straight-backed conventional blades operating with a relative outlet Mach number below 0.5. On the contrary, with an exit Mach number of unity the $\cos^{-1}(o/s)$ rule is reasonable for all blade outlet angles, again for straight-backed blades. At intermediate Mach numbers the outlet angle can be assumed to vary linearly between β_3 as given by figure 4.9 and $\cos^{-1}(o/s)$. Modern turbine blades are usually not straight-backed and some corrections have been proposed. Indeed, the suction surface frequently up to 12° of "unguided" or "uncovered" turning from the throat to be trailing edge and this is reflected in the outlet flow angle. For outlet Mach numbers below 0.5, Ainley & Mathieson (1951) suggested that β_3 was increased by $4(s/e)$ where e is the radius of curvature of suction side of the blade. At an exit number Mach number of 1.0 the outlet angle is given by $\cos^{-1}(o/s) + f(s/e)\sin^{-1}(o/s)$, where the function f was presented graphically. The function can be approximated by

$$f(s/e) = \frac{0.0541(s/e)}{1 - 1.49(s/e) + 0.742(s/e)^2} \quad (\text{E.2})$$

At intermediate Mach numbers, linear interpolation is again used. However, this study assumed straight-backed blades profile.

For supersonic flows, equation 4.52 from Vavra (1969) was implemented.

In implementing such a correlation, the main problem was to find the Mach number at opening of the nozzle, which was lower than the isentropic Mach number because of the post-expansion. At this purpose, some iteration was

used in order to find M_a starting from the isentropic Mach number, given by the familiar formula A.16. Once M_a was determined, p_a was found through equation A.37, assuming ideal conditions, i.e. ideal gas and isentropic process. Through this pressure the fluid deviation was obtained using formula 4.52.

Equation A.37 was not used in other sections of the computational routine, since it does not lead to the downstream conditions, but to those at the opening section. Indeed, the downstream conditions, related to the isentropic Mach number, are those found by the adopted thermodynamic analysis. In the space between the opening and the downstream section, complex phenomena occur. Such phenomena are affecting the deviation of the fluid, as predicted by Vavra (1969).

The computational function for the calculation of blade and fluid angle is here presented.

```
%%
%-----BLADE_R-----
%
% Definition of the blade geometry: pitch, chord, number of blades and
% blade profile. From the blade profile it is possible to re-calculate the
% speed triangles with the updated angles and velocities.
%%
%-----List of Parameters-----
%
% - station 1 = inlet of the nozzle
% - station 21 = outlet of the nozzle
% - station 2 = inlet of the rotor
% - station 3 = exit of the rotor
% - omin = nozzle throat [m]
% - or = rotor opening (rotor is considered only converging) [m]
% - sn = nozzle pitch [m]
% - sr = rotor pitch [m]
% - cn = nozzle chord [m]
% - cr = rotor chord [m]
% - hn = mean nozzle height [m]
% - hr = mean rotor height [m]
% - zn = nozzle number of blades
% - zr = rotor number of blades
% - theta = blade angle [degrees]
% - imin = minimum incidence [degrees]
% - T01 = total temperature at station 1 [K]
% - R = universal gas constant [J/kmol-K]
% - M = molar mass of the working fluid [kg/kmol]
% - gam = specific heat ratio of the working fluid
% - Cp = constant pressure specific heat [J/kg-K]
% - phi = stage flow coefficient
```

```

% - Um = peripheral speed at mean radius [m/s]
% - N = rotational speed [rev/s]
% - rm = mean radius [m]
% - on = nozzle opening [m]
% - alpha = fluid absolute angle at mean radius [degrees]
% - alpha2r = fluid absolute angle at station 2 at root radius [degrees]
% - alpha2t = fluid absolute angle at station 2 at tip radius [degrees]
% - alpha3r = fluid absolute angle at station 3 at root radius [degrees]
% - alpha3t = fluid absolute angle at station 3 at tip radius [degrees]
% - beta2 = fluid relative angle at station 2 at mean radius [degrees]
% - beta2r = fluid relative angle at station 2 at root radius [degrees]
% - beta2t = fluid relative angle at station 2 at tip radius [degrees]
% - beta3 = fluid relative angle at station 3 at mean radius [degrees]
% - beta3r = fluid relative angle at station 3 at root radius [degrees]
% - beta3t = fluid relative angle at station 3 at tip radius [degrees]
% - br = backbone length for the rotor blade [m]
% - Csound = speed of sound [m/s]
% - M3 = absolute Mach number
% - Mw2 = relative Mach number

%%
function [sn, sr, zn, zr, theta1, theta21, theta21r, theta21t, theta2, theta2r, theta2t, theta3, ...
        theta3r, theta3t, alpha2, alpha2r, alpha2t, alpha3, alpha3r, alpha3t, beta2, beta2r, ...
        beta2t, beta3, beta3r, beta3t] = Blade_R ...
    (alpha1, phin, phir, iminn, iminr, cr, Ca2, Ca3, on, or, omin, osn, osr, Um, N, M2, Mw3, ...
    kn, kr, p01, p02, p2, p3, rr2, rt2, rr3, rt3, onomin)

%-----
%-----Pitch and Number of Blades-----
%-----
sn = on / osn;
sr = or / osr;
rm = Um / (N*2*pi);
zn = floor((2 * pi * rm) / sn);
zr = floor((2 * pi * rm) / sr);

% It is known that the nozzle number of blades should be even, while the
% rotor number of blade should be prime.

if mod(zn, 2) == 0;
    zn = zn;
else
    zn = zn + 1;
end
if isprime(zr) == 1
    zr = zr;
else
    zr = ceil((2 * pi * rm) / sr);
end

%-----
%-----Blade Profile and Fluid Deviation-----
%-----
% For subsonic flow the fluid exit angles are calculated with the

```

*% Ainley–Mathieson correlation, while for the supersonic flow the fluid
% exit angles are calculated with the Vavra correlation .*

```
theta21 = acos(on / sn);
if M2 <= 1
    aLOW = (1.151 * acos(on / sn) - 0.1944);
    alpha2 = aLOW;
    if M2 > 0.5
        alpha2 = aLOW + (M2 - 0.5) * (theta21 - aLOW) / 0.5;
    end
else
    K = (kn - 1) / kn;
    pap0cr = (2 / (kn + 1))^(1 / K);
    T1T0cr = 2 / (kn + 1);
    ex = 0.5 + 1 / (kn - 1);
    if on == omin
        Ma = 1;
        Ma2 = 1;
        p2pa = (p2 / p01) / pap0cr;
    else
        Ma = M2;
        Ma2 = Ma * Ma;
        q = (((kn - 1) / (kn + 1)) * Ma2 + ...
            (2 / (kn + 1))) ^ (ex) / Ma;
        while q > onomin || Ma > 1.004
            p01pa = (1 + Ma2 * (kn - 1) / 2)^(1 / K);
            Ma = Ma - 0.005;
            Ma2 = Ma * Ma;
            q = (((kn - 1) / (kn + 1)) * Ma2 ...
                + (2 / (kn + 1))) ^ (ex) / Ma;
        end
        p01pa = (1 + Ma2 * (kn - 1) / 2)^(1 / K);
        p2pa = (p2 / p01) * p01pa;
    end
    x = p2pa * (1 / K) * tan(theta21);
    y = (kn + 1) / (kn - 1);
    z = (1 - p2pa) * (2 * (1 / K) * Ma2 - 1 - (y * p2pa));
    t = z + x * x;
    if t < 0
        t = 0;
    end
    s = ((-x + sqrt(t)) / (1 + kn * Ma2 - p2pa));
    alpha2 = theta21 + atan(s);
end
theta21 = radtodeg(theta21);
alpha2 = (radtodeg(alpha2));
alpha2r = atand((rm / rr2) * tand(alpha2));
alpha2t = atand((rm / rt2) * tand(alpha2));

i21 = abs(theta21 - alpha2);

theta21r = alpha2r - i21;
theta21t = alpha2t - i21;
```

```

beta2 = atand(tand(alpha2) - (1/phin));
beta2r = atand(((rm/rr2) * tand(alpha2)) - ((rr2/rm) * (Um/Ca2)));
beta2t = atand(((rm/rt2) * tand(alpha2)) - ((rt2/rm) * (Um/Ca2)));

theta3 = acos(or/sr);
if Mw3 <= 1
    alow = (1.151 * acos(or/sr) - 0.1944);
    beta3 = alow;
    if Mw3 > 0.5
        beta3 = alow + (Mw3 - 0.5) * (theta3 - alow) / 0.5;
    end
else
    K = (kr - 1) / kr;
    pap0cr = (2 / (kr+1))^(1/K);
    T1T0cr = 2 / (kr+1);
    ex=0.5 + 1/(kr-1);

    Ma = 1;
    Ma2 = 1;
    p3pa = (p3/p02)/pap0cr;

    x = p3pa * (1/K) * tan(theta3);
    y = (kr+1) / (kr-1);
    z = (1-p3pa) * (2 * (1/K) * Ma2 - 1 - (y*p3pa));
    t = z + x * x;
    if t < 0
        t = 0;
    end
    s = ((-x+sqrt(t)) / (1 + kr * Ma2 - p3pa));
    beta3 = theta3 + atan(s);
end

theta3 = radtodeg(theta3);
beta3 = radtodeg(beta3);

i3 = abs(theta3-beta3);

alpha3 = atand(tand(beta3)-(1/phir));
alpha3r = atand((rm/rr3)*tand(alpha3));
alpha3t = atand((rm/rt3)*tand(alpha3));

beta3r = atand(((rm/rr3)*tand(alpha3)) + ((rr3/rm)*(Um/Ca3)));
beta3t = atand(((rm/rt3)*tand(alpha3)) + ((rt3/rm)*(Um/Ca3)));
theta3r = beta3r - i3;
theta3t = beta3t - i3;

theta1 = alpha1 + iminn;
theta2 = beta2 + iminr;
theta2r = beta2r + iminr;
theta2t = beta2t + iminr;

end

```


F

Craig & Cox Figures

This appendix provides all the figures proposed by Craig & Cox (1971), which were used during for the thesis. The computational function related to the losses evaluation is not reported here because too long.

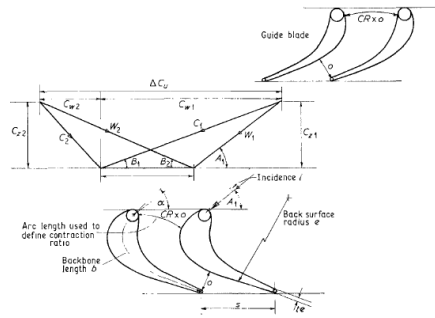


Fig. 1. Turbine blade and velocity triangle notation

Figure F.1: Craig & Cox (1971) Fig. 1

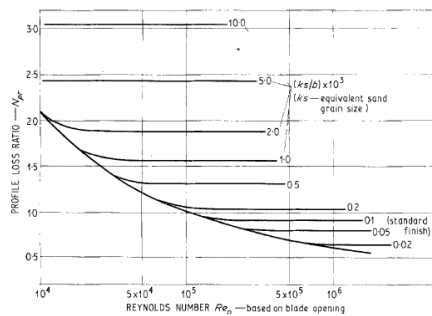


Fig. 3. Profile loss ratio against Reynolds number effect

Figure F.2: Craig & Cox (1971) Fig. 3

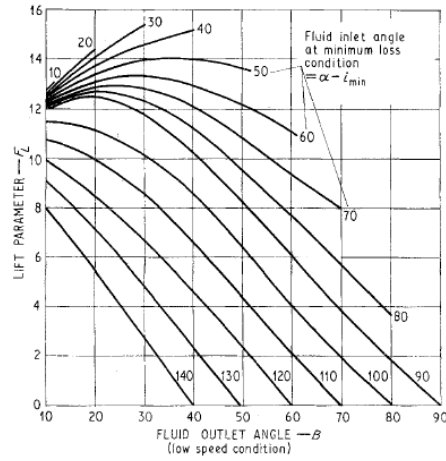


Fig. 4. Lift parameter, F_L

Figure F.3: Craig & Cox (1971) Fig. 4

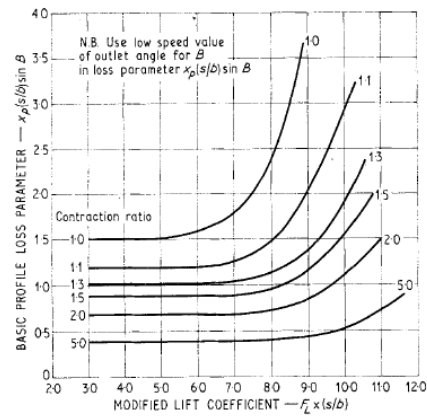


Fig. 5. Basic profile loss

Figure F.4: Craig & Cox (1971) Fig. 5

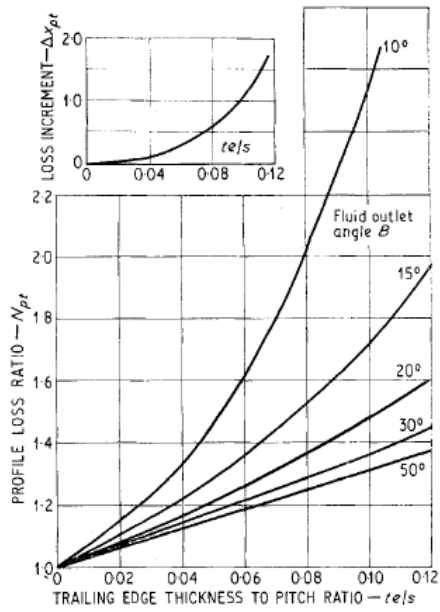


Fig. 6. Trailing edge thickness losses

Figure F.5: Craig & Cox (1971) Fig. 6

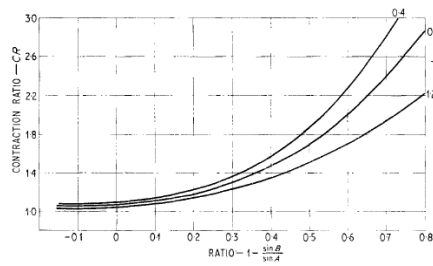


Fig. 7. Contraction ratio for average profiles

Figure F.6: Craig & Cox (1971) Fig. 7

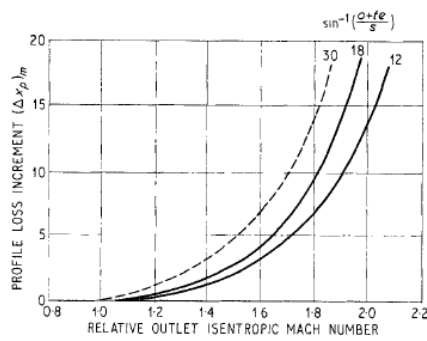


Fig. 8. Mach number loss for convergent blading

Figure F.7: Craig & Cox (1971) Fig. 8

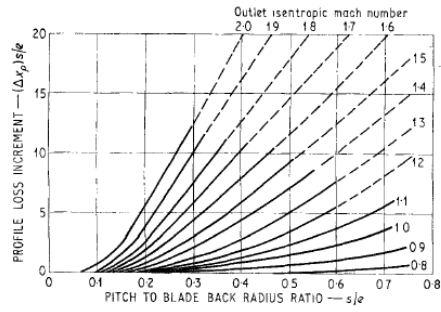


Fig. 9. Blade back radius losses

Figure F.8: Craig & Cox (1971) Fig. 9

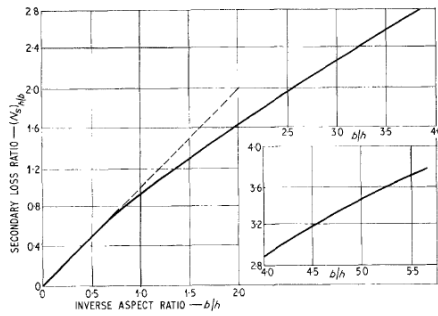


Fig. 17. Secondary loss-aspect ratio factor

Figure F.9: Craig & Cox (1971) Fig. 17

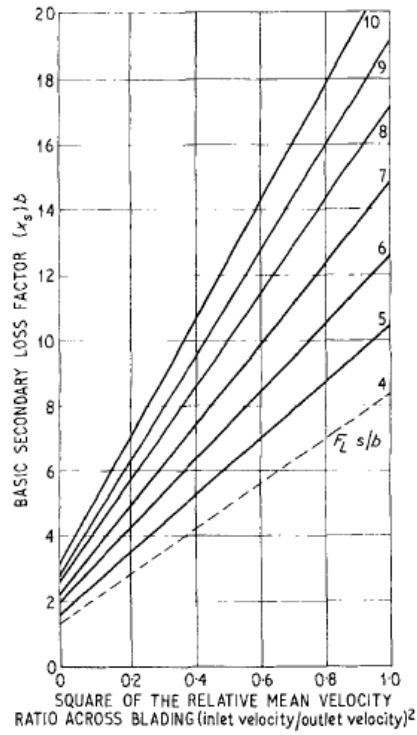


Fig. 18. Secondary loss-basic loss factor

Figure F.10: Craig & Cox (1971) Fig. 18

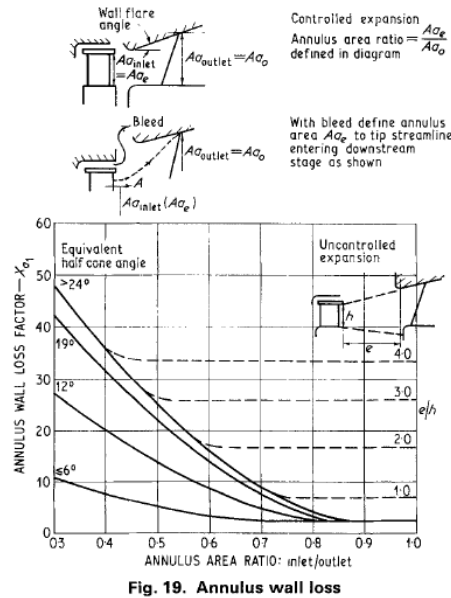


Fig. 19. Annulus wall loss

Figure F.11: Craig & Cox (1971) Fig. 19

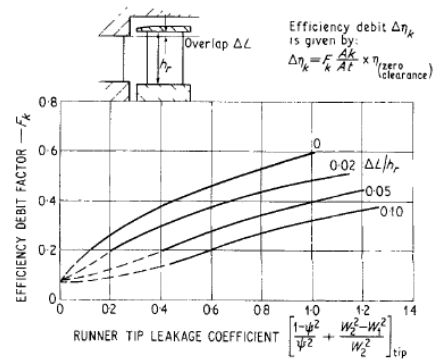


Fig. 21. Shrouded efficiency loss

Figure F.12: Craig & Cox (1971) Fig. 21

G

Validation of the Computational Model

In chapter 5, only a partial description of the validation process for a multi-stage configuration was described. This appendix reports the single-stage validation for the ideal gas model and the multi-stage validation for the real fluid model.

G.1 Ideal Gas Model

G.1.1 Single-Stage Gas Turbine

Stabe et al. (1984)

The validation followed the same path described in Section 5.3 for a real fluid. The input data were the same; they can be found in table 5.5.

The same considerations made for the real fluid model can be repeated for the ideal gas model. Table G.1 reports the results of the validation in terms of turbine performance, blade geometry, thermodynamic states and velocity diagram. The table compares computational and experimental results, reporting the relative error, $\Delta\epsilon_{rel}$. Table G.1 shows that the only parameter affected by a relative error greater than 3% is the fluid outlet angle α_3 , i.e. angle formed by the absolute velocity at the exit of the rotor. However, although the relative error is above the acceptable threshold, the result can be considered satisfying since the absolute error is equal to $\Delta\epsilon_{abs} = 1^\circ$.

Velocity triangles, geometry and T-s diagram at the mean radius were similar to those obtained for an real fluid. They are reported in figures G.1, G.2 and G.3, respectively.

Table G.1: Validation results for the single-stage gas turbine. Ideal gas computational model.

	Comp. Result	Experim. Result	$\Delta\epsilon_{rel}$
Performance			
η_{tt} , [%]	0.891	0.89	0.11 %
P [MW]	0.813	-	-
Geometry			
z_N	26	26	0 %
z_R	49	48	2.041 %
s_N [m]	0.057	0.058	1.7 %
s_R [m]	0.0306	0.0306	0 %
r_m [m]	0.234	0.233	0.47 %
h_2 [m]	0.0364	0.0356	2.292 %
h_3 [m]	0.0359	0.0356	0.956 %
Λ	0.4559	-	-
Thermodynamic States			
T_{02} [K]	422.2	-	-
p_{02} [bar]	2.961	-	-
T_{03} [K]	340.7	-	-
p_{03} [bar]	1.315	-	-
Velocity Triangles			
U_m [m/s]	221	218	1.717 %
$C_{a,2}$ [m/s]	81.2	-	-
$C_{a,3}$ [m/s]	118	-	-
C_2 [m/s]	316.1	-	-
W_3 [m/s]	310.3	-	-
α_2 [°]	75.1	75	0.156 %
β_2 [°]	45.8	45	1.88 %
α_3 [°]	29.2	30.2	3.39 %
β_3 [°]	67.67	67.9	0.373 %
M_2	0.823	0.833	0.85 %
$M_{3,rl}$	0.849	0.863	1.55 %

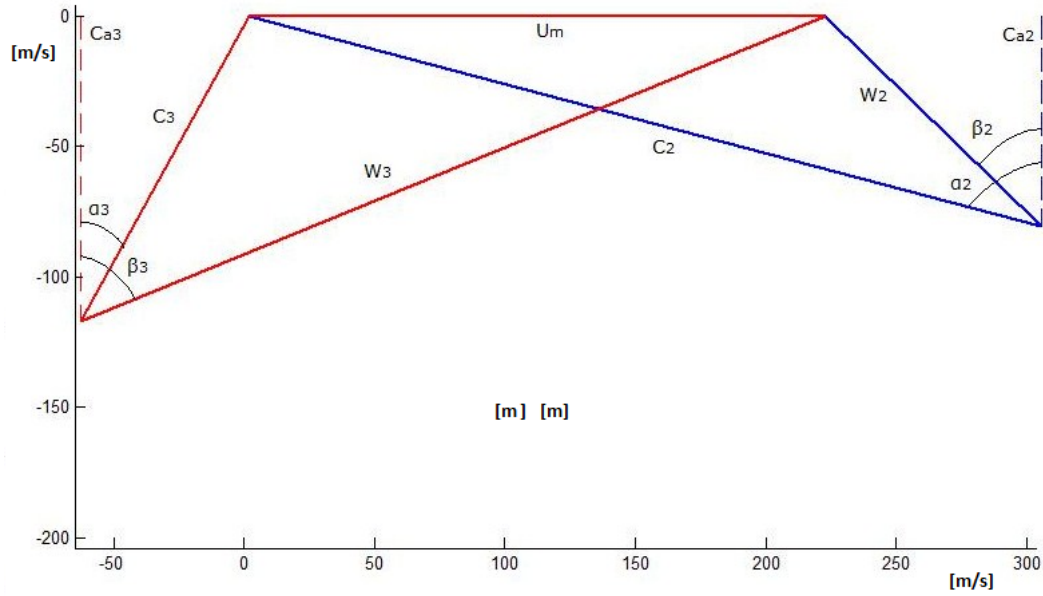


Figure G.1: Velocity triangles for the single-stage gas turbine. Ideal gas computational model.

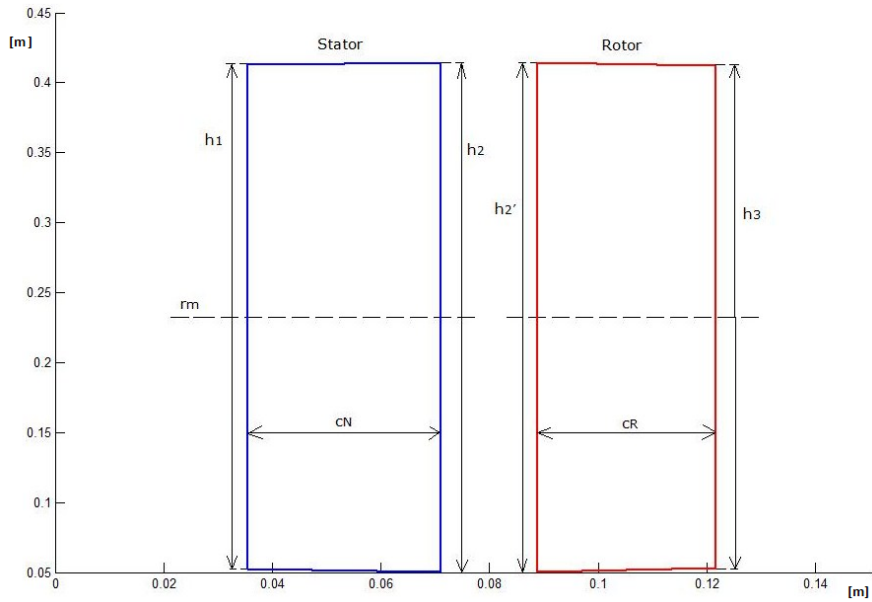


Figure G.2: Blade geometry for the single-stage gas turbine. Ideal gas computational model.

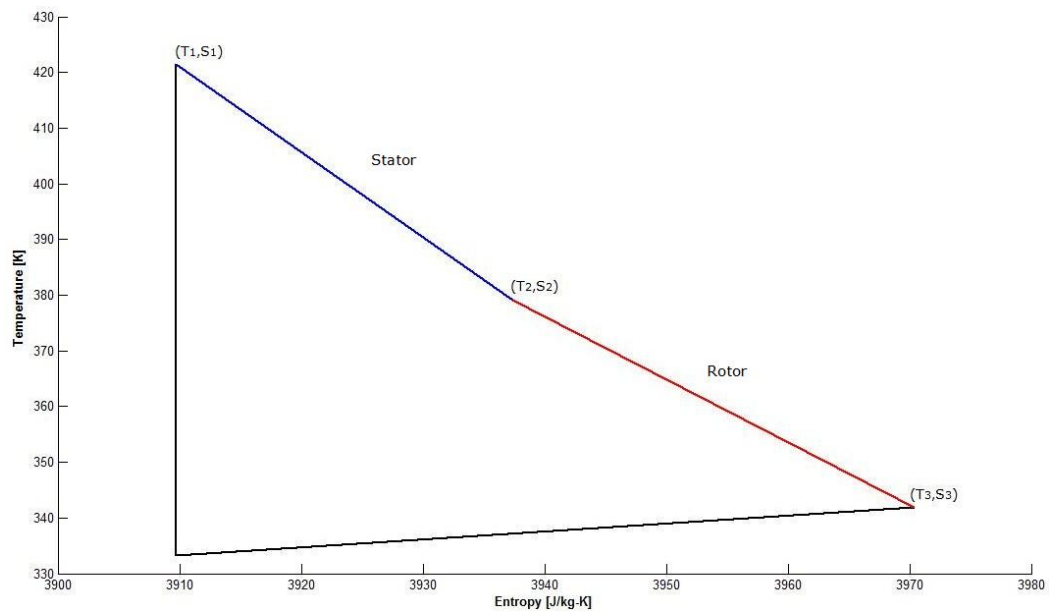


Figure G.3: T-s static diagram for the single-stage gas turbine. Ideal gas computational model.

G.1.2 Multi-Stage Gas Turbine

Kotzing & Evers (1985): Diagrams

Figures G.4 - G.6 show the velocity triangles for the second, third and fourth stage of the expander, respectively.

Figures G.7 - G.8 show the blade geometry for the second and third stage of the expander, respectively.

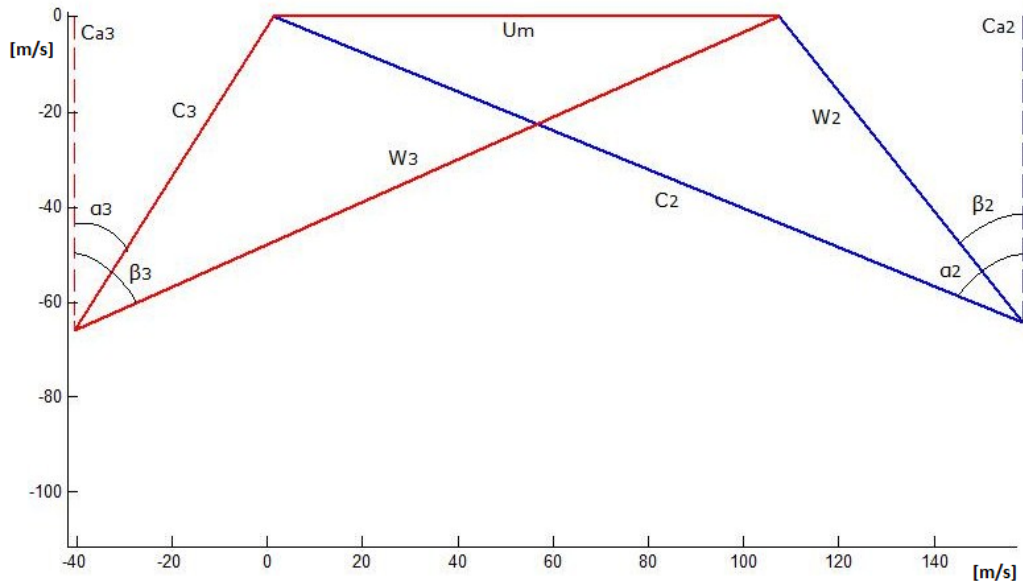


Figure G.4: Velocity triangles for stage 1 of the multi-stage gas turbine. Computational results.

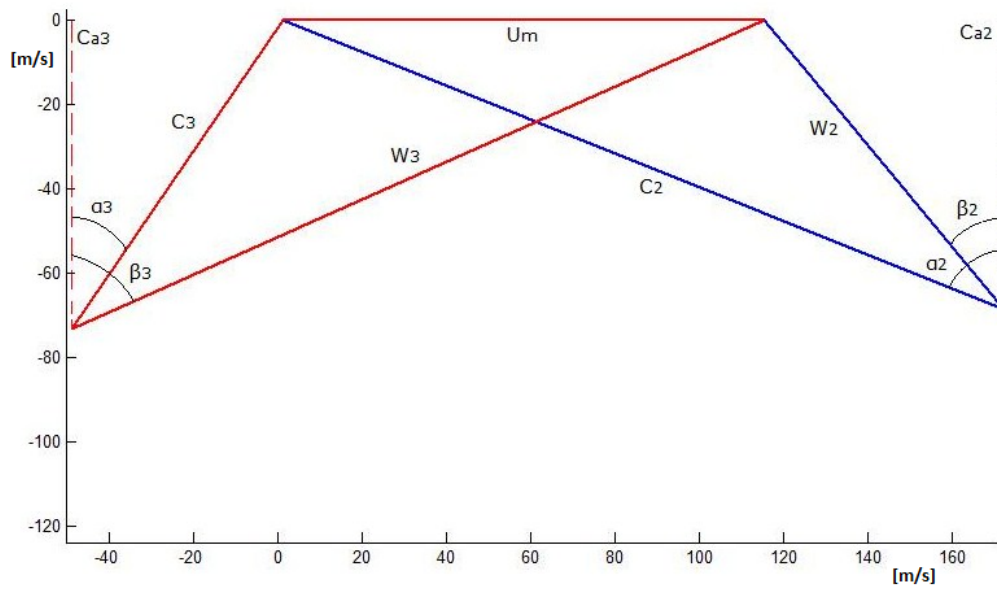


Figure G.5: Velocity triangles for stage 2 of the multi-stage gas turbine. Computational results.

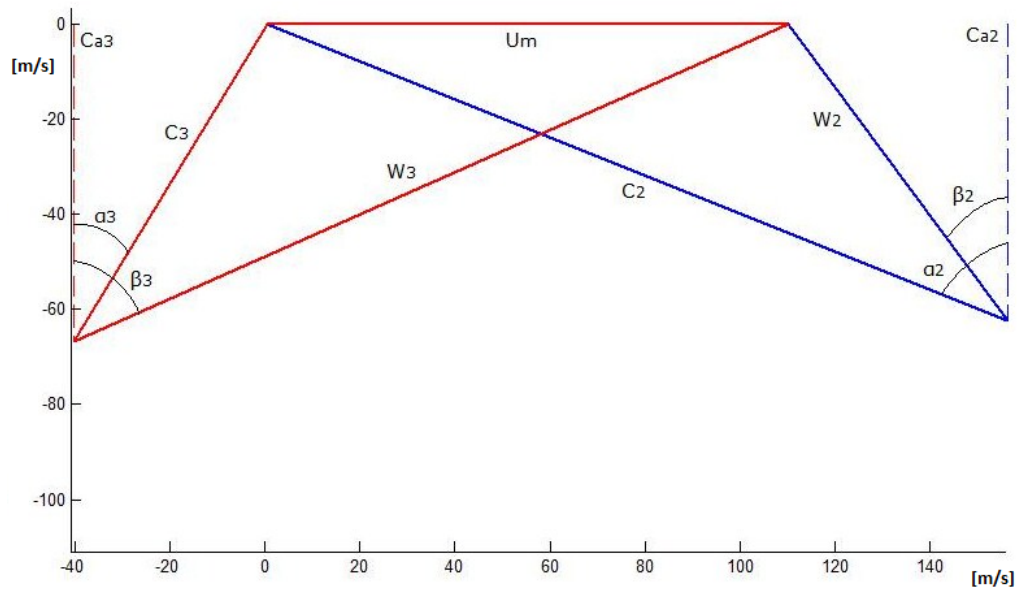


Figure G.6: Velocity triangles for stage 3 of the multi-stage gas turbine. Computational results.

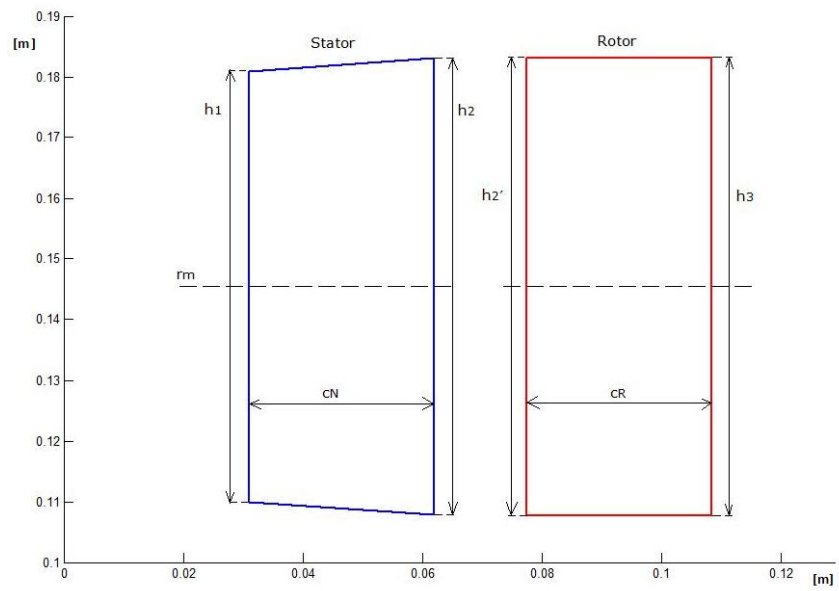


Figure G.7: Blade geometry for stage 2 of the multi-stage gas turbine. Computational result.

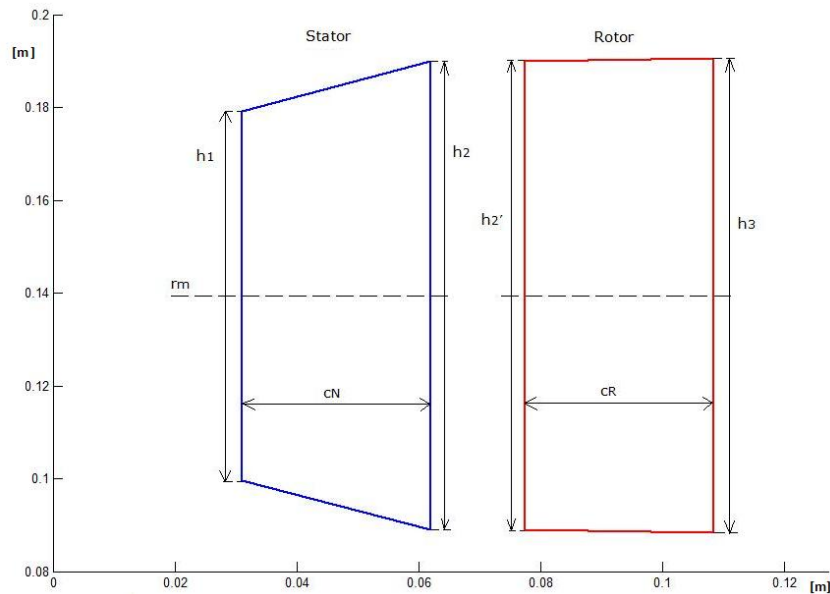


Figure G.8: Blade geometry for stage 3 of the multi-stage gas turbine. Computational result.

G.2 Real Fluid Model

G.2.1 Multi-Stage Gas Turbine

Kotzing & Evers (1985)

The real fluid model was tested for a multi-stage configuration. The input data for the design routine were those of the ideal gas model, reported in table 5.1. Table G.2 shows the validation results for the first two stages, while G.3 displays the those for the third and fourth stage.

The validation gave results very similar to those described in Chapter 5 for the ideal gas model. Table G.4 reports the overall total-to-total efficiency and power output of the four-stage turbine. The computational results proved to be accurate for both the parameters. Figures G.9 - G.12 show the velocity triangles for first, second, third and fourth stage of the expander, respectively.

Furthermore, figures G.13 - G.16 show the blade geometry for first, second, third and fourth stage of the expander, respectively.

Table G.2: Part A - Validation results for Stage 1 and stage 2 of the multi-stage gas turbine. Real fluid computational model.

	Stage 1			Stage 2		
	<i>CR</i>	<i>ER</i>	$\Delta\epsilon_{rel}$	<i>CR</i>	<i>ER</i>	$\Delta\epsilon_{rel}$
Blade Geometry						
h_1 [m]	0.0661	0.064	1.77%	0.0721	-	-
h_2 [m]	0.0723	-	-	0.0763	-	-
h_3 [m]	0.0755	-	-	0.0768	-	-
r_m [m]	0.1357	0.135	0.51%	0.144	0.1425	1.04%
Λ	0.493	0.5	1.42%	0.502	0.5	0.58%
Thermodynamic States						
T_{03} [K]	388.9	384	1.18%	367.1	364	0.58%
p_{03} [bar]	2.10	2.13	1.44%	1.69	1.71	1.58%
p_3 [bar]	2.05	2.08	1.87%	1.65	1.67	1.53%
Velocity Diagram						
U_m [m/s]	106.6	-	-	113.4	-	-
C_3 [m/s]	78.81	78	0.11%	90.09	90	0.11%
α_2 [°]	67.81	68	0.28%	68.16	68	0.23%
β_2 [°]	38.7	39.6	2.47%	39.66	39.6	0.15%
β_3 [°]	66.03	66	0.05%	66.03	66	0.05%
α_3 [°]	22.4	20	10.8%	24.1	20	17.0%
M_2	0.426	-	-	0.473	-	-
$M_{3,rel}$	0.413	-	-	0.467	-	-

Table G.3: Part B - Validation results for the Stage 3 and Stage 4 of the multi-stage gas turbine. Real fluid computational model.

	Stage 3			Stage 4		
	<i>CR</i>	<i>ER</i>	$\Delta\epsilon_{rel}$	<i>CR</i>	<i>ER</i>	$\Delta\epsilon_{rel}$
Blade Geometry						
h_1 [m]	0.0791	-	-	0.098	-	-
h_2 [m]	0.101	-	-	0.104	-	-
h_3 [m]	0.103	-	-	0.104	0.102	2.19%
r_m [m]	0.139	0.161	15.8%	0.146	0.183	25.39%
Λ	0.507	0.5	1.38%	0.495	0.5	0.88%
Thermodynamic States						
T_{03} [K]	345.1	341	1.13%	326.3	319	2.24%
p_{03} [bar]	1.33	1.35	2.16%	1.051	1.05	0.14%
p_3 [bar]	1.28	1.31	2.42%	1.021	1.01	0.96%
Velocity Diagram						
U_m [m/s]	109.8	-	-	114.7	-	-
C_3 [m/s]	76.75	77	0.87%	86.6	86.5	0.28%
α_2 , [°]	68.16	68	0.23%	68.16	68	0.23%
β_2 [°]	38.67	39.6	2.35%	38.75	39.6	2.19%
β_3 [°]	66.03	66	0.05%	66.03	66	0.05%
α_3 [°]	21.87	20	8.55%	22.67	20	11.3%
M_2	0.444	-	-	0.501	-	-
$M_{3,rel}$	0.442	-	-	0.494	-	-

Table G.4: Efficiency and power of the four-stage low speed gas turbine. Real fluid computational model.

	Comp. Result	Experim. Result	$\Delta\epsilon_{rl}$
η_{tt}	0.906	0.913	0.77 %
P [MW]	0.694	0.703	2.59 %

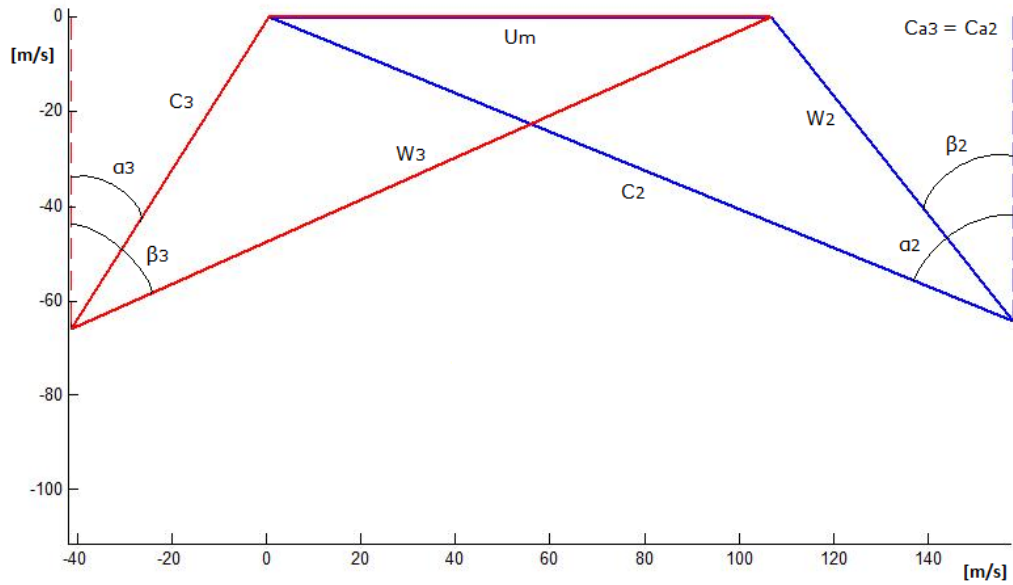


Figure G.9: Velocity triangles of stage 1 of the multi-stage gas turbine. Real fluid computational model.

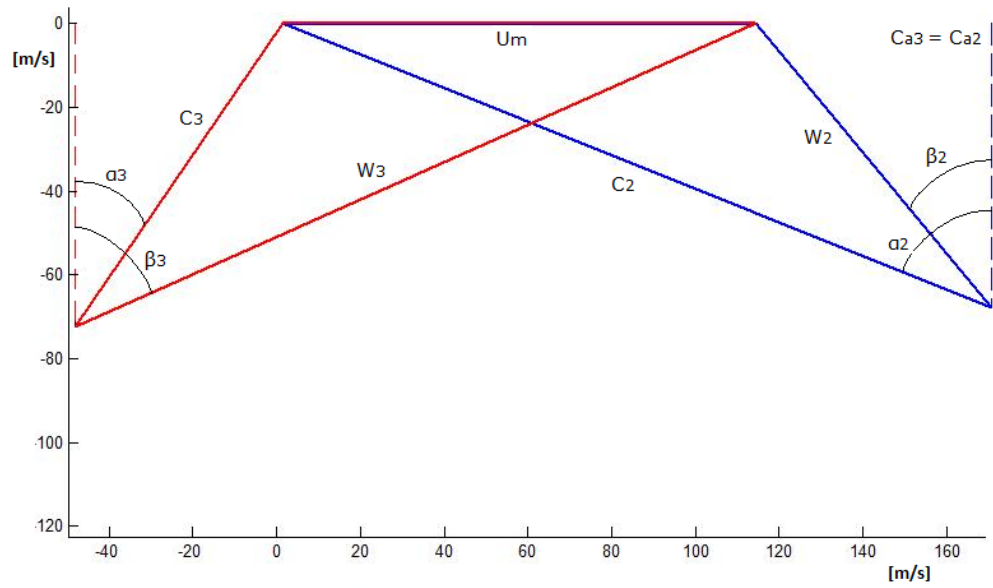


Figure G.10: Velocity triangles of stage 2 of the multi-stage gas turbine. Real fluid computational model.

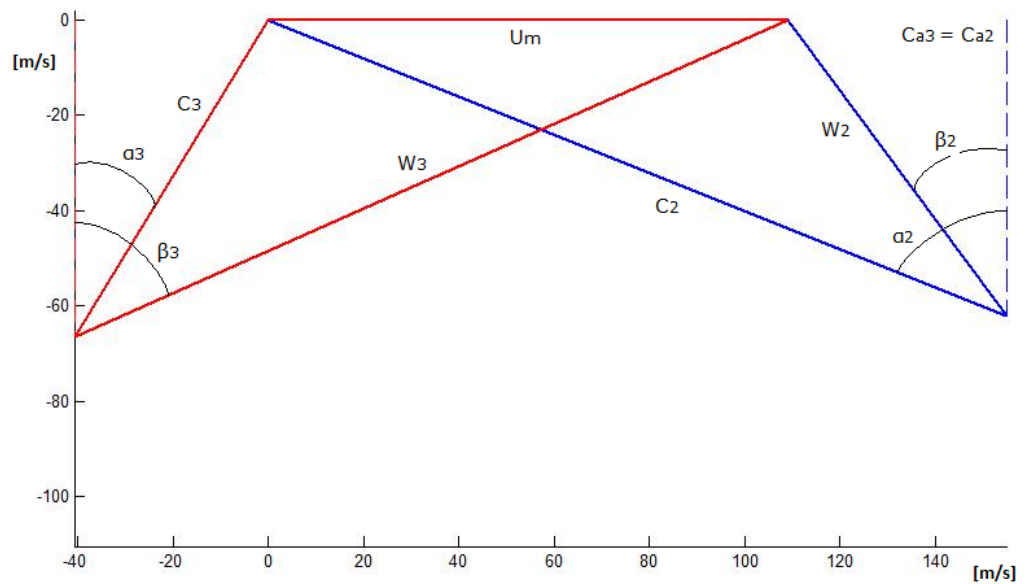


Figure G.11: Velocity triangles of stage 3 of the multi-stage gas turbine. Real fluid computational model.

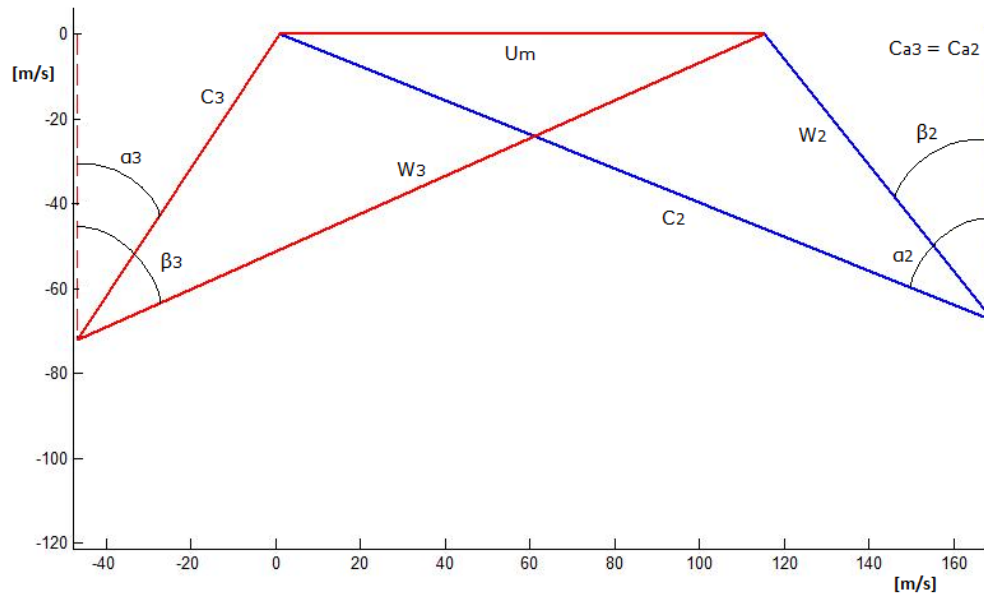


Figure G.12: Velocity triangles of stage 4 of the multi-stage gas turbine. Real fluid computational model.

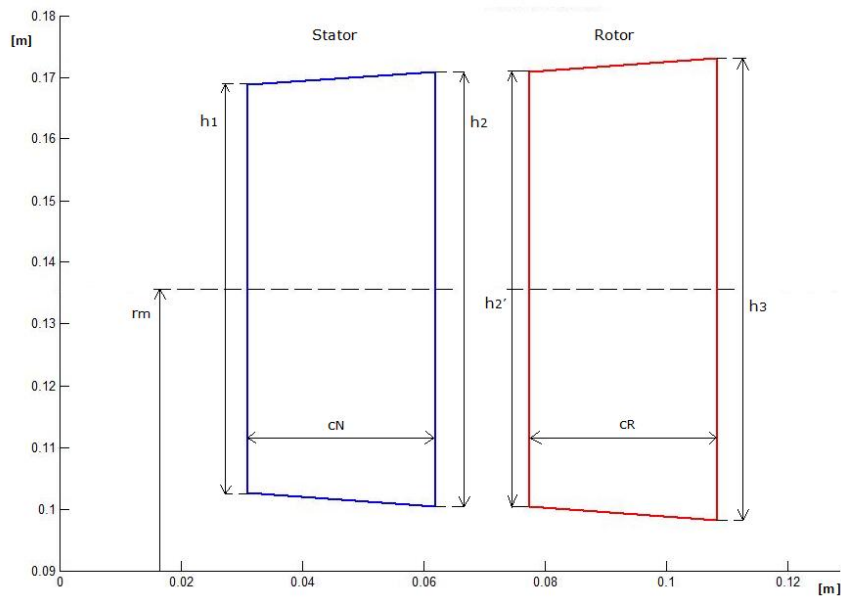


Figure G.13: Blade geometry of stage 1 of the multi-stage gas turbine. Real fluid computational model.

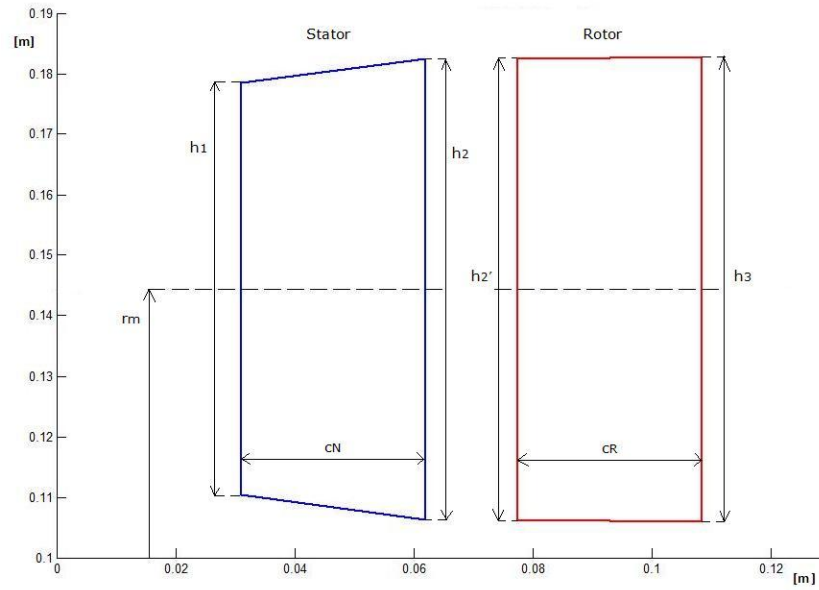


Figure G.14: Blade geometry of stage 2 of the multi-stage gas turbine. Real fluid computational model.

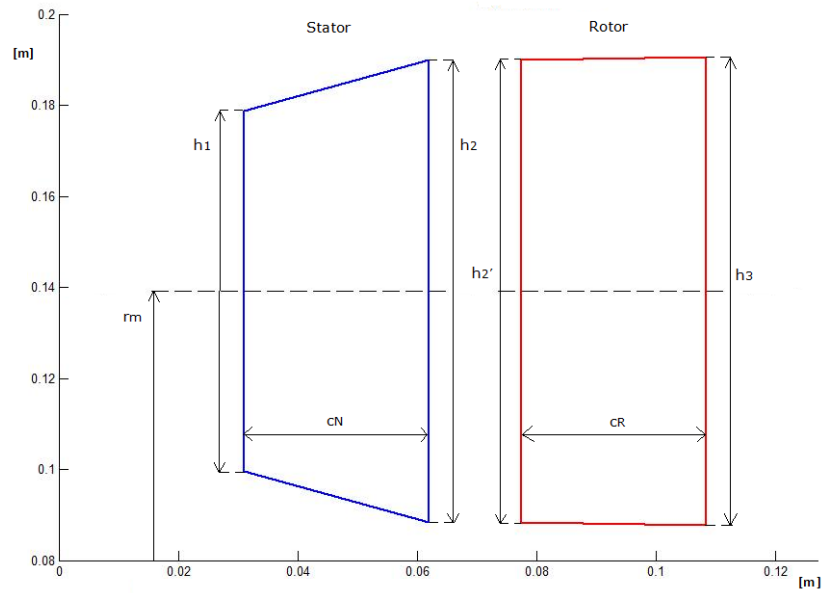


Figure G.15: Blade geometry of stage 3 of the multi-stage gas turbine. Real fluid computational model.

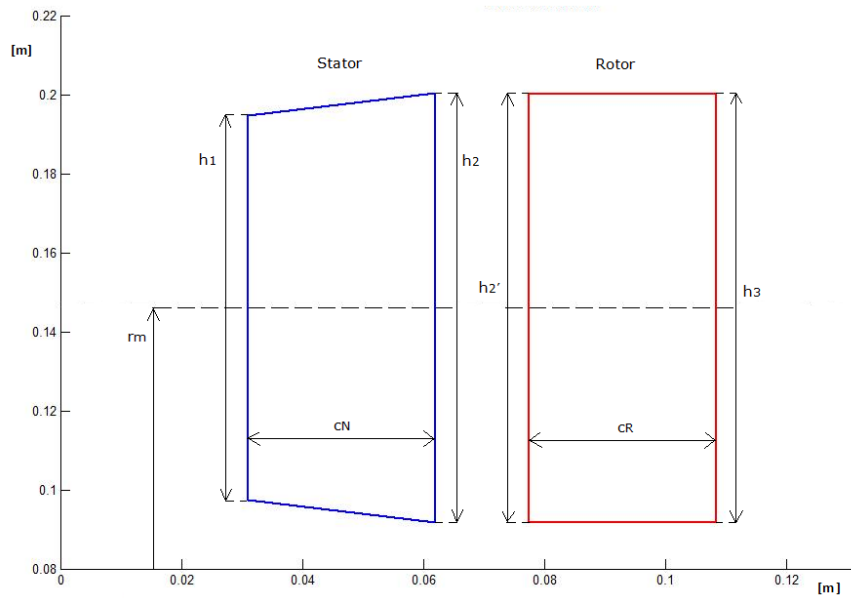


Figure G.16: Blade geometry of stage 4 of the multi-stage gas turbine. Real fluid computational model.

Finally, figure G.17 shows the T-s diagram at mean radius for the four-stage expansion.

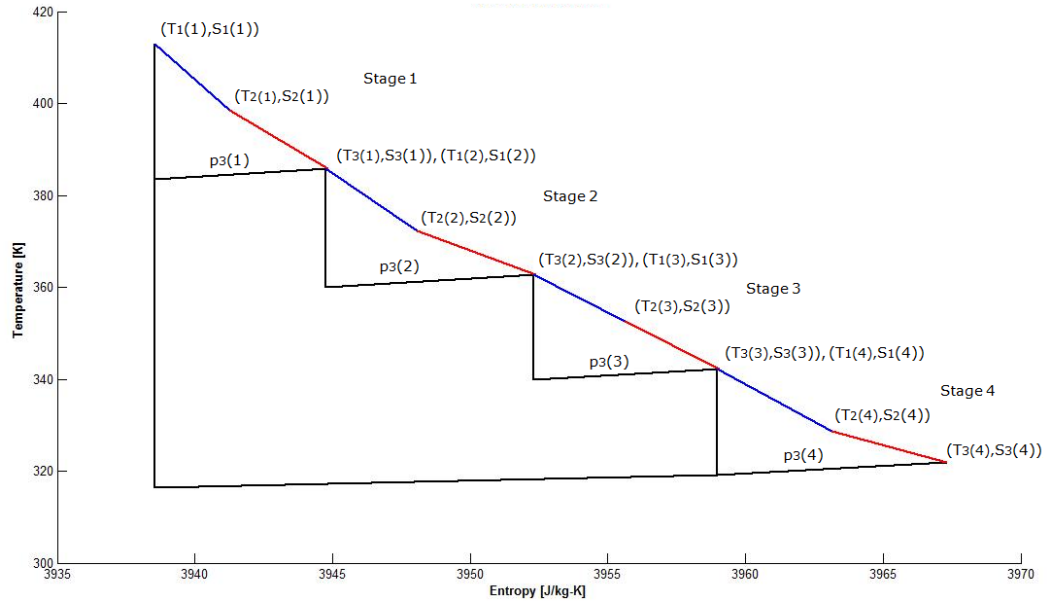


Figure G.17: T-s diagram for the four-stage low speed gas turbine. Real fluid computational model.

H

Optimization Results for Draugen Offshore Platform Applications

This appendix provides the optimization results used to build the efficiency charts for the organic Rankine cycle, the steam Rankine cycle and the air bottoming cycle axial-flow turbines, investigated in the context of the Draugen offshore platform.

H.1 ORC Results

Table H.1: Optimization results for the ORC single-stage axial-flow turbine, $p_{01} = 30$ bar.

\dot{m} [kg/s]	η_{ts}	\dot{V}_{out} [m ³ /s]	\dot{V}_{in} [m ³ /s]	$\frac{V_{ex}}{V_{in}}$	$\frac{\Delta h_{is}^{3/4}}{[m^{3/2}/s^{1/2}]}$	N_s	P [MW]
20	0.685	12.17	0.311	39.14	8469	0.021	2.621
45	0.724	28.85	0.7	41.22	8626	0.0311	5.635
100	0.789	57.19	1.555	36.78	8461	0.045	14.21
200	0.812	117.8	3.111	37.88	8529	0.064	29.52
300	0.818	183.1	4.665	39.24	8599	0.079	45.09
400	0.821	237.3	6.220	38.16	8547	0.090	59.83
500	0.829	290.0	7.775	32.37	8508	0.100	75.04
600	0.818	367.0	9.330	39.34	8604	0.111	90.27
700	0.809	452.7	10.88	41.59	8704	0.122	1.056
800	0.803	480.7	12.44	38.65	8569	0.128	119.4

Table H.2: Optimization results for the ORC single-stage axial-flow turbine, $p_{01} = 20$ bar.

\dot{m} [kg/s]	η_{ts}	\dot{V}_{out} [m ³ /s]	\dot{V}_{in} [m ³ /s]	$\frac{\dot{V}_{ex}}{\dot{V}_{in}}$	$\frac{\Delta h_{is}^{3/4}}{[m^{3/2}/s^{1/2}]}$	Ns	P [MW]
20.00	0.73	12.09	0.53	22.68	8105.25	0.02	2.54
45.00	0.76	30.49	1.20	25.43	8319.60	0.03	5.68
100.00	0.82	59.22	2.66	22.22	8089.57	0.05	13.63
200.00	0.83	122.47	5.33	22.98	8163.85	0.07	28.04
300.00	0.86	174.87	7.99	21.88	8073.96	0.08	42.58
400.00	0.84	236.91	10.66	22.23	8102.19	0.09	56.41
500.00	0.85	306.48	13.32	23.00	8171.58	0.11	71.21
600.00	0.84	387.88	15.99	24.26	8278.43	0.12	86.72
700.00	0.84	418.43	18.65	22.43	8120.31	0.13	98.84
800.00	0.83	485.20	21.32	22.76	8143.66	0.14	111.59

Table H.3: Optimization results for the ORC single-stage axial-flow turbine, $p_{01} = 10$ bar.

\dot{m} [kg/s]	η_{ts}	\dot{V}_{out} [m ³ /s]	\dot{V}_{in} [m ³ /s]	$\frac{\dot{V}_{ex}}{\dot{V}_{in}}$	$\frac{\Delta h_{is}^{3/4}}{[m^{3/2}/s^{1/2}]}$	Ns	P [MW]
20.00	0.74	13.37	1.18	11.37	7158.54	0.03	2.09
45.00	0.81	27.74	2.65	10.45	7000.76	0.04	4.96
100.00	0.86	58.93	5.88	10.02	6916.11	0.06	11.49
200.00	0.86	124.45	11.76	10.59	7039.73	0.08	23.51
300.00	0.87	178.94	17.63	10.15	6949.06	0.10	35.28
400.00	0.87	239.07	23.51	10.17	6954.58	0.11	47.21
500.00	0.85	292.62	29.39	9.96	6899.36	0.12	57.09
600.00	0.81	356.68	35.27	10.11	6920.89	0.14	65.68
700.00	0.84	438.06	41.15	10.65	7045.91	0.15	80.70
800.00	0.83	510.44	47.02	10.85	7085.84	0.16	91.79

Table H.4: Optimization results for the ORC single-stage axial-flow turbine, $p_{01} = 5$ bar.

\dot{m} [kg/s]	η_{ts}	\dot{V}_{out} [m ³ /s]	\dot{V}_{in} [m ³ /s]	$\frac{\dot{V}_{ex}}{\dot{V}_{in}}$	$\frac{\Delta h_{is}^{3/4}}{[m^{3/2}/s^{1/2}]}$	Ns	P [MW]
20.00	0.81	11.99	2.45	4.90	5447.67	0.03	1.58
45.00	0.86	26.52	5.51	4.81	5415.58	0.05	3.75
100.00	0.87	58.98	12.25	4.82	5421.81	0.07	8.47
200.00	0.88	117.38	24.49	4.79	5411.39	0.10	17.07
300.00	0.89	176.30	36.74	4.80	5415.66	0.12	25.74
400.00	0.87	239.17	48.99	4.88	5456.25	0.14	34.04
500.00	0.84	311.43	61.24	5.09	5552.98	0.16	42.01
600.00	0.83	377.84	73.48	5.14	5578.09	0.17	50.07
700.00	0.77	443.25	85.73	5.17	5573.58	0.19	53.67
800.00	0.83	510.44	47.02	10.85	7085.84	0.16	91.79

H.2 SRC Results

Table H.5: Optimization results for the SRC single-stage axial-flow turbine, $p_{01} = 12.57$ bar (design pressure).

\dot{m} [kg/s]	η_{ts}	\dot{V}_{out} [m ³ /s]	\dot{V}_{in} [m ³ /s]	$\frac{V_{ex}}{V_{in}}$	$\frac{\Delta h_{is}^{3/4}}{[m^{3/2}/s^{1/2}]}$	Ns	P [MW]
5.00	0.76	83.24	1.14	73.06	29487.00	0.06	3.71
7.22	0.81	143.30	1.66	86.16	30104.60	0.08	5.64
10.00	0.81	184.26	2.28	80.86	29912.50	0.09	7.98
15.00	0.81	270.66	3.42	79.18	29830.00	0.11	11.85
20.00	0.83	361.74	4.56	79.37	29848.60	0.12	15.93
24.00	0.83	409.21	5.47	74.82	29490.10	0.13	19.21
30.00	0.81	482.98	6.61	73.09	29582.60	0.14	23.28
35.00	0.79	608.21	7.98	76.26	29654.80	0.16	26.51

H.3 ABC Results

Table H.6: Optimization results for the ABC single-stage axial-flow turbine, $p_{01} = 2.46$ bar (design pressure).

\dot{m} [kg/s]	η_{ts}	\dot{V}_{out} [m ³ /s]	\dot{V}_{in} [m ³ /s]	$\frac{V_{ex}}{V_{in}}$	$\frac{\Delta h_{is}^{3/4}}{[m^{3/2}/s^{1/2}]}$	Ns	P [MW]
5.00	0.78	7.48	3.58	2.09	7585.12	0.01	0.59
10.00	0.83	14.64	7.16	2.05	7524.18	0.03	1.24
20.00	0.84	29.24	14.32	2.04	7601.04	0.04	2.60
50.00	0.87	71.88	35.80	2.01	7491.63	0.06	6.54
87.50	0.89	124.01	62.65	1.98	7399.07	0.09	11.50
140.00	0.87	204.54	100.24	2.04	7635.70	0.11	18.61
200.00	0.86	286.96	143.20	2.00	7475.45	0.14	26.14
250.00	0.85	367.15	179.00	2.05	7655.35	0.15	32.95

I

Optimization Results for the Fluid Comparison Application

This appendix provides the optimization results used to build the efficiency charts for the cyclopentane, MDM and R245fa axial-flow turbines.

I.1 Cyclopentane Results

Table I.1: Optimization results for the cyclopentane single-stage axial-flow turbine, $p_{01} = 40$ bar.

\dot{m} [kg/s]	η_{ts}	\dot{V}_{out} [m ³ /s]	\dot{V}_{in} [m ³ /s]	$\frac{\dot{V}_{ex}}{\dot{V}_{in}}$	$\frac{\Delta h_{is}^{3/4}}{[m^{3/2}/s^{1/2}]}$	Ns	P [MW]
20.00	0.74	13.37	1.18	11.37	7158.54	0.03	2.09
72.09	0.79	27.74	2.65	10.45	7000.76	0.04	5.45
100.00	0.84	58.93	5.88	10.02	6916.11	0.06	11.49
200.00	0.85	124.45	11.76	10.59	7039.73	0.08	23.51
300.00	0.86	178.94	17.63	10.15	6949.06	0.10	35.28
400.00	0.86	239.07	23.51	10.17	6954.58	0.11	47.21
500.00	0.84	292.62	29.39	9.96	6899.36	0.12	57.09
600.00	0.82	356.68	35.27	10.11	6920.89	0.14	65.68
700.00	0.83	438.06	41.15	10.65	7045.91	0.15	80.70
800.00	0.83	510.44	47.02	10.85	7085.84	0.16	91.79

Table I.2: Optimization results for the cyclopentane single-stage axial-flow turbine, $p_{01} = 30$ bar.

\dot{m} [kg/s]	η_{ts}	\dot{V}_{out} [m ³ /s]	\dot{V}_{in} [m ³ /s]	$\frac{\dot{V}_{ex}}{\dot{V}_{in}}$	$\frac{\Delta h_{is}^{3/4}}{[m^{3/2}/s^{1/2}]}$	N_s	P [MW]
20.00	0.77	12.68	1.81	8.14	6303.11	0.03	1.84
72.09	0.83	27.13	4.08	7.63	6208.17	0.04	4.36
100.00	0.84	58.95	9.06	7.42	6168.96	0.06	9.98
200.00	0.87	120.92	18.13	7.69	6225.56	0.09	20.29
300.00	0.88	177.62	27.19	7.47	6182.36	0.11	30.51
400.00	0.87	239.12	36.25	7.52	6205.42	0.13	40.62
500.00	0.84	302.03	45.31	7.52	6226.17	0.14	49.55
600.00	0.83	367.26	54.38	7.63	6249.49	0.16	57.87
700.00	0.81	440.66	63.44	7.91	6309.75	0.17	67.19
800.00	0.82	510.44	47.02	10.85	7085.84	0.16	81.32

Table I.3: Optimization results for the cyclopentane single-stage axial-flow turbine, $p_{01} = 20$ bar.

\dot{m} [kg/s]	η_{ts}	\dot{V}_{out} [m ³ /s]	\dot{V}_{in} [m ³ /s]	$\frac{\dot{V}_{ex}}{\dot{V}_{in}}$	$\frac{\Delta h_{is}^{3/4}}{[m^{3/2}/s^{1/2}]}$	N_s	P [MW]
20.00	0.80	11.99	2.45	4.90	5447.67	0.03	1.58
72.09	0.85	26.52	5.51	4.81	5415.58	0.05	3.75
100.00	0.88	58.98	12.25	4.82	5421.81	0.07	8.47
200.00	0.89	117.38	24.49	4.79	5411.39	0.10	17.07
300.00	0.89	176.30	36.74	4.80	5415.66	0.12	25.74
400.00	0.87	239.17	48.99	4.88	5456.25	0.14	34.04
500.00	0.84	311.43	61.24	5.09	5552.98	0.16	42.01
600.00	0.83	377.84	73.48	5.14	5578.09	0.17	50.07
700.00	0.82	443.25	85.73	5.17	5573.58	0.19	58.67
800.00	0.82	510.44	47.02	10.85	7085.84	0.16	69.78

I.2 MDM Results

Table I.4: Optimization results for the MDM single-stage axial-flow turbine, $p_{01} = 13$ bar.

\dot{m} [kg/s]	η_{ts}	\dot{V}_{out} [m ³ /s]	\dot{V}_{in} [m ³ /s]	$\frac{\dot{V}_{ex}}{\dot{V}_{in}}$	$\frac{\Delta h_{is}^{3/4}}{[m^{3/2}/s^{1/2}]}$	Ns	P [MW]
20.00	0.73	2.23	0.24	9.29	2384.28	0.03	0.48
50.00	0.79	5.52	0.61	9.01	2374.84	0.05	1.29
95.64	0.83	10.66	1.15	9.27	2385.84	0.07	2.61
200.00	0.85	22.15	2.41	9.21	2379.79	0.10	5.52
300.00	0.85	33.59	3.61	9.31	2390.61	0.12	8.38
400.00	0.83	45.90	4.81	9.54	2413.33	0.14	11.07
500.00	0.82	57.91	6.01	9.63	2421.96	0.16	13.76
600.00	0.81	70.61	7.22	9.79	2436.21	0.17	16.19
700.00	0.80	83.91	8.42	9.96	2448.30	0.19	18.58

Table I.5: Optimization results for the MDM single-stage axial-flow turbine, $p_{01} = 8.5$ bar.

\dot{m} [kg/s]	η_{ts}	\dot{V}_{out} [m ³ /s]	\dot{V}_{in} [m ³ /s]	$\frac{\dot{V}_{ex}}{\dot{V}_{in}}$	$\frac{\Delta h_{is}^{3/4}}{[m^{3/2}/s^{1/2}]}$	Ns	P [MW]
20.00	0.76	2.50	0.43	5.76	2162.23	0.04	0.44
50.00	0.82	5.67	1.08	5.22	2171.72	0.05	1.19
95.64	0.85	10.74	2.07	5.18	2163.44	0.08	2.34
200.00	0.86	22.05	4.34	5.08	2165.42	0.11	4.97
300.00	0.85	34.15	6.51	5.25	2177.36	0.13	7.46
400.00	0.84	46.28	8.68	5.33	2193.11	0.16	9.78
500.00	0.82	58.92	10.85	5.43	2211.15	0.17	12.02
600.00	0.80	74.32	13.02	5.71	2260.94	0.19	14.30
700.00	0.76	90.17	15.19	5.94	2299.38	0.21	16.29

Table I.6: Optimization results for the MDM single-stage axial-flow turbine, $p_{01} = 4$ bar.

\dot{m} [kg/s]	η_{ts}	\dot{V}_{out} [m ³ /s]	\dot{V}_{in} [m ³ /s]	$\frac{\dot{V}_{ex}}{\dot{V}_{in}}$	$\frac{\Delta h_{is}^{3/4}}{[m^{3/2}/s^{1/2}]}$	Ns	P [MW]
20.00	0.80	2.13	1.04	2.05	1462.28	0.05	0.27
50.00	0.86	5.58	2.60	2.15	1419.29	0.08	0.70
95.64	0.88	10.63	4.97	2.14	1415.09	0.12	1.34
200.00	0.85	23.12	10.38	2.23	1461.51	0.16	4.34
300.00	0.82	35.05	15.57	2.25	1451.51	0.20	6.19

I.3 R245fa Results

Table I.7: Optimization results for the R245fa single-stage axial-flow turbine, $p_{01} = 33$ bar.

\dot{m} [kg/s]	η_{ts}	\dot{V}_{out} [m ³ /s]	\dot{V}_{in} [m ³ /s]	$\frac{\dot{V}_{ex}}{\dot{V}_{in}}$	$\frac{\Delta h_{is}^{3/4}}{[m^{3/2}/s^{1/2}]}$	Ns	P [MW]
50.00	0.73	0.93	0.05	18.22	1345.54	0.04	0.80
100.00	0.77	2.26	0.14	16.67	1210.21	0.06	1.68
202.40	0.83	3.02	0.21	14.57	1170.87	0.07	3.29
300.00	0.74	4.35	0.31	14.17	1138.86	0.09	5.29
400.00	0.73	6.33	0.41	15.47	1205.07	0.10	7.31
500.00	0.70	7.31	0.51	14.29	1146.82	0.12	8.88

Table I.8: Optimization results for the R245fa single-stage axial-flow turbine, $p_{01} = 24$ bar.

\dot{m} [kg/s]	η_{ts}	\dot{V}_{out} [m ³ /s]	\dot{V}_{in} [m ³ /s]	$\frac{\dot{V}_{ex}}{\dot{V}_{in}}$	$\frac{\Delta h_{is}^{3/4}}{[m^{3/2}/s^{1/2}]}$	Ns	P [MW]
20.00	0.68	0.50	0.18	2.74	1730.91	0.02	0.28
50.00	0.77	1.25	0.46	2.73	1732.12	0.03	0.70
100.00	0.83	2.42	0.91	2.64	1697.64	0.05	1.39
202.40	0.85	4.88	1.85	2.63	1694.78	0.07	2.81
300.00	0.87	7.20	2.74	2.62	1691.85	0.08	4.17
400.00	0.87	10.04	3.66	2.74	1750.37	0.09	5.56
500.00	0.89	11.89	4.57	2.60	1680.51	0.10	6.95
600.00	0.89	14.43	5.49	2.63	1692.21	0.11	8.34
700.00	0.88	16.70	6.40	2.61	1684.72	0.12	9.73
800.00	0.88	19.23	7.32	2.63	1694.02	0.13	11.13
900.00	0.87	22.13	8.23	2.69	1723.43	0.14	12.50

Appendix I. Optimization Results for the Fluid Comparison Application

Table I.9: Optimization results for the R245fa single-stage axial-flow turbine, $p_{01} = 17$ bar.

\dot{m} [kg/s]	η_{ts}	\dot{V}_{out} [m ³ /s]	\dot{V}_{in} [m ³ /s]	$\frac{\dot{V}_{ex}}{\dot{V}_{in}}$	$\frac{\Delta h_{is}^{3/4}}{[m^{3/2}/s^{1/2}]}$	Ns	P [MW]
20.00	0.75	0.54	0.29	1.88	1417.14	0.03	0.26
50.00	0.83	1.27	0.72	1.76	1316.22	0.04	0.59
100.00	0.88	2.51	1.44	1.75	1305.55	0.06	1.19
202.40	0.90	5.08	2.91	1.75	1307.03	0.09	2.56
300.00	0.89	7.58	4.31	1.76	1314.86	0.10	3.75
400.00	0.88	10.12	5.75	1.76	1318.14	0.12	5.08
500.00	0.88	12.52	7.18	1.74	1302.74	0.14	6.27
600.00	0.88	15.16	8.62	1.76	1315.96	0.15	7.26
700.00	0.88	17.73	10.06	1.76	1320.10	0.16	8.87
800.00	0.87	20.33	11.49	1.77	1323.90	0.17	10.08

*Una dedica e un ringraziamento devono essere fatti, nella lingua
nativa,*

*Alla mia famiglia, per il supporto incondizionato, per quanto mi
hanno dato e per quello che mi hanno insegnato...*

*Agli amici di sempre, per farmi vivere ogni ritorno come se non fossi
mai partito...*

*Ai compagni di classe, per avere condiviso questo faticoso viaggio,
rendendolo quasi piacevole...*

*Al Californian Team, per avere condiviso con me l'esperienza più
bella della mia vita...*

*Un ringraziamento speciale va a Enrica per farmi ridere quando son
triste e per rendere possibile qualsiasi traguardo...*